University of Bath

PHD

Reduction of axial piston pump pressure ripple

Harrison, Adrian M.

Award date:
1997

Awarding institution:
University of Bath

Link to publication

Alternative formats
If you require this document in an alternative format, please contact:
openaccess@bath.ac.uk

Copyright of this thesis rests with the author. Access is subject to the above licence, if given. If no licence is specified above, original content in this thesis is licensed under the terms of the Creative Commons Attribution-NonCommercial 4.0 International (CC BY-NC-ND 4.0) Licence (https://creativecommons.org/licenses/by-nc-nd/4.0/). Any third-party copyright material present remains the property of its respective owner(s) and is licensed under its existing terms.

Take down policy
If you consider content within Bath's Research Portal to be in breach of UK law, please contact: openaccess@bath.ac.uk with the details. Your claim will be investigated and, where appropriate, the item will be removed from public view as soon as possible.

Download date: 05. May. 2023

Reduction of Axial Piston Pump Pressure Ripple

Submitted by Adrian M. Harrison
for the degree of PhD of the University of Bath 1997

COPYRIGHT

Attention is drawn to the fact that copyright of this thesis rests with its author. This copy of the thesis has been supplied on the condition that anyone who consults it is understood to recognise that its copyright rests with its author and that no quotation from the thesis and no information derived from it may be published without the prior written consent of the author.

This thesis may not be consulted, photocopied or lent to other libraries without the permission of the author and Vickers Inc. of Omaha, Nebraska U.S.A. for 3 years from the date of acceptance of the thesis.

A. M. Harrison

UMI Number: U602174

All rights reserved

INFORMATION TO ALL USERS
The quality of this reproduction is dependent upon the quality of the copy submitted.

In the unlikely event that the author did not send a complete manuscript
and there are missing pages, these will be noted. Also, if material had to be removed,
a note will indicate the deletion.

UMI U602174
Published by ProQuest LLC 2014. Copyright in the Dissertation held by the Author.
Microform Edition © ProQuest LLC.
All rights reserved. This work is protected against
unauthorized copying under Title 17, United States Code.

ProQuest LLC
789 East Eisenhower Parkway
P.O. Box 1346
Ann Arbor, MI 48106-1346

UNIVERSITY OF BATH
LIBRARY
31 - 9 DEC 1997
PH. D.
5118175

Summary

Pressure ripple is a major cause of noise within fluid power systems. Pumps are often the main source of pressure ripple within a system, and axial piston pumps are particularly strong generators. This is a major problem because axial piston pumps are widely used.

The pressure ripple and the associated flow ripple from a commercially available axial piston pump have been measured using the "Secondary source" technique. From the results of this test programme, a digital computer model of the pressures and flows within the cylinders of an axial piston pump has been enhanced and validated. The model operates within the Bathfp environment and has been improved to speed up its operation and to provide information on the swashplate forces and moments.

Using the improved computer model, the performance of a conventional 9 cylinder pump has been compared with that of a similar capacity 10 cylinder pump, and also with a pump featuring solid pistons.

A literature survey has been carried out to assess previous methods for reducing hydraulic system pressure ripple. From this survey, a small number of novel or derivative mechanisms are proposed. Two of these mechanisms were developed further during this project.

One mechanism relies on interference of the pump flow ripple using flow pulses from a specially designed rotary valve. Interference testing has been carried out to prove the concept. However, as a result of this investigation, it is concluded that the concept is unlikely to be commercially viable in its present form.

The second mechanism has been built as an inexpensive modification to a commercially-available axial piston pump. It uses heavily damped check valves (HDCVs) to gradually equalise cylinders to the delivery pressure before they meet a delayed delivery port. Test results from the prototype of this concept are very promising: it produces significant reductions in the delivery pressure ripple and pump casing airborne noise over a wide range of delivery pressures and pump displacements.

The Bathfp simulation model has been extended to predict the behaviour of the HDCV prototype. The effectiveness of the model has been assessed with measurements of the prototype delivery flow ripple. Despite only achieving partial agreement, the model has been helpful in aiding understanding in the interpretation of the delivery flow ripple measurements.

The HDCV prototype is still in the early stages of development. Further work is needed to improve its performance and its reliability.

Acknowledgements

Many people have contributed to the work presented in this thesis. Firstly, I would like to thank my supervisors Prof. Kevin Edge and Dr. Nigel Johnston. Both have provided much needed technical support, particularly in the understanding of the generation and transmission of fluidborne noise. Kevin has also helped greatly in the direction that the project has taken: without his input I would have chased many more wild geese.

From Vickers at Omaha, I must thank Les Claar for his help throughout the course of the project, and specifically for providing a number of one-off components required for testing.

I am indebted to Richard Harris for supplying me with the "Cappa suite" of Bathfp pump models, all of which have worked faultlessly during the duration of the project. I must also thank Derek Tilley. Luke Hickson, Ian James, Johnny Fung and especially Julian Lo for their very valuable help with Bathfp.

The various test arrangements used during the project were built by Joe Wankowski. He was great to work with and was always available when something went wrong. The machining during the project was carried out by John Fortune and Guy Brace and problems with the rig instrumentation were dealt with by Steve Coombes. I must also thank Peter Prest for the design of the phased-lock loop control circuitry and test arrangement.

Contents

Notation

Airborne Noise

P	Sound Pressure
P_o	Reference Sound Pressure
SPL	Sound Pressure Level
SWL	Sound Power Level
W	Sound Power
W_0	Reference Sound Power

Characteristics of fluidborne Noise

γ	Wave propagation constant / polytropic index
ρ_S	Source reflection coefficient
ρ_T	Termination reflection coefficient
ω	Harmonic frequency
ξ	Complex coefficient representing fluid viscosity effects
A	Pipe cross sectional area
A_P	Discharge passageway cross sectional area
B_{eff}	Effective bulk modulus
B_{oil}	Oil bulk modulus
B_{PV}	Volumetric stiffness of a pressure vessel
C	Compressibility
c_o	Local sonic velocity
F	Forward travelling pressure wave at x=0
G	Forward travelling flow wave at x=0
L	Length of pipeline / Inertia
L_P	Length of pump discharge passageway
j	Square root of -1
P	Pressure
P_i	Pressure at inlet of uniform pipeline (in Appendix A)
P_o	Pressure in pipeline at x=0 / Pressure at outlet of uniform pipeline (in Appendix A)
P_x	Pressure in pipeline at distance from pump exit - x
Q_i	Flow at inlet of uniform pipeline (in Appendix A)
Q_o	Flow ripple in pipeline at x=0 / Flow at outlet of uniform pipeline (in Appendix A)
Q_{S_*}	Flow ripple at the pump exit
Q_S	Flow ripple referred to the inner end of the discharge passageway
Q_{S2}	Flow ripple of the secondary source
R	Resistance
V_{air}	Volume fraction of free air
V_P	Effective pump discharge volume
x	Distance along pipeline from pump
Z_E	Entry impedance of the hydraulic circuit
Z_O	Characteristic impedance of pipe
Z_{OP}	Characteristic impedance of pump discharge passageway
Z_S	Source impedance
Z_T	Termination impedance

Operation of an axial-piston pump

α	Angle of the 1st cylinder port passing over BDC (in the "Dual Cylinder" simulations)
β	Swashplate inclined angle at full displacement
β_l	Angle of the 2nd cylinder port passing over BDC (in the "Dual Cylinder" simulations)
ϕ	Projection of θ in the plane of the swashplate
Γ_{cyl}	Cylinder integral area function
Γ_{del}	Delivery port integral area function
Γ_{gr}	Relief groove integral area function
η_v	Volumetric Efficiency
φ	Optimum delivery port delay
θ	Rotation of piston i from BDC

ρ	Density
σ	Cylinder port angular width
ω	Cylinder block angular velocity
ΔP_r	Pressure rise through the pump.
A_{del}	Flow area through the delivery port
A_P	Piston face area
A_{orif}	Flow area between cylinder and delivery or suction ports
A_{suc}	Flow area through the suction port
C_d	Discharge coefficient
C_q	Flow coefficient for flow between cylinder and delivery port
f_x	Piston force in the direction of the yoke axis
f_y	Piston force in the direction of the dead centre axis
f_z	Axial Piston Force
f_p	Pumping frequency
i	Piston number
K_{LC}	Cylinder leakage constant
L_{mean}	Effective mean cylinder length
m	piston mass
m_x	Yoke moment acting to de-swash the pump
m_y	Moment about dead centre axis acting from the delivery to the suction port
m_z	Shaft torque acting against the prime mover
n	Number of pistons in pump
P_{del}	Delivery Pressure
P_{cyl}	Cylinder Pressure
P_{orif}	Instantaneous pressure drop for the flow between cylinder and delivery port
P_{suc}	Suction Pressure
q_{del}	Cylinder inflow through the delivery port
q_{comp}	Drop in mean delivery flowrate caused by compressibility
q_{ideal}	Maximum theoretical pump flowrate
q_{kin}	Kinematic flow function used in the "Dual Cylinder" simulations
q_L	Total pump cylinder leakage flowrate
q_{leak}	Individual cylinder leakage flowrate
q_{max}	Maximum pump kinematic flowrate
q_{min}	Minimum pump kinematic flowrate
q_{net}	Net cylinder inflow
q_{pist}	Cylinder inflow due to the motion of a single piston
q_{suc}	Cylinder inflow through the suction port
R	Cylinder port pitch circle radius
t	Simulation time
totalq	Total pump delivery flowrate
v	piston velocity towards the swashplate
V_{bdc}	Cylinder volume at BDC
V_{comp}	Volume of fluid within each cylinder compressibility effect
V_{cyl}	Cylinder volume
V_{swept}	Swept volume of piston
V_{tdc}	Cylinder unswept volume
x	pump piston axial displacement (towards the swashplate is positive)
X	Pump displacement (0-1)
X^l	Pump displacement projected onto the swashplate axis (0-1)

A Speed Sensing Silencer

A_o	Flow area at the neck of the Helmholtz resonator
B_r	Attenuation bandwidth of the Helmholtz resonator
f_r	Resonant frequency of the Helmholtz resonator
L_o	Length of the neck leading to the Helmholtz resonator volume
V	Volume of the Helmholtz resonator

Operation of the HDCV prototype

α_1 , α_2	Angle from BDC of the HDCV drilling centrelines
α_d , α_s	Angle from BDC of the start of the delivery port / end of suction port
γ	Angle of each cylinder port centreline on ending contact with the suction port

μ	Absolute fluid viscosity
κ_C	Angle subtended by a cylinder port
κ_V	Angle subtended by a HDCV portplate drilling
ξ	Sleeve port flow efflux angle
A_{orifp}	Flow area between cylinder and HDCV drilling
A_{orifx}	Flow area between HDCV port volume and sleeve port opening
A_{pop}	poppet face area
C_{qp}	Flow coefficient for flow between cylinder and HDCV port volume
C_{qx}	Flow coefficient for flow between HDCV port volume and delivery chamber
D_{damp}	Damping orifice diameter
D_{pop}	Poppet diameter
F_f	Sum of flow forces within a HDCV
F_{net}	Net pressure force acting to open the sleeve port of a HDCV
F_P	Differential pressure force acting on the axial faces of a HDCV poppet
F_r	Sum of friction forces opposing the poppet motion
F_s	Compression spring force on a HDCV poppet acting to close the sleeve port
F_x	Net axial force acting on a HDCV poppet
I_P	Integral area function for flow between the cylinder and HDCV port volume
I_X	Integral area function for flow between HDCV port volume and delivery chamber
K_{ch}	Spring chamber volume factor
K_{CL}	Constant for leakage from cylinder to delivery between portplate and HDCV sleeve
K_d	Constant for laminar flow through the HDCV damping orifice
K_f	Constant for HDCV flow forces at the linearised operating point
K_i	Factor to account for the inertia of entrained flow through the HDCV sleeve ports
K_L	Constant for leakage between poppet and sleeve at the linearised operating point
K_P	HDCV compression spring pre-load (when x=0)
K_S	HDCV compression spring constant
K_{SL}	Constant for leakage around HDCV sleeve from delivery to HDCV spring volume
L_{ch}	HDCV spring volume at x=0
L_{damp}	Length of damping orifice
L_{pop}	HDCV poppet length
L_{port}	HDCV port volume at x=0
M_{pop}	poppet mass
p	number of HDCV assemblies used within pump
P_{ch}	Spring chamber pressure
P_{crack}	HDCV sleeve port cracking pressure
P_{orifp}	Instantaneous pressure drop for flow between cylinder and HDCV port volume
P_{orifx}	Instantaneous pressure drop for flow between HDCV port volume and delivery
P_{port}	HDCV port pressure
q_{chnet}	Net HDCV spring chamber inflow
q_{cleak}	leakage flowrate from cylinder to delivery between portplate and HDCV sleeve
q_d	Flowrate through a damping orifice
q_p	HDCV port inflow from the overlapping cylinder port
q_{pnet}	Net HDCV port inflow
q_{sleak}	leakage flowrate around HDCV sleeve from delivery to HDCV spring volume
q_x	HDCV port outflow to the delivery chamber
r	sleeve port radius
s	Laplace operator
v	poppet velocity towards the spring chamber
V_1, V_2	Initial and final flow velocity through a sleeve port
V_{ch}	Spring chamber volume
V_{port}	HDCV port volume
V_{suc}	Cylinder volume on lending communication with the suction port
x	poppet axial displacement from cracking towards the spring chamber
x_{lap}	Overlapping poppet displacement when a sleeve port is fully closed

1.0 Introduction

There has been a growth in the use of oil-hydraulic systems over the last 40 years to the point where hydraulics can now be seen in a wide variety of environments, from hospitals to coal mines, and from aircraft to submarines. Component costs have been reduced and efficiencies increased and there has been a drive for higher operating speeds and pressures. This in turn has resulted in noisier hydraulic systems. The problem of noise in fluid power systems is well known, particularly in mobile applications where the operator is often close to the noise source.

The need for noise control in hydraulically-powered machinery has been driven mainly by the need to meet government safety legislation concerning the conservation of hearing. However, the price and performance of many competing hydraulic components are now very similar and so noise control is becoming a pressing commercial necessity. Where significant noise reductions are achieved, then a significant commercial advantage can be gained over the competition. Specifically, the current noise levels of some hydraulic systems are becoming increasingly unacceptable for the following reasons [1];

a) Legislation exists (which is likely to be tightened) to limit the maximum noise levels to which workers can be exposed.

b) There is an increasing public awareness of the harmful effects of excessive noise levels on hearing, on productivity, and on work efficiency and safety.

c) The continuing trend towards higher system operating pressure will tend to produce higher noise levels.

d) Fluid power systems face competition in some applications from electric and electro-mechanical drives, which are often perceived to be quieter than hydraulic equivalents.

Of the range of hydraulic components targetted for noise reduction, pumps have received particular attention. Pumps have been identified as a major cause of hydraulic system noise, and one of the most widely used and noisiest is the axial-piston pump, which is the main subject of this research project.

This chapter outlines how hydraulic system noise is produced by an axial piston pump and the approach taken during this project to reduce it.

1.1 The Problem of Hydraulic Noise

Noise from hydraulic systems is complex and has a number of sources, such as the oscillation of valve spools or poppets, and from cavitation within pumps or downstream of restrictions. However, excluding the noise from the prime mover, hydraulic system noise is caused predominately by the cyclic action of hydraulic pumps and motors.

For a pump delivering oil at high pressure, cyclic loads are created which act on the moving elements of the pump. These loads cause vibration which is transmitted through the pump casing to the rest of the system causing component vibration and airborne noise [2]. Also, the pump flow is not constant but consists of a flow ripple which is superimposed upon the mean flowrate. The flow ripple tends to have a periodic waveform due to the cyclic nature of a pump's operation, and different classes of pump have different characteristic flow ripple waveforms. This flow ripple interacts with the characteristics of the load circuit to produce a pressure ripple which also leads to component vibration and airborne noise [3].

The transmission of pump casing vibration is known as Structureborne Noise (SBN) and can be reduced with flexible couplings and mountings and by the use of flexible hose [4].

The pressure ripple is known as Fluidborne Noise (FBN) and is more difficult to isolate. An FBN silencer can be used at the pump delivery port, but is only effective over a limited frequency range, and reductions in FBN at low frequency are limited by the size of the silencer [3]. The reduction of FBN is particularly important because it can be transmitted quite efficiently throughout large systems. As a consequence, for many hydraulic systems, FBN is the principal source of hydraulic noise. Additionally, pressure ripple can contribute to fatigue failure of system components and so can play an important part in determining the overall reliability of a hydraulic system [3].

Compared to other positive displacement pumps, the flow ripple, and thus the pressure ripple, generated by axial piston pumps is relatively large. This is partly because axial piston pumps usually employ a small number of pumping chambers which give rise to larger flow pulsations superimposed on the mean delivery flow [5]. It is also because the fluid compression within axial piston pumps is relatively sudden. In gear pumps, leakage past the gear teeth causes the fluid compression to be much more gradual [6].

Axial piston pump pressure ripple is a major problem: their compact size, high power density and large speed range, combined with a variable displacement capability and high overall efficiency makes them otherwise ideal for a range of industrial and mobile applications. To address the problem of axial-piston pump noise, and in particular the problem of the relatively large inherent flow ripple, Vickers Inc. of Omaha, Nebraska, U.S.A. funded a three year project which was carried out at the Bath University Fluid Power Centre, finishing in April 1996.

1.2 Project Aims

The primary aim of the project was to produce the working prototype of a commercially-viable mechanism which reduces the flow ripple from an axial-piston pump to cause an overall reduction in the airborne noise caused by the pump.

The secondary aim was that the mechanism should employ a principle of operation that can be applied to reduce the flow ripple from other types of positive-displacement pumps and motors.

1.3 Project Strategy

To achieve the project aims a test pump was provided by Vickers on which a prototype mechanism could be tested and developed. To arrive at a working prototype, the following project objectives were identified:

1 Carry out a detailed analysis of the problem

2 Assess the previous work that had been carried out in this field. From this work arrive at a small number of alternative low-noise designs.

3 Carry out testing to investigate the pump flow ripple, and from the results validate a simulation model of the pumping dynamics.

4 Develop the simulation model to predict the effect of the most promising low-noise designs upon the behaviour of the standard pump.

5 Use simulation work to arrive at a set of parameters for a prototype design. With these parameters, undertake the assembly, test and development of the different prospective mechanisms and optimise a final prototype to suit a wide range of operating conditions.

At the start of the project a lot of the groundwork for this project had already been done at Bath during earlier research projects. In particular there had been previous attempts to reduce the flow ripple from a gear pump [7] and from an axial-piston pump [8]. Also, a reliable test method for determining the pump source flow ripple had been developed [9,10]. Furthermore, a number of projects had led to the development of software for the simulation of axial piston pump flow ripple [11,12].

1.4 Scope of Thesis

This thesis reports the research undertaken to fulfil the project aims. It is comprised of ten chapters:

A review of the theory behind the generation and transmission of hydraulic system noise is given in chapter 2. The mechanisms of airborne and structureborne noise are briefly outlined to give a background for the interpretation of results from the later chapters. Fluidborne noise is dealt with in more depth, showing the significance of the fundamental wave propagation equations. The case of a simple hydraulic circuit consisting of a pump, a pipe and a load is examined and discussed.

Chapter 3 explains the operation of an axial piston pump. The generation of cyclic loads due to pressure forces within the pump are explained and described mathematically. Likewise, the pump's periodic delivery flow ripple is described, and the effect of the operating condition upon the flow ripple is investigated.

Chapter 4 describes the operation of the digital simulation model used to predict axial piston pump flow ripple. The development of the simulation program during the project is also described, and the assumptions inherent in the results are discussed.

Chapter 5 describes results of the testing carried out to establish the source characteristics of a commercially-available axial piston pump. The test rig and test method are described, and some of the problems encountered during testing are outlined. The measured pump source impedance is compared with theoretical impedance models. The pump flow ripple measurements from the test rig are compared with compressible volume calculations and also with that predicted by the simulation model.

Chapter 6 reviews attempts to reduce pump-generated FBN from hydraulic systems. The mechanisms devised by previous workers are described and assessed. The concepts of two novel solutions, the Rotary Valve Pulse Generator, and the Heavily Damped Check Valve (HDCV) mechanism, are introduced and explained.

Chapter 7 reports the development of a rotary valve pulse generator and its use in cancelling the delivery flow ripple from an axial piston pump.

Chapter 8 describes the initial design and analysis of the HDCV prototype. The development of a simulation model is detailed and the simulated behaviour of the prototype mechanism is analysed.

Chapter 9 describes the development of the HDCV prototype towards a final design. The fluidborne and airborne noise from the final design is compared against that of the unmodified pump.

Chapter 10 draws together the project conclusions and suggests areas for further research into the subject.

2.0 The Nature of Hydraulic System Noise

2.1 Introduction

The purpose of this chapter is twofold:

1 To review how the different forms of hydraulic system noise are generated and transmitted. This will provide the background to results presented in the later chapters. More emphasis is placed upon fluidborne noise as this is the main subject of interest.

2 To show the importance that a reduction in pump source flow ripple has in reducing overall hydraulic system noise.

2.2 Characteristics of hydraulic system noise

The most obvious form of hydraulic system noise is airborne noise (ABN) that is detected by the ear. However, machines also produce structureborne noise (SBN) which is the vibration of components and mountings, and fluidborne noise (FBN) which is the pressure pulsation that occurs in the working fluid. FBN is caused primarily by unsteady flow from pumps and motors but also from valve instability or cavitation. SBN is caused directly by the mechanical action of pumps and motors, but also occurs as a result of unsteady forces caused by FBN .

To investigate the causes of ABN within a system, it is often necessary to measure over discrete frequency ranges to create a noise spectrum. From analysis of the spectrum, different distinct noise sources can be isolated. To reduce the overall system noise, it is necessary to quieten the noise sources that produce the largest noise harmonics, as these typically dominate the noise from other less noisy sources.

In figure 2.1 [13], the noise generation and transmission paths for a hydraulic system are identified. The noise sources are at the top of the diagram. Noise from these sources is then propagated through different paths which eventually contribute to the overall system ABN.

The system noise is highly dependent upon the operating conditions, such as the pump/motor speeds, delivery and suction pressures and the fluid condition. At higher operating speeds and lower fluid temperatures cavitation is more likely which can cause a dramatic increase in the system noise. However, cavitation can normally be avoided by careful pump installation and by minimising the free air within the system fluid.

Valve noise also contributes to the system FBN. Normally this noise is very broadband and contains no dominant harmonics. However, at conditions where the demand signal or the pump pressure ripple causes the valve element to resonate then the valve can produce significant levels of SBN as well as increased FBN at harmonics of the resonant frequency.

The FBN and SBN from pumps and motors is often the greatest source of noise within a hydraulic system. They generally produce noise at harmonics of the pumping frequency, and these often cause the largest individual ABN harmonics radiated from the system.

The displacement and the delivery and suction pressures have a large effect upon the FBN and SBN from the pump or motor. Pumps and motors are genererally optimised to produce lower levels of FBN and SBN at a particular operating point. Away from this condition then the FBN and SBN increases significantly and the pump or motor is then likely to cause a significant increase in the system ABN.

The FBN caused by cavitation, pump or motor flow ripple, and valve instability can have a significant effect on the overall system ABN [3]. It is efficiently transmitted throughout hydraulic systems and can induce SBN in components that then act as "sound boards" to produce high levels of ABN.

One way to reduce the transmission of FBN is to isolate the sources of FBN with flexible hose. However, the largest FBN harmonics from pumps and motors are usually below 1kHz, and in this region the attenuation properties of flexible hose diminish [4]. At these lower frequencies the FBN from pumps and motors can be isolated with specially designed FBN silencers. However, silencers can be bulky and expensive and their performance is dependent upon the system design and more importantly upon the operating speed of the pump or motor [6]. The remaining method for reducing system FBN is to reduce it at source. The various approaches to achieve this within a pump or motor are discussed in 2.4.3.

Like FBN, hydraulic system SBN can be reduced by impeding its transmission throughout the system or else by reducing the SBN at source. For a pump, SBN is created by transmission of mechanical vibration from the pump casing and indirectly throughout the circuit by the fluidborne noise inherent in the pumping action (See figure 2.1).

The SBN transmitted by the casing can be largely reduced by isolating the hydraulic circuit with flexible hoses and by isolating the prime mover with a flexible coupling [4]. To reduce the actual vibration of the pump casing, it is necessary to ensure that out of balance forces present in the pumping action are minimised. In recent years this has been carried out using modal analysis techniques and finite element analysis to aid in the design of pump casings [14].

The system ABN is most effectively reduced by attenuating the system FBN and SBN. Enclosures and cladding can also be used, although this is only possible around individual components. A drawback of enclosures is the added cost as well as the impracticality; on mobile machinery with many articulated elements in a hostile environment then even partial enclosure is impractical.

2.3 Airborne and Structureborne Noise

SBN is much more powerful than ABN, typically having 1000 times more energy. Some machine structures are good at transmitting SBN, and may even resonate and reinforce it. Transmission is by bending, torsional, shear and/or compression waves that travel through solid members like sound waves travel through air.

A pump has a stiff casing which is a poor sound radiator. However when the SBN from a pump reaches a compliant member that is also a good sound radiator (such as a poorly mounted pipe or reservoir) then high airborne noise levels can be created.

2.3.1 Characteristics of Airborne Noise

Any machine which vibrates will radiate acoustical energy (sound power measured in watts) and this results in a pressure variation in the atmosphere (sound pressure measured in N/m^2).

The human ear has a wide dynamic range of response to the pressure variations of airborne noise. The threshold of hearing is approximately $2x10^{-5}$ N/m^2 (rms), and the threshold of pain is around $60N/m^2$ (rms). The ratio of these two extreme sound pressure levels is three million to one and so a logarithmic scale is used to compress this range into more meaningful terms:

$$SPL(dB)= 20\log_{10}(P/P_0) \qquad (2.1)$$

Where P_0 is the reference pressure level at the threshold of hearing ($2x10^{-5}$ N/m^2).

The sound power is proportional to the square of the sound pressure and is expressed in similar terms:

$$SWL(dB) = 10\log_{10}(W/W_0) \qquad (2.2)$$

Using this convention, a change in sound power level will correspond to an equal decibel change in the sound pressure level.

The human ear does not respond equally to all frequencies, and is most sensitive in the region between 1 and 5kHz. For a truer measure of the perceived loudness of a noise then a correction curve can be applied to the spectrum of the measured sound pressure. Several filters have been designed to mimic the ear's non-linear response. The correction from three such filters ("A", "B", and "C" weighted curves) is shown in figure 2.2. The "A" weighted correction is most commonly used, and is generally accepted as the standard. Measurements that have been corrected with the "A" weighting are designated dB(A).

2.4 Fluidborne Noise

Fluidborne noise generates structural vibration which contributes to degrade overall hydraulic system performance. Hydraulic line vibrations can cause rigid pipes to fail by fatigue, and flexible hose to fail by chafing.

FBN can also interfere with electronic controls that depend on pressure measurements to monitor and control system behaviour. In this way FBN can limit system resolution and cause the need for more sophisticated electronics to process signals from sensitive pressure transducers.

In this section, a physical description is given of the hydraulic system FBN produced by the operation of pumps and motors. A mathematical appreciation of hydraulic system FBN is also given and a general set of methods to reduce system FBN are discussed. Only the periodic FBN caused by pump flow ripple is analysed, although this is equally applicable to motor noise.

2.4.1 Characteristics of Fluidborne Noise

2.4.1.1 Pump Flow Ripple

Positive displacement pump FBN is due primarily to fluid compressibility and the discrete nature of the pumping process. This is influenced by pumping geometry, cavitation, machining imperfections, and even small variations in the drive speed.

Pumps divide the inlet fluid into a series of pumping chamber volumes, compress these volumes to raise their pressure and then recombine the volumes into the discharge flow. Pump delivery therefore consists of a steady mean flow with a superimposed ripple or fluctuation which repeats at the pumping frequency (shaft rotational frequency multiplied by the number of pumping elements).

A particular type of pump tends to exhibit a particular flow ripple waveform or 'signature' and different types will produce flow ripple with different characteristics. This flow ripple is a pump characteristic and is virtually independent of the circuit to which it is connected, although it does depend on operating conditions such as pressure, speed, and temperature. The resultant pressure ripple is, however, very strongly dependent upon the characteristics of the circuit as well as the pump itself. Many hydraulic circuits tend to be highly resonant and, if a resonant mode is excited, very high pressure ripple levels can result [13].

2.4.1.2 Fluid Compressibility

The compressibility of the working fluid has a great effect upon the FBN characteristics of a circuit. The term used to account for compressibility is the effective bulk modulus, B_{eff}, where,

$$\text{Compressibility} \propto \frac{1}{B_{eff}}$$

The effective bulk modulus can be difficult to predict and can be affected by compliance in the pressure vessel and by the presence of entrained air in the fluid. For the analysis of fluidborne noise, B_{eff} is the isentropic, tangent bulk modulus: since small changes about the mean pressure are assumed and the pressure changes are rapid and so the heat transfer is regarded as negligible [13]. If the free air contained within the fluid is assumed to follow a polytropic process then;

$$\frac{1}{B_{eff}} = \frac{1 - V_{air}}{B_{oil}} + \frac{V_{air}}{\gamma P} + \frac{1}{B_{pv}} \qquad (2.1)$$

V_{air} is the volume fraction of free air within the pressurised volume. P is the pressure, γ is the polytropic index (usually taken as 1.4) and B_{PV} is the volumetric stiffness of the pressure vessel.

2.4.2 The Analysis of Fluidborne Noise

Flow and pressure fluctuations in a hydraulic circuit often exhibit complex wave forms, but since those from pumps and motors are periodic, then it is possible to analyse them in terms of harmonic components using Fourier series. Each flow or pressure signal can then be represented by the sum of several sinusoidal waves, having frequencies of integer multiples of the fundamental pumping frequency.

To analyse such a system, the noise frequencies of interest reach into the 1 to 5 kHz region and so a lumped parameter approach becomes invalid, as explained by McCloy and Martin [15] and also by Watton [16]. Instead a more accurate approach is found by using transmission line equations.

Pressure and flow ripple can be represented as amplitude and phase spectra. The complex ratio of the pressure ripple to flow ripple at a given frequency is known as the impedance. This is analogous to electrical circuit theory, with pressure ripple equivalent to voltage and flow ripple equivalent to current.

2.4.2.1 Fluidborne Noise in a Simple System

A pump or motor is commonly represented as a source flow ripple Q_s, in parallel to a source impedance Z_s (a Norton model). The simplest real hydraulic circuit that can be represented with the 'Norton' model is that of a pump discharging into a straight length of pipeline terminated with a restrictor valve. This circuit is shown in figure 2.3.

Flow and pressure fluctuations within this circuit can be explained by considering one harmonic of the pump flow ripple.

The motion of the pumping elements causes a flow disturbance which varies periodically. This flow variation produces a corresponding pressure variation which propagates along the pipe at the speed of sound in the fluid (approx. 1400 m/s in oil).

This pressure wave, known as the incident wave, is superimposed upon the mean pressure level generated by the resistance of the valve to the mean flow, and travels to the end of the line, where it is reflected back toward the pump by the valve.

The reflected wave is at the same frequency as the incident wave, but may be of lower amplitude because of the energy lost during reflection. When the reflected wave reaches the pump it is again reflected and this process continues until the wave energy is lost through reflections at the source and termination, and friction in the pipe.

The interaction of the incident wave and the subsequent reflections results in the formation of a 'standing wave' at the incident wave frequency. The standing wave in a line has positions of high pressure fluctuations (anti-nodes) and low pressure fluctuations (nodes). These nodes and anti-nodes repeat at a distance of half a wavelength. Line lengths which produce large pressure fluctuations are referred to as resonant lengths for the system at a particular frequency. Resonant lengths are also half a wavelength apart.

2.4.2.2 Analysis of Fluidborne Noise in a Simple System

Plane wave propagation theory was used by Bowns and McCandlish [17], and later by Johnston [6], to model the pressure fluctuations produced in a simple pipe. To simplify the analysis, a number of assumptions were made about the pipe flow [6]:

1 The fluid is homogenous and Newtonian.

2 Heat transfer effects are negligible, and conditions are isentropic.

3 Flow is laminar and axisymmetric.

4 The pressure distribution across the pipe is uniform.

5 Perturbations are small such that any variations in the fluid properties are negligible.

6 Waves propagating in the pipe wall are neglected.

7 The mean fluid velocity is negligible compared with the speed of sound in the fluid.

The analysis was applied to the simple hydraulic circuit already described using figure 2.3, and as before consists of a positive displacement pump discharging into a straight rigid pipe, terminated with a restrictor valve. The equation of the pressure at a particular frequency ω, within the pipeline of length L at position x comes from the Transmission Line Equation [6]:

$$P_x = \frac{Q_s Z_s Z_o}{Z_s + Z_o}\left(\frac{e^{-\gamma x} + \rho_T e^{-\gamma(2L-x)}}{1-\rho_T \rho_S e^{-2\gamma L}}\right) \qquad (2.2)$$

$$Z_o = \frac{\sqrt{(\rho B_{eff})}}{A}\xi \qquad (2.3)$$

And

$$\gamma = j\omega\sqrt{\left(\frac{\rho}{B_{eff}}\right)}\xi \qquad (2.4)$$

Equation 2.2 represents the pressure standing wave in an hydraulic line. The pump is characterised by its source flow ripple (Q_S) and its source impedance (Z_S). It is assumed that the flow ripple is generated at the pump exit. The restrictor valve at the end of the line determines the mean pressure level and offers an impedance to the system known as the "termination impedance" (Z_T).

The pipeline, attached to the pump discharge flange contains fluid at the mean pressure level and is represented by its "characteristic impedance" (Z_O) which is a function of the pipe flow area, the pipe friction, the fluid density and the effective bulk modulus. The attenuation and phase shift of the transmitted wave along the line are characterised by the "wave propagation constant" (γ) which is also dependent upon pipeline dimensions, fluid properties and operating conditions. Both Z_O and γ are affected by fluid viscosity effects represented by the complex coefficient, ξ.

The reflection coefficients ρ_S and ρ_T determine the relationship between the incident and reflected waves at the source and termination respectively. These are functions of the line and end impedances,

$$\rho_S = \left(\frac{Z_S - Z_O}{Z_S + Z_O}\right) \qquad (2.5b)$$

$$\rho_T = \left(\frac{Z_T - Z_O}{Z_T + Z_O}\right) \qquad (2.5b)$$

As a reflected wave cannot have an amplitude greater than the incident wave which caused it, reflection coefficients have amplitudes which are less than or equal to unity.

Equation 2.2 consists of two distinct groups of terms:

1 $$\frac{Q_S Z_S Z_O}{Z_S + Z_O}$$

This expression has units of pressure and represents the pressure that would be generated at the pump exit in the absence of any reflections from the valve termination.

2 $$\left(\frac{e^{-\gamma X} + \rho_T e^{-\gamma(2L-X)}}{1 - \rho_S \rho_T e^{-2\gamma L}}\right)$$

The remainder of Equation 2.2 is non-dimensional and represents the behaviour of the waves generated by part 1. The $e^{-\gamma x}$ numerator term represents the wave travelling in the positive direction. The $\rho_T e^{-\gamma(2L-x)}$ term represents the wave after reflection at the termination, ρ_T being the amplitude and phase change which occurs at the reflection, and (2L-x) the total

distance travelled by the wave from the source. The denominator, when multiplied by the sum of the incident and reflected waves, represents the cumulative effect of all the reflections that occur at the source and termination.

2.4.2.3 The Effect of Pump Source Characteristics upon FBN

From application of the work of Bowns and McCandlish [17], a study was carried out by Edge [21], towards a method of assessment for pump FBN. As part of this work, an evaluation was carried out of the FBN generating potential of a pump, without the influence of system parameters. This was achieved by considering the pressure fluctuations at the pump discharge flange using equation 2.2. Taking x=0,

$$P_O = \frac{Q_S Z_S Z_O}{Z_S + Z_O}\left(\frac{1+\rho_T e^{-2\gamma L}}{1-\rho_S \rho_T e^{-2\gamma L}}\right) \tag{2.6}$$

If the entry impedance of the system at the pump flange is given by

$$Z_E = Z_O\left(\frac{1+\rho_T e^{-2\gamma L}}{1-\rho_T e^{-2\gamma L}}\right) \tag{2.7}$$

then

$$P_0 = Q_S\left(\frac{Z_S Z_E}{Z_S + Z_E}\right) \tag{2.8}$$

or

$$P_0 = \frac{Q_S Z_S}{1+\frac{Z_S}{Z_E}} \tag{2.9}$$

The pressure fluctuation at the pump flange is now expressed in terms of two pump dependent parameters, the source flow fluctuation Qs and the source impedance Zs, and a single system parameter, the system entry impedance Z_E. In this form, it is easier to see the effect of the various parameters on the FBN generating potential of the pump. Each parameter is a phasor quantity, evaluated for a single frequency at the pump outlet flange. The full characteristic would be obtained by summing all of the significant harmonic components of source flow ripple.

Considering equation 2.9 in detail, the following points are apparent:-

1 P_O is directly proportional to Q_S. Any reduction in Q_S results in a direct reduction in P_O. This is a prime area for further consideration.

2 If $|Z_S| \ll |Z_E|$ then $P_O = Q_S.Z_S$. The pressure ripple at the pump flange is only dependent upon the pump characteristics Q_S and Z_S and the product of the two terms is the pump FBN characteristic known as the "Blocked Acoustic Pressure". The "High Impedance Pipe" method has been developed to measure this characteristic [18]. However, as stated by Johnston and Longmore [19], there are difficulties with this method. In

particular, complications arise in obtaining a sufficiently high circuit impedance. Also the technique does not allow the separation of Q_S and Z_S, and the measured quantity can be misleading, tending to over-emphasise the lower harmonics.

3 If $|Z_S| \rangle\rangle |Z_E|$ then $P_O = Q_S Z_E$, independent of Z_S. In this situation P_O is determined largely by the system entry impedance, which in most circumstances is unknown. A reduction in P_O is still possible by a reduction in Q_S.

4 As $Z_E \rightarrow 0$ then P_O becomes small. In this case, P_O is still affected by Q_S, but not so much by Z_s . A reduction in Z_E could be achieved with an accumulator or silencer, although their performance would be frequency and circuit dependent.

5 As $Z_S \rightarrow -Z_E$ then P_O becomes large and sensitive to Z_S. This shows that if the pump source impedance is or tends to 180 degrees out of phase with the system entry impedance i.e. mismatched, then large amplitudes of P_O are possible especially with pumps of compact design having high source impedances. This is the resonant condition.

6 If $Z_E = Z_O$ then a reflectionless line is assumed and,

$$P_o = Q_S\left(\frac{Z_S Z_o}{Z_S + Z_o}\right)$$

In this case the pressure ripple at the pump flange is known as the "Anechoic" Pressure Ripple. This is another quantity that can be used to measure the FBN from a pump [19]. However, there are problems in that it is difficult to achieve a reflectionless line [20].

Summarising these points, which include the extremes of pump and system impedance matching and mismatching, it can be seen that the fluidborne noise generating potential of a pump and system is greatly influenced by the relative amplitudes and phases of Z_S and Z_E.

2.4.2.4 The Modelling of the Pump Discharge Passageway

In the previous sections, the pump source flow ripple has been assumed to be generated at the pump outlet. However this is not an accurate model of a real pump, in which the flow ripple generating mechanism is situated some distance inside the pump discharge passageway. In order to establish the flow ripple from the pump as generated at the point of flow ripple generation, a model of the pump discharge passageway is required.

Pump impedance spectra may be experimentally determined if the source flow fluctuation Q_O and the isolated pressure fluctuation P_O are known from the defining impedance relationship (See Appendix A):

$$Z_S = -P_O/Q_O \qquad (2.10)$$

The ability to determine experimentally the impedance of a pump has led a number of researchers to propose theoretical models for the impedance characteristics of pumps.

It was shown by Edge [21] and Davidson [22] that, at low frequencies, the source impedance of a positive displacement pump is dependent on the compressibility of the volume of fluid contained in the discharge passageway. At higher frequencies fluid inertia and distributed parameter effects become important. Furthermore the measured source impedance suggested a larger volume than that of the discharge passageway. This was attributed to pump compliance or reduced fluid stiffness due to air release, and meant that pump source impedance had to be measured and could not be deduced from dimensions of the discharge passageway.

Edge[21], Edge and Wing[23], and Johnston[6] showed that for most pumps, the source impedance can be represented as a short length of pipe of constant cross-sectional area A_P and length l_P with a closed end. Ignoring viscous friction, this model is defined by the equation:

$$Z_s = \frac{Z_{op}}{j\tan\left(\omega\frac{L_p}{c_o}\right)} \tag{2.11}$$

Alternatively, if friction and fluid inertia effects are included then the discharge passageway can taken as a compressible volume, an inertia and a resistance (i.e. equivalent to the electrical analogy of a simple RLC network, a Helmholtz model) where the following relation applies [13]:

$$Z_S = R + j\omega\frac{L_p\rho}{A_p} + \frac{B_{eff}}{j\omega V_p} \tag{2.12}$$

Both of these expressions are derived in Appendix A. In many cases, one of these models gives a good representation of the form of pump impedance spectra. When the models are fitted to low frequency impedance results then the compressibility effects dominate. Therefore, if the volume of the discharge passageway is known then the effective bulk modulus of the fluid in the discharge passageway can be estimated. This is particularly useful as air release effects within the pump can cause significant reductions from the expected values (See section 5.3.4).

2.4.2.5 The Referral of the Pump Source Flow Ripple

With a valid model of the pump discharge passageway, the flow ripple at the pump exit (Q_S) can be referred to the point of flow ripple generation within the pump (the internal flow ripple, Q_S^*).

The flow ripple at the pump exit differs from the internal flow ripple, particularly at frequencies close to the anti-resonant frequency of the pump source impedance. This is important because the simulation model (See chapter 4) only predicts the pump flow ripple at the point of generation and so can only be validated with the measured internal flow ripple.

An expression for the internal flow ripple was formulated by Edge and Johnston [9], whereby they assumed that Q_S^* occurs at the end of an idealised discharge passageway, as described in 2.4.2.4.

For the idealised discharge passageway ignoring the effects of viscous friction, based on the impedance relationship of equation 2.11, then [9],

$$Q_s^* = Q_s \cos\left(\omega \frac{L_p}{c_o}\right) \tag{2.13}$$

Similarly, for the idealised discharge passageway based upon the Helmholtz impedance model of equation 2.12, then

$$Q_s^* = Q_s\left[1 + j\omega \frac{V_p}{B_{eff}}\left(R + j\omega \frac{L_p \rho}{A_p}\right)\right] \tag{2.14}$$

For both of these models A_P is assumed to be the flow area of the discharge passageway at the pump exit. Both of these expressions are derived in Appendix A.

So, provided that one of these models can be applied to Z_S, then it is possible to refer the flow ripple from the measurements at the pump exit to within the pump without any knowledge of its internal dimensions.

2.4.3 The Reduction of Fluidborne Noise

For a simple hydraulic system, as represented in figure 2.3, there are three system parameters that can be adjusted to give a reduction in the system pressure ripple;

1 The circuit entry impedance, Z_E.

2 The pump source impedance, Z_S.

3 The pump source flow ripple, Q_S.

This section discusses the adjustment of each of these parameters to reduce system FBN.

2.4.3.1 Alteration of Circuit Entry Impedance

From equation 2.9, $$P_O = \frac{Q_S Z_S}{1 + \frac{Z_S}{Z_E}}$$

The pressure ripple at the pump exit, P_O, can be lowered by reducing the circuit entry impedance. However, this measure is impractical as the requirements for a low entry impedance are large pipe diameters and low mean pressure. This is because Z_O is inversely proportional to the pipe cross-sectional area and valve termination impedance is proportional to the mean pressure level. These requirements are directly opposed to the principal advantage of modern hydraulic systems which is that of high power density.

Alternatively, the circuit entry impedance could be tuned to the pump source impedance to minimize the pressure ripple in the load circuit. The objective of this approach would be to prevent circuit dimensions that cause a resonant pressure ripple condition within the circuit. This is a complex task if a trial and error approach is to be avoided. The mathematical equations describing the pressure ripple in a circuit become very complex for all but the

simplest circuits. Computerised techniques are necessary for the analysis of practical hydraulic circuits, and for this purpose a computer package has been written at Bath University [24].

Even after careful system design, problems are still encountered with a variable speed pump, in that the resonant lengths of the system are dependent upon the frequencies of the pump harmonics: if the pump has a wide operating speed range then it may be difficult or impossible to avoid a resonant condition.

2.4.3.2 Reduction of Pump Source Impedance

The source impedance of a pump can have a significant effect on the pressure ripple generated in a system. By again referring to Equation 2.9;

$$P_O = \frac{Q_S Z_S}{1 + \frac{Z_S}{Z_E}}$$

then it is clear that a reduction in the pump source impedance leads directly to a reduction in the circuit entry pressure ripple.

From the work of Edge [21], and Davidson [22], it is clear that the most obvious method to reduce Z_S is to increase the pump discharge volume. This has previously been attempted upon an external gear pump by Lipscombe [25]. Lipscombe achieved a reduction in pressure ripple of 20%, but concluded the method to be limited by attendant increases in SBN from the pump casing as well as by a volume envelope restraint on the pump itself.

Johnston also considered this method of reducing system FBN [6]. He concluded that any reduction in entry pressure ripple would be extremely system specific. Altering the source impedance characteristics would affect the source reflection coefficient, ρ_S, and hence the resonant characteristics of the system. Therefore in one circuit the pressure ripple may be reduced, but the opposite effect may then be produced in a different circuit.

2.4.3.3 Reduction of Pump Source Flow Ripple

The source flow ripple Q_S, when related to a positive displacement pump, is directly dependent upon the fundamental geometry of the pumping mechanism. Different pumping actions can produce significantly different variations in the delivery flow.

However, from equation 2.9, it can be seen that the pump exit pressure ripple is proportional to the pump source flow ripple. So, a reduction in the pump source flow ripple leads directly to a proportionate reduction in pump exit pressure ripple. Furthermore, this change is independent of the circuit, so a reduction of pump source flow ripple will reduce the pump exit flow ripple of any load circuit. It also follows that if the source flow ripple could be reduced to zero then this would also reduce the pump exit pressure ripple to zero.

From this reasoning, it can be concluded that the reduction of source flow ripple provides the greatest scope for the reduction of system pressure ripple. Furthermore, from the discussion of section 2.2 it can also be concluded that the reduction of pump source flow ripple has the greatest potential in the reduction of overall hydraulic system noise

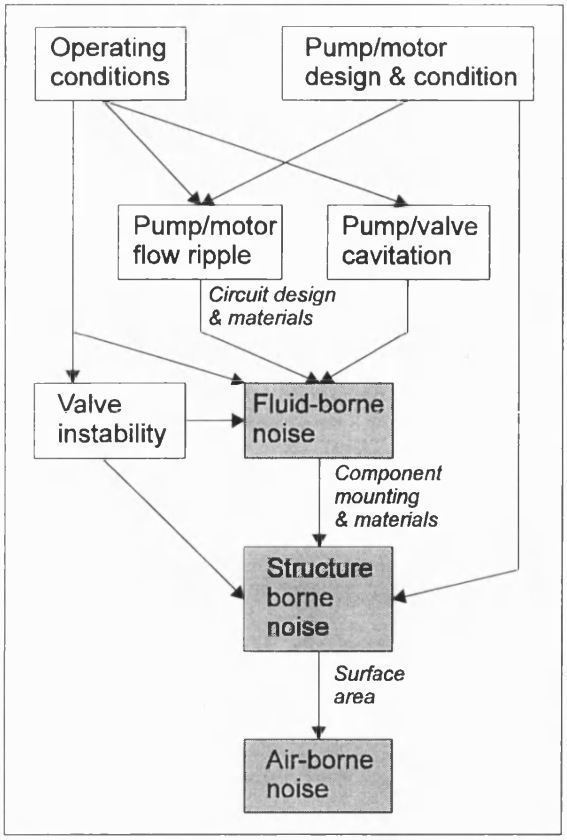

Figure 2.1 - Generation and transmission of noise. (from [13])

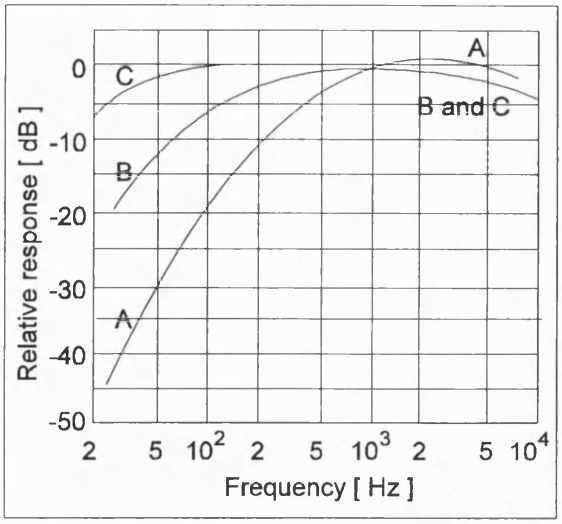

Figure 2.2 - Frequency Weightings (from [13])

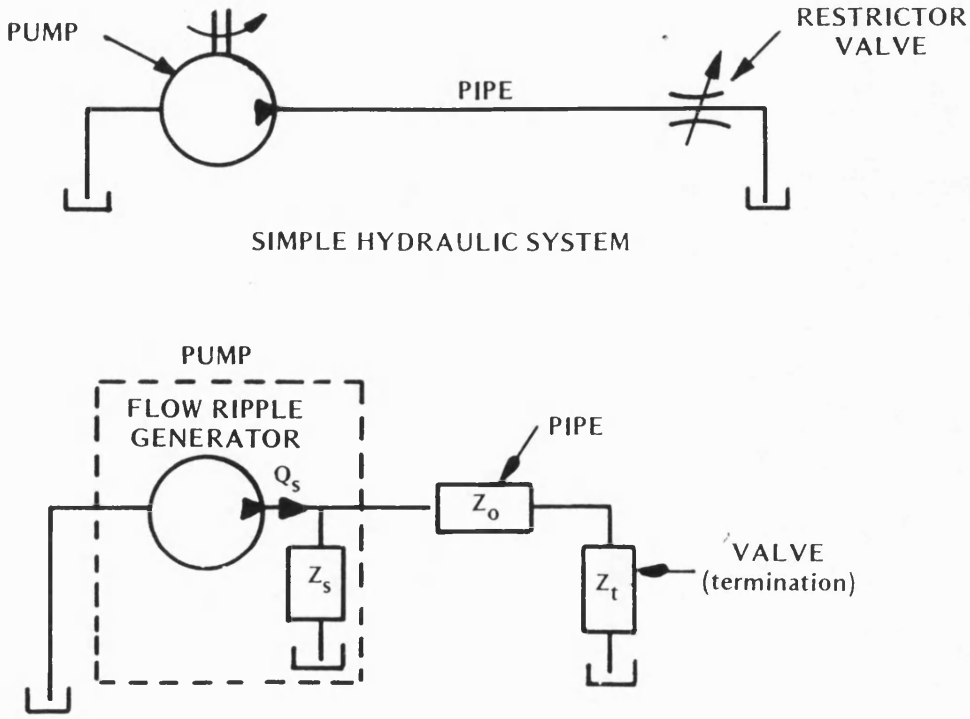

Figure 2.3
A simple hydraulic circuit and its impedance representation (from [4])

3.0 Noise Generation within an Axial Piston Pump

3.1 Introduction

This chapter shows how FBN and SBN are produced as a by-product of the pumping process within an axial piston pump and also why this type of positive displacement pump is regarded as particularly noisy.

3.1.1 Axial Piston Pump Mode of Operation

Figure 3.1 shows the basic design of an axial piston pump. It consists of a cylinder block that rides on a drive shaft and rotates with it. As the cylinder block rotates, pistons within the block reciprocate axially in a near sinusoidal fashion. The pistons' axial motion is due to their contact, through shoes (or slippers) with the inclined swashplate. Although pressure forces the pistons and shoes against the swashplate on the pumping stroke, a shoeplate is usually provided to maintain the contact during the suction stroke. In variable displacement units, the swashplate is mounted on a yoke which allows its inclination to be varied to adjust the pump displacement [5].

The cylinder block also bears against a valve plate. Kidney-shaped ports in this plate alternately connect cylinders to the inlet and discharge ports. The switch from inlet to discharge occurs when each piston is at its most extended position. This position is referred to as Bottom Dead Centre, (BDC). The switch from discharge back to inlet occurs 180 degrees later when each piston reaches its greatest penetration into the cylinder block. This is called Top Dead Centre (TDC).

3.1.2 Sources of Noise From an Axial Piston Pump

Foster and Hannan [26] list the four basic mechanisms by which noise is generated within any positive-displacement pump.

1 Structural noise. Produced by vibration of pump structural elements, due to the changing internal loads imposed on the pump components.

2 Fluidborne noise. Caused by resonance of components and oil columns in the hydraulic system, excited by pressure pulsations inside the pump.

3 Cavitation noise.

4 Noise caused by turbulent flow in regions of the pump.

As Foster and Hannan state, noise from sources 3 and 4 can usually be eliminated by careful pump installation and by attention to the design of the flow passageways within the pump. The structureborne and fluidborne noise from a positive displacement pump are unavoidable. Their generation is analysed in the following sections.

3.2 The Generation of FBN within an Axial Piston Pump

The flow ripple from an axial piston pump consists of two separate components caused by the near-sinusoidal motion of the pistons and by the compressibility of the working fluid.

The fluidborne noise generated by positive displacement pumps is transmitted within both the pump inlet and delivery lines. The delivery line is normally at a higher mean pressure and so has the potential for creating much higher levels of FBN than the inlet line. Accordingly, the analysis will concentrate on the generation of FBN within the delivery chamber. In the following analysis, the following assumptions are made (from [5] and [11]):

1 The force exerted by each piston acts on the swashplate through the piston's axial centreline.

2 The friction force between the piston slipper and the swashplate is zero.

3 There is perfect coupling between the piston and the swashplate. In practice, there will be compliance between the slipper pads and the swashplate, and the slipper pads may lift under certain circumstances.

4 The swashplate and its mounting points within the pump casing are assumed to be infinitely stiff.

5 The cylinder block is rotating around the driveshaft at a constant speed

6 Radial acceleration forces on the pistons are assumed to be zero

3.2.1 The Kinematic Flow Ripple

The pumping action of a positive displacement pump divides the inlet fluid stream into a series of pumping chamber volumes which are physically separated from the inlet chamber and then displaced into the delivery fluid stream. For an axial piston pump, the volume in one cylinder is a sine function of shaft rotation. Neglecting leakage, inertia and compressibility effects, the pump delivery flow is the sum of equally spaced half-sine discharge volumes from all of the pump cylinders. Such a flow summation for a nine cylinder pump is shown in figure 3.2. The resulting flow ripple is known as the "kinematic" flow ripple, and occurs even when the pump is not raising fluid pressure.

The pump kinematic flowrate can be deduced from expressions of piston displacement and velocity within each cylinder bore. For explanation purposes it is assumed that the pump is set to full displacement (X=1). It is also assumed that the portplate is designed so that the switch from inlet to delivery occurs at BDC, and the switch from discharge to inlet occurs at 180° from BDC (neutral portplate timing).

Each piston rotates about the driveshaft axis on a pitch circle of radius R against a swashplate which, at full displacement, is inclined at angle β to the plane of the portplate (See figure 3.3). At time, t=0 then piston no. i=1 is at BDC and the cylinder volume is at its

maximum value. The axial displacement and velocity of the i'th piston in a pump with n pistons is given by,

$$x = (RX\tan\beta)\cos(\omega t + [2(i-1)\pi/n]) \tag{3.1}$$

$$v = -(\omega RX\tan\beta)\sin(\omega t + [2(i-1)\pi/n]) \tag{3.2}$$

When v is negative then the piston is on its delivery stroke and the volume of the cylinder is decreasing. Therefore the "flowrate" into the cylinder from the piston motion is given by,

$$q_{pist} = A_P(\omega RX\tan\beta)\sin(\omega t + [2(i-1)\pi/n]) \tag{3.3}$$

With the neutrally timed portplate then the flowrate from the delivery port to the cylinder is

$$\begin{array}{ll} q_{del} = -q_{pist} & \text{if } q_{pist} > 0 \\ q_{del} = 0 & \text{if } q_{pist} < 0 \end{array} \tag{3.4a}$$

The flowrate from the suction port to the cylinder is

$$\begin{array}{ll} q_{suc} = 0 & \text{if } q_{pist} > 0 \\ q_{suc} = +q_{pist} & \text{if } q_{pist} < 0 \end{array} \tag{3.4b}$$

Viersma described the kinematic flow ripple mathematically [27]. He did this by considering the flow from n pistons as a continually rotating set of n vectors of amplitude A, equally spaced at $2\pi/n$ radians. The total pump delivery flow is then the summation of the positive vertical components of the n vectors. From this analysis, table 3.1 compares the kinematic flow ripple from an odd and an even number of pistons.

Table 3.1

Axial Piston Pump Flow Ripple		n=even	n=odd
Maximum Flow	q_{max}	$2A$	$2A\cos\left(\frac{\pi}{2n}\right)$
Minimum Flow	q_{min}	$2A\cos\left(\frac{\pi}{n}\right)$	$2A\cos^2\left(\frac{\pi}{2n}\right)$
Deviation	$\frac{1}{2}(q_{max} - q_{min})$	$2A\sin^2\left(\frac{\pi}{2n}\right)$	$2A\cos\left(\frac{\pi}{2n}\right)\sin^2\left(\frac{\pi}{4n}\right)$
Nominal Flow	$\frac{1}{2}(q_{max} + q_{min})$	$2A\cos^2\left(\frac{\pi}{2n}\right)$	$2A\cos\left(\frac{\pi}{2n}\right)\cos^2\left(\frac{\pi}{4n}\right)$
Specific Deviation	$\frac{\frac{1}{2}(q_{max} - q_{min})}{\frac{1}{2}(q_{max} + q_{min})}$	$\tan^2\left(\frac{\pi}{2n}\right) \approx \left(\frac{\pi}{2n}\right)^2$	$\tan^2\left(\frac{\pi}{4n}\right) \approx \left(\frac{\pi}{4n}\right)^2$

Where, $A = A_P\,\omega RX\tan\beta$

Figure 3.4 compares the kinematic flow ripple from a 9 cylinder pump with that from a 10 cylinder pump of the same displacement. The kinematic flow from 10 cylinders repeats at piston frequency, which is half the equivalent frequency of the 9 cylinder flow ripple.

Accordingly the kinematic flow ripple from the 10 cylinder pump is larger than that from the 9 cylinder pump. This result is borne out by Viersma's analysis: the specific deviation of a nine piston pump kinematic flow ripple is only 0.76% of the mean flow, whereas that for the 10 piston pump is much bigger - 2.47% of the mean flow. This is often argued to be the main reason for the preponderance of odd-pistoned units over even-pistoned units (This argument is investigated in 6.3.1).

3.2.2 The Compressibility Flow Ripple

In the delivery line this flow ripple is caused by compression of the cylinder contents at BDC from the inlet pressure to the delivery pressure. As such, this flow ripple occurs at the piston frequency. Its shape and magnitude depend on the difference between the cylinder pressure and the delivery pressure at the start of communication between the two volumes.

As the cylinder block rotates from BDC towards the start of the delivery port, the motion of the piston on the inclined swashplate reduces the cylinder volume and so acts to increase the cylinder pressure. If the delivery port is delayed to the point where the cylinder pressure equals the delivery pressure then optimal pre-compression takes place.

The delivery port delay needed for optimal cylinder compression can be calculated from compressible volume considerations: if the suction port is neutrally-timed, then the cylinder pressure can be calculated from the compression of the cylinder volume at BDC. Neglecting cylinder leakage, then the following expressions can be applied (see figure 3.3):

$$\frac{V_{bdc} - V_{cyl}}{V_{bdc}} = \frac{P_{del} - P_{suc}}{B_{eff}} \tag{3.5}$$

$$V_{bdc} = A_P L_{mean} + A_P R X \tan\beta \tag{3.6}$$

$$V_{cyl} = A_P (L_{mean} + R X \tan\beta \cos\theta) \tag{3.7}$$

From equations 3.5 - 3.7, the angle subtended by each cylinder port from BDC for cylinder compression to the delivery pressure can be expressed:

$$\theta = \cos^{-1}\left[1 - \left(\frac{P_{del} - P_{suc}}{B_{eff}}\right)\left(\frac{L_{mean}}{RX\tan\beta} + 1\right)\right] \tag{3.8}$$

The optimum delivery port delay is at angle φ past BDC. σ is the angular width of each cylinder port and so,

$$\varphi = \frac{\sigma}{2} + \cos^{-1}\left[1 - \left(\frac{P_{del} - P_{suc}}{B_{eff}}\right)\left(\frac{L_{mean}}{RX\tan\beta} + 1\right)\right] \tag{3.9}$$

The flow ripple simulated for the unboosted test pump (See 1.3) operating at 250 bar and full displacement with optimal delivery port timing for that condition is shown in figure 3.5.

If the delivery port is delayed further then the cylinder pressure will rise above the delivery pressure. When this cylinder meets the delivery port there would be a rapid outflow of fluid from the cylinder. The delivery flow ripple for such a situation is shown in figure 3.6.

Conversely, if the delivery port is too far advanced then the cylinder pressure will be lower than the delivery pressure when the cylinder meets the delivery port. In this case there is a rapid flow of fluid into the cylinder from the delivery port. The delivery flow ripple for this case is shown in figure 3.7.

From figures 3.4 and 3.7 it is clear that the compressibility flow ripple has a much greater effect on the pump delivery flow ripple than the kinematic flow ripple.

The angular difference between the start of the three different delivery ports is only 10 degrees. Clearly then, the shape of the compressibility flow ripple is very sensitive to the delay of the delivery port from BDC. Furthermore, the delay necessary for optimal pre-compression is highly dependent upon the operating condition. In particular the pressure difference between inlet and delivery ports, the inclined angle of the swashplate, the condition of the working fluid, and to a lesser degree the pump speed will all have an effect on the pump's ideal timing. Accordingly, this simple delivery port design is only suitable for one operating condition and as such is rarely specified.

3.2.3 Pressure Relief Grooves

The problem with the simple delivery port is that the cylinder port opens to the delivery port very suddenly. This leads to a sudden change in cylinder pressure and a large, short-duration cylinder flow. To make the pressure-equalisation of the cylinder more gradual, a pressure relief groove is machined in the valve plate on the leading radius of the delivery port.

An example of a triangular, sloping relief groove is shown in figure 3.8. There are many designs of relief groove, but they all exhibit very similar modes of operation. The pressure relief groove is initially restrictive, thereby limiting the rate at which fluid flows from the delivery port back into the cylinder [11]. As the cylinder block rotates, the groove then opens up quite rapidly to avoid the cylinder pressure rising too far above the delivery pressure. In this way, the cylinder pressure is caused to rise more gradually, which in turn "spreads out" the compressibility reverse flow.

The flow ripple from a typical pump using a relief groove at the start of the delivery port are shown in figure 3.9a. In this figure flow ripples are shown for the pump operating at full flow and three different delivery pressures; 150, 200 and 250 bar. The corresponding flow ripples for a similar pump with no relief groove are shown in figure 3.9b. This second pump has the delivery port delayed to give optimal pre-compression at the 200 bar, full flow condition.

Clearly, the pump using the pressure relief groove produces a less pronounced flow ripple. The second pump produces less flow ripple at its design condition, but away from that condition it is much worse than the pump using the relief groove. This point illustrates that another advantage of the relief groove is to make the pump flow ripple less sensitive to the pump operating condition. Accordingly, a pump with a well designed relief groove can operate over a range of pressures and flows and produce a fairly constant level of fluid-borne noise.

3.2.4 The Effect of Axial Piston Pump Flow Ripple upon System ABN

The action of the pressure relief groove to "spread out" the compressibility flow ripple has the effect of reducing the higher frequency FBN harmonics, as can be seen from figures 3.9a and 3.9b. This is significant as it will lead to smaller high frequency airborne noise harmonics, and so may cause the attached circuit to sound less noisy (see 2.3.1). Even with the use of pressure relief grooves, the compressibility flow ripple causes the fluid-borne noise from an axial piston pump generally to be greater than that from other designs of positive displacement pump of the same displacement [6].

The effect of the compressibility flow ripple is to produce significant FBN harmonics in the 1 to 5 kHz region. This in turn can cause circuit excitation and airborne noise at frequencies where the human ear has a sensitive response. Consequently, axial piston pumps generally sound more noisy than other positive displacement pumps.

3.2.5 The Effect of Compressibility on Pump Losses

The volume of fluid associated with the compressibility flow ripple is independent of the portplate design. This volume corresponds to the amount of fluid needed to compress the cylinder contents at BDC from the inlet pressure to the delivery pressure. The compressibility loss is not unique to axial piston pumps but is a characteristic of all positive displacement pumps. The fluid present in the compressibility flow ripple can be estimated with equation 3.5:-

$$V_{comp} = \frac{(P_{del} - P_{suc})V_{bdc}}{B_{eff}} \tag{3.10}$$

The drop in mean flow rate is then calculated by multiplying the compressibility volume by the pumping frequency:

$$q_{comp} = V_{comp} f_p \tag{3.11}$$

The theoretical maximum flowrate from the pump is found from,

$$q_{ideal} = f_p(V_{bdc} - V_{tdc}) \tag{3.12}$$

Where the cylinder volume at BDC and TDC varies with pump displacement according to,

$$V_{bdc} = A_P(L_{mean} + RX\tan\beta) \tag{3.6}$$

$$V_{tdc} = A_P(L_{mean} - RX\tan\beta) \tag{3.13}$$

So, from equations 3.6 and 3.13, the flowrate lost to compressibility and the maximum theoretical pump flowrate can be expressed by,

$$q_{comp} = f_p \frac{(P_{del} - P_{suc})}{B_{eff}} A_P(L_{mean} + RX\tan\beta) \tag{3.14}$$

$$q_{ideal} = 2f_p A_P RX\tan\beta \tag{3.15}$$

The effect of compressibility on the pump volumetric efficiency can therefore be expressed:

$$\eta_v = 100\left[1 - \frac{(P_{del} - P_{suc})}{2B_{eff}} \frac{(L_{mean} + RX\tan\beta)}{RX\tan\beta}\right]\% \tag{3.16}$$

L_{mean} is a measure of the unswept cylinder volume, V_{tdc} (see Eq. 3.13). When L_{mean} is significantly larger than the cylinder swept displacement ($2RX\tan\beta$) then the compressibility flow loss becomes more dependent upon delivery pressure than it is upon pump displacement (see Eq. 3.14). This is investigated in 5.3.3

3.3 The Generation of SBN within an Axial Piston Pump

For an axial piston pump, structureborne noise is caused by the pressure ripple and also by the combined cylinder pressure forces acting on the swashplate. In this analysis only the SBN caused by the cylinder pressure forces is considered.

As each cylinder alternates between inlet at low pressure and delivery at high pressure, then the pressure force from each piston switches from a minimum to a maximum in almost a square-wave fashion. The axial-pressure forces combined from all the pistons lead to a net axial force on the swashplate about the dead centre axis, and also to a moment on the swashplate in both the yoke and the driveshaft axes. It is these forces and moments that contribute to vibration of the pump casing which is transmitted from the pump as SBN.

3.3.1 Piston Forces and Moments

Figure 3.10 shows the geometry of the pressure forces within an axial piston pump. The shaft centreline is the Z axis. The swashplate tilts about the yoke or X axis. The Y axis crosses through BDC and TDC and is called the dead centre axis. The Y^{l} axis is the projection of the Y axis onto the swashplate.

The swashplate inclination is measured from the Y axis and is indicated by the angle β. The angle of each piston from BDC about the driveshaft axis is indicated by the angle θ. The projection of θ onto the swashplate is given by the angle ϕ.

Each piston-slipper assembly has a mass m, and rotates about the driveshaft axis on a pitch circle radius of length R. The instantaneous cylinder pressure is indicated by P_{cyl}, and the piston face area by A_P.

Starting with equation 3.1, and using the assumptions listed in section 3.2, then expressions for the forces and moments from a single piston can be expressed using the analysis presented by Skaistis [5]. Table 3.2 summarises the forces and moments from a single piston within an axial piston pump:

Table 3.2

Axis	Force	Moment
Swashplate Yoke (X)	0	$-\frac{f_z}{X^{l}\cos^2\beta}R\cos\theta$
Dead-Centre (Y)	$f_Z \tan\beta$	$f_z R\sin\theta$
Driveshaft (Z)	f_Z	$f_z RX\tan\beta\sin\theta$

Where $f_z = P_{cyl}A_P - m\ddot{x}$ (3.17)

The piston acceleration term, $m\ddot{x}$, can have a significant effect upon the pump SBN and ABN. When the cylinders are at delivery pressure then the cylinder pressure clamps the piston and slipper pads to the swashplate. Between 90° and 270° past BDC, the piston is accelerating towards the swashplate and so the acceleration term reduces this clamping action. However, at TDC (θ=180°) the cylinder de-pressurises and the piston acceleration is at its maximum value towards the swashplate. This can cause the piston and slipper pad to lift from the swashplate. If an appreciable lift occurs then a violent impact takes place as each piston passes through TDC. This is known as "Piston Pounding" and causes the SBN and ABN from the pump to increase significantly. To prevent this effect, a shoe plate is usually fitted to hold the slipper pads onto the swashplate (See fig. 3.1).

3.3.2 Total Piston Forces and Moments

For this analysis it is assumed that the pump is neutrally timed (See figure 3.3). To simplify the analysis it is assumed that cylinder pressure changes at BDC and TDC are instantaneous, and that the inertias of the piston-slipper pad assemblies are negligible. The suction pressure is assumed to be 0 bar (gauge) and the pump is set to full displacement (X=1).The axial force from each piston is then given by removing inertia from equation 3.17:

$$f_z = P_{cyl} A_P \tag{3.18}$$

$$\begin{aligned} P_{cyl} &= P_{del} \qquad 0^0 \le \theta \le 180^0 \\ P_{cyl} &= 0 \qquad 180^0 < \theta < 360^0 \end{aligned} \tag{3.19}$$

From table 3.2, the forces and moments from the motion of a single piston can be sketched:

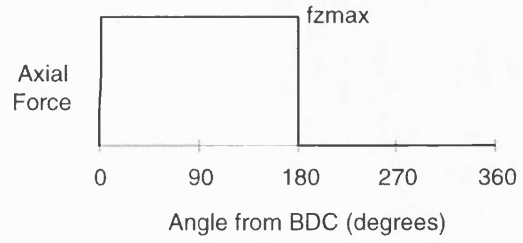

$$f_z(max) = P_{del} A_P$$

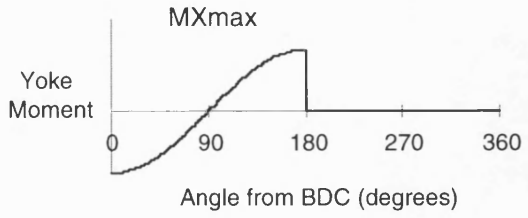

$$m_x(max) = \frac{P_{del}}{\cos^2\beta} R$$

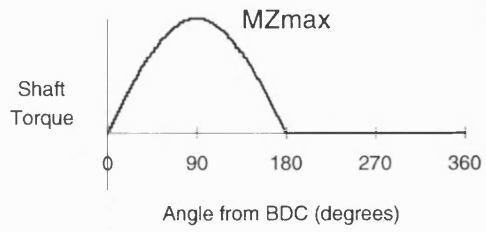

$$m_z(max) = P_{del} R \tan\beta$$

When the contribution of all the pistons are added then the results for an odd number of pistons are considerably different to those from an even number of pistons. Figure 3.11 compares the summation of the axial piston force, the yoke moment, and the shaft torque from a nine and a ten piston pump.The results are counter-intuitive: despite the 10 piston axial force being constant, the distribution of the nine-piston axial forces around the swashplate leads to a smaller variation in the yoke moment and shaft torque. (See 6.3.1)

3.3.3 The Effect of Piston forces and moments upon Pump SBN

All of the forces and moments discussed in 3.3.1 and 3.3.2 give rise to bending and torsion of the swashplate yoke and the driveshaft, which in turn cause vibration of the pump casing (SBN). Skaistis [5] attempted to estimate the relative importance of the forces and moments towards noise generation: To do this, he compared their range of variation as well as their maximum values.

A comparison was made of the forces and moments within a neutrally-timed nine-piston pump (as analysed in 3.3.2). The maximum value and cyclic range of the forces and moments were calculated. A structure's stiffness relative to a given forcing function tends to be proportional to the function's maximum value [5]. Therefore, the ratio of the cyclic range to the maximum was also calculated as a rough guide to each function's noise producing potential. The results are shown in the table below:

Table 3.3

Function	Maximum	Range	Range/Max. (%)
F_Z	$5P_{del}A_P$	$P_{del}A_P$	20
F_Y	$1.58P_{del}A_P$	$0.32P_{del}A_P$	20
M_X	$0.53RP_{del}A_P$	$1.06P_{del}A_P$	200
M_Y	$2.83P_{del}A_P$	$0.043P_{del}A_P$	1.4
M_Z	$0.89P_{del}A_P$	$0.012P_{del}A_P$	1.4

The yoke moment, M_X, shows the greatest potential as a noise source because of its high ratio of range to maximum. The next highest is the axial force which has only one-tenth the potential.

Figure 3.11 shows that an even number of pistons would generally create a much greater variation in yoke moment than an odd number of pistons. Given that the yoke moment is a prime source of SBN, then it can be expected that pumps with an even number of pistons suffer greater pump casing vibration than pumps with an odd number of pistons. This would partly explain the rarity of axial piston pumps with an even number of pistons.

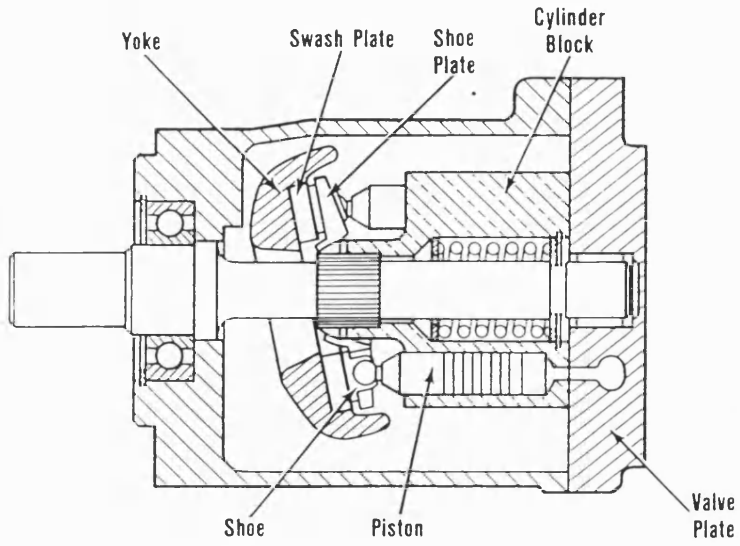

Figure 3.1
The main elements of an axial piston pump (from [5])

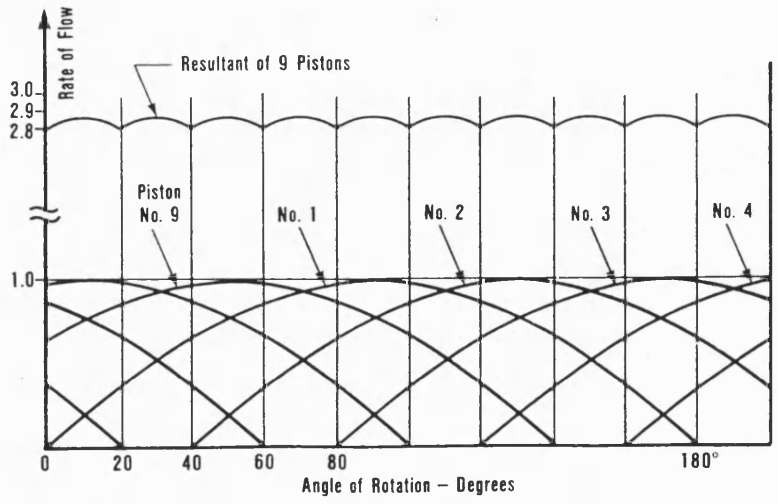

Figure 3.2
Kinematic flow ripple from a 9-cylinder pump (from [5])

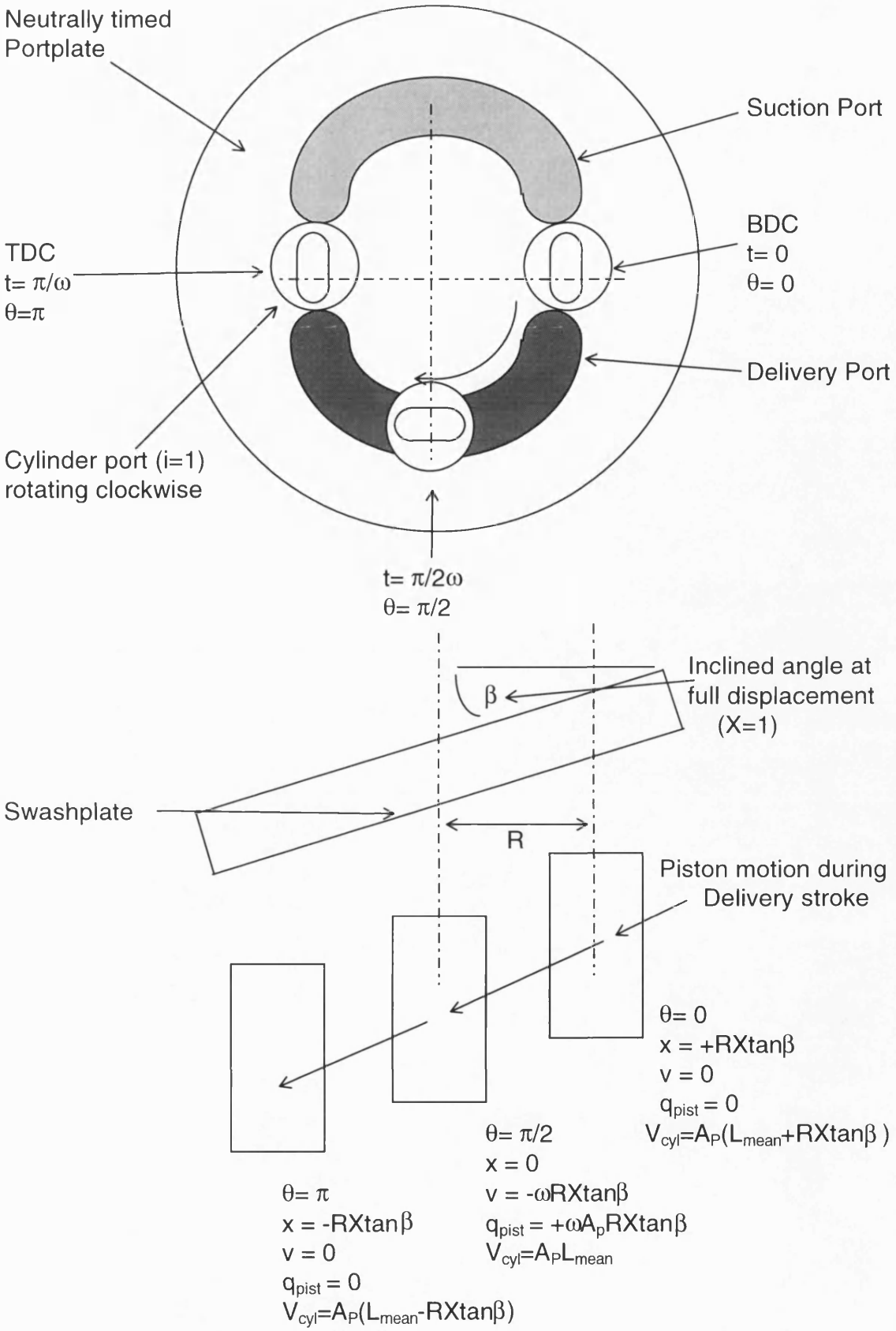

Figure 3.3
Sketch illustrating the terms used to mathematically describe the kinematic flow ripple

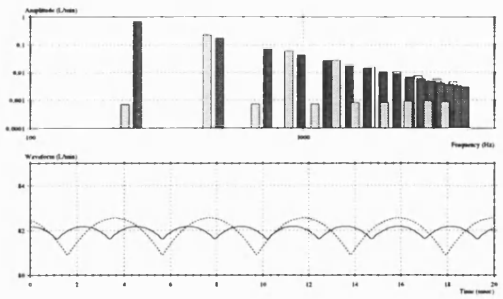

Figure 3.4

Simulated kinematic flow ripple
from 9 and 10 pistons
(9=continuous, 10=dashed)

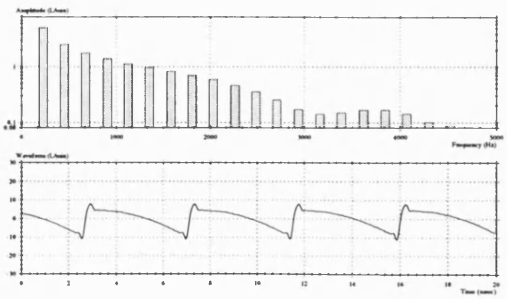

Figure 3.5

Simulated delivery flow ripple
from a pump exhibiting optimal
cylinder pre-compression

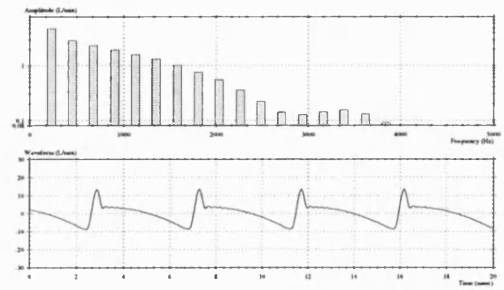

Figure 3.6

Simulated delivery flow ripple from
a pump exhibiting optimal cylinder
over-compression

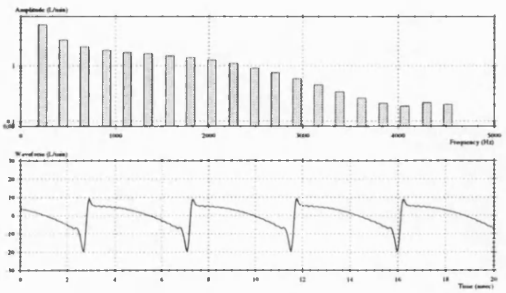

Figure 3.7

Simulated delivery flow ripple from
a pump exhibiting optimal cylinder
under-compression

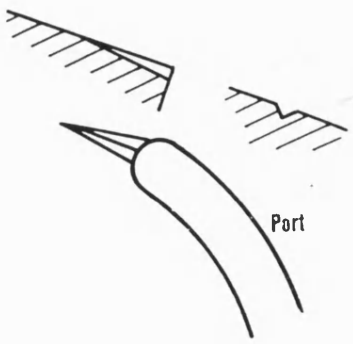

Figure 3.8
Sketch of a relief groove (from [5])

a)

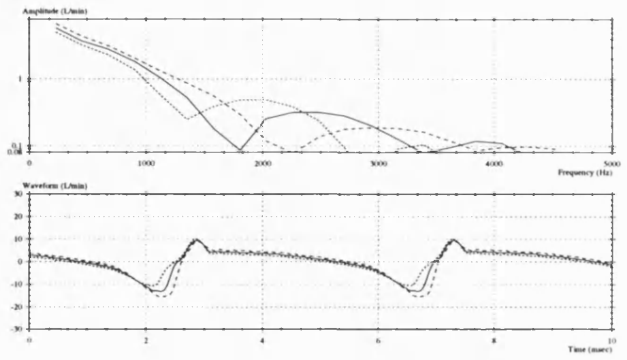

b)

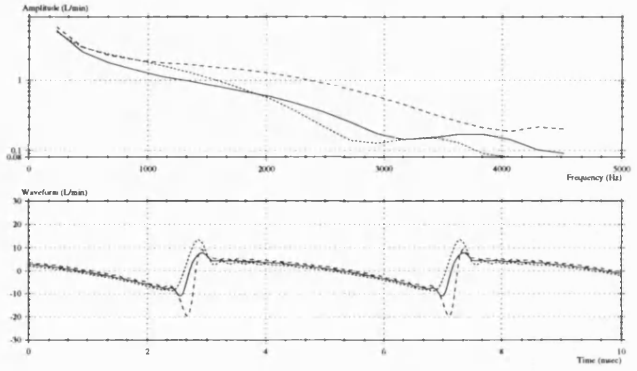

———	Optimal cylinder pre-compression	200 bar delivery
.....	Cylinder over-compression	150 bar delivery
- - - - -	Cylinder under-compression	250 bar delivery

Figures 3.9a - b
Simulated delivery flow ripple waveform and spectral envelopes from a pump with (a) and without (b) a relief groove

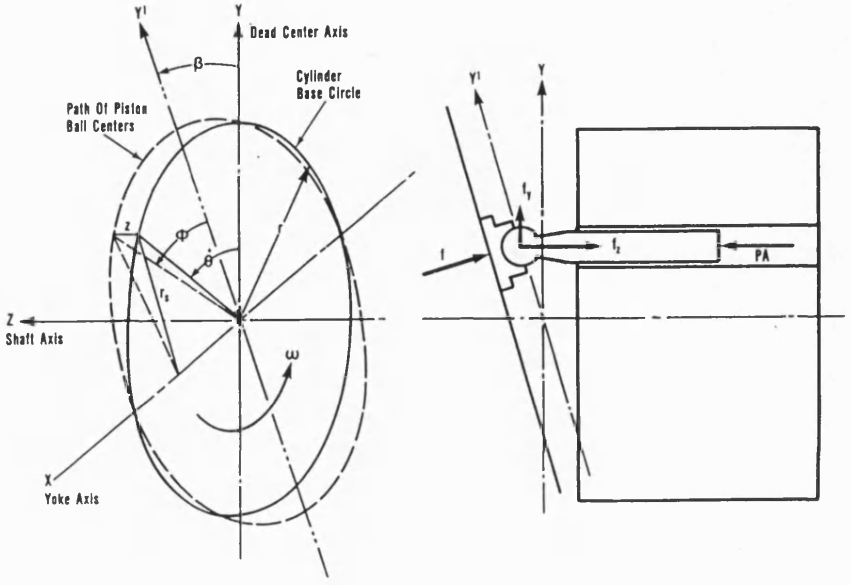

Figure 3.10
Diagram illustrating the piston forces and moments in an axial piston pump (from [5])

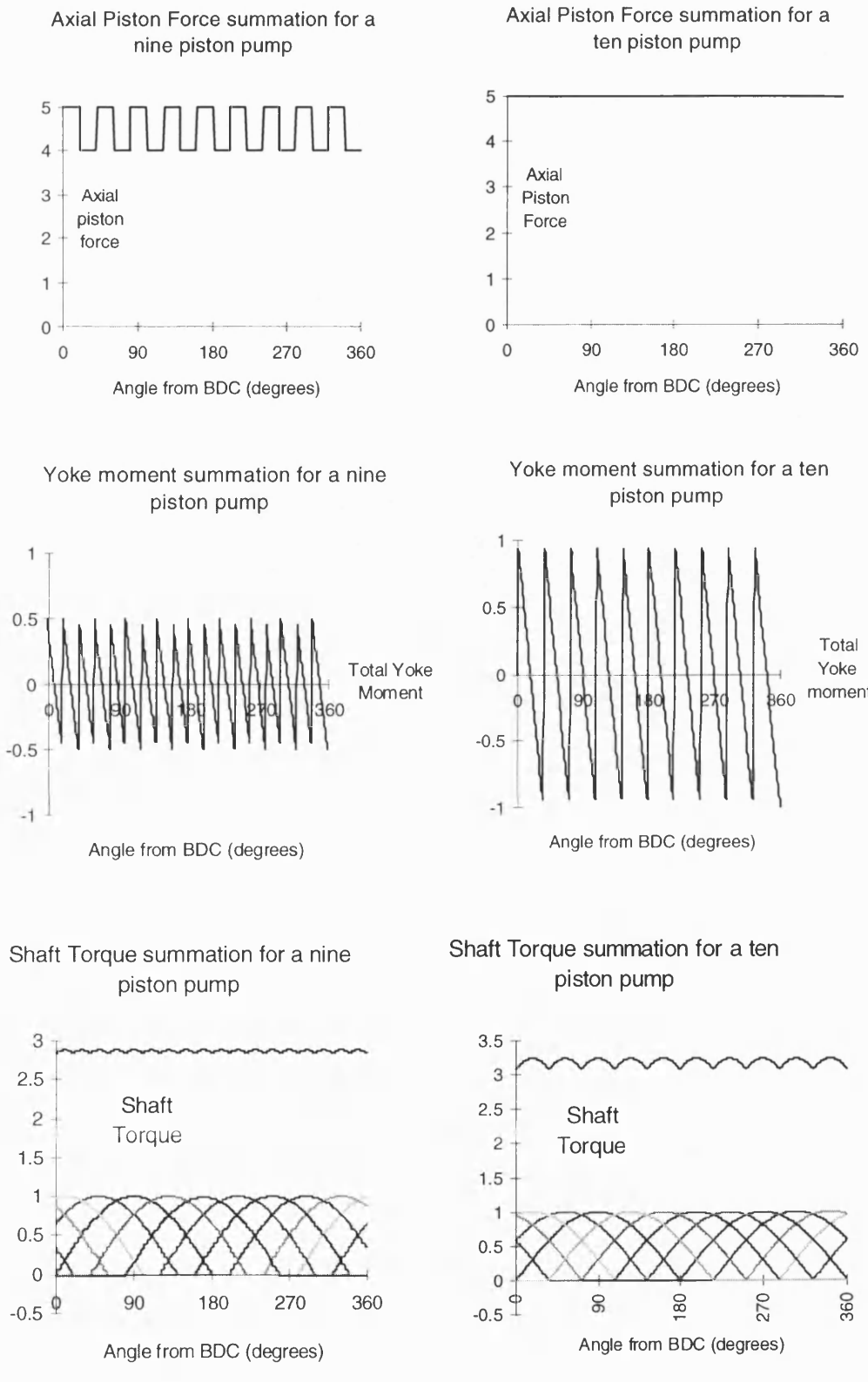

Figure 3.11
Forces and moments generated by 9 and 10 piston pumps

4.0 The Digital Simulation of Axial Piston Pump Flow Ripple

4.1 Introduction

The purpose of the simulation work reported here was to aid the design of a pump that produces a small flow ripple over a wide range of operating conditions.

Prior to this project, a set of simulation models had been developed at Bath to describe the behaviour of axial piston pumps by Edge, Harris and Tilley [12] . These models mainly predict single cylinder pressures and flows and were written for use within the Bathfp simulation environment. The models are collectively known as the "Cappa" suite and form the basis of the pump simulations carried out during this project. The models were validated by test work outlined in chapter 5. Further changes were made to the validated models for the prediction of flow ripple from a low noise pump design. These changes are described in chapter 8.

The original Cappa suite single-cylinder models have been modified to create a "Dual Cylinder" model. This model provides directly available information on the pump delivery flow ripple and additionally the piston forces and moments

In this chapter the operation of the Cappa suite within Bathfp is described. The development of the Cappa suite with the addition of the "Dual Cylinder" model is also described.

4.2 Modelling of Axial Piston Pump Flow Ripple

One of the first experimentally-validated studies of axial piston pump dynamics was carried out by Zaichenko and Boltyanaskii [28]. They carried out an investigation of portplate design and demonstrated experimentally and theoretically the reduction in pump noise that can be achieved with well designed relief grooves. Their work was limited though because, in the absence of a computer, they could not solve theoretical flow equations numerically. As a result, the pressure relief groove profiles had to be designed to allow simplification of the system flow equations.

The first detailed study of the cylinder pressures within an axial piston pump was carried out by Helgestad [29]. For this, he installed a miniature pressure transducer within one of the cylinder barrels of a commercial axial piston pump. Using a slip ring arrangement, the transducer allowed measurement of the cylinder pressure as the cylinder barrel rotated. He used this apparatus to develop the first digital computer model of the cylinder pressures and flows within an axial piston pump. A number of different relief groove designs were investigated using this model, including "V", square and circular section grooves. The pressure drop across the relief groove was modelled as a conventional orifice and the effect of flow direction, groove cross section and Reynolds number upon the discharge coefficient were all investigated using a "Quasi-Static" test rig [29]. It was found that the portplate discharge coefficient varied between 0.7 and 1.0 with Reynolds number and flow direction. However, the inclusion of these effects to the computer model had

little effect on the simulated cylinder pressure and flow and so a constant value of 0.7 was used for the discharge coefficient to model portplate flow.

Helgestad's model was taken further by Foster and Hannan [26]. The pump inlet pressure was assumed constant as before, but the delivery pressure was calculated from the interaction of the simulated flow ripple with the characteristic impedance of a long line without reflection. Also, the effect of leakage on the cylinder pressure was assumed to be minor and so was excluded from the model. Fair agreement between theory and practice was achieved with this simplified model. However, the model consistently under-estimated the size of cylinder pressure overshoots at BDC and undershoots at TDC, and failed to predict a high frequency oscillatory flow also seen by Helgestad.

With their model, Foster and Hannan investigated the effect of portplate timing on the cylinder pressure rise at BDC. One of the conclusions of the work was that, from a noise standpoint, pump designs with an even number of cylinders would be viable since the kinematic flow ripple is normally significantly smaller than that produced by compressibility effects.

This work was developed further by Martin and Taylor [30] who arrived at a design process for pressure relief grooves with the purpose of minimising the pump FBN over a wide range of operating conditions. The process was extended to include the design of low-noise birotational portplates. Square-ended kidney ports were investigated, but found to be intolerant to changes in operating condition. The concept of a variably-timed portplate was also discussed.

The benefits of the above design process were investigated by Kelsey et al. [31] on a commercial pump. They found that the volumetric efficiency could be increased and the shock loading reduced within the correctly-timed pump. In a related study, Foster et al. [32] experimented with different hydraulic fluids. The effect of the fluid bulk modulus, density, and viscosity was discussed and the effect of increased leakage on pump FBN was measured experimentally. It was concluded that axial piston pumps designed for operation with mineral oils could not easily be used with oil/water emulsions without a major increase in the generated FBN.

The simulation method of Helgestad, Foster and Hannan, was analysed by Darling [33]. He showed that the earlier models, based on fluid compliance, were highly inaccurate at high speeds and loads. He showed that the fluid momentum at the point of port opening was of considerable importance, and using an improved model, managed to successfully predict cavitation in the cylinder bore at high-speed, low boost conditions.

Palmberg [34] redefined the fluid momentum relationship found by Edge and Darling [11] to derive a dimensioning criterion for obtaining an optimum groove design for a given pump. He also developed two simulation models, one for a single cylinder and one for the complete machine. He compared his simulation results with flow ripple measurements from a pump discharging to an anechoic termination. The overall agreement was good throughout the measured spectrum comprising 33 harmonics of the pumping frequency.

More recently, Harris et al. [12,35] extended the work of Edge and Darling to investigate the suction performance and swashplate wear within axial piston pumps. This work involved more complex simulations and the models were adapted to the Bathfp simulation environment to utilise a more computationally efficient integrator (See 4.3.1). The models adapted by Harris were validated experimentally and documented to form the "Cappa" software suite for use within the Bathfp simulation environment.

4.3 Description of the Simulation Model

All of the pump simulations have been carried out using the "Cappa" software suite within Bathfp [36,37]. The simulations were carried out in the UNIX operating system. Initially a SPARC10 processor with SunOS 4.1.3 was used. Later simulations were carried out with a PC using a 120MHz Pentium processor running Solaris 2.4 (for X86).

This section describes the operation of Bathfp and the Cappa suite. The operation and limitations of both the original single cylinder model and the later "Dual Cylinder" model are described. Validation of the simulation work is shown at the end of Chapter 5 where delivery flow ripple measurements are compared with flow ripple simulations from the Cappa suite.

4.3.1 The Bathfp Simulation Environment

Bathfp is a simulation package for the analysis and design of fluid power systems that was introduced in 1990 [38]. It operates by splitting the simulation process into four distinct phases. These are carried out in four program modes: Circuit Drawing Mode, Model Selection Mode, Parameter Definition Mode, and Run Mode.

The circuit under investigation is built on the screen using component icons normally represented by conventional mechanical and hydraulic symbols (See Figure 4.1). During Circuit Drawing Mode these icons are selected, added to the circuit, repositioned or deleted using a cursor and mouse.

The component icons have simulation models associated with them. These models contain the equations governing the component dynamic and steady state response and take the form of self-contained computational object code written in either C or FORTRAN. During Model Selection Mode a model is selected for each of the component icons. Each component icon typically has a range of models to choose from. The model chosen depends on the assumptions used for the component behaviour. Within Bathfp there is a library of such models containing the dynamic performance characteristics of a large number of pneumatic, electrical and hydraulic components.

Once all of the circuit components have been associated with simulation models then Bathfp can generate simulation code for the whole circuit. To do this it compiles and links the object code of the individual component models to create a FORTRAN or C program, its

corresponding object code and an executable file to describe the behaviour of the complete circuit. Once this process has finished then during Parameter Definition Mode the physical parameters and initial conditions of the component models are specified. Bathfp then stores these settings in a parameter text file which is accessed by the executable file during simulation runs.

In Run Mode, simulations may be initiated and graphs plotted of the system performance. Before a run is started, the simulation duration and plot interval are selected and the choice is made of the system integrator. This information is stored in an ASCII simulation file. During a run, the circuit executable accesses the simulation file and stores values of plot variables to a binary results file for each simulation time step. This results file is then interrogated when graphs are plotted of the system performance.

One of the main benefits of Bathfp is that it can solve system differential equations by making use of the advanced LSODA numerical integration algorithm [39]. This employs Gear's method for stiff systems and Adam's method for non-stiff systems. A decision process is built into the integrator to switch between the different methods, depending on the numerical characteristics of the system; namely the Eigenvalues and the presence or not of discontinuities.

System discontinuities are a particular problem. All numerical methods for solving Ordinary Differential Equations assume that the functions are "smooth". Unfortunately, functions arising in engineering applications often are only smooth over a limited portion of their range, as demonstrated by the effect of stiction on the motion of moving valve elements. On stepping over a discontinuity then the integrator has to be informed so that it can accurately locate the point at which the discontinuity occurred. The integrator can then be restarted from that point on the subsequent section of smooth function. Failure to do this causes the integrator to slow or crash.

Within Bathfp there is a discontinuity handling facility which allows dialogue between the system integrator and the component models. This is important because all of the component models involving discontinuities must be written according to a strict protocol to allow this facility to work properly.

4.3.2 The Cappa Suite

The Cappa suite divides the pump into individual models, each relating to a specific component within the pump. The purpose of this division is to represent the pump system as a collection of elements of lower complexity to facilitate model writing and verification. It also allows flexibility in the mathematical modelling of individual components. For example, different relief groove models can be swapped at the model selection stage to investigate the effect of groove designs on a given pump. Within Cappa, a pump is represented by the following component model types:

1 cylinder volume;

2 piston;

3 portplate;

4 kidney port relief grooves;

5 kidney port bridges;

6 suction and delivery passageways.

In addition there is a global model which contains subroutines and global information needed by the other models such as the pump speed and the total number of pistons in the pump. The icons representing these models are shown connected together in the Bathfp environment in figure 4.1.

The circuit shown in figure 4.1 represents a particular arrangement of models from the Cappa suite for the simulation of the pressure and flow for a single cylinder. Using this model each pump cylinder is assumed to produce identical pressures and flows, and the suction and delivery pressures are assumed to be constant. The total pump flow is then obtained by summing the simulated cylinder flow for each cylinder of the pump, taking into account the phase difference between the cylinders.

The main advantage of the single cylinder model is the short simulation run times. The pump "circuit" is run only as a single cylinder and for the duration of only a single pump revolution.

4.3.3 Operation of the Single Cylinder Pump Model

This section presents the equations and assumptions used in one of the single cylinder circuits made up with models from the Cappa suite. The application of these equations within the different component models is then described.

The model described in this section was first proposed and validated by Edge and Darling [11]. The model was then adapted for use within Bathfp by Harris [37].

4.3.3.1 Theoretical Basis of the Single Cylinder Model

Inherent in this model is the assumption that all of the pump cylinders behave in an identical fashion. This presumes the absence of significant inter-cylinder effects and also of interaction between the pump cylinders and the suction and delivery lines.

Darling investigated the validity of summing single cylinder simulation results to represent the behaviour of the whole pump [33]. For this he simulated the pressure and flow for all the cylinders of a nine cylinder pump. To investigate circuit and cylinder interaction he simulated the lumped parameter behaviour of the cylinder pressures and flows within both an open and a closed system. From this study, Darling found that both inter-cylinder effects between suction and delivery and the effects of circuit interaction were minor, and concluded that they could be neglected.

In a further study, Darling investigated the effect of wave propagation within the suction and delivery lines and also within the individual cylinder volumes. Once again he found these effects to be minor and concluded that they could be neglected.

As a result of these studies, Darling used the Single Cylinder model to predict the total suction and delivery flow from the pump.

4.3.3.2 The Equations of the Single Cylinder Model

Figure 4.2 shows the basic elements of the model. The model features one differential equation to calculate the cylinder pressure:

$$P_{cyl} = \int \frac{B_{eff}}{V_{cyl}} q_{net} dt \tag{4.1}$$

where

$$V_{cyl} = A_P L_{mean} + V_{swept} \tag{4.2}$$

and

$$q_{net} = q_{suc} + q_{del} + q_{pist} \tag{4.3}$$

The net cylinder inflow term q_{net}, neglects any leakage from the cylinder, either through to the slipper pad, or else in the oil film between the cylinder block and portplate. Helgestad modelled these effects and concluded that they had only a very small effect upon the cylinder pressure and flow ripple [29].

The flowrate due to the piston motion, q_{pist}, and the swept volume V_{swept}, are functions of the piston face area, the pump speed and displacement, and the piston pitch circle radius (As shown in 3.2.1 and 3.2.2):

$$q_{pist} = A_P(\omega RX\tan\beta)\sin(\omega t + [2(i-1)\pi / n]) \tag{3.3}$$

And from figure 3.3,

$$V_{swept} = A_P RX\tan\beta\cos(\omega t + [2(i-1)\pi / n]) \tag{4.4}$$

The effective bulk modulus, B_{eff}, is as described in section 2.4.1.2. For the working fluid, the adiabatic secant bulk modulus is used since the rates of change of pressure are relatively rapid and the changes in pressure are large compared to the mean pressure. Both the fluid bulk modulus and the density are assumed to be independent of fluid pressure: An increase of 200bar would only increase the bulk modulus by approximately 5% and the density by only 2% [33].

The most complex part of the model is the calculation of the overlapping flow areas between the cylinder port and the portplate kidney ports (A_{suc} and A_{del}). These areas are a function of the cylinder angle relative to the portplate (θ). The minimum flow area can be calculated for a variety of different relief groove profiles. Provision is also made for the inclusion

of relief grooves at the start and finish of both the delivery and the suction kidney ports. The change in flow area due to portplate bridges is also taken into account [33].

A_{suc} and A_{del} are included in two pairs of equations which calculate the cylinder flows to the delivery and suction ports. Flow through a sharp edged orifice is assumed and a differential term is included to account for fluid inertia effects. For the flow between the delivery port and the cylinder then,

$$q_{del} = \int \frac{P_{del} - P_{cyl} - P_{orif}}{\rho \Gamma_{del}} dt \qquad (4.5)$$

Where

$$P_{orif} = \left(\frac{q_{del}}{C_q A_{del}} \right)^2 \frac{\rho}{2} \qquad (4.6)$$

q_{del} represents cylinder inflow and P_{del}, is assumed constant (see 4.3.3.1). The flow area A_{del} is taken as the minimum cross-sectional area through which the flow can pass. The axial dimension of the orifice is normally neglected because the orifice diameter is much smaller than its length. This assumption is borne out by the experimental work of Helgestad [29].

A constant inlet and delivery flow coefficient are used in the model. A value of 0.7 is assumed, again based on experimental results produced by Helgestad.

Γ_{del} is the integral area function of the fluid being accelerated between the delivery port and the cylinder [33]. When the cylinder is in contact with a delivery port relief groove then;

$$\Gamma_{del} = \Gamma_{cyl} + \Gamma_{gr} \qquad (4.7)$$

where

$$\Gamma_{cyl} = V_{cyl}/A_P^2 \qquad (4.8)$$

and

$$\Gamma_{gr} = \int_{x2}^{x1} \frac{1}{a} dx \qquad \text{(See figure 4.3)} \qquad (4.9)$$

4.3.3.3 Application of the Single Cylinder Model within Bathfp

The single cylinder model described in 4.3.3.2 was adapted by Harris for use within Bathfp [37], and demonstrated good agreement with test results [12].

The theoretical model is divided into separate simulation models as described in 4.3.2. Each simulation model calculates system equations and passes the calculation results to the connected models. The arrangement of the models for the prediction of the test pump flow ripple is shown in figure 4.4 (The corresponding Bathfp icons are shown in figure 4.1). The test pump is as described in 5.2.2 and features a single triangular, sloping relief groove at the start of the delivery port.

The cylinder pressure is calculated within the cylinder model using equations 4.1, 4.2, and 4.3. The flowrate due to the piston motion, q_{pist}, and the swept volume, V_{swept}, are calculated in the piston model. The cylinder flow is calculated in the portplate model with equations 4.5 and 4.6.

The overlapping flow areas between the cylinder port and the delivery and suction ports are calculated in the portplate model and are modified by the area restrictions imposed by bridges and relief grooves. This area restriction information is supplied to the portplate model by the bridge model and the four relief groove models.

The cylinder integral area function is calculated within the cylinder model using equation 4.8 and is then passed to the portplate model. Relief groove integral area functions are calculated using the exact integral expressions within each of the four relief groove models (see figure 4.4): their calculation depends on the groove profile and the Cappa suite features a number of different relief groove models for different groove designs. The models shown in figure 4.4 correspond to the portplate design for the test pump.

It is possible to use more involved models from the Cappa suite to simulate the behaviour of the test pump. In particular there is a range of cylinder models using different assumptions for cavitation and air release. During the course of this project these models were tried but had only a minor effect on the simulated delivery flow ripple. Furthermore, in the absence of cavitation, the total effect of suction port air release can be accounted for with a reduction in the fluid bulk modulus within the delivery port [33]. This was confirmed by agreement of the model with the measured delivery flow ripple (See 5.3.4). Accordingly, the model employed did not calculate the effects of cavitation and air release.

4.3.3.4 Calculation of Pump Flows from the Single Cylinder Model

The simulation circuit described in 4.3.3.3 calculates the flow from a single cylinder of an axial-piston pump. The total pump flow ripple is calculated by summation of the cylinder inflows from the delivery and suction ports over a full 360° rotation of the cylinder block.

The summation is carried out by post-processing the simulation results file. First, the data for q_{del} and q_{suc} are copied from the results file and sent to two text files. Fourier analysis is then used to convert the time-domain data held in the two text files into a frequency spectrum of the pump flow ripple harmonics at multiples of the pumping frequency. The time domain waveform of the flow ripple is then obtained by summing the amplitude and phase data from the frequency spectrum.

The post-processing is carried out using two programs written to complement the Cappa suite [37]: the extraction of the flow ripple data from the Bathfp simulation results file is carried out using a FORTRAN program called "Strip". The generation of frequency spectra from the flow ripple data is carried out using the FORTRAN program "Fourier".

The time domain flow ripple waveform was produced with the program used to display test data [40]. This was convenient when comparing measured and simulated flow ripple results.

4.3.3.5 Simulation Results from the Single Cylinder Model

This section shows typical simulation results for the test pump using the single cylinder model. The results are generated for the test pump boosted to 5 bar, running at 1500rev/min and full displacement for a delivery pressure of 250 bar.

A sketch of the test pump portplate showing the delivery and suction timing is shown in figure 4.5. The corresponding simulated flow area between this portplate and a single cylinder port is shown in figure 4.6. The area restrictions of the delivery port bridges can be clearly identified, as well as the gradual opening effect of the relief groove at the start of delivery. The trailing edge of the suction port overlaps the cylinder port at BDC. This will reduce the pump volumetric efficiency but was probably included to make the delivery relief groove more effective at reducing delivery flow ripple.

The simulated single cylinder pressure and inflow from delivery are shown in figures 4.7a) and b) . The effect of fluid compressibility at BDC is clear, although the restriction of the delivery port bridges appears to have no effect upon the cylinder pressure and flow.

Figure 4.8 shows the delivery flow ripple produced from summation of the single cylinder flows. At BDC, the compressibility reverse flow into the cylinder causes over-compression (See fig. 4.7a). The relief groove helps to meter this reverse flow and the flow ripple is not excessive.

4.3.3.6 Limitations of the Single Cylinder Model

Delivery flow predictions from the single cylinder model of 4.3.3.3 closely matched flow ripple measurements from the test pump (See 5.3.4). Despite this, a number of drawbacks with the model became apparent:

1 The delivery flow ripple could not be monitored during a simulation run: it could only be displayed after post-processing of the simulation results using Fourier Analysis.

2 The model produced no information on piston forces and swashplate moments caused by the variation of cylinder pressure. These effects are useful in that they can be used to estimate the level of SBN generated by the pump casing.

3 The model could only be used to optimise the parameters of a conventionally-designed axial-piston pump: the model could not be used to examine the performance of new low-noise pump designs.

The first rwo problems were overcome by further development of the Cappa suite models and of the simulation technique itself. All of these changes were based upon a novel "Dual

Cylinder" simulation model. The modification of the simulation model to analyse the behaviour of a novel pump design (3) was carried out and is dealt with in chapter 8.

4.3.4 The "Dual Cylinder" Pump Model

The "Dual Cylinder" model was developed from the Cappa suite single cylinder model presented in 4.3. Its purpose is to provide information on the pump delivery flow ripple, the total piston forces and the total swashplate moments.

4.3.4.1 The need for a "Dual Cylinder" model

One method to calculate the pump delivery flow is to sum the flow from nine identical, phase-shifted, cylinder models. The drawback is that simulation run times and results files increase in size in proportion to the number of pump cylinders. Also, in the absence of cavitation, the suction flow ripple of the test pump has little effect upon the delivery flow ripple (See 4.3.3.1). Therefore any simulation time spent during a cylinder's inlet stroke is wasted; only simulation of the cylinder delivery stroke is required.

During a cylinder delivery stroke, the cylinder outflow is nominally sinusoidal, starting and ending at zero flowrate. Deviation from this ideal behaviour occurs at the extremes of the delivery stroke where the effects of fluid compressibility and portplate timing intervene.

At the beginning of the delivery stroke, cylinder outflow is dependent upon the pump operating conditions and cannot be assumed sinusoidal. In this region, the cylinder outflow must be simulated using the equations of the single cylinder model (See 4.3.3.2). The cylinder outflow becomes sinusoidal once the cylinder pressure has equalised to the delivery pressure, and from this point can be expressed by the piston kinematic flowrate, q_{pist}.

At the end of the delivery stroke, the cylinder outflow depends on the pump operating conditions and the port timing. However, for the test pump, each cylinder ends communication with the delivery port almost exactly at TDC (see figure 4.5). Therefore, for the test pump, the cylinder outflow at the end of delivery can be assumed to be sinusoidal up to TDC (at $\theta = 180°$). Past this point then the cylinder no longer communicates with the delivery port and the cylinder outflow to delivery is zero.

For the test pump, the cylinders equalise to the delivery pressure within the region subtending 40° past BDC (see fig. 4.7a). So, after 40° past BDC, the cylinder outflow can be regarded as that of the piston kinematic flowrate, q_{pist}. Conceivably then, the single cylinder model equations of 4.3.3.2 need only be applied when the cylinders pass through the 40° sector following BDC. The delivery flowrate from the other 8 cylinders could be calculated from the individual piston kinematic flowrates. The total delivery flow ripple would then be the summation of the sinusoidal flow to delivery from 8 cylinders with that of the single cylinder that is passing through

the 40° region past BDC. In this way, the 9-cylinder delivery flowrate could be simulated with a relatively simple modification to the single cylinder model.

A drawback with applying the single cylinder model only to the 40° region past BDC is that pumps with very late delivery timing could not be simulated. For these pumps, the cylinders may not have reached the delivery pressure by 40° and so the assumption that the cylinder outflow is sinusoidal from this point would be wrong. To overcome this problem then the single cylinder model could be applied over 2 cylinder sectors to the 80° region past BDC. The pump delivery flowrate would then be the summation of flow from these 2 cylinders with the piston kinematic flowrate from the remaining 7 cylinders. This is the basis for the "Dual Cylinder" model which is outlined in the next section.

4.3.4.2 The "Dual Cylinder" action

The "Dual Cylinder" model has been developed to simulate efficiently the behaviour of pumps with a wide range of delivery timing. For a pump with n cylinders, this model calculates the instantaneous pump delivery flowrate according to the following summation:

$$totalq = \sum_{i=1}^{i=n} q_{kin}\left(\omega t + \frac{2\pi i}{n}\right) - \left(q_{del}(\alpha) + q_{kin}(\alpha)\right) - \left(q_{del}(\beta_l) + q_{kin}(\beta_l)\right) \qquad (4.10)$$

Kinematic flow to delivery

compressibility flow to delivery

$$q_{kin}(\theta) = A_P(\omega R X \tan\beta)\sin(\theta) \quad (0 \le \theta \le \pi)$$
$$= 0 \quad (\pi < \theta < 2\pi) \qquad (4.11)$$

q_{del} (a cylinder inflow) is calculated with Eq 4.5 (See 4.3.3.2).

α and β_l are used to mimic the movement of successive cylinders in the region that subtends two cylinder sectors past BDC. In this region, the cylinder pressures and flows are calculated by application of the single cylinder model at angles of α and β_l past BDC. α and β_l are sawtooth functions which cycle between 0 and $4\pi/n$ as shown in figure 4.9a. With this mechanism, the pressure and flow from a pump with n cylinders can be simulated using only 2 sets of cylinder variables.

So, for a nine cylinder pump, the delivery flow from the two cylinders passing through the 80° sector from BDC is calculated using the differential equations of the single cylinder model. The delivery flow from the remaining seven cylinders is taken as their respective piston kinematic flowrates.

The basic elements of this model are shown in figure 4.9b, which can be compared to the single cylinder model shown in figure 4.2. The different phases of the delivery flow calculation for each cylinder corresponding to equations 4.10 and 4.11 are shown in figure 4.10.

To carry out the dual-cylinder action, a new set of Cappa Suite models were created from the existing single cylinder models. The models predicted identical cylinder pressures and flows to the single cylinder model that had been validated with test results.

To speed the simulation, the calculations for the bridge area restrictions were removed. This was justified by the fact that the bridges appeared to have no effect upon the simulated cylinder pressure and flow. Also, the instantaneous air release equations had been proved to be inaccurate and so were also removed. Instead the effect of air release was partially accounted for by the correction factor used to lower the oil bulk modulus (See 4.3.3.3).

The processing of the cylinder flow into the delivery flow is superseded by the "Dual Cylinder" model. However, the use of Fourier Analysis is still necessary as it provides frequency domain information of the pump delivery flow ripple that would otherwise be unavailable. With the "Dual Cylinder" model, the Fourier Analysis is carried out upon the delivery flow ripple rather than on a single cylinder flow.

The "Dual Cylinder" model was developed to investigate the effect of delivery timing upon the delivery flow from the test pump. It can be applied to a wide range of pump configurations but is not as flexible as the single cylinder model. At present, the "Dual Cylinder" model has the following additional limitations:

1 The model assumes that the pump suction flow ripple has no effect upon the delivery flow ripple. For the case of the test pump running at 1500rev/min this has been seen to be valid (see figure 5.18). However, for pumps prone to cavitation this model would not provide accurate delivery flow ripple predictions.

2 The cylinder port at BDC does not overlap the delivery port, and is at the pressure of the suction port (assumed constant).

3 The contribution of a cylinder flow to the delivery flow is assumed to end at TDC. Again, this is valid in the case of the test pump (See fig 4.5).

4 No account is taken of the restriction of bridges within the delivery kidney port.

5 The pump cannot be simulated under motoring conditions, where the delivery port is at a lower pressure than the suction port.

4.3.4.3 Calculation of the Piston Forces and Swashplate Moments

The single cylinder model cannot calculate the total piston forces and swashplate moments since these effects are generated by the interaction of pressure within all of the individual cylinders.

It is possible to estimate the cylinder pressure from all of the pump cylinders by further developing the "Dual Cylinder" model. The pressure of each cylinder is calculated using the following assumptions (See figure 4.11):

1 In the two-cylinder sector past BDC (80° for a nine-cylinder pump), the cylinder pressure is determined using the equations of the single cylinder model (See 4.3.3.2).

2 Between the end of the two-cylinder sector and TDC, the cylinder pressure is that of the delivery port (assumed constant).

3 At TDC the cylinder pressure equals delivery pressure and the flow area between the cylinder port and the delivery port is zero (as for the test pump).

4 Between TDC and the start of the suction port, the minimum cylinder pressure is that of the oil vapour pressure (-0.99 bar gauge). In this region any leakage from the cylinder to the portplate and slipper pad is ignored and the drop in cylinder pressure is determined from the following equation:

$$P_{cyl} = P_{del} - \left[\frac{(V_{cyl} - V_{tdc})}{V_{tdc}} B_{eff} \right] \qquad (4.12)$$

Where

$$V_{tdc} = A_P(L_{mean} - RX\tan\beta) \qquad (3.13)$$

5 Any cylinder port overlapping the suction port is at suction pressure (assumed constant).

Using these assumptions, the "Dual Cylinder" model calculates the pressure within all nine cylinders. The various piston forces and swashplate moments are then calculated for each cylinder using the equations detailed in 3.3.1. Finally, the model sums all of the individual cylinder effects to calculate the total piston forces and swashplate moments acting on the pump driveshaft and casing.

Figures 4.12 to 4.14 show the simulated axial force, yoke moment, and shaft torque for the test pump operating at 250 bar delivery pressure and full displacement. The single cylinder characteristics shown in figures 4.12a,13a and 14a show the same features as those predicted for a neutrally-timed pump (See 3.3.2). However, the full pump characteristics of figures 4.12b, 13b, and 14b are sigificantly different to those of the neutrally-timed nine cylinder pump shown in figure 3.11. This shows the importance of the relief groove and the portplate delivery and suction timing on the total pump forces and moments.

Figure 4.12a shows that the piston inertia forces are a very small component of the overall axial force from a single piston. At BDC, the piston is accelerating towards the portplate and so contributes a positive component to the overall axial piston force. Towards TDC this gradually reverses so that at 200° the axial force on the swashplate is less than zero. This would be the point where the piston may lift from the portplate, although this force is very small, and under test at this condition piston pounding was not apparent.

The axial force stays high until well past TDC, indicating that the suction port is delayed. The summed axial force from all of the pistons is much smoother than the square wave characteristic predicted for the neutrally-timed pump shown in figure 3.11. This difference is due

to the assumption made in 3.3.2 that the pressure changes at BDC and TDC are instantaneous. Figure 4.12b clearly shows that the pressure changes in the test pump are not instantaneous, due to fluid compressibility and, at BDC, due to the relief groove.

Figures 4.13a and b show that the delayed delivery and suction ports of the test pump cause a moment on the swashplate acting to de-swash the pump. This moment is counteracted by that from the bias piston of the pump swashplate servo-mechanism.

Figure 4.14a shows that the delayed suction port causes the pressurised cylinders to provide a driving torque on the cylinder block at the start of the suction stroke. The summed shaft torque from all of the pistons is relatively constant compared to the variation in the total yoke moment (See figures 4.13b and 4.14b). This enforces the assertion made in section 3.3.3 that the yoke moment variation is likely to create higher levels of casing SBN than the variation in shaft torque.

4.3.4.4 Estimation of the Cylinder Leakage

An attempt was made to improve the accuracy of the simulation model by including the effects of cylinder leakage. Volumetric efficiency measurements, provided by Vickers for the test pump [41], were used to estimate leakage levels.

The Vickers-supplied volumetric efficiency figures are shown in Table 4.1. For the figures shown in table 4.1, 100% efficiency corresponds to the theoretical pump flowrate due to the piston motion. Also, to produce these figures, the flowrate at different delivery pressures was measured with a flowmeter placed downstream of the test circuit loading valve. This is important as the loss in flowrate due to fluid compressibility will be recovered at the lower pressure. Accordingly, the figures of table 4.1 do not include the losses due to fluid compressibility (See 3.2.5).

Table 4.1

P_{del} (bar)	η_V (%)	Leakage (L/min)
100	99.00	1.03
150	98.27	1.78
200	97.21	2.88
250	96.03	4.10

The Vickers figures were provided for a pump operating at full displacement, a single speed of 1800rev/min, a single fluid temperature of 50°C, and a suction pressure of 0 bar gauge. The full pump displacement is 57.4cm^3/rev and so the ideal pump flowrate is 103.32L/min.

In practice the leakage from an axial piston pump for a given fluid temperature increases with both speed [42] and cylinder pressure. However, no data were available for the variation in the test pump volumetric efficiency with speed, and so the leakage is assumed to be independent of pump speed within the speed range of interest (1000 to 2000rev/min). Again, since the

simulation is being used for a comparative study then it is expected that the effects of speed between alternative designs will cancel out.

Assuming a constant fluid temperature, then the overall pump leakage can be expressed as a function of the delivery pressure. Dorey [42] concluded that the leakage loss is non-linear with delivery pressure, following a relationship of the form, $q_L \propto K_{LC} P_{del}^{n}$, where n is between 1.5 and 2. For this study, a relationship has been fitted to the empirical slip loss figures shown in table 4.1, where $K_{LC}=459 \times 10^{-6}$ and n=1.65. Table 4.2 compares the empirical leakage with that of the fitted equation:

Table 4.2

P_{del} (bar)	Leakage (L/min) (empirical)	Leakage (L/min) (Modelled (q_L))	Error (%)
100	1.03	0.92	-10.7
150	1.78	1.78	0.0
200	2.89	2.87	-0.7
250	4.13	4.15	+0.5

The leakage term, q_L, is incorporated into the "Dual Cylinder" model by assuming that leakage only occurs when a cylinder port overlaps the delivery port. This is the assumption made by Helgestad [29], and also by Zeiger and Akers [43], and in this case the total pump leakage is assumed to be divided between half of the pump cylinders. Neglecting the cylinder pressurisation period after BDC, then the expression for the individual cylinder leakage can be of the same form as the previously expressed overall pump leakage:

$$q_{leak} = \frac{2}{n}\left(K_{LC} P_{cyl}^{n}\right) \tag{4.13}$$

For the cylinders using the equations of the single cylinder model (See 4.3.4.2) then the flow continuity now includes this leakage:

$$q_{net} = q_{suc} + q_{del} + q_{pist} - q_{leak} \tag{4.14}$$

The flow summation for the "Dual Cylinder" model (See 4.3.4.2) must also include this leakage:

$$\begin{aligned} totalq = & \sum_{i=1}^{i=n} q_{kin}\left(\omega t + \frac{2\pi i}{n}\right) - \left(q_{del}(\alpha) + q_{kin}(\alpha)\right) - \left(q_{del}(\beta_l) + q_{kin}(\beta_l)\right) \\ & - \sum_{i=1}^{i=n} \frac{2}{n}\left(K_{LC} P_{cyl}(i)^{n}\right) \end{aligned} \tag{4.15}$$

The "Dual Cylinder" model produced identical cylinder pressure and delivery flow ripple results to those produced by the test-validated single cylinder model. This indicates that although the leakage effects modelled in the "Dual Cylinder" model will affect the mean level of the delivery flow, they have a negligible effect upon the delivery flow ripple. This justifies the assumption to neglect leakage effects within the simple orifice model (See 4.3.3.2).

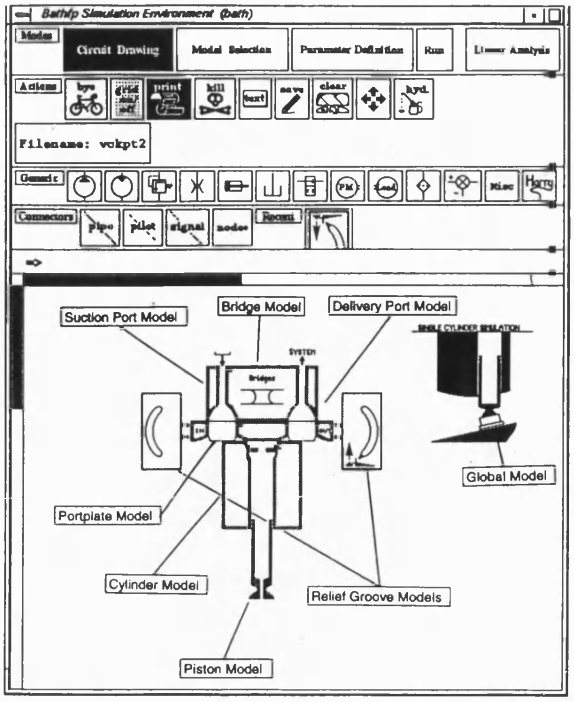

Figure 4.1
The Bathfp simulation window featuring a single-cylinder pump "circuit" using icons and models from the "Cappa" suite

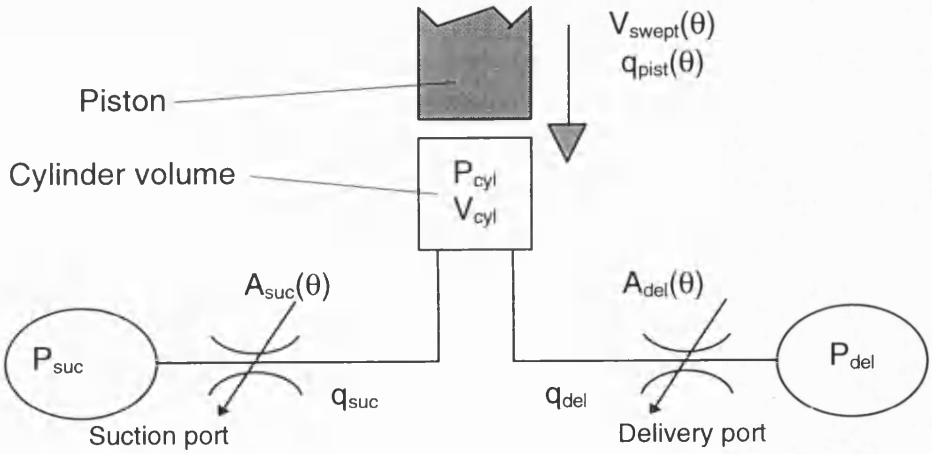

Figure 4.2
Schematic of the original single-cylinder simulation

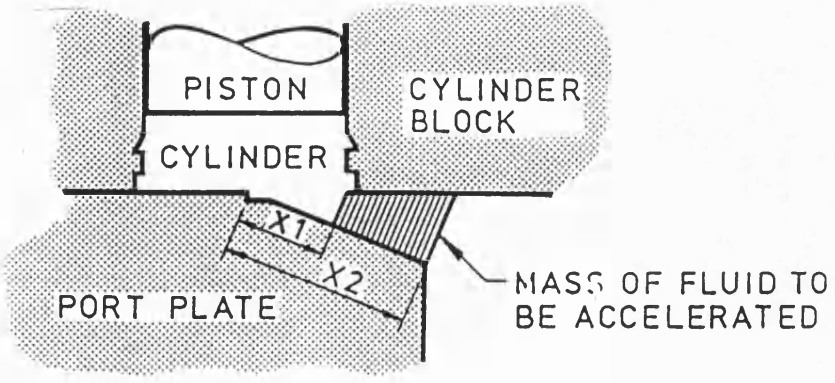

Figure 4.3
Estimation of the mass of fluid accelerated through a relief groove using an integral area function (from [33])

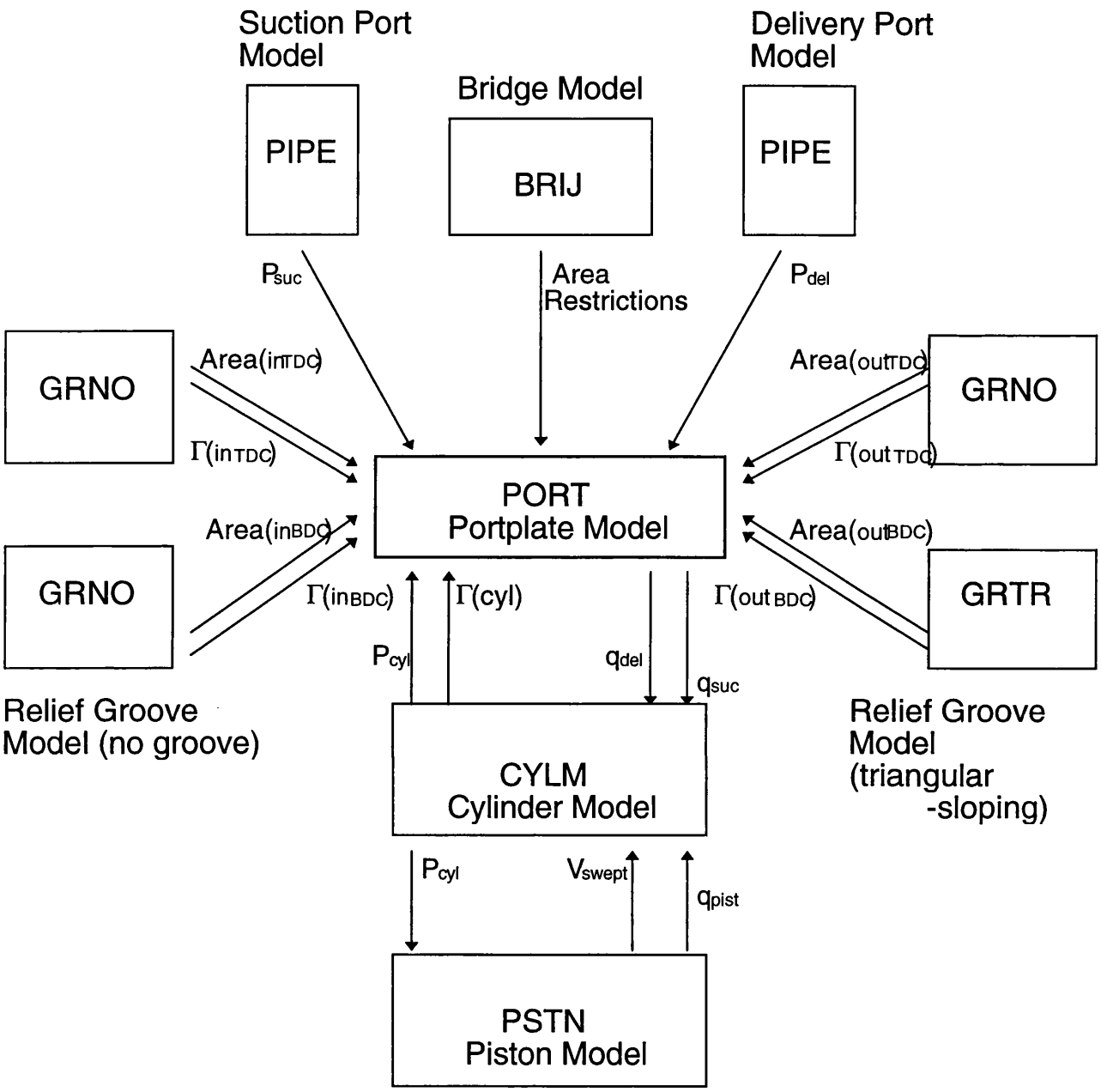

Figure 4.4
Diagram showing the arrangement of models within a "Cappa" suite single-cylinder pump circuit

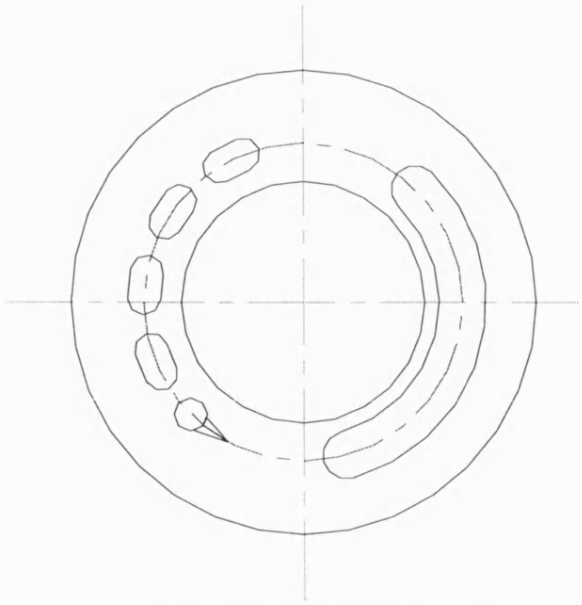

(Each cylinder port subtends an angle of 31.75 degrees).

Portplate Feature	Angle from BDC (degrees)
Start of relief groove	28.0
Lead radius of Delivery Port	39.0
Range of 1st. Delivery Port Bridge	50.0 to 57.0
Range of 2nd. Delivery Port Bridge	78.5 to 85.5
Range of 3rd. Delivery Port Bridge	107.0 to 114.0
Range of 4th. Delivery Port Bridge	135.5 to 142.5
End of Delivery Port	164.0
Range of Suction Port	216.2 to 353.0

Figure 4.5
Timing details for the test pump portplate

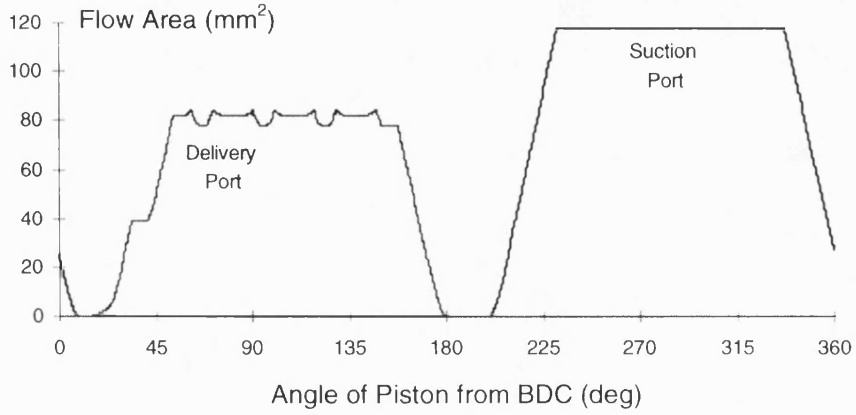

Figure 4.6
The simulated overlapping flow area between a single cylinder and the delivery and suction ports for one complete pump revolution

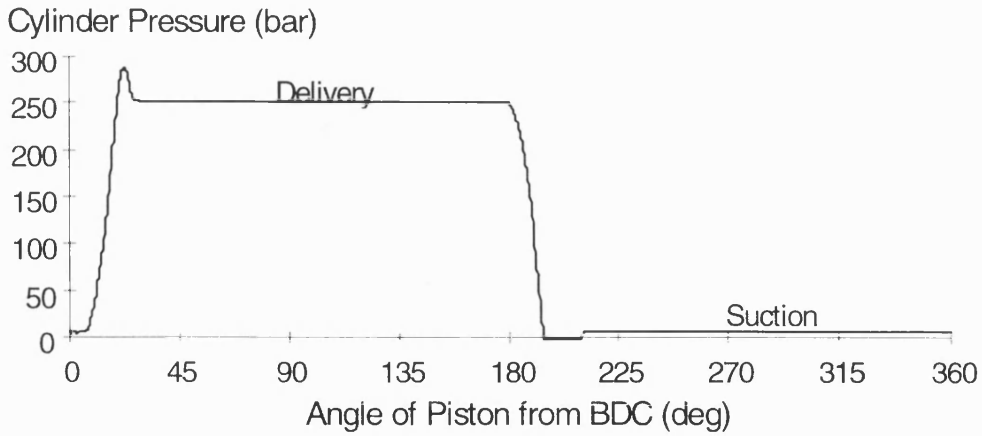

Figure 4.7a
The simulated cylinder pressure for one complete pump revolution

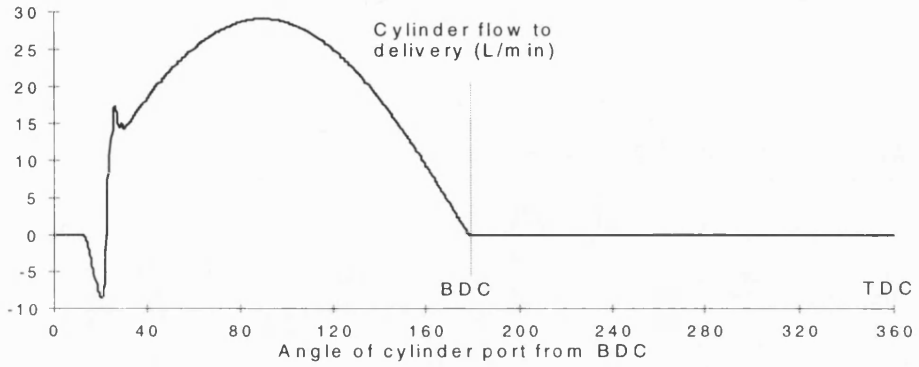

Figure 4.7b
The simulated delivery flow from a single cylinder for one complete pump revolution

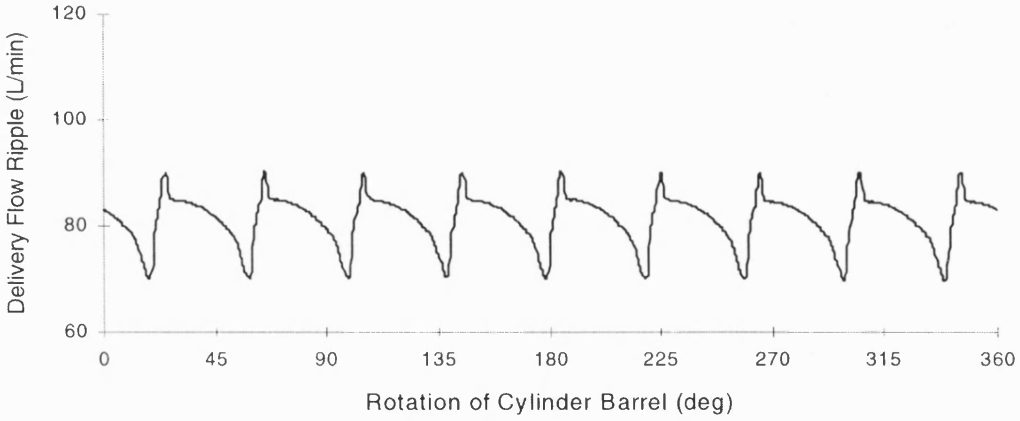

Figure 4.8
The simulated delivery flow from all of the pump cylinders for one complete pump revolution

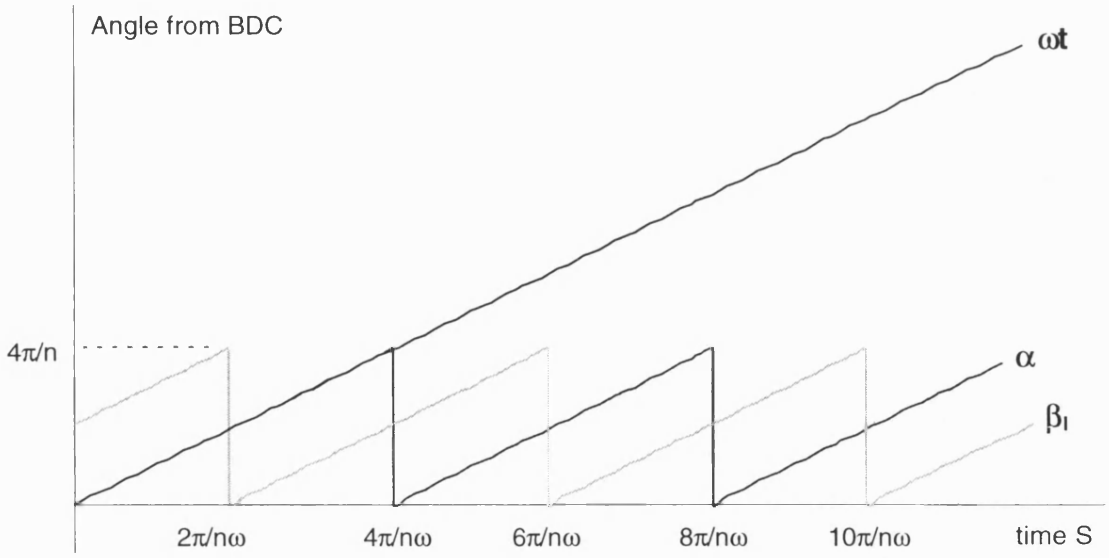

Figure 4.9a
The sawtooth functions used in the dual cylinder model to simulate the flows and pressures from all of the pump cylinders

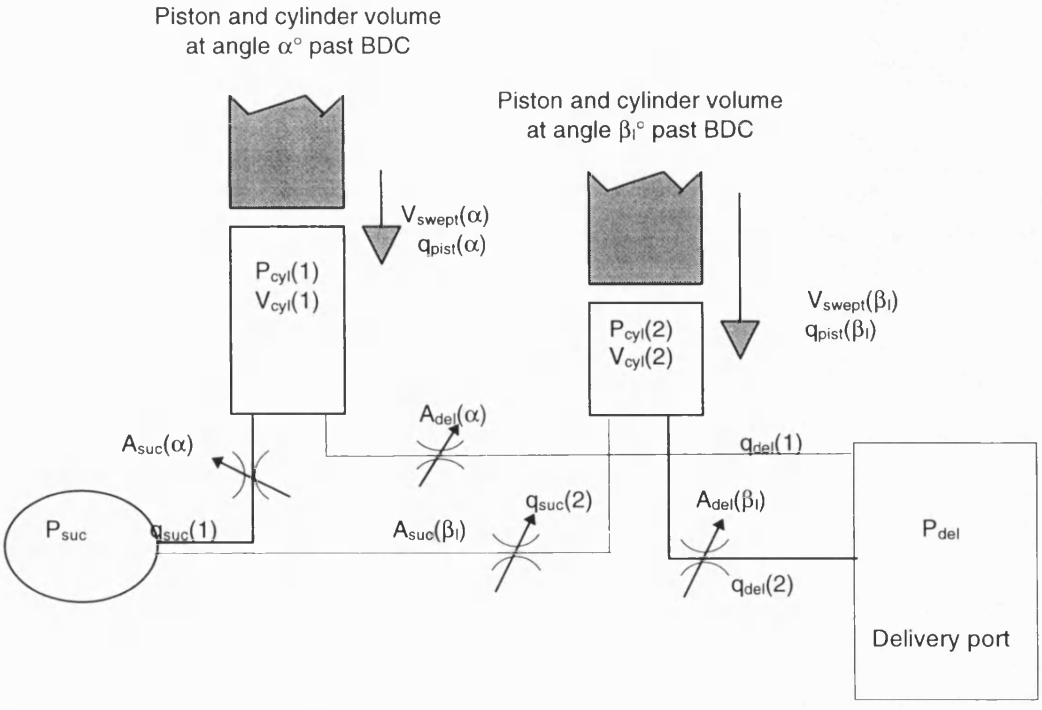

(Where q_{del} represents a cylinder inflow from the delivery port)

Figure 4.9b
Schematic of the dual-cylinder simulation

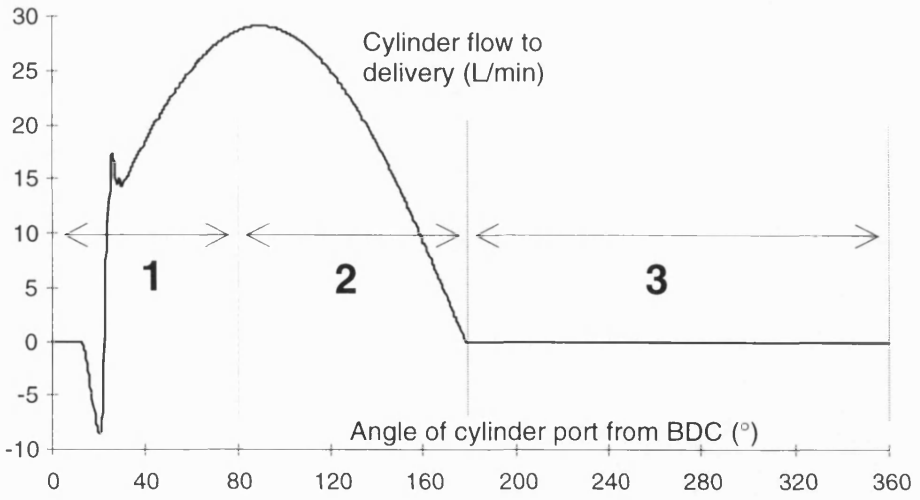

1) $q_{del}(\alpha)$ 2) $A_P(\omega RX\tan\beta)\sin(\theta)$ 3) 0

Figure 4.10
Modelling the delivery flowrate from each cylinder within the dual cylinder model

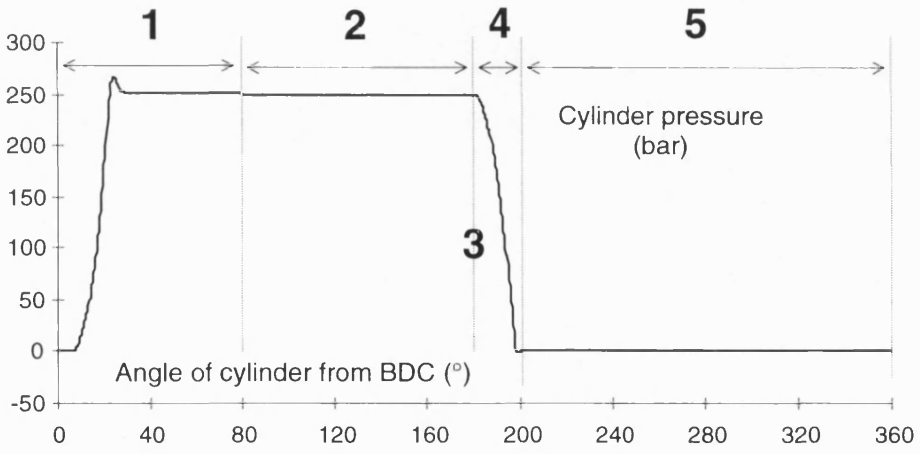

1 $P_{cyl} = \int \frac{B_{eff}}{V_{cyl}} q_{net} dt$ **2,3** $P_{cyl} = P_{del}$

4 $P_{cyl} = P_{del} - \left[\frac{(V_{cyl} - V_{tdc})}{V_{tdc}} B_{eff} \right]$ **5** $P_{cyl} = 0$

Figure 4.11
Modelling the pressure of each cylinder within the dual cylinder model

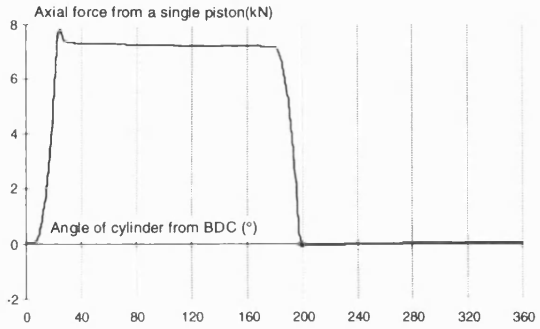

Figure 4.12a
The simulated axial force from a single piston for the test pump at 250 bar delivery pressure and 100% displacement

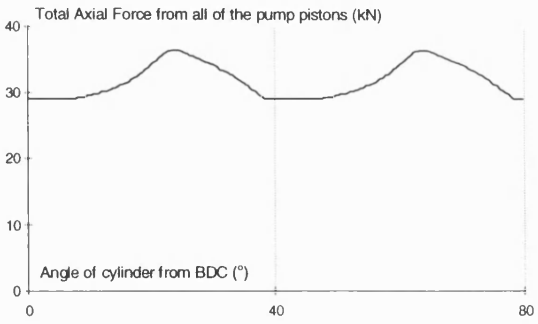

Figure 4.12b
The simulated total axial force from all 9 pistons of the test pump at 250 bar delivery pressure and 100% displacement

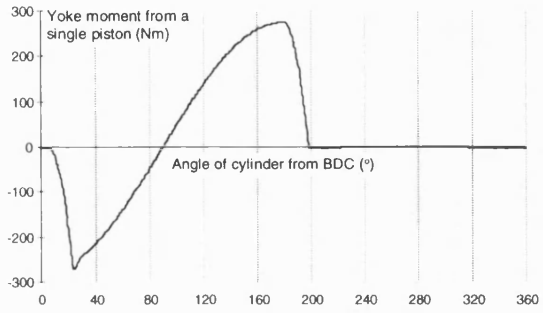

Figure 4.13a
The simulated yoke moment from a single piston for the test pump at 250 bar delivery pressure and 100% displacement

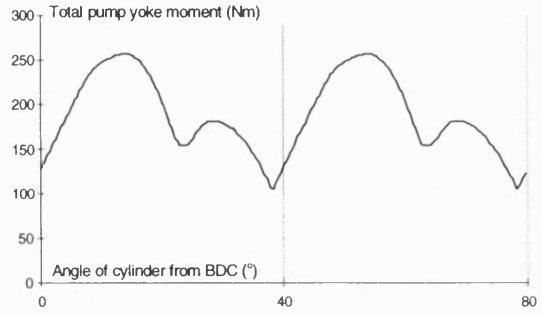

Figure 4.13b
The simulated total yoke moment from all the pistons of the test pump at 250 bar delivery pressure and 100% displacement

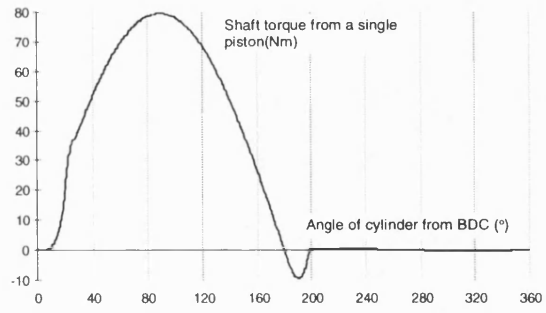

Figure 4.14a
The simulated shaft torque from a single piston for the test pump at 250 bar delivery pressure and 100% displacement

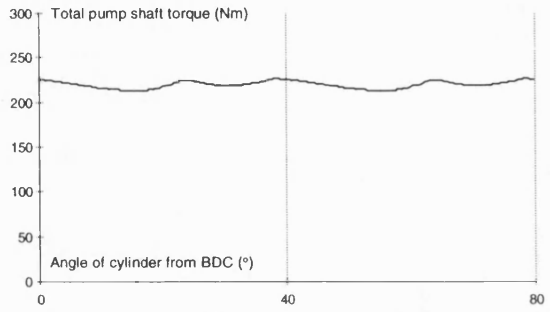

Figure 4.14b
The simulated shaft torque moment from all the pistons of the test pump at 250 bar delivery pressure and 100% displacement

5.0 Investigation of the Test Pump Flow Ripple

5.1 Introduction

This chapter presents source impedance and source flow ripple measurements from the delivery port of the test pump. The purpose was to determine the internal flow ripple over a wide range of operating conditions. Using these results, the simulation model for the pumping dynamics described in chapter 4 was validated.

To enable a proper interpretation of the test measurements, a description of the test method is given. The application of this method into a suitable pump test rig is then described.

The internal flow ripple measurements are tested against compressible volume calculations, and then compared with simulation results.

5.1.1 Characteristics of Flow Ripple Measurement Techniques

As positive displacement pumps are flow sources, there is a need for methods that can measure flow. The bandwidth of the method has to range from below 100Hz up to several kHz. Laser and hot wire anenometry can be used to measure fluid velocity variations over this range of frequencies, although these methods are complex and intrusive. Also, these methods only give the fluid velocity at a given point, and so to deduce the total flowrate a number of measurements would be needed to establish the velocity profile of the pipe flow. Furthermore, the use of a laser is often inpractical because of the need for "portholes" in the pipe.

In the absence of a suitable method for direct measurement of flow in this frequency range, indirect methods are necessary. Pressure is measured much more readily as there are many commercially available piezoelectric and piezoresistive pressure transducers with the necessary measurement bandwidth. For this reason, methods to measure flow ripple generally rely on the measurement of pressure ripple from the pump under test.

Because of the complex pattern of pressure standing waves within a pressurised hydraulic system, it is not possible to obtain the pump flow ripple by simply measuring the pressure at a particular point. To deduce the pump flow ripple, the impedance of the measurement system at the transducer location must be established.

5.2 Description of Pump Flow Ripple Test Rig

The "Secondary Source" method was used to measure the test pump source impedance and internal flow ripple. This section describes the application of this measurement technique.

5.2.1 Description of the "Secondary Source" Test Method

This method has been adopted by the British Standards Institution [44] for the measurement of pump fluidborne noise characteristics. It is described in detail by Johnston[6]

and by Edge and Johnston[9], and enables the flow ripple and source impedance of a pump to be measured in terms of harmonic spectra.

5.2.1.1 The Principle of the "Secondary Source" Method

The method is based on the measurement of pressure ripple harmonics at either 2 or 3 points along the length of the pipe connected to the port of the pump, and makes use in the analysis of the variations in pressure ripple which occur with distance along the pipe. The test circuit is based upon the simple system analysed by Bowns and McCandlish [17]. Accordingly, the Transmission Line Equation can be used to analyse the circuit pressure ripple.

The basis of the method is to use a secondary source of pressure ripple at the termination of a simple pump-pipeline-termination system. Provided that the frequencies of the harmonic components of the pressure ripple from the pump and the second source are different, then the pressure ripple produced from either source can be examined in isolation.

Figure 5.1 shows a schematic diagram of the hydraulic circuit employed for the "Secondary source" test method.

5.2.1.2 Determination of the Pump Source Impedance

For the pressure ripple from the pump under test at a distance x from the pump exit along the pipe of length L, the Transmission Line Equation gives (See 2.4.2.2):

$$P_x = \frac{Q_S Z_S Z_O}{Z_S + Z_O}\left(\frac{e^{-\gamma X} + \rho_T e^{-\gamma(2L-X)}}{1-\rho_S \rho_T e^{-2\gamma L}}\right) \qquad (5.1)$$

In this simple system, the pump impedance, Z_S, is actually equivalent to the termination impedance for harmonics generated by the secondary source. This gives the equivalent expression for the pressure ripple from the secondary source [6]:

$$P_x = \frac{Q_{S2} Z_T Z_O}{Z_T + Z_O}\left(\frac{e^{-\gamma X} + \rho_S e^{-\gamma(2L-X)}}{1-\rho_S \rho_T e^{-2\gamma L}}\right) \qquad (5.2)$$

From manipulation of the pump pressure ripple harmonics, Equation 5.1 is used to arrive at Z_T, and from a similar manipulation of the secondary source pressure ripple harmonics, Equation 5.2 is used to find Z_S.

5.2.1.3 The Determination of the Pump Exit Flow Ripple

With Z_S and Z_T established, then from manipulation of the pump pressure ripple harmonics it is straightforward to find the flow ripple from the pump at the pump exit, Q_S [6].

One problem is that the values of Z_S generated from the secondary source pressure ripple are at different frequencies to those of the pump pressure ripple. Numerical interpolation or curve-fitting is used to produce values of Z_S at the harmonic frequencies of the pump pressure ripple [6].

5.2.1.4 Determination of the Pump Internal Flow Ripple

With the calculation of the flow ripple at the pump exit, Q_S, the final stage of the test method involves the referral of this flow ripple to the point of generation at the end of the pump discharge passageway.

With a Helmholtz model of the pump discharge passageway, the referred source flow ripple, Q_S^*, (for each harmonic of the pumping frequency) is found using the following equation, (previously shown in 2.4.2.5):

$$Q_S^* = Q_S\left[1+j\omega\frac{V_P}{B_{eff}}\left(R+j\omega\frac{\rho L_P}{A_P}\right)\right] \tag{5.3}$$

To solve this equation, values for R, $(L_P\rho/A_P)$ and (V_p/B_{eff}) are needed. These values are estimated by curve-fitting a Helmholtz model of the pump source impedance onto the previously measured source impedance spectrum. When the pump source impedance is represented by a Helmholtz model then,

$$Z_s = R+j\omega\frac{\rho L_p}{A_p}+\frac{B_{eff}}{j\omega V_p} \tag{5.4}$$

R, $(L_P\rho/A_P)$ and (V_p/B_{eff}) are extracted as parameters of the curve-fitted model (5.4). Equations 5.3 and 5.4 are derived in Appendix A.

Using this method, very good agreement has been achieved between curve-fitted source impedance spectra and impedance spectra determined experimentally [10].

5.2.1.5 The Need for Three Pressure Transducers.

The previous analysis can be carried out using only two pressure transducers. However, three transducers can be used at different spacings along the measurement section. There are two benefits from this arrangement:

a) At harmonic frequencies corresponding to whole or half wavelengths equal or near to the spacing between two transducers, then the pressure ripple at each transducer is equal in amplitude and in phase or anti-phase with that at the other transducer. Small experimental errors can then lead to large errors in the results. With the choice of transducer spacings available from three transducers, this condition can be avoided.

b) From the procedure described by Johnston and Edge [45], three transducers enable the measurement of the speed of sound in the fluid to be directly calculated from pressure ripple measurements.

5.2.2 Description of the "Secondary Source" Test Rig

For accuracy, the three transducer test method was used to determine the internal delivery flow ripple. Diagrams of the test circuit are shown in figures 5.1, 5.2 and 5.3. Details of the measurement equipment are given in Appendix B.

The pump was fed from a reservoir approximately 2 metres above the level of the pump. The suction line was a flexible pipe of 2" internal diameter and approximately 5 metres

long. The unboosted pump inlet pressure at full displacement and at a fluid temperature of 40 degrees was 0.11 bar gauge. The working fluid was standard mineral oil (BP HLP32).

Delivery pressure was varied with a needle valve placed downstream of the measurement section. Pump displacement was varied by adjustment of the pressure compensator on the pump against the closure of the needle valve. Pump displacement was not measured directly but instead was inferred from measurement of the pump flowrate in the circuit return line.

With reference to section 6.7 of BS.6335 pt.1, the pump flow ripple was measured using method 1: three pressure transducers were fitted at distances of 8.0 cm, 49.0 cm, and 78.0 cm from a 79mm long adaptor fitted to the pump delivery flange face. The diameter of the steel pipe used for the test section was chosen to ensure laminar flow at full displacement. Due to material limitations the eventual bore size was 26.42mm. Laminar conditions are necessary to ensure consistency with the mathematical assumptions made in the analysis detailed in Appendix C of the BS [44].

The secondary source was a rotary valve powered by a variable speed d.c. servomotor. The valve was designed to provide a bleed-off from the high pressure line during a small section of its revolution. When driven at a constant speed, this produces a flow-ripple consisting of a train of very short duration negative pulses.

Trigger signals from the driveshaft of both the test pump and the rotary valve were provided by optical pick-ups. The signals from the three pressure transducers and the two optical pick-ups were sent to a PC. The signals were captured using a Keighley Metrabyte DAS-58 data acquisition card.

All of the necessary post-processing and analysis was carried out with the PC using "FBN2" [40], an analysis package written at Bath University specifically for this test method.

5.2.3 Development of the Test Rig

During the course of testing a number of problems were encountered that led to the development of the final test rig. This section details the different stages of this process.

5.2.3.1 Cavitation during Unboosted Testing

The test pump was fed from a reservoir approximately 2 metres above the level of the pump. The suction line originally had a 90° bend close to the pump flange.

With this suction line, boosted tests were carried out using an in-line boost pump giving an inlet pressure at the pump flange of 5 bar. These tests produced sensible results and there were no signs of cavitation.

With the same suction line arrangement, unboosted tests were attempted but were unsatisfactory due to cavitation. This was despite the presence of a small positive gauge

pressure during operation as measured just upstream of the 90° bend. To prevent the cavitation, the pump test rig was moved closer to the reservoir and the 90° bend removed.

Using the new suction line a positive head of 0.11 bar gauge was present during all subsequent unboosted testing and no further cavitation problems were encountered. As a result this is the existing suction line arrangement.

In this instance the presence of a 90° bend in the suction line was critical to the subsequent unboosted pump performance.

5.2.3.2 Pressure Compensation with the modified Valve Block

On the original (factory - assembled) test pump a standard valve block is fitted together with a pressure compensator. By adjustment of the compensator setting against the closure of the circuit loading valve it is possible to operate the pump over the working range of displacement and delivery pressure.

The compensator works by bleeding a pilot pressure from the pump discharge passageway to the swashplate servo control mechanism, to create a nominally constant delivery pressure with variations in mean flow.

During the course of testing it became necessary to replace the standard valve block with a similar valve block without the pilot drillings that connect the discharge passageway to the pressure compensator. Because of this, once the new valve block was fitted to the test pump the pressure compensation action was disabled. As a result, the swashplate was only acted on by the pressure forces on the pistons from the inlet and delivery kidney ports. This meant that at a delivery pressure of 90bar the swashplate was forced to a reduced inclined angle and the pump flow dropped.

To regain displacement control for higher loads it was necessary to feed delivery pressure into the swashplate servo control mechanism externally. This was achieved by feeding delivery pressure to a drilling in the new valve block that was otherwise redundant. To avoid affecting the pump impedance characteristics, the delivery pressure was fed via a pilot line from the termination end of the measurement section. This change to the test rig is shown in figure 5.2.

To allow control of the pump displacement at different loads, a restrictor was placed in the pilot line. The displacement adjustment was then achieved by balancing the closure of the pilot line restrictor with that of the circuit loading valve (See Appendix C).

Impedance measurements of the pump with and without the external pressure feed were taken. These results showed that the external pressure feed made a negligible difference to the pump impedance characteristic.

Using the new displacement adjustment arrangement with the new valve block it is possible to achieve any swash angle at delivery pressures above 90 bar. Below 90bar only full displacement conditions could be achieved.

5.3 Evaluation of Test Results

The next sections describe the following work:

a) The choice of source impedance model.

b) The form of the measured source impedance spectrum compared with that of a theoretical pump model.

c) Source flow ripple measurements assessed against compressible volume considerations.

d) A comparison and discussion of the simulated and the measured flow ripple.

e) The problems encountered with the simulation of Cavitation and Air Release

5.3.1 Initial Choice of Pump Impedance Model

The simulated delivery flow ripple results can only be compared with measured values of the internal delivery flow ripple as seen at the point of flow ripple generation inside the pump. The "Secondary Source" test method only gives direct measurement of the flow ripple as far as the pump exit. To find the internal flow ripple then the flow ripple measured at the pump exit has to be referred to some point within the pump discharge passageway.

The flow referral process relies on a relationship whose parameters can be provided by an impedance model of the pump discharge passageway (see section 2.4.2.5). From inspection of initial results a Helmholtz model was chosen for this purpose.

A Helmholtz model accounts for the compressive, inertial, and resistive properties of the fluid within a discharge passageway which is assumed to be of constant cross-section and which is connected to a volume chamber. The use of the model within the analysis is outlined in section 2.4.2.4. At low frequencies the compressibility effect of the volume chamber is dominant, with the effect of the fluid inertia in the passageway increasing with frequency. By least-squares curve-fitting the model to the measured impedance spectrum, then the model parameters for the pump can be deduced.

5.3.2 Source Impedance Measurements

Unless otherwise stated, the pump source impedance spectra shown in the figures represent a least-squares weighted curve fit of the measured impedance values. This approach minimises experimental scatter to establish trends in the results more clearly.

During the course of testing, the test pump was fitted with one of two different valve blocks. The two valve blocks had different discharge passageways (See 5.2.3.2) and were used to examine the effect upon the source impedance spectrum of pilot drillings connecting the discharge passageway to the pressure compensator. The pump with the standard valve block featured the pilot drillings through to the pressure compensator. The discharge passageway that featured no pilot drillings was fitted used in the modified valve block. Both valve blocks are detailed in Appendix C.

5.3.2.1 Measurements using the standard Valve Block

These results were obtained using the "Secondary Source" technique using the test circuit illustrated in figure 5.1.

The variation of the source impedance with pump displacement at 140 bar delivery pressure and 5 bar suction pressure is shown in figures 5.4a and b. Figure 5.4a shows the measured impedance spectra and figure 5.4b shows the least-squares weighted curve fitted impedance spectra.

The variation of the source impedance at full displacement with delivery pressure is shown in figures 5.5a and b. Figure 5.5a shows the measured impedance spectra and figure 5.5b shows the least-squares weighted curve fitted impedance spectra. Figure 5.6 shows a typical impedance characteristic displayed with a curve-fitted Helmholtz model characteristic. The measured source impedance differs from the model impedance in the following respects:

a) Above 2000 Hz, the measured impedance suffers from experimental scatter. Figures 5.4a and 5.5a show that this effect is present at the other operating conditions but that it starts earlier - at 1600 Hz in some cases.

b) Below 300 Hz there is a large inertial component demonstrated by the phase which approaches +90°. Figures 5.4b and 5.5b show that this effect is present at other operating conditions but that the size of the effect does not follow any clear trend with delivery pressure or displacement.

c) Between 700 and 1300 Hz there is a resonance causing a change in amplitude and a phase difference that approaches 0°. Figure 5.4b shows that with decreasing delivery flow, the shape of the effect "flattens" and moves to a higher frequency.

The experimental scatter in the results above 2000Hz, (a), is due to the pressure ripple from the rotary valve being relatively small compared to that from the test pump. The higher frequency harmonics from the rotary valve are diminished by viscous friction effects and so become indistinct from the much larger pressure ripple from the test pump.

The low frequency behaviour, (b), is caused by leakage through the swashplate servo-mechanism. This is investigated further in 5.3.2.2. It may also be influenced by the measurement pipeline being too short (0.715m) to adequately measure the pressure standing waves at lower frequencies.

The resonance feature, (c), resembles the effect that would be caused by a branch resonator [46]. This is consistent with the discharge passageway of the test pump which features drillings leading to the pressure compensator (See Appendix C). Conversely, the Helmholtz model is based upon the assumption of a constant cross-section passageway connected to a volume chamber and does not account for such a feature.

To investigate the effect of the pressure compensator itself, impedance measurements were carried out at full displacement and different delivery pressures with the pressure compensator replaced by a blanking plate. The resulting impedance spectra showed that the pressure compensator made no difference to the resonance feature.

5.3.2.2 Measurements with the modified Valve Block

To investigate the effect of the drilled passageways, a new valve block was machined that had no side-drillings inside the discharge passageway. The pump was then tested with this modified valve block. The results were obtained using the "Secondary Source" technique using the test circuit illustrated in figure 5.2.

Figure 5.7 shows the measured source impedance using the modified valve block together with the comparable source impedance measured using the standard valve block. This figure clearly shows that the mid-frequency range resonance is removed with the absence of the drillings from the discharge passageway.

The modified valve block was also used to investigate the low frequency effect (<200Hz.) mentioned above. A direct comparison was made between the source impedance spectrum from the test pump at full displacement using the different valve blocks. These impedance spectra are shown in figures 5.8 and 5.9 respectively. All of the spectra show a low frequency inertial effect, (where the amplitude ratio increases with frequency and the phase tends to +90°), but in all cases it is largely confined to below 200Hz.

Impedance results from the pump at 60% displacement using the standard and the modified valve blocks are compared in figure 5.10. Figure 5.11 shows the same comparison at 20% displacement. In both cases the low frequency effect is much more significant with the standard valve block.

The standard valve block features the pressure compensator, and when the pump is operated below full displacement the pressure compensator spool is in position to allow flow at delivery pressure through to the control piston (See Appendix C). This leakage to the control piston is very likely to change the source impedance of the test pump. For the pump with the modified valve block, displacement is controlled by pressure supplied from the far end of the measurement section, and so would not affect the pump source impedance (See figure 5.2).

5.3.2.3 Final Choice of Pump Impedance Model

Consideration of all the impedance measurements taken from the test pump with the modified valve block shows that the source impedance is largely independent of the operating condition. Specifically, between 200 and 1700Hz, the source impedance is almost unchanged for delivery pressures between 90 to 250 bar (gauge), suction pressures between 0 to 5 bar (gauge) and pump displacements between 20% to 100%.

The frequency range between 200 and 1700Hz includes the first seven pumping harmonics of the nine-piston test pump operating at the drive speed of 1500rev/min. Therefore, if the pump flow ripple is dominated by the first seven flow ripple harmonics then a single representative impedance spectrum could be used to calculate all of the flow ripple results. To investigate this, the impedance model and spectrum shown in figure 5.12 at 220 bar and full displacement was used initially to process all of the flow ripple measurements from the test pump fitted with the modified valve block (see 5.3.3.1).

As shown in figure 5.6, the Helmholtz impedance model is unsuitable for calculating the pump internal flow ripple from the standard valve block. Instead a "Parallel Helmholtz" model is used which provides much better agreement with the measured impedance spectrum. This is illustrated in figure 5.13 which shows a typical measured impedance spectrum from the standard valve block together with a fitted parallel impedance model.

The impedance network for the Parallel Helmholtz model is shown in figure 5.14. The expression for the pump source impedance for a parallel Helmholtz model is also derived in Appendix A and is shown below:

$$Z_s = \frac{(Z_{R1} + Z_{L1} + Z_{C1})(Z_{R2} + Z_{L2} + Z_{C2})}{Z_{R1} + Z_{L1} + Z_{C1} + Z_{R2} + Z_{L2} + Z_{C2}} \qquad (5.5)$$

Although the source impedance from this model is more complex than that for the conventional Helmholtz model, the flow referral expression for the two models is the same (See 5.2.1.4 and Appendix A).

The source impedance of the standard valve block is more dependent upon the delivery pressure and pump displacement than the modified valve block. Therefore, to calculate the flow ripple from the standard valve block, the measured impedance for each operating condition is used. A separate parallel Helmholtz model is then fitted to each measured impedance spectrum to calculate the internal flow ripple.

5.3.3 Pump Internal Flow Ripple Measurements

This section presents internal flow ripple measurements from the test pump fitted with both the standard and the modified valve block (See 5.3.2.2).

The internal flow ripple established from the modified valve block is demonstrated to be more reliable than that from the standard valve block. The internal flow ripple from the modified valve block is then shown to compare well with compressible volume calculations.

5.3.3.1 The Effect of the different valve blocks

The internal flow ripple with the modified valve block was calculated using the impedance model and measured spectrum displayed in figure 5.12. For the frequency range of the first 7 pumping harmonics, the source impedance measured from the modified valve block was largely independent of delivery pressure and mean flow (See 5.3.2.3). Therefore, provided that the pump internal flow ripple was adequately represented by these first 7 harmonics, then the impedance spectrum of figure 5.12 could be used to represent the pump source impedance over the whole operating range.

Figure 5.15 shows that the internal flow ripple from the modified valve block for the 250bar, full displacement condition can be closely represented by using only the first five flow ripple harmonics. This was representative of all the test conditions, and vindicates the use of a single impedance spectrum for calculation of the internal flow ripple from the modified valve block.

The measured internal flow ripple from the two different valve blocks is compared in figure 5.16 for the 250 bar delivery pressure, full displacement condition. The measured internal flow ripple from the different valve blocks is very similar. However, the 5th. 6th. and 7th. harmonics from the standard valve block are clearly smaller than those from the modified valve block. In this frequency range, differences of internal flow ripple between the two valve blocks were also recorded for all of the other test conditions.

In this region, the pump impedance falls close to the level of the line characteristic impedance (2.3 x 10^9 Ns/m^5). Also, these harmonics fall within the frequency range of the Helmholtz resonator effect measured from the standard valve block (See 5.3.2.2). Therefore, it is likely that the difference in internal flow ripple measured for the two valve blocks is caused by this Helmholtz resonator effect.

The difference in the internal flow ripple measured from the two valve blocks was not expected: the internal flow ripple is generated within the cylinders and at the portplate and so should not be affected by the design of valve block.

The difference in flow ripples may be caused by the parallel Helmholtz impedance model that was used to process the flow ripple from the standard valve block. In this model the branch between the two separate Helmholtz networks occurs at the pump exit (See fig 5.14). However, the side-drillings occur at a distance inside the discharge passageway of the standard valve block. Therefore, a more representative impedance network may be the one shown in figure 5.17. This change would affect the flow referral equation (See Eq. 5.3) and may bring the internal flow ripples from the two valve blocks into agreement. However, a difficulty in applying the model is in the estimation of the two separate inductance terms L_1 and L_3. For this reason a model of the network shown in figure 5.17 was not applied.

The low frequency impedance behaviour (See 5.3.2.2) did not affect the internal flow ripple measured from the pump fitted with the standard valve block. In some cases the inertial component of this effect was significant up to 300Hz (See figures 5.10 and 5.11), and so it was expected to affect the first harmonic of the pump flow ripple (@225 Hz). The reason for the independence of the pump flow ripple from this effect has not been explained. However, the measurement pipeline may be too short to measure accurately at these lower frequencies and so may have exaggerated the the size of this impedance effect.

Figure 5.16 shows that the difference in the internal flow ripple waveform for the two valve blocks is very small. However, because of the difficulty in modelling the impedance of the standard valve block, the internal flow ripple measurements from the modified valve block have been taken as the most accurate. As a result, the measurements from the modified valve block are used in the following section for comparison with the results of simulation.

5.3.3.2 Internal Flow Ripple from the modified valve block

Figure 5.18 shows that the delivery flow ripple at the 250 bar, full displacement condition is virtually unaffected by boost pressure between 0.11 and 5 bar (gauge). This

independence from boost pressure is exhibited at all the other measured operating conditions down to a delivery pressure of 90bar and a displacement of 20%.

Figure 5.19 shows the variation in the source flow ripple for the unboosted test pump (at 0.11bar gauge) with delivery pressure at full displacement. Figures 5.20 and 5.21 show similar characteristics and trends at 60% and 20% displacement respectively. Figure 5.22 shows the variation in source flow ripple with displacement for the unboosted test pump at 250 bar delivery pressure.

These results show that the compressibility reverse flow increases with delivery pressure and also with pump displacement. The results also show that the compressibility reverse flow for this pump is more dependent upon the mean delivery pressure than it is upon the pump displacement.

The dependence of the test pump compressibility reverse flow upon the delivery pressure rather than the mean flow was checked using compressible volume calculations. From 3.2.5, the volume of fluid needed to compress the cylinder contents at BDC to the delivery pressure can be estimated from the relationship;

$$V_{comp} = \frac{(P_{del} - P_{suc})V_{bdc}}{B_{eff}} \qquad (3.10)$$

From detail drawings of the test pump; V_{bdc} =13.23cm^3 at full displacement
=10.90cm^3 at 20% displacement.

Assuming that the effective bulk modulus is equivalent to that of the fluid, then from manufacturer's data B_{eff} =17052bar

The cylinder compressibility volume (V_{comp}) was calculated for four (unboosted) operating conditions. The results are presented in table 5.1:

Table 5.1

Delivery Pressure bar	Displacement %	V_{bdc} mm^3	V_{comp} mm^3
250	100	**13230**	**195**
250	20	**10900**	**160**
90	100	**13230**	**70**
90	20	**10900**	**58**

The theoretical results for the test pump shown in table 5.1 agree with the measured trend, i.e. the compressibility reverse flow is more dependent upon delivery pressure than it is upon the mean flow.

The mean flow has a relatively small effect on the compressibility reverse flow because the comparatively large unswept cylinder volume is unaffected by changes in pump displacement. Other pump designs with a smaller unswept volume would give rise to a compressibility flow ripple that is more sensitive to changes in mean flow (See 3.2.5).

5.3.4 Internal Flow Ripple Simulation Results

This section compares the simulated delivery flow ripple (See 4.3.4) with the internal flow ripple measured from the test pump fitted with the modified valve block.

Figure 5.23 shows that the measured delivery flow ripple for the unboosted test pump at 250 bar and full displacement is significantly larger than the comparable flow ripple predicted by simulation. This is also the case for all of the other measured operating conditions. This phenomenon has been previously shown by Weddfelt [47] and is likely to be caused by air-release within the suction chamber causing a lower fluid bulk modulus than that quoted for the working fluid at saturation pressure.

During an earlier study on axial piston pump dynamics, Darling [33] made a correction to the effective bulk modulus to take into account the effects of air release. Darling found that an effective bulk modulus of 10000bar was needed to produce good correlation between previous simulations and experimental results. During this study the simulation cylinder fluid bulk modulus was changed from 17052bar to 11000bar and, as before, much better agreement was achieved.

The reduced value of the fluid bulk modulus was compared with a value established from the previously-measured pump source impedance spectrum (see figure 5.12). As stated in section 5.3.3.1, the source impedance results were modelled with a Helmholtz model. For this model, the source impedance Z_S, is described by the following expression (See 2.4.2.4);

$$Z_s = R + j\omega\frac{\rho L_p}{A_p} + \frac{B_{eff}}{j\omega V_p} \qquad (5.6)$$

Assuming that the fluid resistance, R, is small [6], then at low frequencies the compressibility term dominates and Z_S can be expressed by the following equation:

$$Z_s \approx \frac{B_{eff}}{j\omega V_p} \qquad (5.7)$$

At 1000Hz, $Z_S \approx 3.10^9 Ns/m^5$ (From figure 5.12).

V_P was physically measured to be $50cm^3$.

Therefore the effective fluid bulk modulus estimated from equation 5.7 is 9425bar. This is significantly lower than the value of 17052bar quoted as the bulk modulus for the working fluid, but is much closer to the value of 11000bar assumed for the simulation studies

Simulated flow ripple results using fluid bulk modulus of 11000 bar are shown in figures 5.24 to 5.27. Good agreement between predictions and test results is achieved in the operating range between 90bar, 20% displacement and 250bar, 100% displacement.

The simulated flow ripple results were compared with the compressible volume calculations presented in 5.3.3.2. Using equation 5.6 and correcting for a lower effective fluid bulk modulus of 11000bar, the theoretical volume of the compressibility flow losses were calculated. (V_{comp} theory)

The comparable simulation compressibility volumes were estimated from simulated flow ripple waveforms (V_{comp} sim). The comparison between the compressibility volumes estimated from theory (See 5.3.3) and simulation is given below:

Table 5.2

Delivery Pressure bar	Displacement %	V_{bdc} mm^3	V_{comp} (theory) mm^3	V_{comp} (sim) mm^3
250	100	13230	**301**	**326**
250	20	10900	**248**	**251**
90	100	13230	**108**	**134**
90	20	10900	**89**	**96**

Considering the likely inaccuracies in the estimation of the theoretical and simulated compressibility volumes, it can be concluded that the simulation and test flow ripple results give adequate agreement with compressible volume calculations.

5.3.5. Problems in the simulation of Cavitation and Air Release

The good agreement between the measured pump internal flow ripple and that generated by simulation has been based on the assumption of an artificially low value for the fluid bulk modulus: a value of 11000bar has been used instead of the manufacturer's stated value for the fluid of 17052bar.

The correction in bulk modulus is necessary to account for the effects of air release from fluid within the pump. During the simulation work an attempt was made to use a more sophisticated model to take into account the effects of delayed air-release and cavitation. The model used is based upon the work of Harris et al. [12].

The aim was to achieve agreement with the measured internal flow ripple without using a correction factor for the bulk modulus. Different air-release time constants were tried, from 0.1 to 40ms, but inconsistent results were obtained and the study was terminated.

Further work should involve a re-appraisal of the air-release model: under certain conditions the existing model gave unrealistic values for the amount of free air in the cylinder.

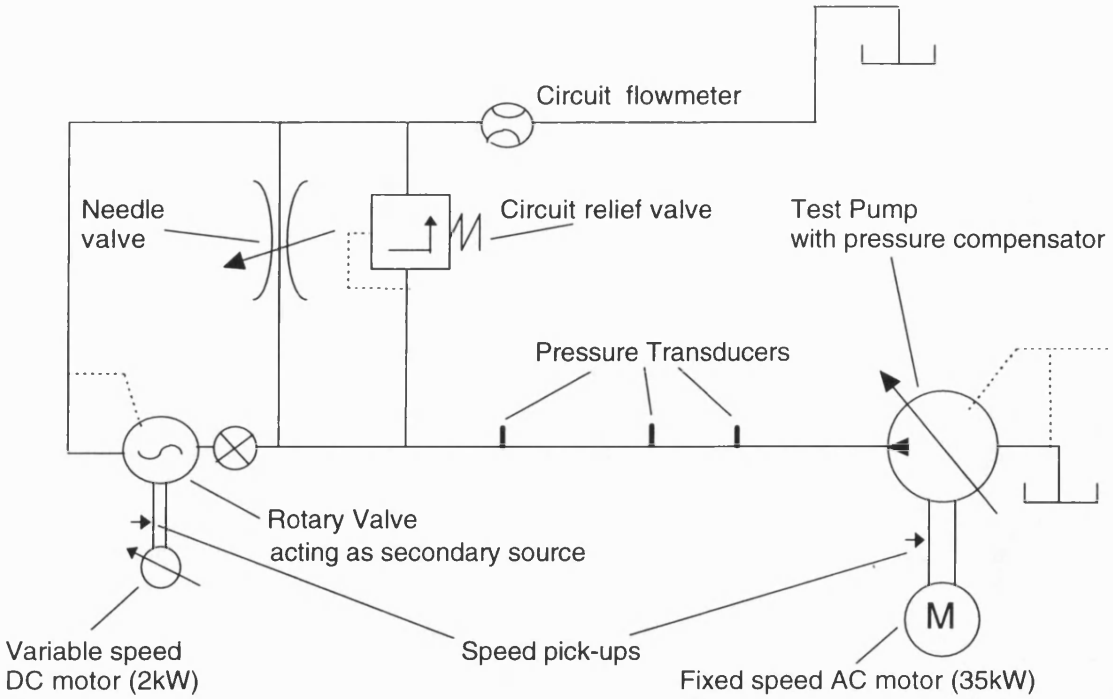

Figure 5.1
Hydraulic circuit used to measure the delivery flow ripple of the test pump fitted with the standard valve block

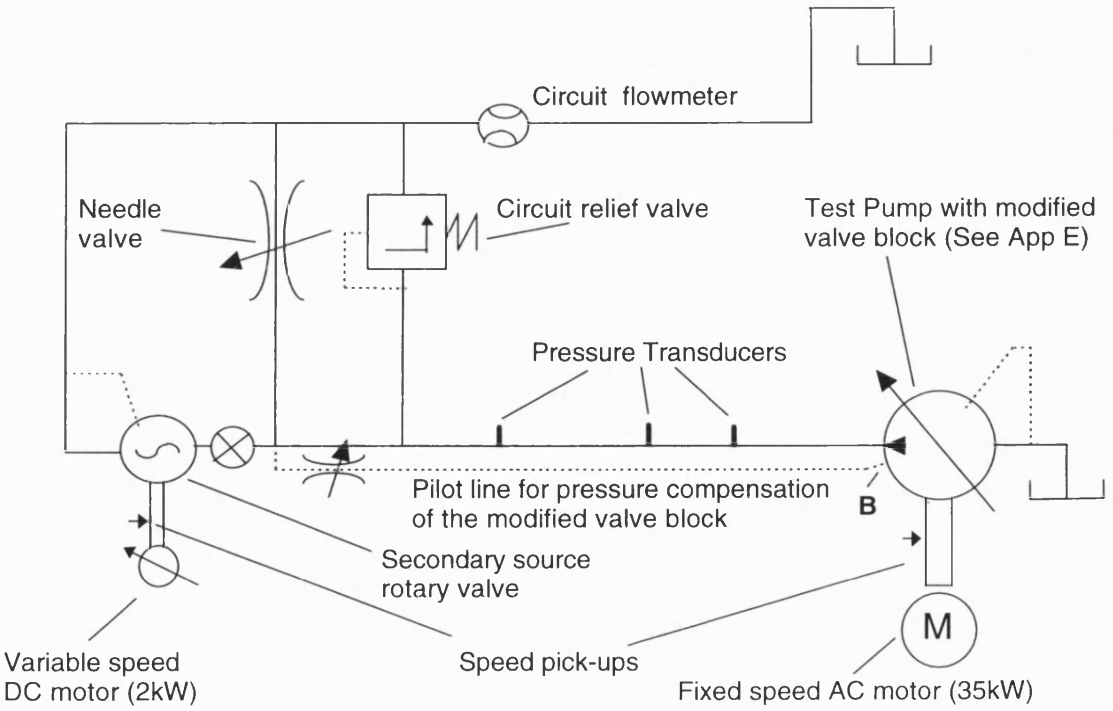

Figure 5.2
Hydraulic circuit used to measure the delivery flow ripple of the test pump fitted with the modified valve block

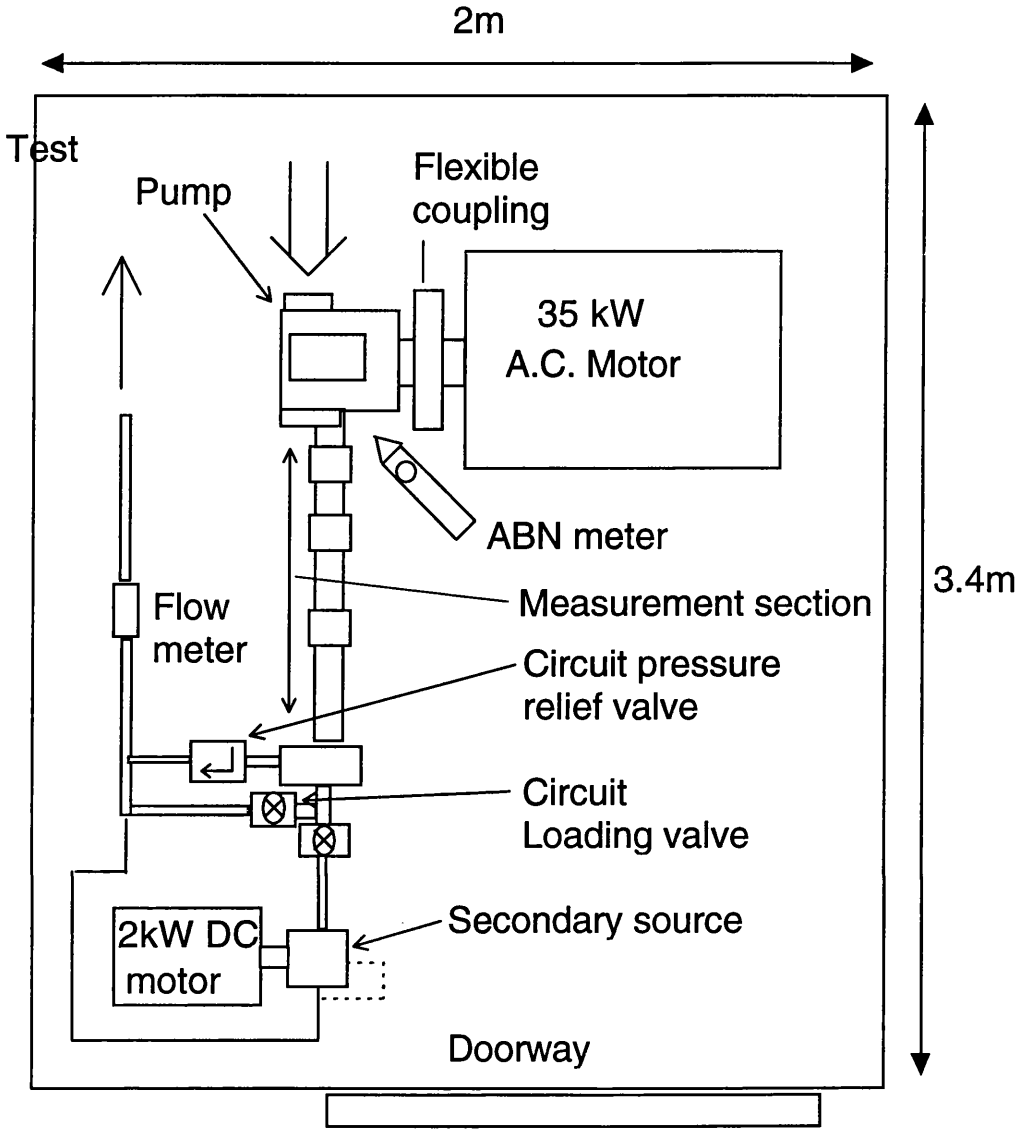

Figure 5.3
Plan view of the cell containing the pump test rig

a) Measured Impedance Spectra

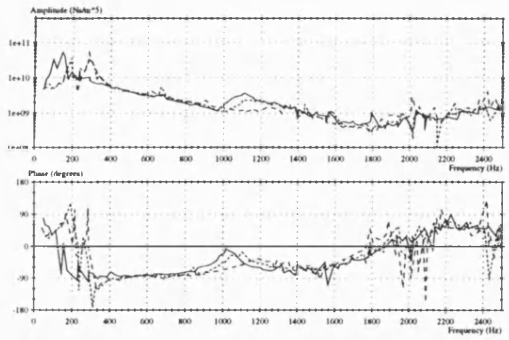

b) Smoothed Impedance Spectra

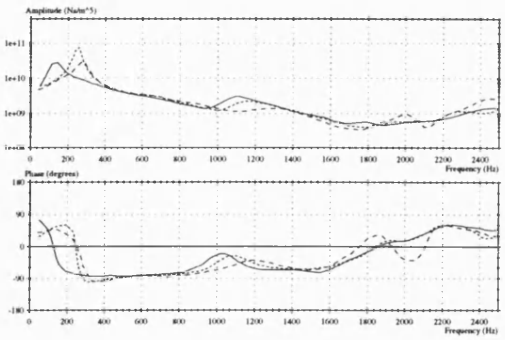

——————— 140 bar/ 5 bar; 100% displacement
..... 140 bar/ 5 bar; 67% displacement
– – – – – – – – – – – – 140 bar/ 5 bar; 33% displacement

Figure 5.4a - b
Source impedance measurements of the pump fitted with the standard valve block

a) Measured Impedance Spectra

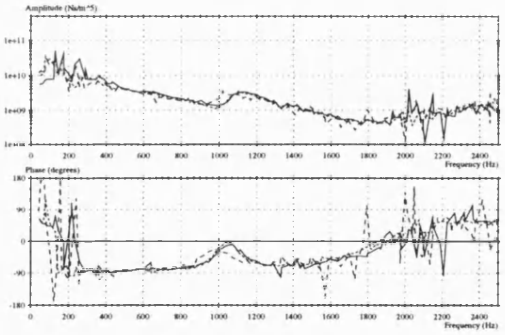

b) Smoothed Impedance Spectra

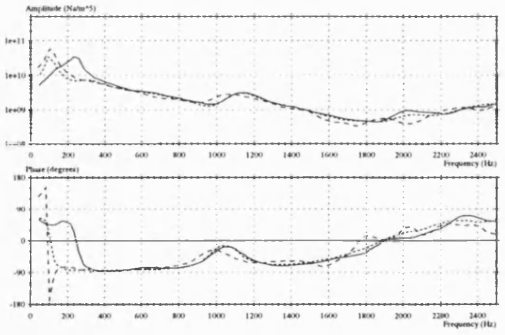

——————— 250 bar/ 5 bar; 100% displacement
..... 180 bar/ 5 bar; 100% displacement
– – – – – – – – – – – – 90 bar/ 5 bar; 100% displacement

Figure 5.5a - b
Source impedance measurements of the pump fitted with the standard valve block

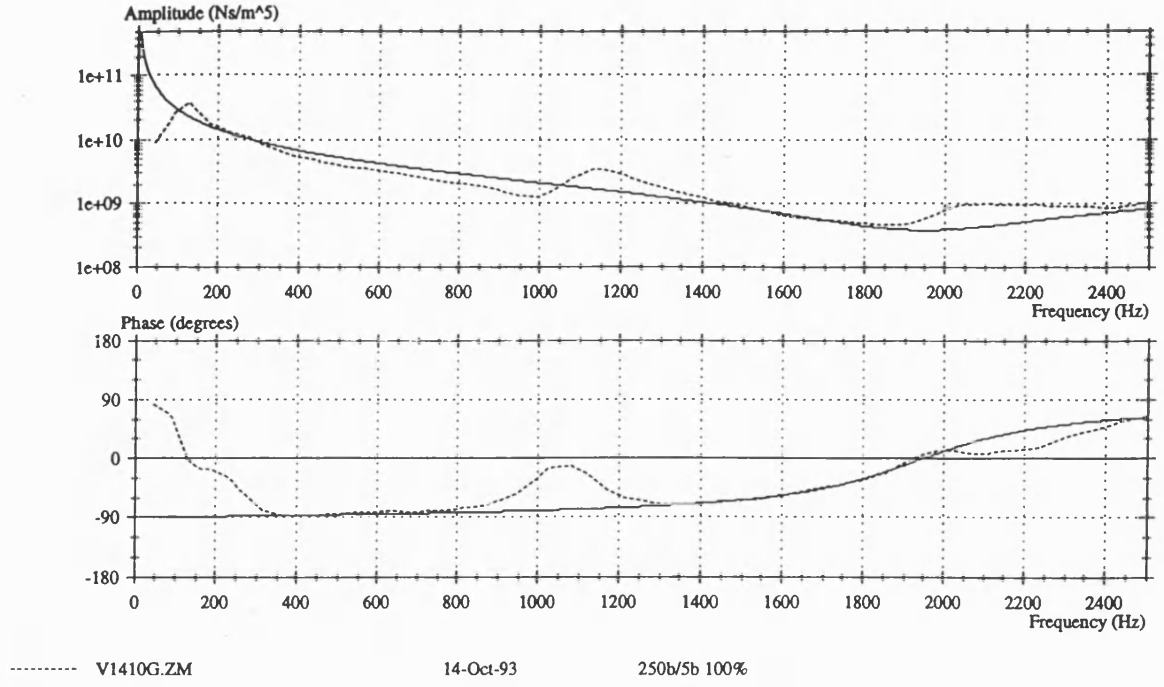

Figure 5.6
Measured source impedance of the test pump (with the standard valve block) superimposed in solid with a Helmholtz impedance model

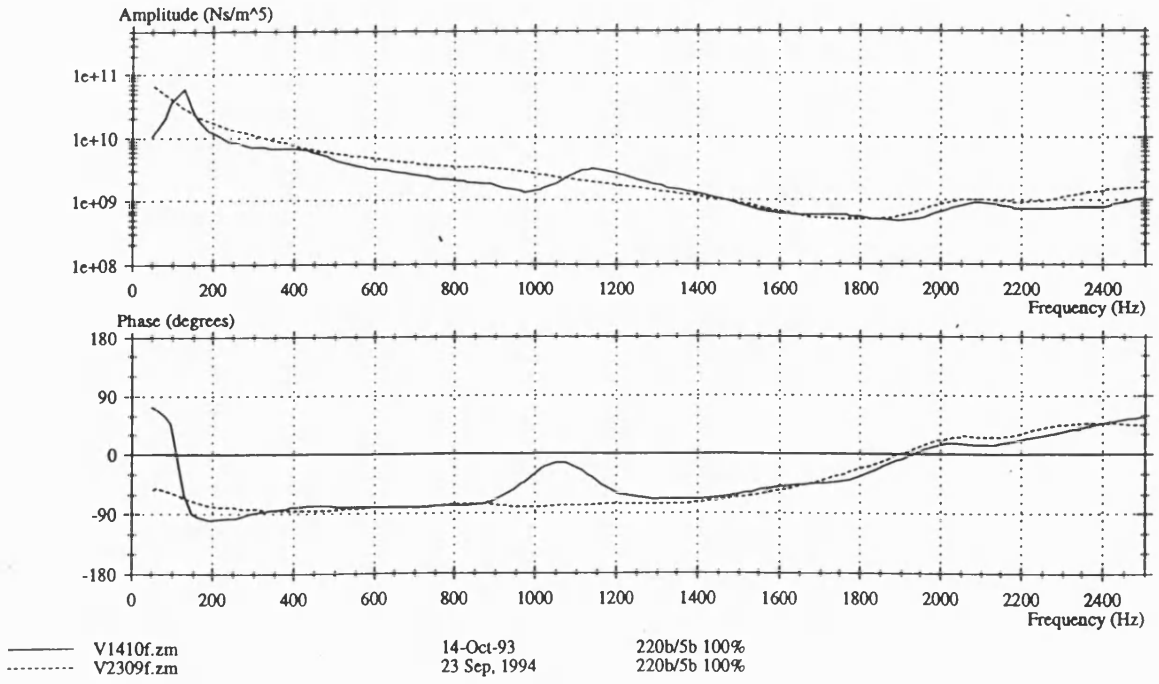

Figure 5.7
Measured source impedance of the test pump with the standard valve block (Solid) and with the modified valve block (dashed)

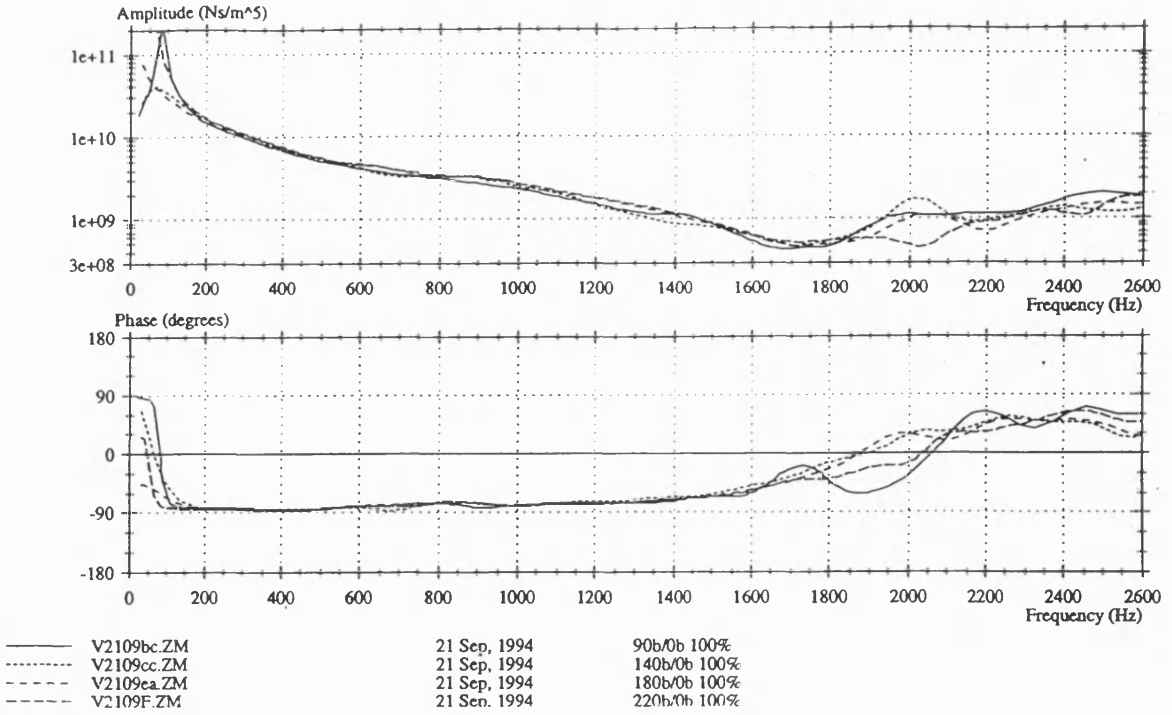

Figure 5.8
Measured source impedance of the test pump at 100% displacement
and fitted with the modified valve block

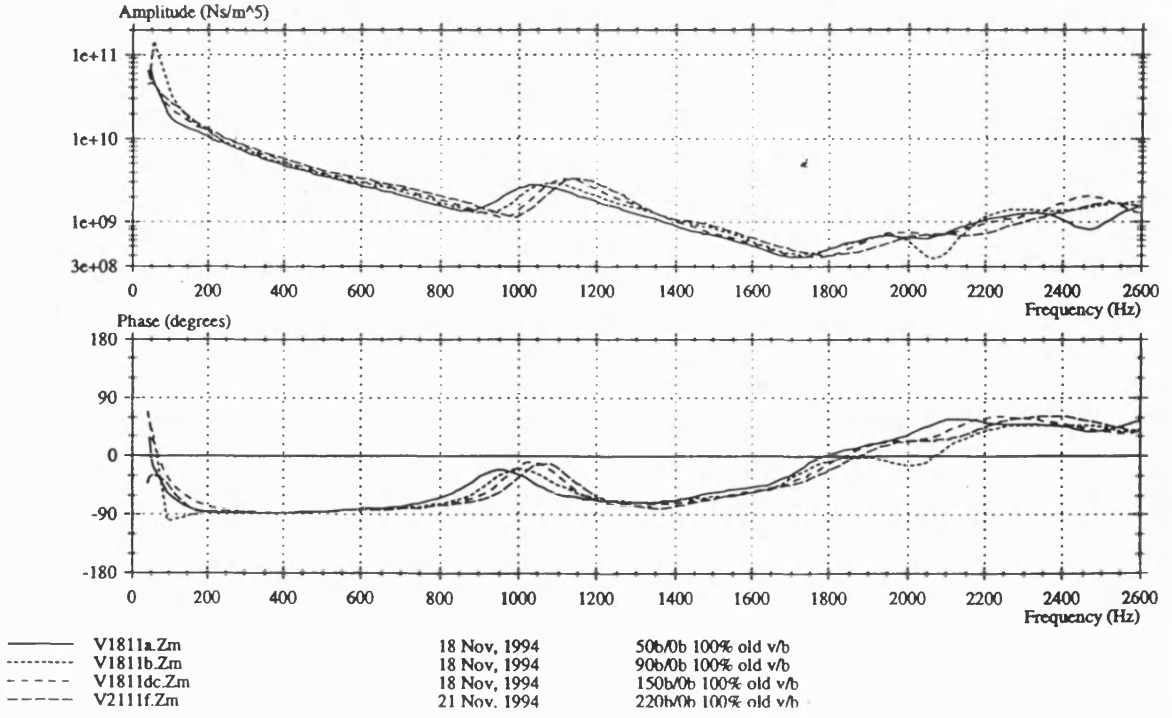

Figure 5.9
Measured source impedance of the test pump at 100% displacement
and fitted with the standard valve block

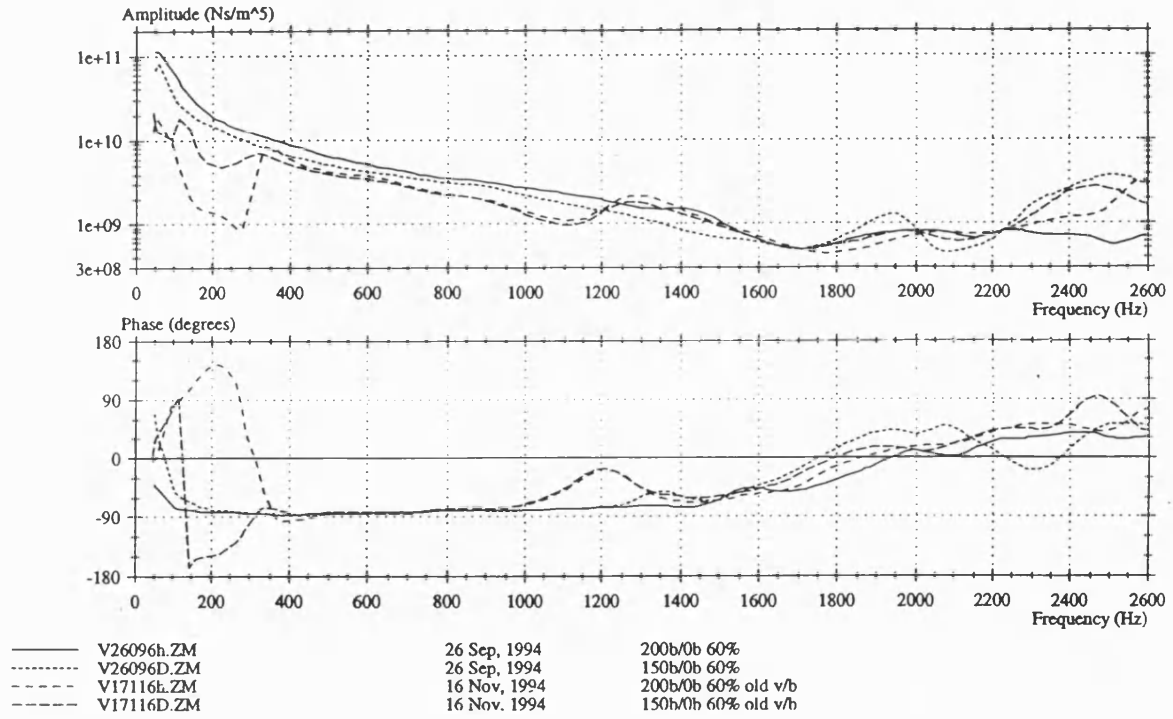

Figure 5.10
Comparison of source impedance measurements for the test pump at 60% displacement with the old and the new valve blocks

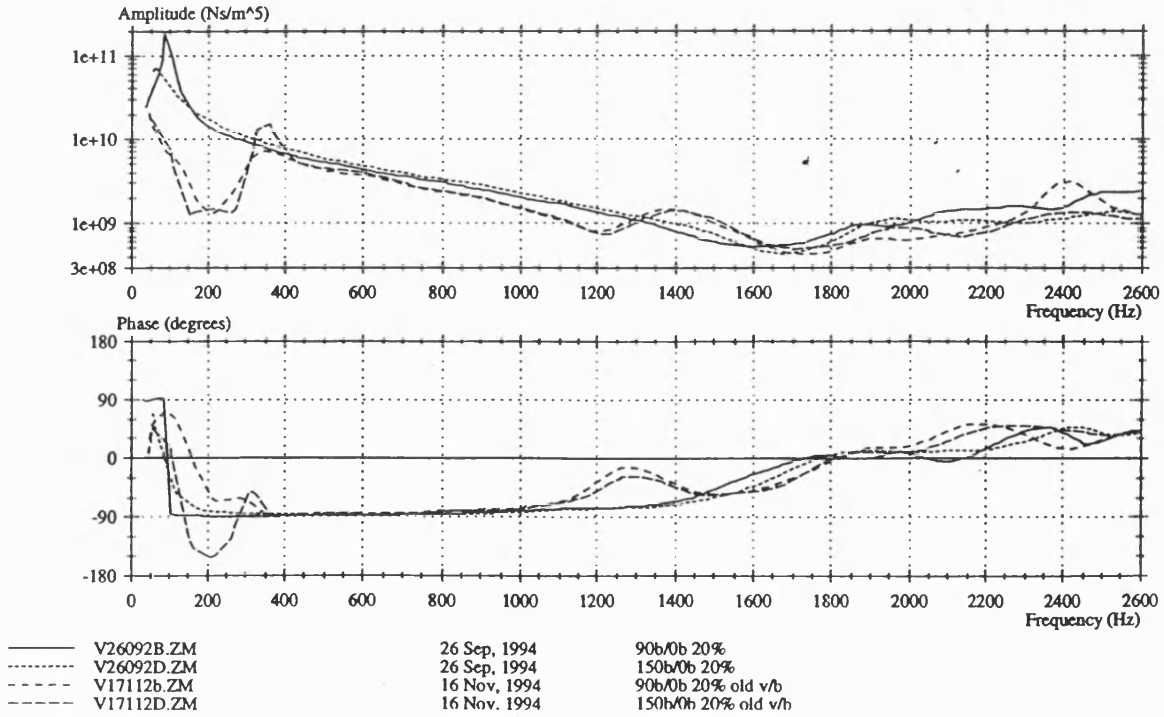

Figure 5.11
Comparison of source impedance measurements for the test pump at 20% displacement with the old and the new valve blocks

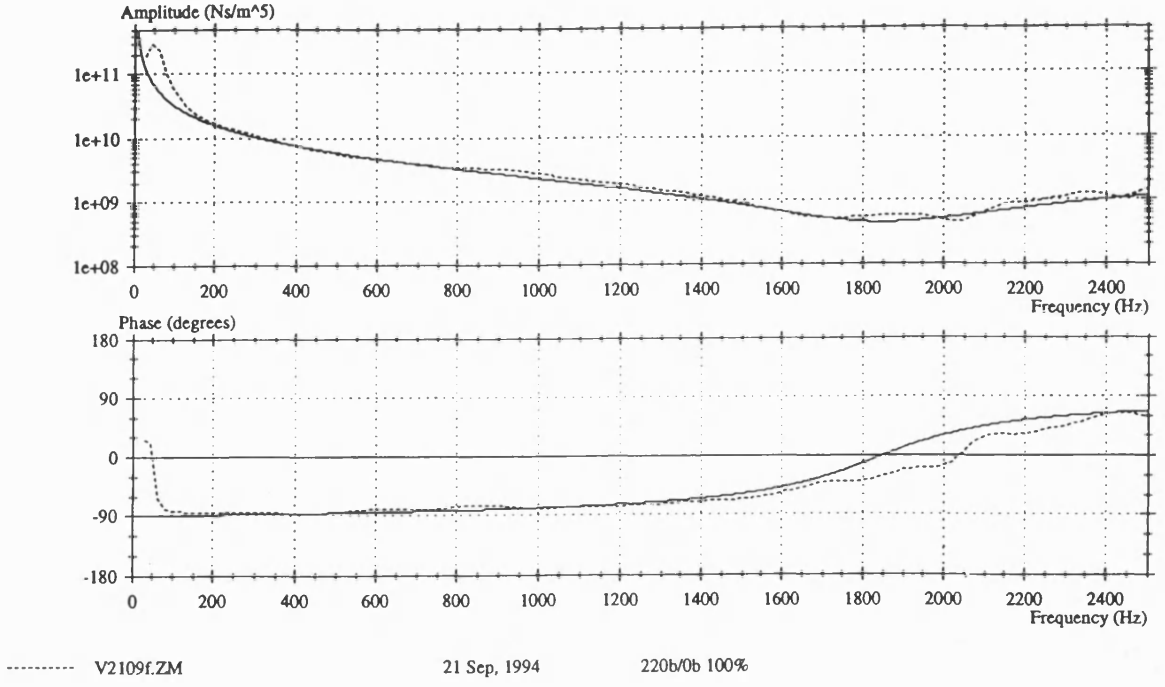

Figure 5.12
Measured source impedance of the test pump (with the modified valve block) superimposed in solid with a Helmholtz impedance model

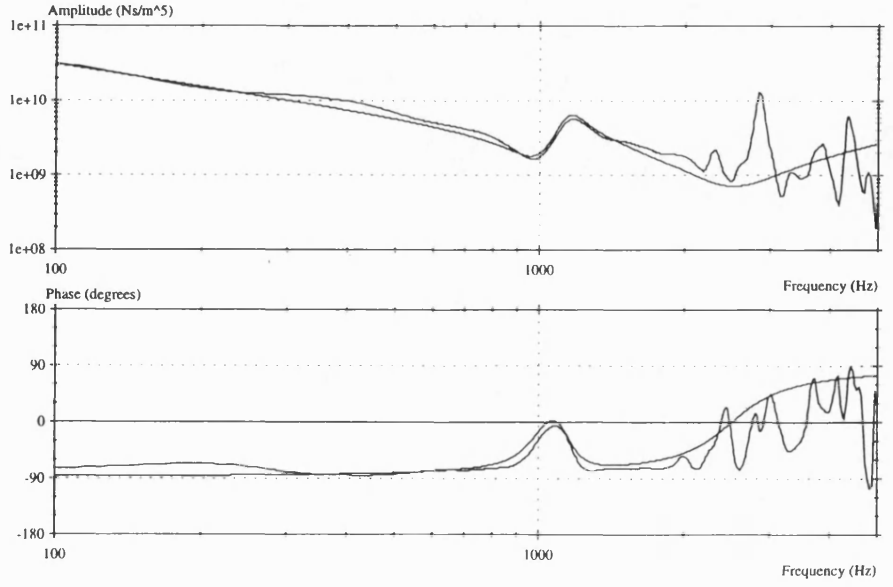

Figure 5.13
Measured source impedance of the test pump (with the standard valve block) superimposed in solid with a Parallel Helmholtz impedance model

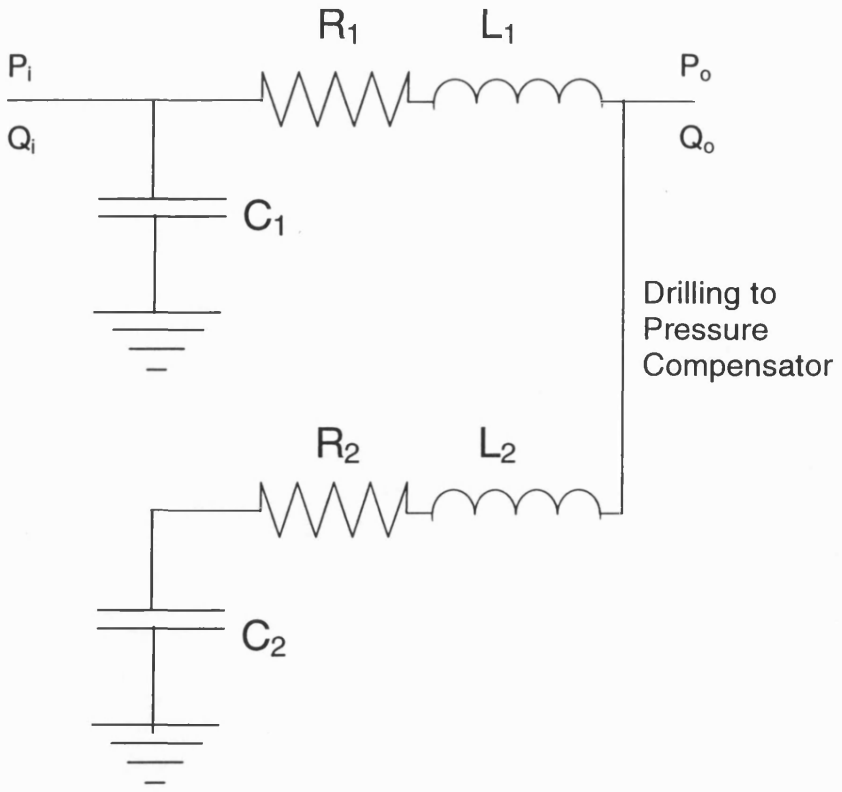

Figure 5.14
The impedance network for the Parallel Helmholtz model

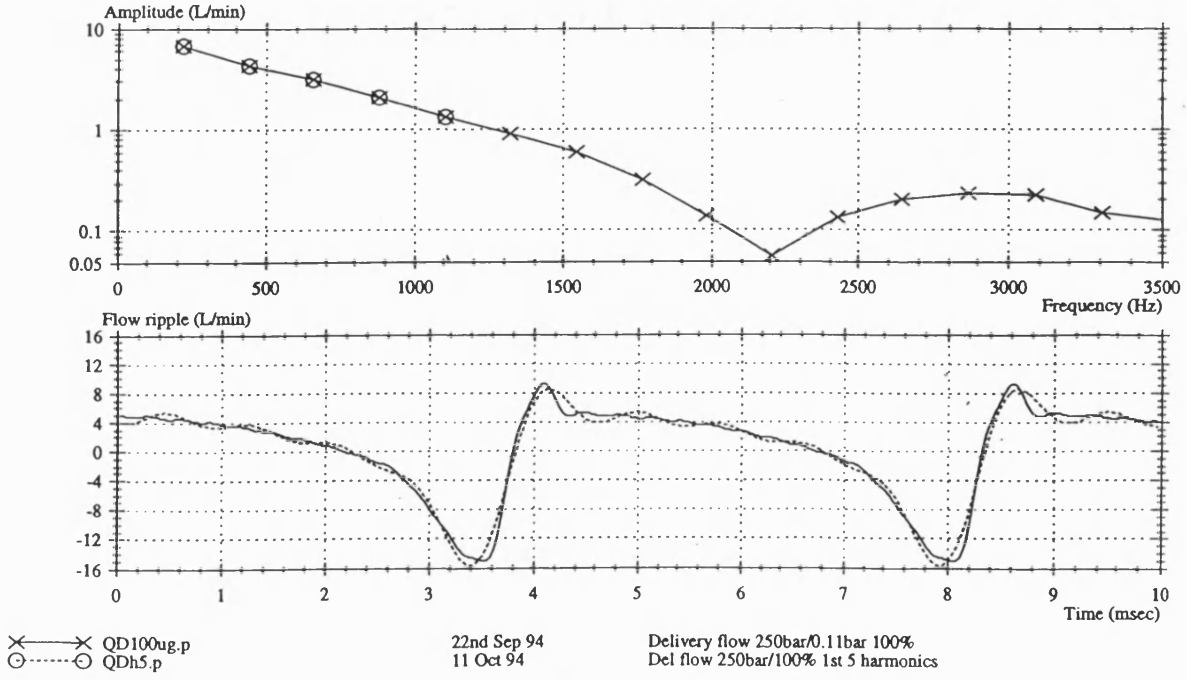

Figure 5.15
Internal flow ripple from the test pump constructed from the first 5 measured harmonics (dashed) and the first 16 harmonics (solid)

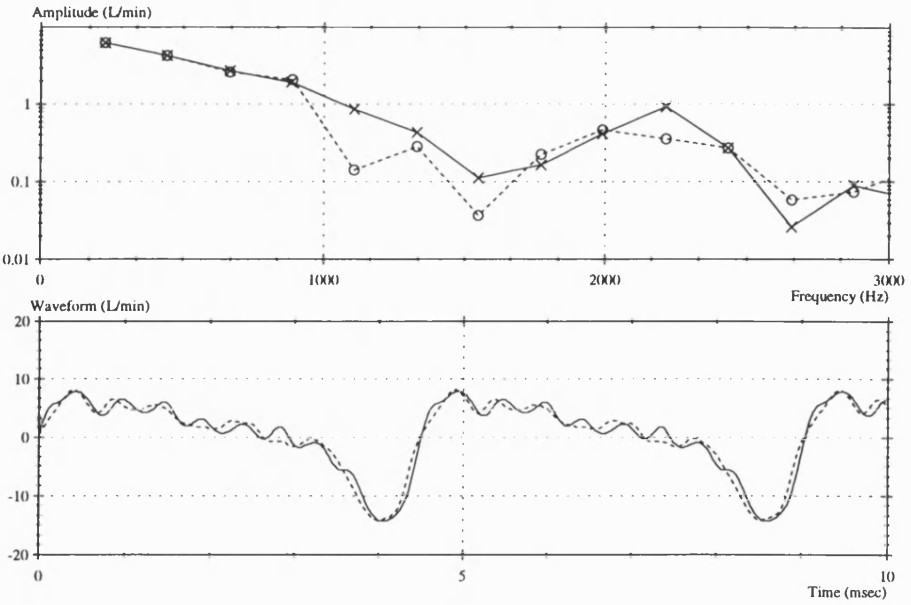

Figure 5.16
Measured Internal flow ripple from the test pump fitted with the standard valve block (dashed) and the modified valve block (solid)

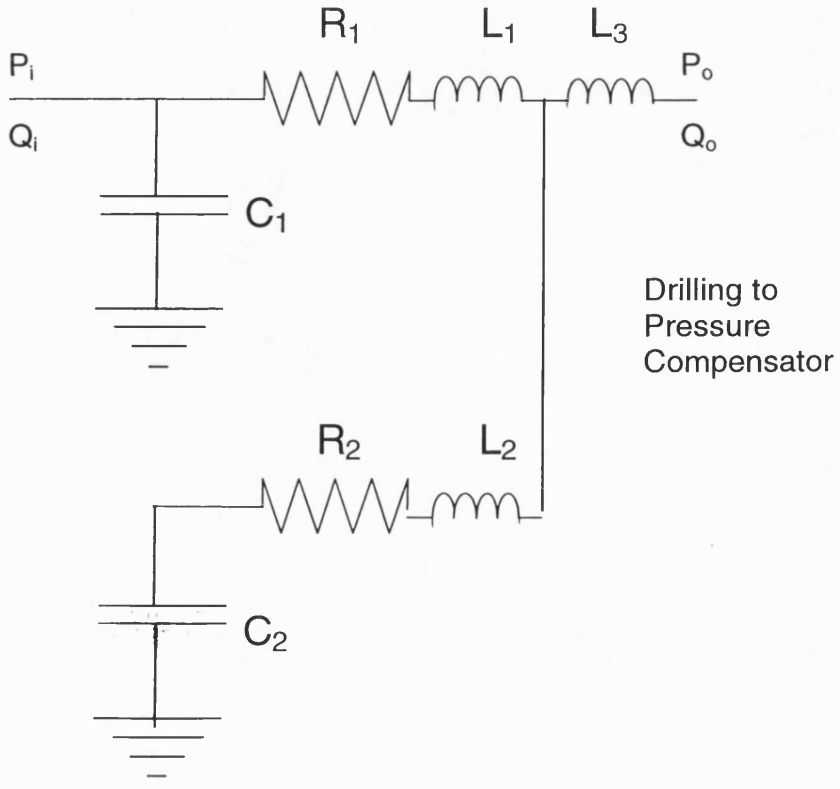

Figure 5.17
The impedance network for an alternative Parallel Helmholtz model

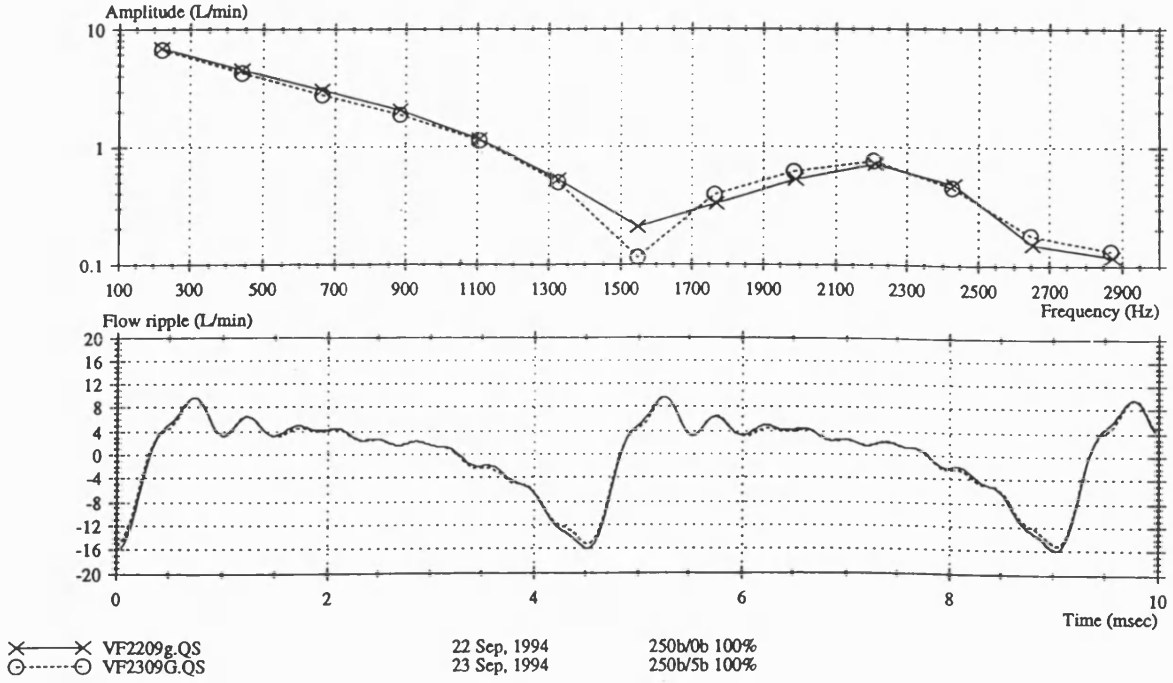

Figure 5.18
Measured Internal flow ripple from the test pump with 0 bar and
5 bar boost pressure

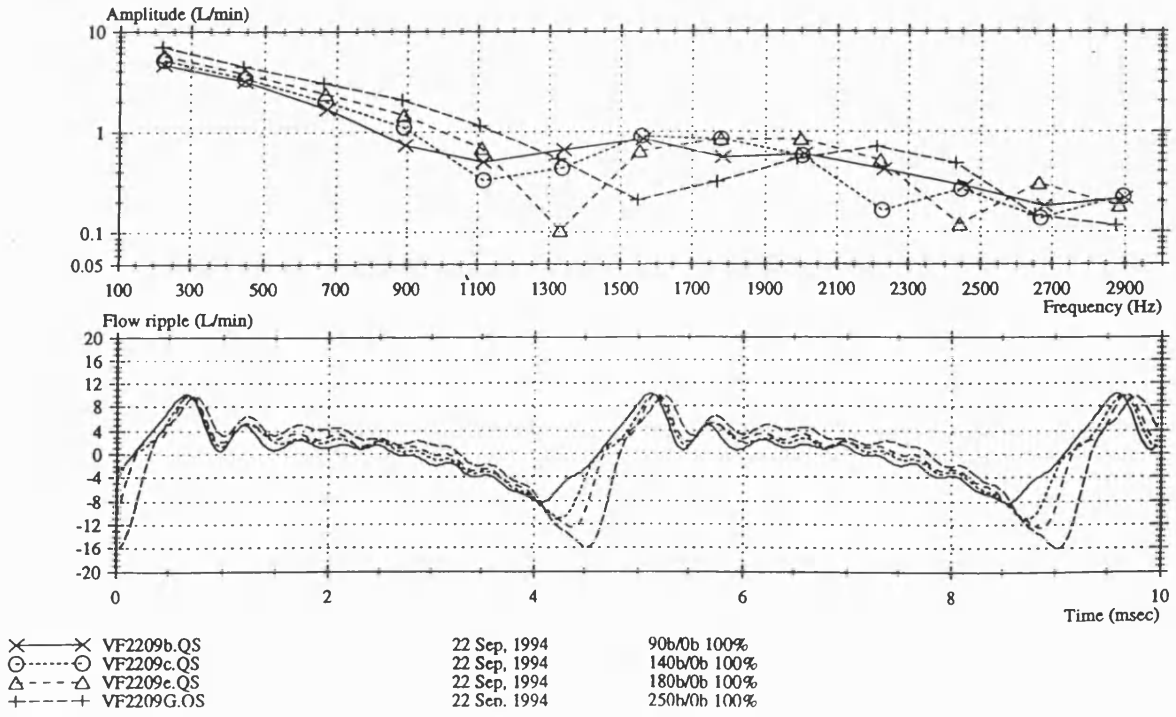

Figure 5.19
Measured Internal flow ripple from the unboosted test pump at
100% displacement and various delivery pressures

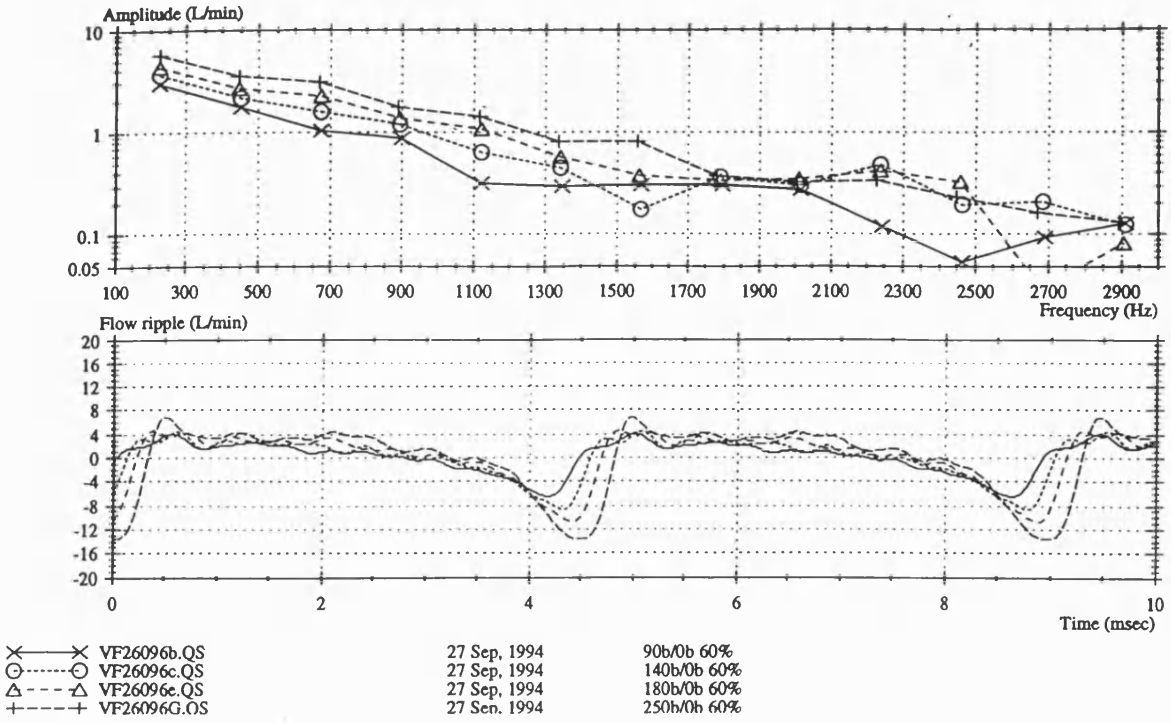

Figure 5.20
Measured Internal flow ripple from the unboosted test pump at
60% displacement and various delivery pressures

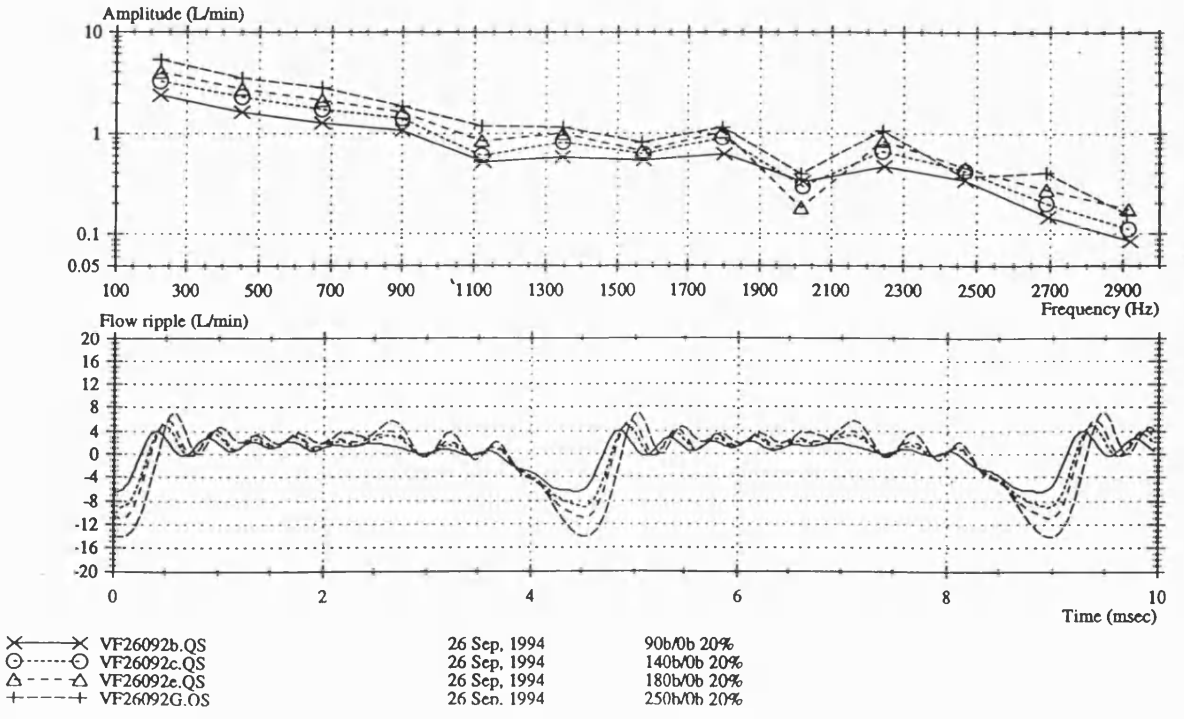

Figure 5.21
Measured Internal flow ripple from the unboosted test pump at
20% displacement and various delivery pressures

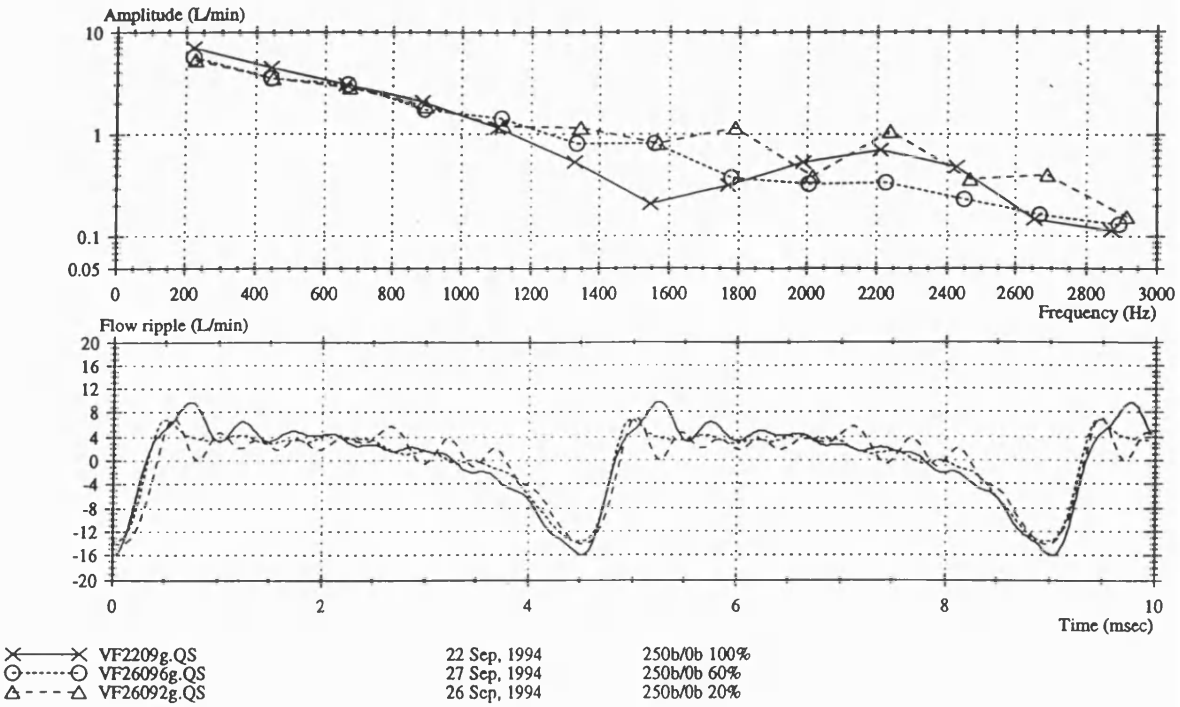

Figure 5.22
Measured Internal flow ripple from the unboosted test pump at 250 bar delivery pressure and various displacements

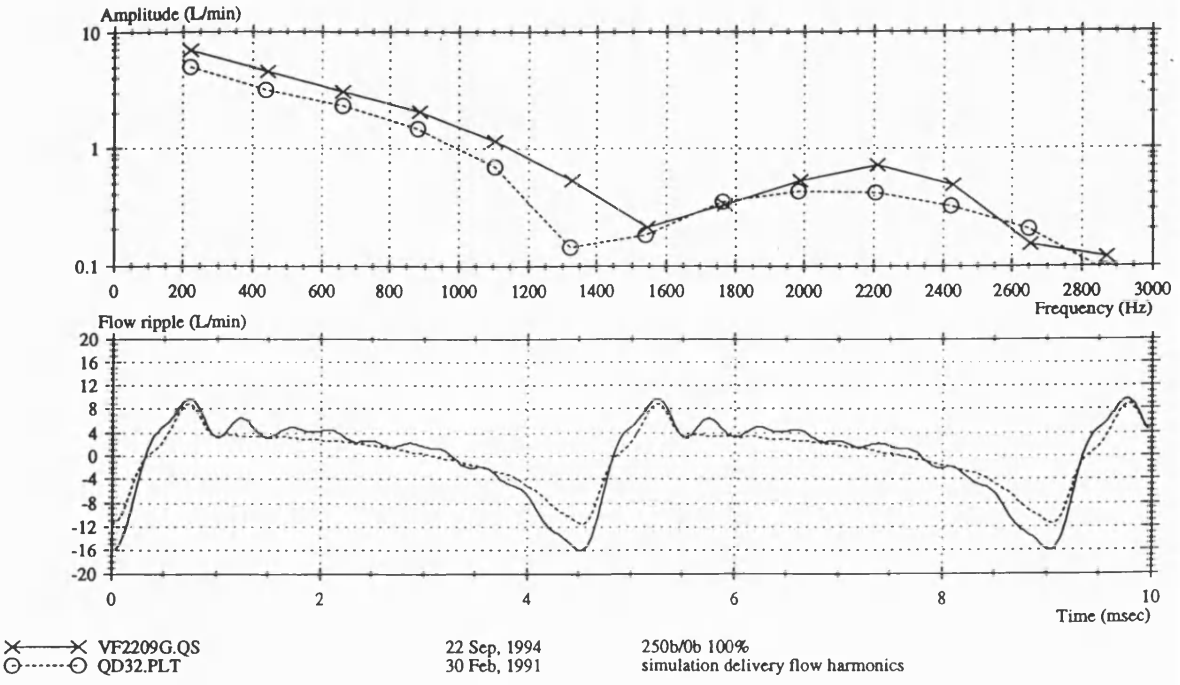

Figure 5.23
Measured and simulated Internal flow ripple for the unboosted test pump at 250 bar delivery pressure and 100% displacements using a simulated fluid bulk modulus of 17052 bar

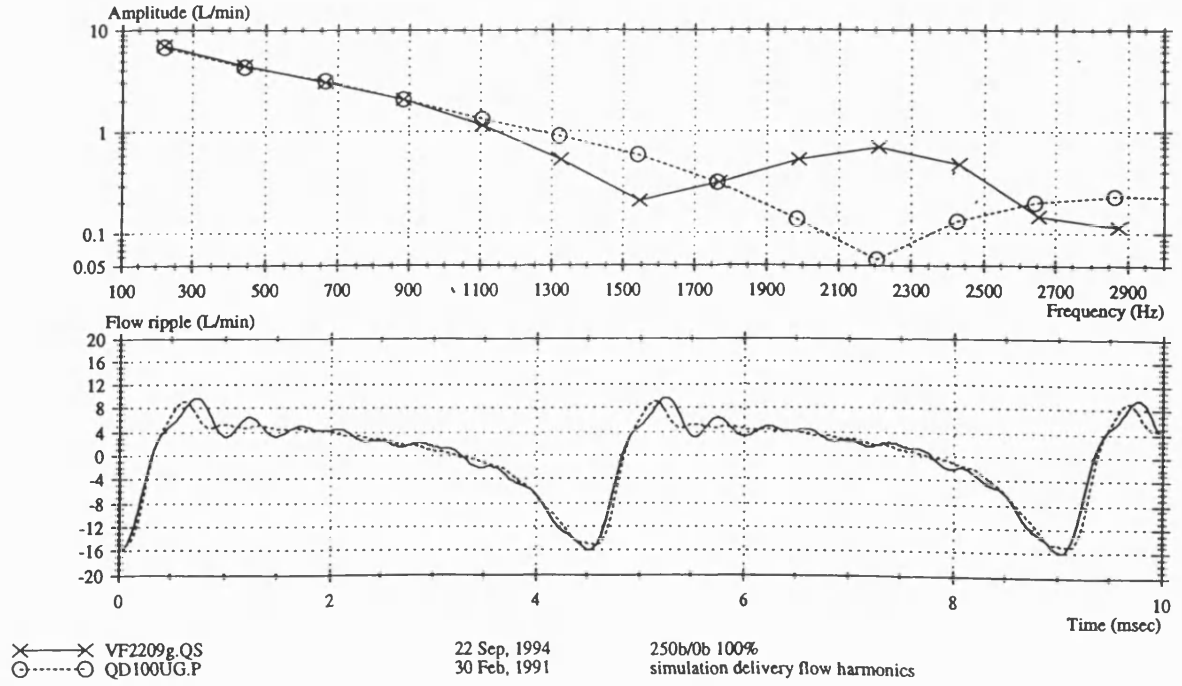

Figure 5.24
Measured and simulated Internal flow ripple for the unboosted test pump at 250 bar delivery pressure and 100% displacements using a simulated fluid bulk modulus of 11000 bar

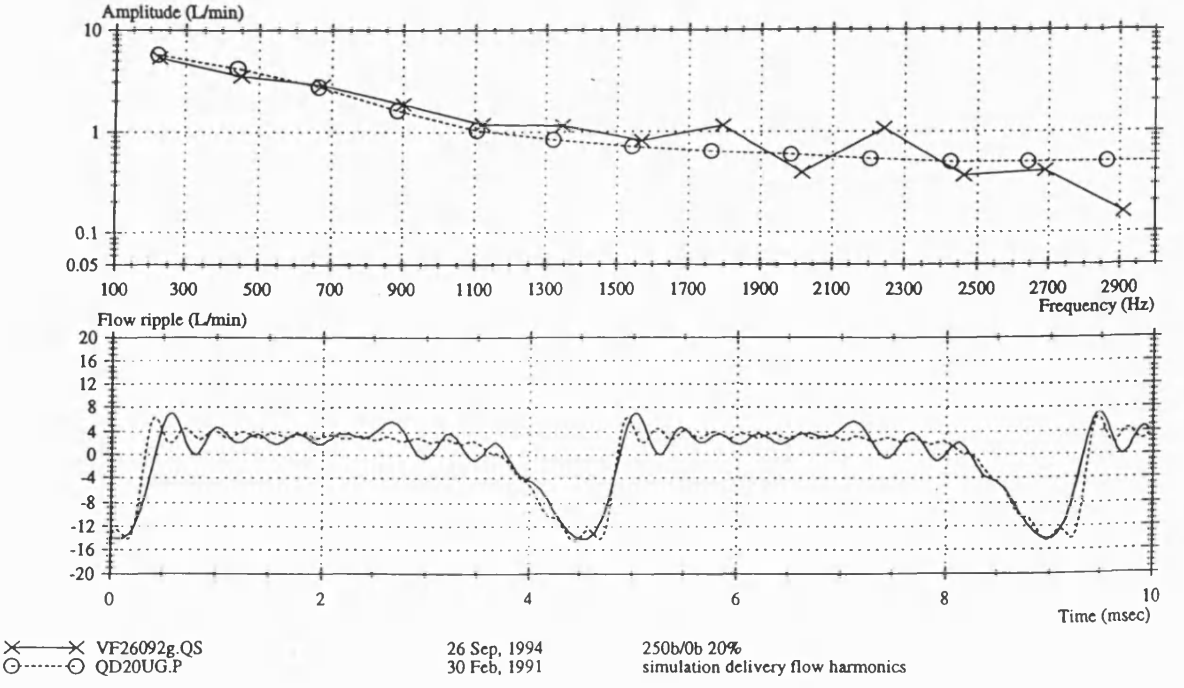

Figure 5.25
Measured and simulated Internal flow ripple for the unboosted test pump at 250 bar delivery pressure and 20% displacements using a simulated fluid bulk modulus of 11000 bar

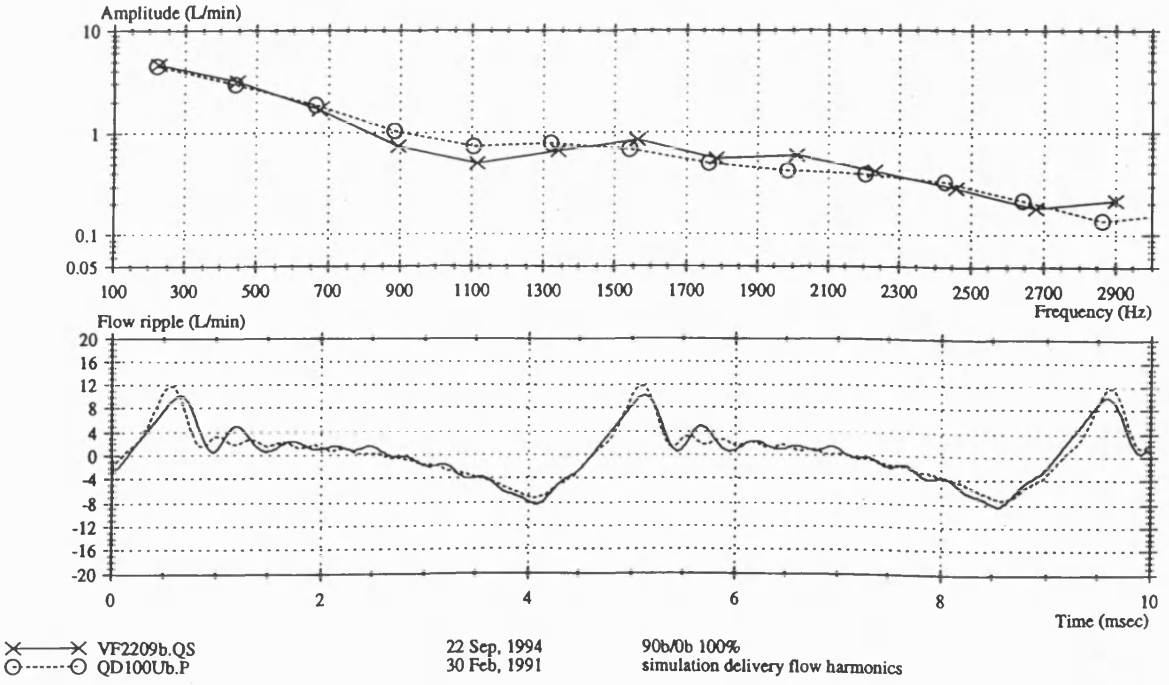

Figure 5.26
Measured and simulated Internal flow ripple for the unboosted test pump at 90 bar delivery pressure and 100% displacements using a simulated fluid bulk modulus of 11000 bar

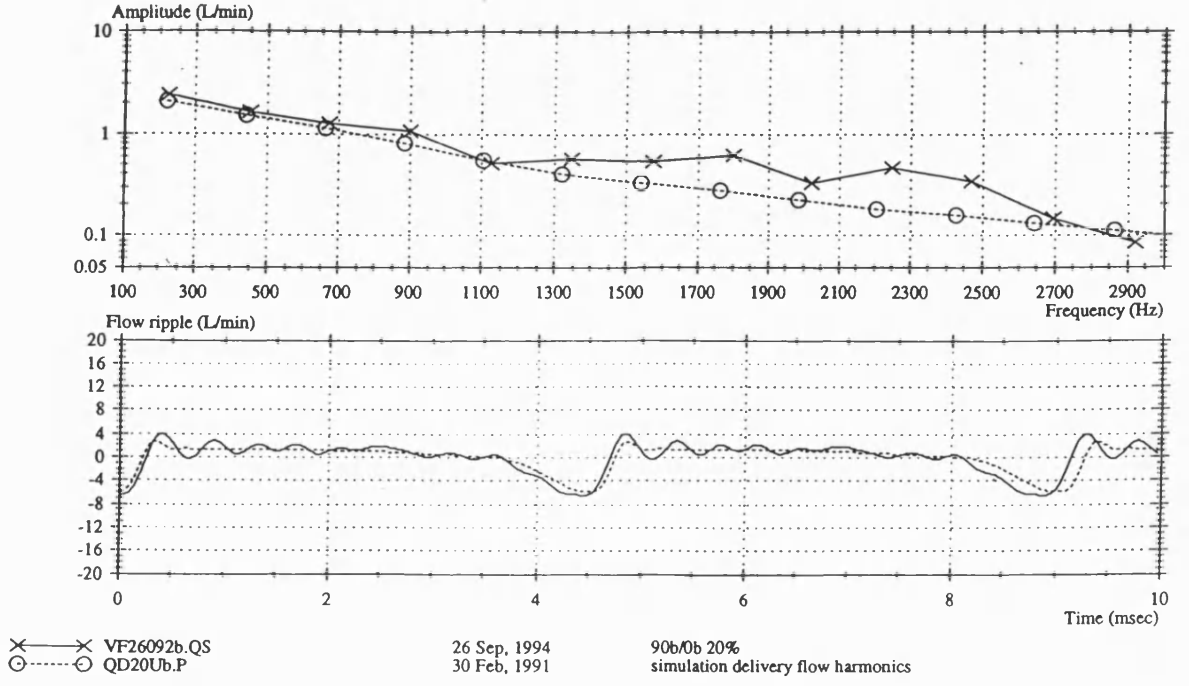

Figure 5.27
Measured and simulated Internal flow ripple for the unboosted test pump at 90 bar delivery pressure and 20% displacements using a simulated fluid bulk modulus of 11000 bar

6.0 Methods to Reduce Pump Flow Ripple

6.1 Introduction

This chapter introduces the different methods used to reduce pump source flow ripple for the purpose of reducing system FBN. These methods are divided into two categories; those applicable to all pumps, and those only applicable to axial-piston pumps. The methods applicable to all pumps include the use of hydraulic silencers and anti-noise systems. The methods only applicable to axial-piston pumps include the use of an even number of cylinders, solid pistons, and various means of achieving variable delivery and suction timing.

The concepts for a number of novel methods are discussed. Two of these concepts were investigated in detail during the project and are discussed in chapters 7, 8 and 9.

6.1.1 The Importance of Pump Source Flow Ripple

The pressure ripple caused by a pump within a hydraulic circuit can be reduced by adjusting three system parameters:

a) Circuit Entry Impedance

b) Pump Source Impedance

c) Pump Source Flow Ripple

The merits of adjusting each of these parameters were discussed in 2.4.3. The study produced two main conclusions:

a) The reduction in system pressure ripple from alteration of the circuit and pump impedances is frequency dependent and sensitive to changes in the pump speed.

b) Reduction of pump source flow ripple causes a proportional decrease in system pressure ripple. The decrease in system pressure ripple is independent of the connected load circuit.

Accordingly, the reduction of pump source flow ripple is the most promising method of reducing the system pressure ripple.

6.1.2 The Distinction between Active and Passive Devices

Over the last 30 years, numerous devices have been developed to reduce pump flow ripple. All of the devices can be classed either as "Active" or "Passive". Active mechanisms can be defined as those which need an additional power supply, whereas passive devices can be defined as those which utilise the existing pump input power.

A typical active device would be that of an "anti-noise" device. Such a device would apply a source of flow ripple which when combined with the pump flow ripple produces destructive interference giving a cancelling or neutralising effect. Conceivably, an anti-noise device could produce large reductions in the flow ripple from any positive displacement pump. Anti-noise devices have drawbacks though; the device used to generate the cancellation flow

has to perform over a large bandwidth, and is likely to incur losses that reduce the overall efficiency. Also, an anti-noise device has to respond to changes in pump speed, pressure and displacement and so is likely to be of a complex design. Because of these disadvantages, passive means of reducing pump flow ripple are much more common.

Examples of passive devices include hydraulic silencers and pressure relief grooves. A hydraulic silencer acts on the system pressure ripple, and pressure relief grooves act on the individual cylinder flows that make up the pump flow ripple.

Passive devices are usually less complex and so cheaper than active devices. However, the performance of a passive device is dependent upon the pump operating condition. This means that passive devices are normally optimised for a particular operating condition.

At the moment, all of the quietest commercially-available pumps use passive devices that do not respond to changes in the pump operating condition. Consequently, pumps tend to generate higher levels of FBN when operating away from the condition optimised for by the passive mechanism.

Axial piston pumps produce a delivery flow ripple which is highly dependent upon the pump operating condition. Therefore future reductions in flow ripple from axial piston pumps are more likely to be achieved using either active or passive devices that can respond to changes in the pump operating condition.

6.1.3 Requirements of a Device to Reduce Pump Flow Ripple

The requirement is for a device which reduces pump source flow ripple to achieve a significant overall reduction in system airborne noise.

The required features of the pump flow ripple reduction device are direct consequences of the project aims presented in 1.3. The device must additionally form part of a commercially viable solution, which is cheap, low maintenance, and robust for industrial and mobile applications.

From the delivery flow ripple results for the test pump shown in chapter 5, it is clear that the device should primarily act on the compressibility flow ripple. In the specific case of the test pump, the form and magnitude of the compressibility flow ripple is largely independent of pump displacement. For the prototype mechanism then, it may only be necessary for it to respond to changes in delivery pressure and pump shaft speed.

With an active anti-noise mechanism it may be possible to simply "fill in" the compressibility reverse flow. A mechanical method of achieving this is difficult though, due to the very short duration of each compressibility reverse flow. For the nine-cylinder test pump running at 1500rev/min the individual cylinder reverse flows reach a peak value of 20L/min and are generated every 4.44ms, each one taking place over a duration of 1.5ms. Another problem is that the size and shape of the reverse flow varies with the pump operating condition. The device would need the ability to respond precisely to transient changes in the

delivery pressure, displacement and speed. Otherwise the device itself may create a significant amount of unwanted fluid-borne noise.

With a passive device the aim would be to "spread out" the compressibility reverse flow with the aim of reducing the flow ripple harmonics in the 1 to 5 kHz region. In this way, the method would have a similar effect to a pressure relief groove. However, unlike a pressure relief groove, the device would need the ability to respond to changes in the pump speed, pressure and displacement.

Since the overall mechanical efficiency of the pump and device is important, an active device would only be viable if it has only a marginal effect upon the pump efficiency.

6.2 Methods for all Positive Displacement Pumps

6.2.1 Hydraulic Silencers

Hydraulic silencers are used to attenuate the pressure ripple transmitted by a pump to its connected load system. A wide range of silencers is available and when used correctly can be highly effective in reducing the pressure ripple within a circuit [6].

6.2.1.1 Dissipative Silencers

Silencers are passive devices and they fall into two main groups, dissipative and reactive. Dissipative silencers absorb the energy from pressure ripple as heat using a resilient lining, generally attached internally to the wall of the silencer [48]. This type can be effective in low pressure gaseous systems, but suitable materials with the required acoustical and mechanical properties have yet to be developed for high pressure hydraulic systems: The energy dissipation action is not efficient and the lining materials tend to lose their resilience and lead to system contamination. For these reasons, reactive silencers are more common.

6.2.1.2 Reactive Silencers

Reactive or reflective silencers rely on discontinuities in the shape of the noise path to reflect pressure waves back to the source. The simplest type of reactive silencer is the expansion chamber (fig. 6.1a). These are usually sized slightly shorter than one-half wavelength of the fundamental pumping frequency for a particular pump speed [5]. This silencer attenuates FBN over wide bandwidth, although at frequencies with wavelengths that are integer multiples of the chamber length then the attenuation is minimal. This is significant as the silencer will become ineffective at certain conditions if the pump speed is variable. To provide more broadband attenuation a pipe resonator is used, which is simply a silencer containing a set of expansion chambers connected with mode cancellation pipes (fig 6.1b) [46].

A Helmholtz resonator can be created by adding a volume into a side branch (fig 6.1c). The fluid in the volume and its connecting line causes a resonant subsystem that can attenuate pressure waves at frequencies near to the resonant frequency. Accumulators are often used for this purpose (fig. 6.1d), where a gas volume is enclosed in a rubber bag

surrounded by the working fluid. In this case the gas volume acts to reduce the stiffness of the resonator and so decreases the unit's resonant frequency without increasing its size.

Reactive silencers have a number of drawbacks. Their performance is highly system dependent and in some cases can cause an increase in the FBN transmitted from the pump. Also, reactive silencers are usually large in order to attenuate low frequencies, and heavy because high strength is needed to withstand high mean pressures. As a result, reactive silencers tend to be expensive and are normally only suitable for situations in which the FBN level is critical.

6.2.1.3 A Speed Sensing Silencer

The attenuation (or Transmission Loss) from a Helmholtz resonator is shown in figure 6.2. Clearly the attenuation is only narrow band, centered about the resonant frequency, f_r. This frequency depends on the resonator dimensions, and is chosen to correspond to a particular pumping harmonic. The maximum attenuation of the pump pressure ripple will then occur at this frequency. When the pump speed changes the pumping harmonic moves from the resonant frequency and the attenuation from the resonator is reduced. However, the attenuation would be maintained if the resonant frequency also moved to the new frequency of the pumping harmonic. Henderson [4] presented expressions for the dependence of the bandwidth and resonant frequency upon the resonator dimensions:

$$f_r \propto \sqrt{\frac{A_o}{L_o V}} \tag{6.1}$$

$$B_r \propto \sqrt{\frac{A_o V}{L_o}} \tag{6.2}$$

The resonant frequency could be reduced by restricting the flow area into the resonator volume (A_o). However, this would also reduce the bandwidth and so at lower frequencies the flow area would need to be controlled carefully to ensure that the resonant frequency is close enough to the pumping harmonic to provide significant attenuation. At higher frequencies, the bandwidth also increases and so the control of the flow area is not so critical. The increase in bandwidth with frequency is fortunate as at higher pump speeds, the pressure ripple at a particular pumping harmonic is likely to be larger.

The flow area into the resonator volume could be varied with a valve which is actuated according to the pump speed. The actuation could be electro-mechanical or hydro-mechanical and so may be quite inexpensive to manufacture. No researchers appear to have explored this possibility.

6.2.2 Anti-Noise Devices

These active devices create a second source of noise which, when combined with the original noise source, causes destructive interference or cancellation. This principle has previously been used to reduce noise within gaseous systems. Chaplin [49] used the technique to quieten the exhaust noise emitted by a diesel engine. A microphone monitored

the ABN from the exhaust and fed a proportional signal to a microprocessor which synchronised the signal with engine rotation, and controlled a waveform generator to produce an inverse signal. A loudspeaker converted this inverse signal into a pressure fluctuation which was directed at the exhaust outlet. The anti-noise combined with the exhaust noise resulting in a 20dB reduction in the airborne noise level in the frequency range of 50 to 150Hz.

A major difficulty in applying this principle to the FBN in a hydraulic system is that much more power is needed to create an effective level of flow ripple cancellation. A particular problem is posed by the need to create an inverse pressure variation about a mean level which may vary between zero and 300 bar.

In a hydraulic system, pressure variations are caused directly by volume changes within the fluid. Accordingly, if flow is removed at the point where a pressure peak exists and added at a pressure trough then a considerable reduction in the pressure variation can be achieved. The following sections show the various methods that have been investigated to carry out this high-frequency insertion and extraction of fluid.

6.2.2.1 FBN Cancellation using flow from a Servo Valve.

In 1977, Rebel [50] attempted to carry out FBN cancellation by introducing a high frequency flow fluctuation using a fast-response servo valve. He used two different anti-noise circuit configurations as shown in figures 6.3 and 6.4. The first configuration (fig. 6.3) used the servo valve to bleed off flow from the delivery flow of a pump exhibiting flow variations above the mean pump flow. An alternative scheme (fig. 6.4), used a second pump to provide additional flow to cancel flow variations below the mean pump flow. Initially, open loop control permitted single sinusoidal control of the valve to cancel individual flow ripple harmonics. However, closed loop control was much more effective in that the measured pump pressure ripple signal was used to cancel numerous harmonics of the pump flow ripple.

Rebel carried out cancellation tests on a radial 3 piston pump, operating at a maximum speed of 2000rpm, and achieved a measure of success. He found that the servo valve could cause a 9dB reduction in the pump FBN with open loop control, operating at the pump fundamental frequency. Under closed loop control, a larger reduction of 17dB was achieved with the servo valve producing a cancellation effect upon a number of the lower pump flow ripple harmonics.

However, Rebel concluded that the system was not commercially viable: the cancellation of higher frequency components was limited above 50Hz by the frequency response of the servo valve. Also, bleeding off and adding fluid reduced the overall system efficiency with the cost of an additional hydraulic pump for the "added" flow. Furthermore, the cost of the servo valve would probably be comparable to that of the pump it was quietening.

6.2.2.2 FBN Cancellation using the motion of a Servo Actuator.

In 1990, Kojima and Shinada started a project with the aim of developing a sophisticated anti-noise attenuator for pressure pulsations in generalised piping systems [51].

A scheme showing the main elements of the attenuator system is shown in figure 6.5. In this case, the changing velocity of a servo actuator within a side-branch is used to attenuate flow variations within a duct from a pulsation source.

The servo actuator is controlled using a Digital Signal Processor (DSP) to cancel the forward component of the pressure wave from the pulsation source. The DSP calculates the necessary actuator velocity in real time by analysing the signals from two high bandwidth pressure transducers placed in the duct a distance ahead of the actuator. Technical difficulties arose in the real time measurement of the pressure wave [51], and in the real time control of the servo actuator [52]. The stability of the controller was particularly important. During some tests the actuator became unstable and caused wave addition rather than wave cancellation: in these situations the wave addition caused the system to "Howl".

Kojima et al. have achieved a degree of success. By 1993 a system was developed that could attenuate the sinusoidal pressure variations from a magnetic vibrator by as much as 25dB in the frequency range between 20 and 250Hz [52]. More recently [53], a system was described that can produce wide-band cancellation of 20dB at frequencies up to 800Hz.

It is conceivable that with further development, a system could be produced that would provide attenuation into the 1 to 5 kHz region that could greatly attenuate the flow ripple and airborne noise from positive displacement pumps. However, the cost of the servo actuator, the pressure transducers and the DSP will prevent such a system from gaining widespread commercial use in the near future. It is more likely that this type of system will be designed for one-off applications such as pipelines and chemical plant where the cost of such a system could be accommodated.

6.2.2.3 FBN Cancellation using High Speed Actuation Technology.

Both of the anti-noise systems described by Rebel [50] and Kojima [51] rely on a servo valve to provide the high frequency oscillation necessary for controllable flow ripple cancellation. However, the use of a servo valve implies high cost and only limited performance in the 1 to 5 kHz frequency range. For this reason a study has been carried out to find new, high bandwidth actuation technologies that might be used in a device to replace the servo valve. Three technologies were investigated:

a) piezoelectric actuators;
b) electro-rheological fluids;
c) magnetostrictive actuators.

Before attempting to design an actuation mechanism using these technologies, an initial survey of their basic characteristics was carried out.

6.2.2.3.1 Characteristics of piezoelectric actuators

A piezoelectric actuator is an electromechanical device that undergoes a dimensional change when an electrical voltage is applied [54]. Piezoelectric devices can be operated over millions of cycles without wear or deterioration and the speed of response is very high, limited only by the inertia of the load and the output capability of the electronic driver.

All piezoelectric actuators are made from PZT (Lead Zirconate Titanate). Commercially available actuators vary both in the exact composition of the PZT and also in their mechanical construction. Many commercial devices have the actuator in a levered arrangement to amplify the available output movement [55]. Table 6.2 compares two commercially available actuators to show the range of available performance:

Table 6.1

Actuator type	High voltage levered	Low voltage linear
Drive voltage	1600 v d.c.	100v d.c.
Max. extension	0.7mm	0.09mm
Max. pushing force	80N	3000N
Resonant frequency	380Hz	5500Hz
Stiffness	0.13N/μm	33N/μm
Cost of controller(1993)	$2800	$3430
Cost of actuator(1993)	$1970	$3520
Total cost	$4770	$6950

This table shows that the levered and the linear actuators are suitable for two different applications. The levered actuator achieves a relatively large extension at the expense of a relatively small pushing force and bandwidth. The linear actuator can achieve a much higher pushing force and bandwidth but only over a much shorter extension. However, in both cases the costs of the controller and actuator are prohibitively expensive. Furthermore, in both cases, a relatively high voltage must be controlled over the desired frequency range. The high cost of such a controller is unlikely to fall dramatically in the foreseeable future.

6.2.2.3.2 Characteristics of electro-rheological fluids

Electro-rheological (ER) fluids are normally free-flowing liquids, but if they are exposed to large electric fields then flow resistance increases, roughly in proportion to the strength of the field applied; eventually they become virtually solid [56]. This change is reversible. It is not strictly an actuation mechanism, but rather a dissipative medium. It has been considered here with a mind to using the viscosity properties of ER fluids in some novel FBN-reducing mechanism.

With modern ER fluids, a field strength of 1000V/mm is needed to solidify the fluid [57]. The current is extremely small (about 5mA) and so the power requirement is small (25W at 20% efficiency). Also, the fluids are highly temperature dependent, the required drive current doubling every 6 to 12 degrees C. A fluid will have a typical response time of 0.7ms to a step change in electric field strength.

The total system cost is high to include the cost of a high-voltage controller. Furthermore, unlike piezoelectric actuators, there are no "off the shelf" devices and so, once again, the unit cost will be too high for consideration in a commercial device.

One interesting development is that fluids are now being formulated that respond to a magnetic field instead of an electric field [58]. These "Electro-Rheological Magnetic" (ERM) fluids operate only on a battery voltage of around 10V and generate much higher fluid shear stresses than a conventional ER fluid: for an ER fluid an electric field strength of 1000V/mm would give a fluid shear stress of around 5kPa, whereas a 10V voltage across an ERM fluid could give a fluid shear stress of 250kPa. Again, ERM fluids are likely to be too costly to consider for this project, but this example does show how this new technology is advancing and points possibly to its widespread application in the field of active vibration control in the not too distant future.

6.2.2.3.3 Characteristics of magnetostrictive actuators

Magnetostrictive alloys are materials which change dimensions in a changing magnetic field [59]. Recently a new material, Terfenol-D, has been developed which greatly outperforms all previous alloys; In a magnetic field of 2000 Oersteds, Terfenol-D can achieve strains of 0.3%. Furthermore, the frequency response of actuators made from Terfenol-D (in the form of long, solid rods) can be very fast at up to 5kHz.

Once again, there is a cost penalty, with commercially available actuators costing more than $2500. There is also a high power requirement to produce the rapidly fluctuating magnetic field.

Another major drawback with Terfenol-D at present is that it is still under development and so samples from different production batches can have widely different properties. Other more reliable magnetostrictive alloys are available, but only with achievable strains in the region of 0.002% which is far too small for practical purposes.

6.2.2.3.4 Appraisal of high speed actuation methods

The high cost of all three technologies immediately limits their application as elements of a prospective flow ripple suppression mechanism. In highly critical military applications their high cost could be justified, but in a commercial environment they would not be viable.

6.2.2.4 FBN Cancellation using a Multi-lobed Cam.

In 1987, Lipscombe developed a specially designed FBN cancellation mechanism for an external gear pump [7]. The mechanism differs from those of Rebel and Kojima in that it is purely mechanical and involves no costly servovalve or complex electronic controller. Instead, it consists of a multi-lobed cam mounted on the pump drive shaft which drives a radial piston assembly in such a way that the flow fluctuations created are very nearly equal and opposite to those produced by the pump (See figure 6.6).

Figure 6.7 shows that the multi-lobed cam can be highly effective; almost eliminating the first four harmonics of the pump pressure ripple. Also, since it is fitted to the pump driveshaft, then it is speed sensing, and a similar mechanism could potentially be added to reduce flow ripple in the suction line.

It was suggested that a similar device could be applied to an axial piston pump. However, the complex piston-pump flow-ripple waveform presents difficulties in achieving a satisfactory cam-following action for the radial pistons. Also, unlike gear pumps, the flow-ripple from piston-pumps is highly dependent on mean delivery pressure and so the cam mechanism would need an additional pressure compensation feature.

For the particular case of a well-timed axial piston pump, such as the test pump (See Appendix C), a multi-lobed cam could probably be made to work effectively: the delayed delivery timing and the good design of the relief groove cause a "rounded" delivery flow ripple waveform which is predominately the same shape over the whole operating range (See 5.3.4). This "rounded" flow ripple waveform would allow an easier cam following profile that a set of spring-loaded radial pistons could follow. Also, the pressure compensation action could be provided with a conical cam profile, actuated by a simple servo system.

The detail design of the cam profile in 3 dimensions would present difficulties, as would the exact design of the cam pressure compensation assembly. Also the 3 dimensional cam may be difficult to machine. However, the eventual design would be straightforward to assemble and could potentially provide large reductions in the pump flow ripple.

6.2.2.5 FBN Cancellation using a Rotary Valve

As stated in section 6.2.2, pressure ripple is caused by volume changes within the fluid. To reduce pressure ripple, flow should be removed at points where pressure peaks exist and added at positions of pressure troughs. One device that could carry out the necessary high frequency flow addition and removal is a rotary valve (See figure 6.8).

The clearance between the rotor and sleeve is very small and the width of the rotor slots is equal to the distance between the high and low pressure ports. During a single rotor revolution, the flow path between the sleeve ports opens to produce 4 very sharp flow pulses. These flow pulses could be used to produce the necessary flow addition or removal from the delivery chamber. Rotary valves of this type can be used in FBN testing. The sharp flow pulses have a wide bandwidth and this is often used as the second source of pressure ripple for Secondary Source testing [10].

For pumps operating at conditions where there are significant cylinder inflows at the start of delivery, flow pulses from the rotary valve would replace the lost flow from the delivery chamber and so reduce the delivery pressure ripple (See 6.2.2). Like the multi-lobed cam (6.2.2.4), the rotary valve would be powered by the pump drive-shaft. However, unlike the multi-lobed cam, a gearbox of some kind would be needed to account for the difference between the pulses per revolution from the rotary valve and the cylinder inflows per revolution from the pump.

A second source of pressure, higher than the delivery pressure, would be needed upstream of the rotary valve. The rotary valve would then cause flow pulses into the delivery chamber by momentarily opening and closing the flow path between this second pressure source and the delivery chamber.

The mean flow through the rotary valve would be small compared to the main pump flow and so the second pressure source could be provided by the flow from a small gear pump. This ancillary pump would produce a very small flow ripple compared to the main pump and would also be driven by the main pump driveshaft. In this way the ancillary pump would provide proportionately more flow to the rotary valve as the speed of the main pump increases.

The flow from the ancillary pump is continuous and the flow from the rotary valve is intermittent. Therefore a device, such as an accumulator, is needed to store the flow energy from the ancilliary pump for when the rotary valve is closed. Also, the ancillary pump could be supplied either from return, or from the delivery of the main pump. Diagrams for schemes using both options are shown in figures 6.9a and b.

The pressure drop across the rotary valve would be used to control the size of the flow pulses. This pressure drop would be controlled according to the main pump pressures and mean flow. This could be achieved with a servo mechanism that varies the opening of a restrictor in parallel to the ancillary pump.

All of the elements of this design could be contained within a small manifold that would bolt on to a specially adapted pump. The most expensive element of the design would be the gearbox needed to match the pumping frequency with the pulse rate from the rotary valve. However, if the rotary valve was designed to produce the same number of pulses per revolution as the number of pump cylinders, then the gearbox would not be needed and the rotary valve could be driven directly from the pump driveshaft. In this case the design would be fairly cheap to mass produce and fairly easy to adapt to existing pump designs.

This is potentially an effective solution. However, the viability of this scheme depends upon the detail design of the rotary valve. The rotary valve would be designed to meet two main requirements:

a) Minimise the pressure difference across the valve to generate the necessary flow pulses. If it is too large then the overall pump efficiency will drop to an unacceptable level.

b) Match the flow pulses to the size and shape of the main pump delivery flow ripple for a range of operating conditions.

6.3 Methods Specifically for Axial Piston Pumps

6.3.1 The Use of an Even Number of Pistons

Foster and Hannan [26] argued that even-pistoned pumps could be less noisy than odd-pistoned pumps. They reasoned that the reduced variation in axial piston force on the swashplate (See 3.3.2) would cause lower levels of structureborne noise from the pump casing. In support of this, various studies have been carried out [14, 60] to demonstrate that the structural and airborne noise from the pump case would be reduced when using an even number of pistons. However, all of these studies assumed the variation in the axial piston

force on the swashplate to be the main forcing function governing the generation of SBN from the pump casing.

Contrary to this, Petterson [61] found that the variation of the axial piston force had little effect on the overall pump noise. Moreover, Skaistis [5] has proposed that a much more influential phenomena is the variation in the swashplate yoke moment, caused by the force from the pressurised cylinders (See 3.3.3).

To investigate the noise-generating potential of odd and even-pistoned pumps, a simulation study was carried out with the "Dual Cylinder" Bathfp model described in chapter 4. As a basis for the comparison, delivery flow ripple was used to estimate the FBN generating potential, and Yoke moment variation was used to estimate the SBN generating potential.

In the simulation study, the nine cylinder test pump was compared with an equivalent 10 cylinder pump. To give a fair comparison, the same stroke and piston p.c.d. were used, whilst the piston diameter was scaled to give the same pump displacement. One of the model assumptions is that of neutral delivery timing at TDC (See 4.3.4). To keep with this assumption the delivery ports of the two pumps end at slightly different angles. The two alternative pump schemes are shown more fully in figures 6.10 a) and b).

The start of the portplate delivery port was the same for both pumps. The portplate had previously been optimised for the 9 cylinder pump, and so this tended to disadvantage the 10 cylinder unit. However, since the total cylinder dead volume and the piston stroke and p.c.d. were the same for both pumps, then the delivery timing of the 10 cylinder pump will be very similar to the 9 cylinder pump, and so this disadvantage was ignored.

The comparison was carried out for an unboosted pump operating at a single speed of 1500rpm. To investigate the effect of operating conditions upon the different pump schemes, three combinations of delivery pressure and mean flow were simulated. The three operating conditions correspond to a very advanced delivery timing (50 bar, 100% displacement), a very retarded delivery timing (250bar, 20% displacement), and the maximum power condition (250 bar , 100% displacement).

The delivery flow ripple of the 9 and 10 cylinder pumps for the three operating conditions is shown in figures 6.11a), b), and c). For all of the simulations, the effect of the kinematic flow ripple is small compared with that of the compressibility flow ripple. For all three operating conditions, the 10 cylinder flow ripple is similar and smaller than the nine cylinder flow ripple. This result is expected due to the smaller individual cylinder volumes within the 10 cylinder pump. If a similar 8 cylinder pump had been used then the delivery flow ripple for this pump is likely to have been larger than that of the nine cylinder pump.

The variation of yoke moment for the two pumps over the three operating conditions is compared in figures 6.12a), b), and c). These simulations show that the 10 cylinder yoke moment variation is significantly larger than that of the nine cylinder pump. The results are similar to those shown in figure 3.11 that compare 9 and 10 cylinder pumps that are neutrally-timed (See 3.3.2).

Assuming that the yoke moment has a large effect on the pump SBN then, for a given pump displacement, an odd-pistoned pump is likely to create less noise than the equivalent even-pistoned pump.

6.3.2 The Use of Solid Pistons

The test pump uses pistons which are hollowed out. This reduces the inertia of the pump rotating assembly, but also contributes to the cylinder volume throughout the pumping cycle. By using solid pistons (although still retaining a drilling to allow lubrication of the slipper pads) the cylinder volume at BDC would be reduced. This would have the effect of reducing the volume of the compressibility flow ripple and so would reduce pump flow ripple.

To investigate the effect of replacing the hollow pistons with solid ones, a simulation study was carried out using the "Dual Cylinder" Bathfp model described in chapter 4. The parameters of the test pump were used to compare the delivery flow ripple and yoke moment of a hollow-pistoned pump with the equivalent solid-pistoned pump. The two pump schemes are shown in figures 6.10a) and c).

To ensure a fair comparison, the delivery port of the pump with the solid pistons was brought forward: the cylinders of this pump naturally contain a smaller dead volume and so will typically require a smaller delay to achieve pre-compression to the delivery pressure.

The comparison between the two pumps was simulated over the three operating conditions used for the simulation study of 6.3.1. The simulated delivery flow ripple of the two pumps at these conditions is shown in figures 6.13a), b) and c). As anticipated, the pump with the solid pistons produces a significantly smaller flow ripple for all three conditions.

The simulated yoke moment of the two pumps for the same three operating conditions is shown in figure 6.14a), b) and c). For both the 50bar, 100% displacement and the 250 bar, 20% displacement condition, the solid piston pump produces a similar yoke moment to that produced by the standard pump. However, at the maximum power condition, the yoke moment variation for the solid-piston pump is a lot worse. At this condition then the solid-piston pump would probably create a lot more airborne noise.

An increased yoke moment variation was expected since the cylinder pressure is likely to change more rapidly with the reduced cylinder volume: on communication with the delivery port this causes a faster change in the axial piston force and so would be expected to adversely affect the yoke moment.

An additional effect of the increased mass of the solid piston is that at TDC, the inertia of the piston may cause the slipper pad to lose contact with the running surface of the swashplate. Under these conditions the slipper pad typically impacts back onto the swashplate causing a large increase in the noise from the pump (See 3.3.1). This can be investigated by simulating the axial force holding a single slipper pad onto the swashplate during a full displacement condition when the axial piston velocities and accelerations are at their greatest.

Figure 6.15 compares this axial piston force for both the hollow and the solid piston schemes. The force on both pistons becomes negative when the cylinder pressure initially drops to low pressure. However, this effect is greater with the solid piston and so the piston pounding is more likely.

To reduce the likelihood of piston pounding, it may be possible to fit low-mass inserts into the hollow pistons. However, the increased yoke moment variation demonstrated in figure 6.14b) would still be present and so even with low-mass piston inserts, the solid-piston pump may still be noisier, over a large proportion of the operating range, than an equivalent pump with hollow pistons.

In conclusion, simulation showed that the use of solid-pistons would be more beneficial than the use of an even number of pistons. In particular, solid pistons will lead to significant reductions in the pump pressure ripple. However, at some conditions, the yoke moment is larger than that from the standard pump, and the effects of piston pounding would be more likely and so an overall benefit from using solid pistons is not ensured.

6.3.3 Schemes using Variable Portplate Timing

Relatively low levels of delivery flow ripple take place when pump cylinders are optimally pre-compressed (See 3.2.2); each cylinder is close to delivery pressure on meeting the delivery port and this prevents rapid cylinder flows to and from the delivery chamber.

The angle from BDC needed for cylinder compression to delivery pressure depends on the fluid properties, pump displacement and the pressure difference between suction and delivery. To achieve optimal pre-compression over a wide range of operating conditions a variable-timing mechanism is needed that responds to changes in the pump speed, displacement and pressure. The use of variable timing to achieve optimal pre-compression has been widely investigated.

6.3.3.1 Angular actuation of the portplate

A variable timing mechanism that has been proposed by several researchers is one that actuates the angular position of the portplate. In such a design, a servo mechanism would rotate the portplate relative to the swashplate yoke axis. This would then vary the delay of the delivery port depending on the pump speed, displacement and port pressures. In 1973, a sketch of such a system was presented by Currie and Kane [62] (See figure 6.16).

In 1978, Martin and Taylor [30] discussed the concept but considered it to be flawed; any delay given to the delivery port will also be applied to the suction port. With large delivery delays the end of the delivery port can extend over TDC and so reduce the pump volumetric efficiency. Also, a delayed suction port is likely to cause cavitation in the cylinder at the start of the suction stroke.

The concept of a variably-timed portplate was further examined in 1989 by Edge and Lui [8]. The proposed actuation mechanism consisted of a spring-loaded cylinder fed by delivery pressure to adjust the angular position of the port-plate so that the point of port

opening was delayed by an amount dependent on the mean delivery pressure. The feasibility of the concept was tested using a manual adjustment of the port-plate. A more complex actuation mechanism was designed and tested by Grahl [63] which also responded to changes in the pump mean flow.

Both designs reduced the pressure ripple. However, when the port retardation was high, cavitation occurred and the pump volumetric efficiency dropped, as predicted by Martin and Taylor [30]. Edge and Lui concluded that the major problem with variable port-plate timing is the lack of independent control over the inlet and delivery timing.

6.3.3.2 Independent Suction and Delivery Timing

There have been a number of attempts to uncouple the timing of the suction and delivery ports by using independent mechanisms acting at the start of both ports. One such scheme was patented by Boyer in 1979 [64] (See figure 6.17).

Boyer's portplate scheme attempts to produce variable suction and delivery timing through a mechanism that reacts to changes in delivery pressure. Referring to figure 6.17, one cylindrical chamber (18) opens directly to the pump delivery line, and another identical cylindrical chamber opens directly to the pump inlet line. The cylindrical chambers both contain a piston (19) whose position is controlled by a servo mechanism operated on by the port pressures. Before the start of the inlet and delivery kidney ports, ten radial slots (17) have been drilled into the portplate. These slots connect the running surface of the portplate with the pump inlet and delivery ports underneath the portplate. As the pistons (18) change position, the number of slots blocked by the pistons changes. This then advances or retards the start of suction and delivery to minimise the pump FBN.

The same principle of independent control for the suction and delivery timing was presented in a 1985 patent from Boltyanaskii and Levontin [65] (See figure 6.18) . The basis of the solution is an attempt to produce the effect of a "variable" relief groove through a mechanism that reacts to variations in delivery pressure. Referring to figure 6.18, on the delivery side, port 4 in the portplate opens to the cylinder that has just finished contact with the inlet kidney port. Delivery pressure is supplied to port 4 via annulus 10 and variable opening 9. On the inlet side, port 5 in the portplate opens to the cylinder that has just finished contact with the delivery kidney port. Inlet pressure is supplied to port 5 via annulus 17 and variable opening 16.

When the delivery pressure is zero bar(gauge) both pistons 7 and 14 are in the extreme right hand position and so the flow path through to ports 4 and 5 is blocked. As the delivery pressure increases, these pistons are forced to the left and springs 8 and 15 are compressed. This increases the area of the flow path through ports 4 and 5 to provide a larger pre-compression flow on the delivery side and a larger pressure relief flow on the inlet side. The overall effect is to reduce the reverse flows at the start of delivery and inlet.

A more promising mechanism was designed and tested by Grahl in 1989 [63] (See figure 6.19). Three drillings in the portplate ahead of a delayed delivery port were supplied

with delivery pressure through a slot in the spool of a spring-loaded pressure compensator. As the pressure difference between suction and delivery increased, then the pressure compensator spool moved to progressively close off the three drillings and so delay the delivery timing. Grahl made plans for a further flow compensation mechanism, but only tested the device with pressure compensation . With a delivery pressure of 25 bar, the mechanism reduced the airborne noise from the pump by up to 4.5dB. However, above 50bar, the mechanism made the pump noisier than an unmodified pump (See figure 6.20). Above this pressure the mechanism caused the pump cylinders to over-pressurise. He could not explain this effect and apparently did not take the work further.

Neither of the schemes patented by Boyer [64] and Boltyanskii [65] have been adapted within a commercially available pump. The main reason for this is probably their high cost; both schemes would significantly add to the manufacturing cost of any commercial pump. Also, as demonstrated by the work of Grahl [63], the servo mechanisms controlling the variable timing elements may be difficult to design in order to exhibit the necessary pressure, flow and speed compensation characteristics.

6.3.4 Schemes using Fixed Portplate Timing

An alternative approach to variable timing is to use mechanisms that pre-compress the cylinder contents to the delivery pressure in time for communication with a fixed delivery port.

6.3.4.1 Inter-Cylinder Pressurisation

A scheme was patented by Heyl in 1980 [66] (See figs. 6.21 to 6.23). The basis of this design is to supply a pre-compression flow from a cylinder at delivery pressure to the following cylinder at BDC. This pre-compression flow is regulated according to both delivery pressure and the pump speed.

Referring to figures 6.21 and 6.22, the cylinder 3a is at low pressure and has just finished contact with the inlet kidney port. At the same time cylinder 3b would be at delivery pressure. High pressure fluid from cylinder 3b would flow through duct 9 into piston chamber 8 and then into cylinder 3a through duct 10. Ducts 9 and 10 would be partly covered by piston 11. Piston 11 is under the influence of three vertical forces; delivery pressure on the piston face acting upwards, a downward force from the compression spring 12, and another upward force through linkage 15 from hinged mass 14.

When the delivery pressure is low then cylinder 3a would need less pre-compression flow to reduce the flow noise. In this case, piston 11 would be pushed to a low position by the compression spring and so ducts 9 and 10 would be covered to a greater extent. As the delivery pressure increases then piston 11 is forced of rise and cover less of ducts 9 and 10. This in turn allows more pre-compression flow into cylinder 3a.

When the pump speed is low then the flowrate needed to produce the necessary pre-compression will also be relatively low. As the pump speed increases then the required flowrate from cylinder 3b to cylinder 3a also increases. This action is provided by the upward

force on piston 11 from the hinged mass 14. As the rotational speed of the cylinder block rises then the upward force through linkage 13 also rises, itself generated by the centripetal acceleration of the mass 14 about the hinge 15.

An alternative method of speed "governing" is shown in figure 6.23. In this case, the hinged mass is replaced by the angled block 28, the ball bearing 24 and the sliding assembly 25,26. As the pump speed increases then the centripetal acceleration on the ball bearing 24 would cause it to move outwards, in turn causing an upward force on face 27 and so on linkage 23 through the sliding assembly 25,26.

Again, it is unlikely that this design would be implemented on any commercial pump. It is doubtful that it would work reliably, and may also be prone to volumetric efficiency losses due to leakage to return through the inter-cylinder passageways. This design would also be very costly to manufacture.

6.3.4.2 The Pre-Compression Filter Volume

A much more viable scheme for variable cylinder pre-compression, known as the a "Precompression Filter Volume" (PCFV) has been recently developed by Petterson et al. [61,67,68,69]. A PCFV is a volume used to store part of the oil needed to pre-compress the cylinders as they pass BDC. During the phase of pressure equalisation between the cylinder and the PCFV, both are disconnected from the inlet and outlet port of the pump. This is ensured by the geometry of the port-plate (see fig.6.24).

The cylinder is connected to the PCFV by a hole in the port-plate, positioned so that the cylinder has to leave the inlet kidney port before the hole is reached. A PCFV of about 2-3 times the volume of one cylinder is sufficient to reduce the flow ripple significantly. Figure 6.25 shows the improvement in source flow ripple produced by the PCFV compared to the flow-ripple using a plain port plate with no relief grooves.

Once again the mechanism is not ideal. Since the PCFV has no control element to tune its operation, the performance of the mechanism will vary over all of the pump's operating conditions. This emphasises the need for very careful design to provide adequate flow ripple attenuation over a wide range of operating conditions. In particular, the volume of the PCFV and the diameter and length of the connecting channel from the PCFV and the port-plate are critical; if these are inadequately matched then the PCFV will not adequately recharge back to delivery pressure after each pre-compression cycle.

At the present time, results from the PCFV mechanism have only been published for its application on fixed displacement pumps [61]. This is significant because the PCFV may not have the necessary range of operation to work effectively over both a range of delivery pressures and a range of pump displacements. This would be a significant disadvantage of the PCFV mechanism, as many axial piston pump applications rely on its variable displacement capability.

A similar study was carried out by Harris et al. [35] on a PEV (Pre-Expansion Volume) instead placed just ahead of TDC in an attempt to minimise or eliminate cavitation. In this

case it was found that a pre-expansion volume of 2-3 times the cylinder unswept volume could effectively limit the occurrence of cavitation at the start of the suction stroke.

6.3.4.3 The Vortex Diode

Very recently, Pettersson, Weddfelt et al. [61,70] attempted to achieve a self-adjusting method of ideal pre-compression using a fluidic device known as a Vortex Diode placed ahead of the delivery port (fig 6.26). The important characteristic of a Vortex Diode is that it presents a different flow resistance depending on the direction of the flow through the component. Previous work using water with a steady-state pressure drop across similar components had measured diodicity (ratio of resistance) of 100:1. With this difference of resistance in the two flow directions then it would be possible to use a Vortex Diode as a "smart" check valve with no moving parts subject to wear.

In practice the Vortex Diode did not exhibit the diodicity needed to make the concept viable. The reasons for the low diodicity were;

a) The higher viscosity of the hydraulic fluid

b) Under rapidly changing conditions the diodicity is almost non-existent as a vortex cannot form.

c) For some operating conditions, a restrictor is needed in-line with the diode to prevent an initial cylinder pressure overshoot. The restrictor has the effect of further reducing the valve diodicity.

6.3.4.4 Pre-Compression with a Check Valve

In 1974, Helgelstad et al. [29] outlined a scheme whereby the delivery port opened relatively late in the cycle and allowed a one-way valve in the port-plate to open when the cylinder pressure reached delivery pressure. In theory this would produce optimal cylinder pre-compression for every pump operating condition (See figure 6.27).

The valve would close each time it came into contact with a low pressure cylinder, and then open again as each cylinder reached the delivery pressure. Because of this, Helgestad stated that the valve may only have a limited life; a nine piston pump operating at 1500rev/min would cause the valve to switch 810,000 times per hour. Furthermore, at higher pump speeds, the frequency response of the valve may limit its switching performance.

A working version of the concept was designed and tested in 1989 by Grahl [63] (See figure 6.28). He found that the use of a conventional check valve reduced the airborne noise from a 7 piston pump operating at 1500rev/min by as much as 3dB at lower delivery pressures. However, at higher delivery pressures the check valve was ineffective, and above 100 bar caused the pump to emit more airborne noise than a standard pump.

The reason for the increase in noise at higher delivery pressures was not explained, but is likely to be caused partly by the stronger impacts of the moving valve element between its end stops. Throughout the test work, the performance of the valve did not degrade. However, Grahl stated that with more testing he expected the valve to suffer from fatigue.

6.3.4.5 Pre-Compression with a Heavily Damped Check Valve

The principle of using a check valve ahead of a delayed delivery port is promising. The need for a complex mechanism to respond to changes in the pump operating condition is made redundant; instead the valve responds to the cylinder pressure directly and so is self-tuning. However, as shown above, a check valve is unsuitable due its very rapid switching action.

To prevent the rapid switching action, but still retain the self-tuning characteristic, the check valve could be heavily damped. This is very promising, although the level of damping applied to the valve is important; if too much damping is applied then the valve response will be slow and the pump could become noisy when the operating condition changes. If too little damping is applied then the valve element will switch rapidly as before.

6.4 Review of Promising Methods

In sections 6.2 and 6.3, a number of prospective methods for reducing pump FBN have been presented. Five of these methods are promising enough to warrant further work.

The speed sensing Helmholtz resonator is very promising in that it may be fairly straightforward to test and develop. The control element in the neck of the Helmholtz resonator could be controlled with a small solenoid valve supplied with an electrical control signal based on the pump speed. It may be possible to design a generic unit that can be fitted as a "bolt on" attachment to a variety of different proprietary silencers. However, as regards this project, this solution may be better applied to a pump with a dominant fundamental harmonic, such as a gear pump. Accordingly, the development of this unit is regarded as too far from the project remit, specifically to reduce the FBN from axial-piston pumps.

To develop a pump with solid pistons using lightweight piston inserts, the following work would have to be carried out:

a) redesign of the piston assemblies and portplate;

b) manufacture of the redesigned pump;

c) instigation of a development project to optimise the pump performance.

These activities are not suited to the capabilities and resources available this project at Bath. It is recommended that the work be continued at Vickers: the technology is well understood and the simulation facilities at Omaha would be able to produce an optimised design.

The three remaining promising methods, the 3 dimensional multi-lobed cam, the rotary valve pulse generator, and the heavily damped check valve, would have involved too much work to investigate all three satisfactorily. Accordingly, it was decided to develop the rotary valve and the heavily damped check valve concepts, as these were considered to be more novel than the 3-dimensional multi-lobed cam. The development of the rotary valve and heavily damped check valve concepts is outlined in chapters 7, 8 and 9.

a) Expansion chamber b) Pipe resonator c) Helmholtz resonator d) Accumulator

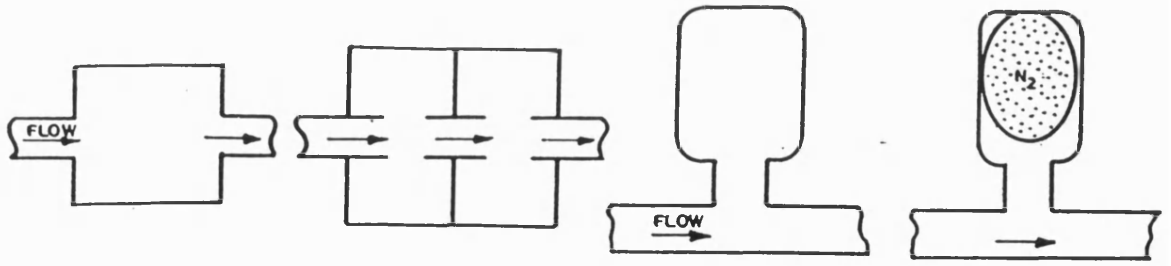

Figure 6.1a - d
Various types of reactive silencer (from [46])

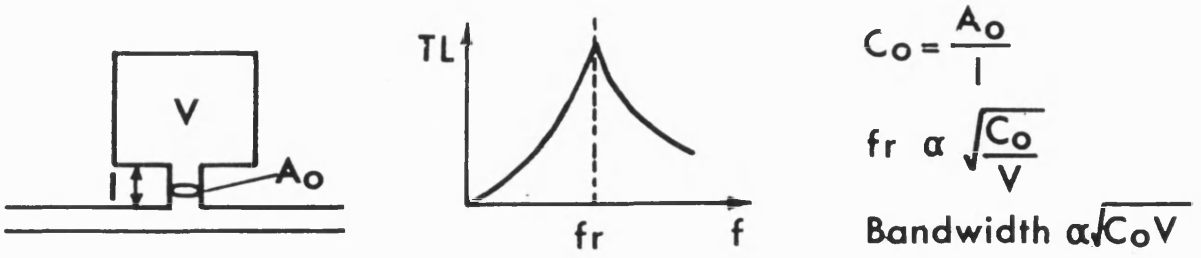

Figure 6.2
Helmholtz resonator characteristics (from [4])

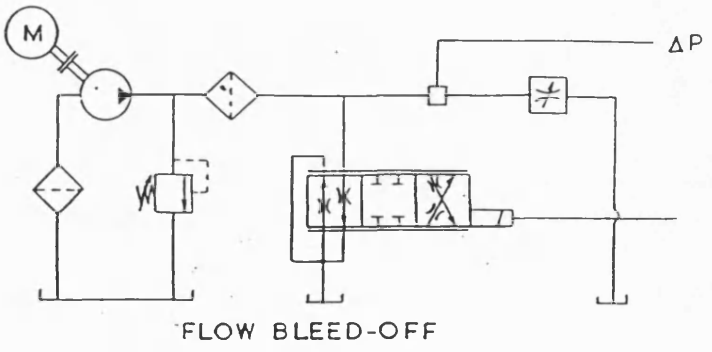

Figure 6.3
Using a servo-valve to cancel pump FBN (from [7])

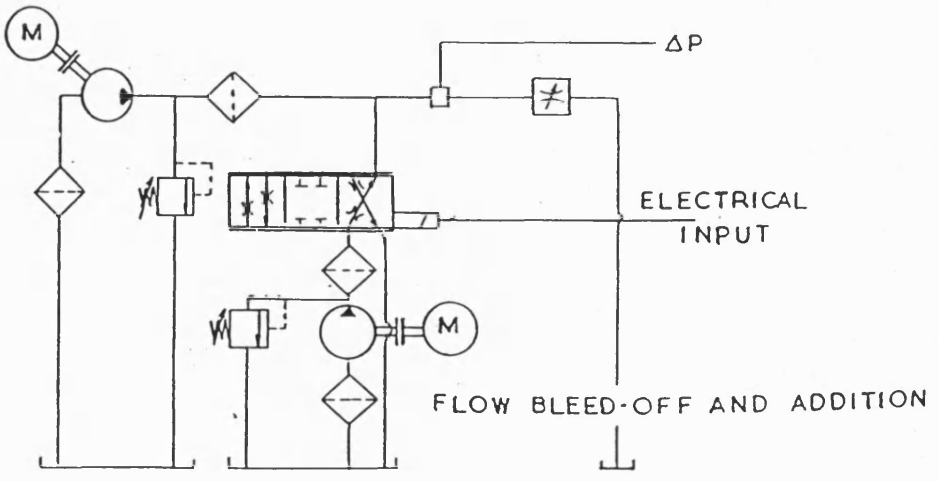

Figure 6.4
Using a servo-valve to cancel pump FBN (from [7])

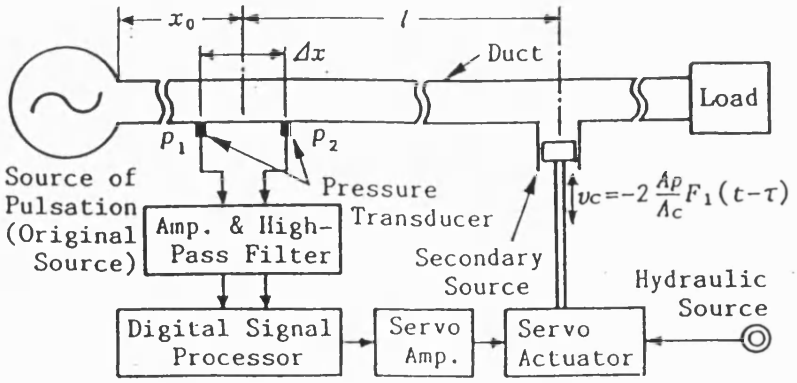

Figure 6.5
Scheme of the Kojima anti-noise system (from [52])

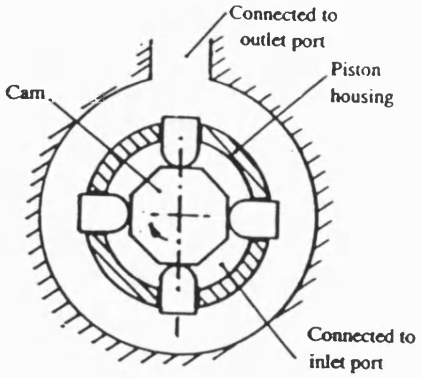

Figure 6.6
Schematic of the Lipscombe multi-lobe cam mechanism(from [7])

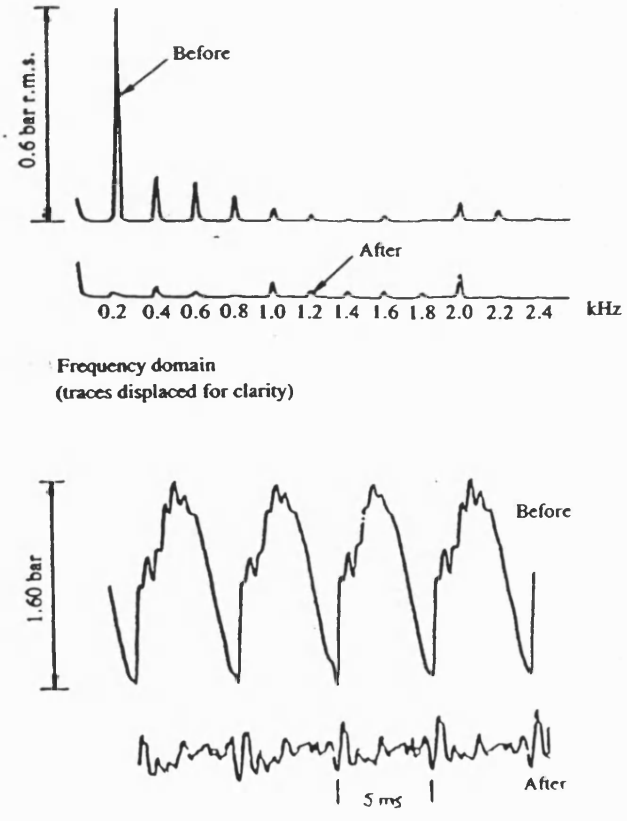

Figure 6.7
Reductions in pump FBN achieved using the Lipscombe multi-lobe cam (from [7])

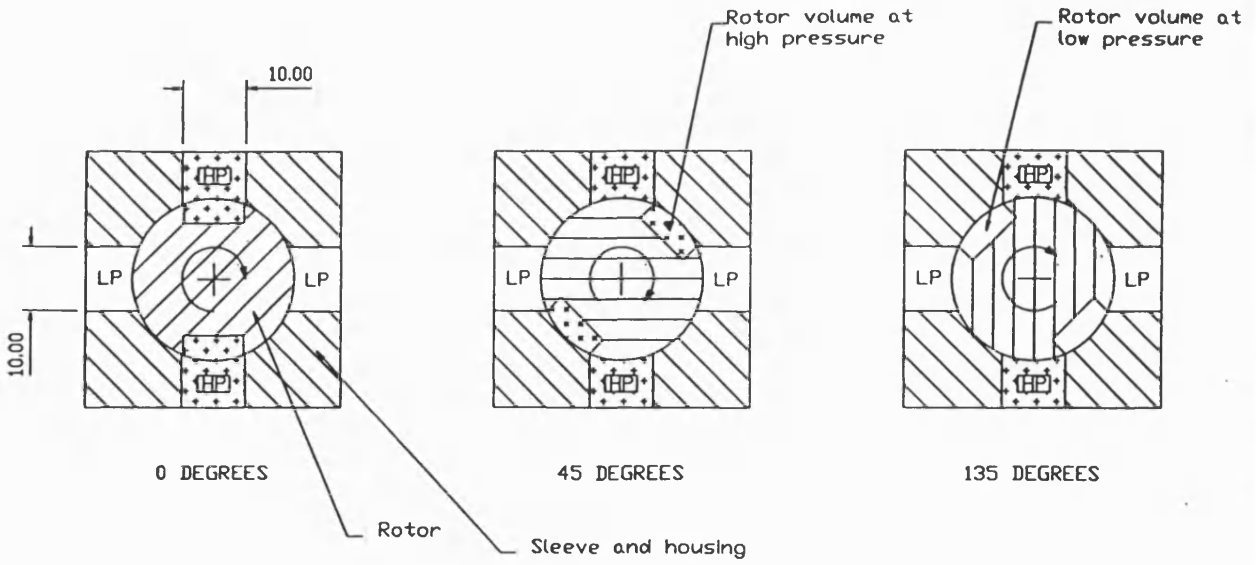

Figure 6.8
Schematic showing the rotor motion within a rotary valve

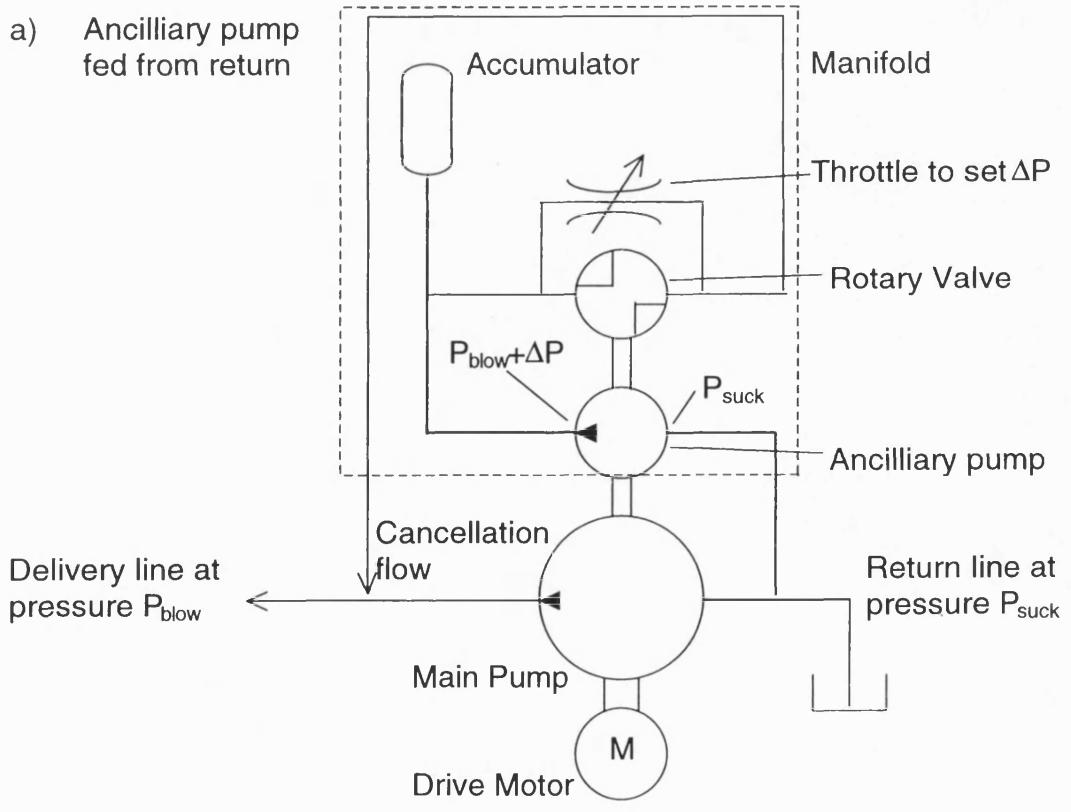

Figure 6.9a
Scheme showing a rotary valve supplied at low pressure

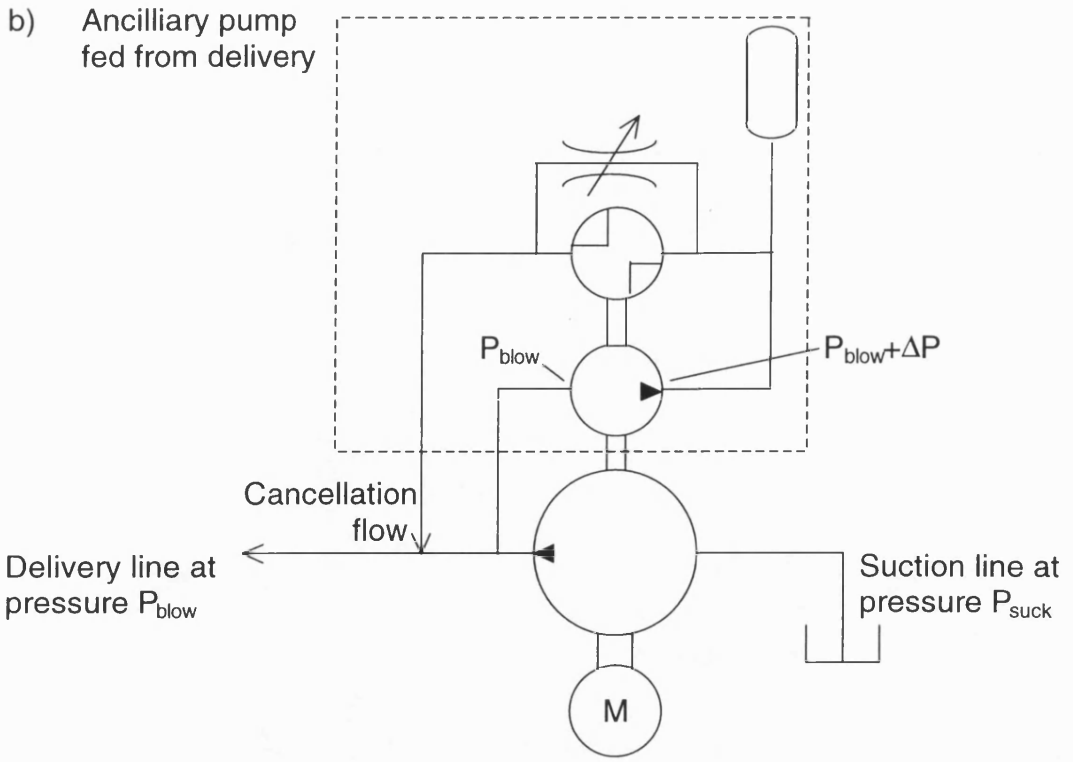

Figure 6.9b
Scheme showing a rotary valve supplied by delivery pressure

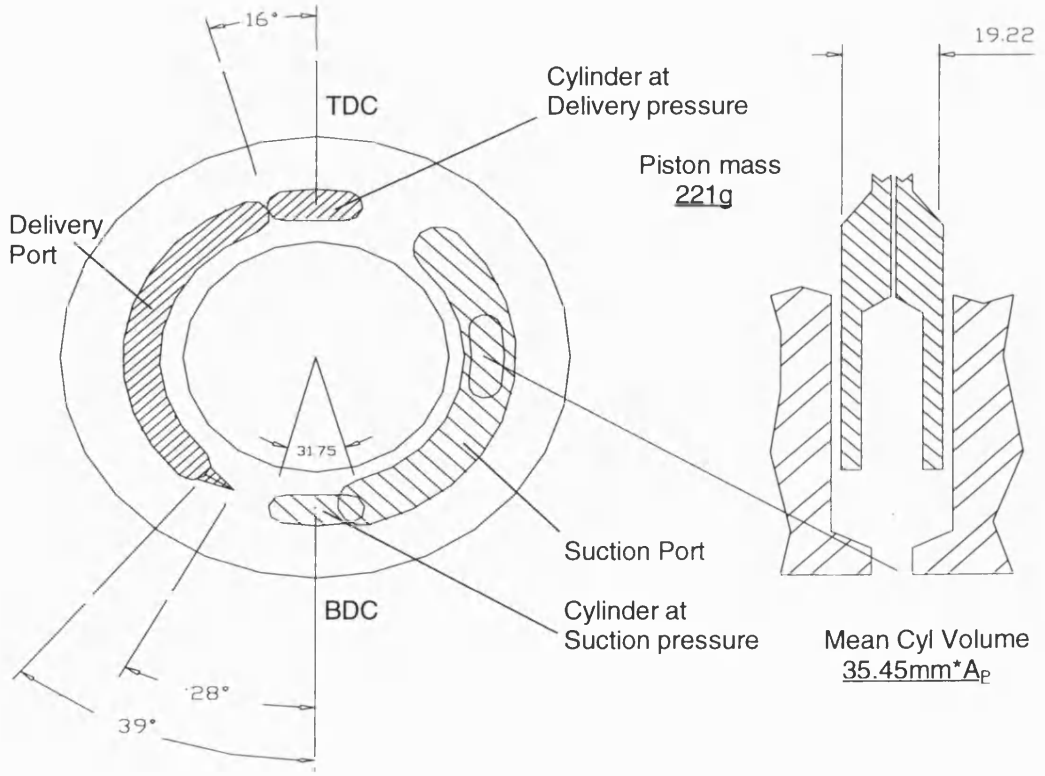

Figure 6.10a
Simulation parameters for a 9 cylinder pump with hollow pistons

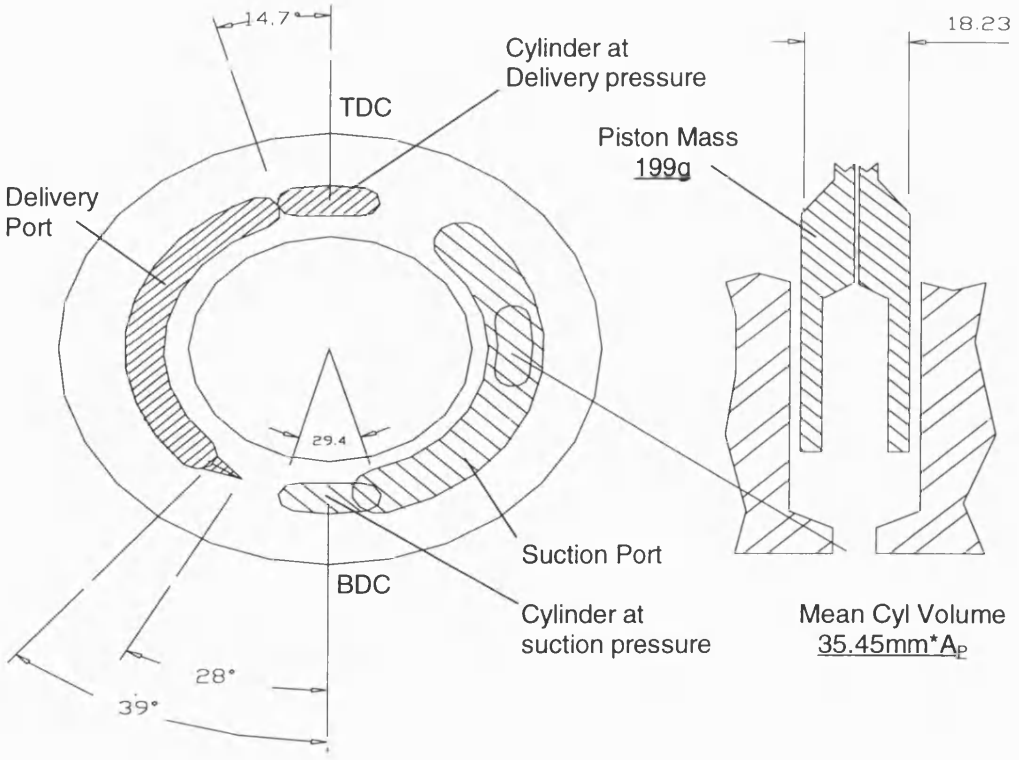

Figure 6.10b
Simulation parameters for a 10 cylinder pump with hollow pistons

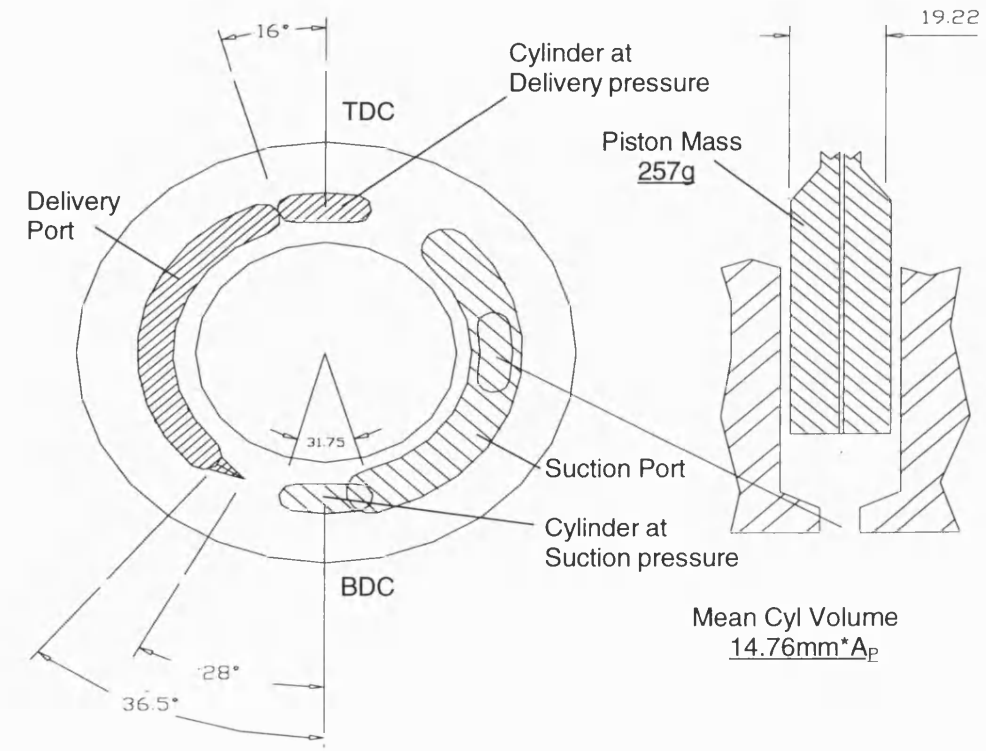

Figure 6.10c
Simulation parameters for a 9 cylinder pump with solid pistons

a) 50 bar delivery pressure, 100% displacement

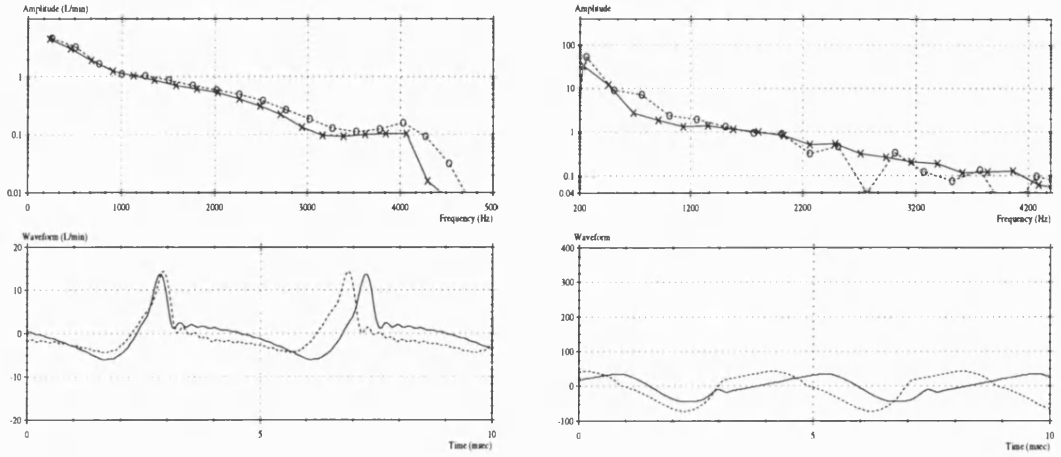

b) 250 bar delivery pressure, 100% displacement

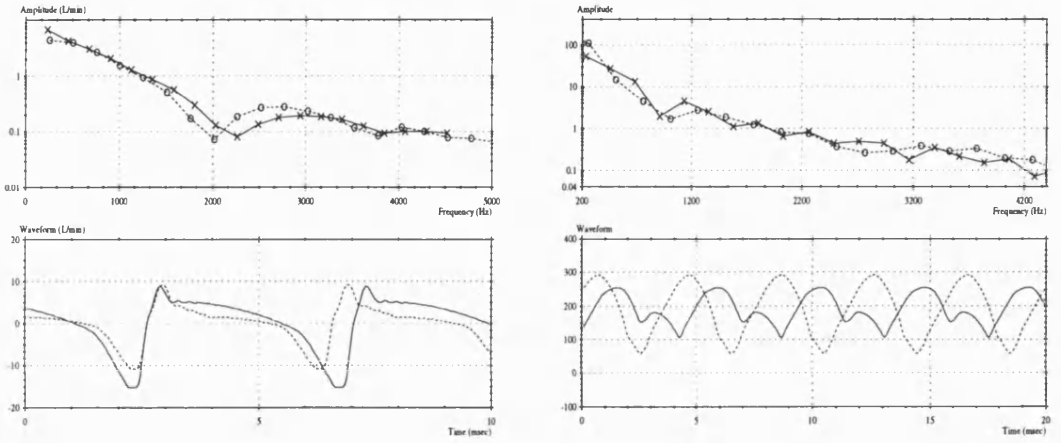

c) 250 bar delivery pressure, 20% displacement

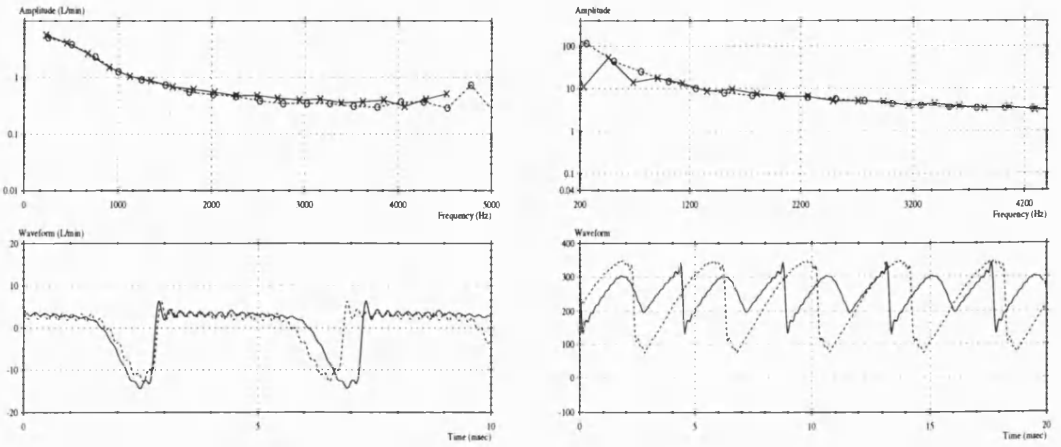

Figure 6.11a - c
Simulated delivery flow ripple for the 9-cylinder (continuous) and 10 cylinder (dashed) schemes that use hollow pistons

Figure 6.12a - c
Simulated yoke moment ripple (Nm) for the 9 cylinder (continuous) and 10 cylinder (dashed) schemes that use hollow pistons

a) 50 bar delivery pressure, 100% displacement

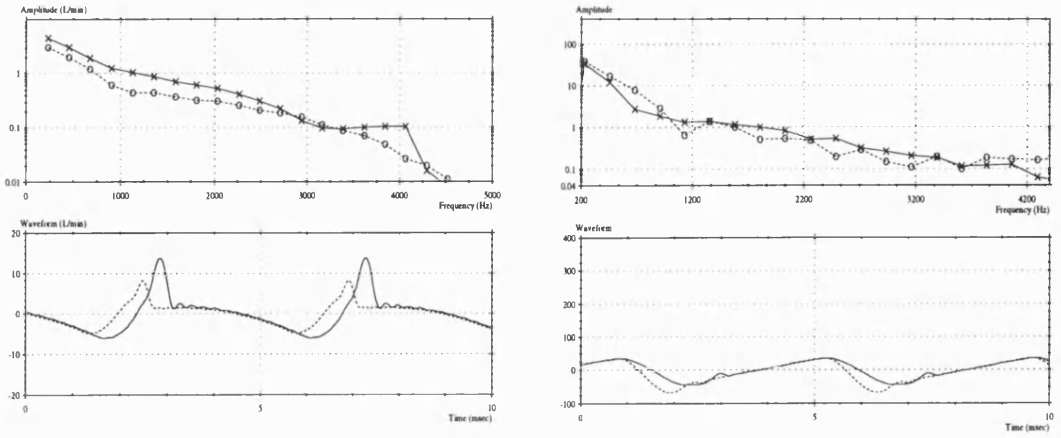

b) 250 bar delivery pressure, 100% displacement

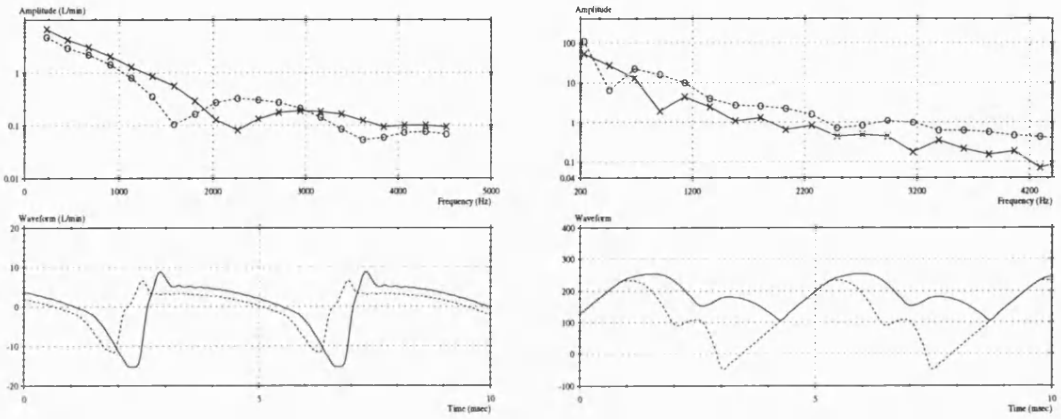

c) 250 bar delivery pressure, 20% displacement

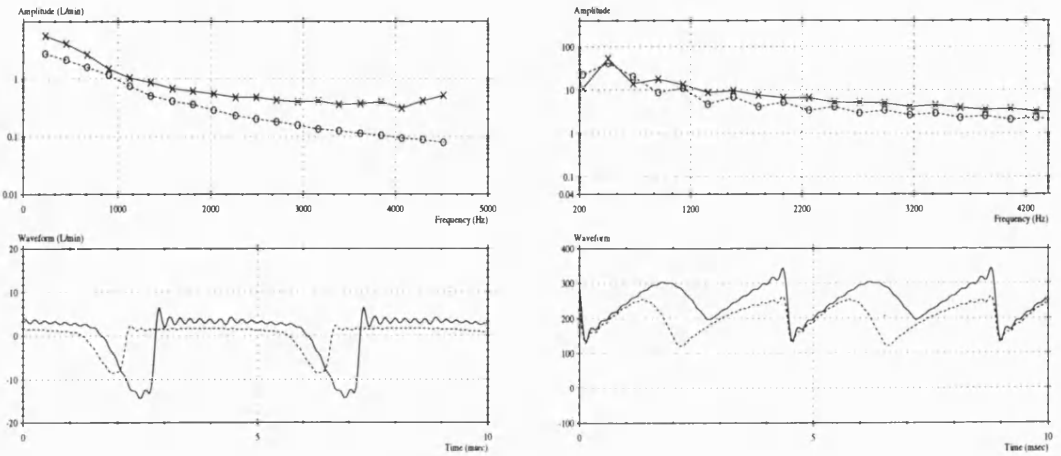

Figure 6.13a - c
Simulated delivery flow ripple for a 9 cylinder pump with hollow pistons (continuous) and with solid pistons (dashed)

Figure 6.14a - c
Simulated yoke moment ripple (Nm) for a 9 cylinder pump with hollow pistons (continuous) and with solid pistons (dashed)

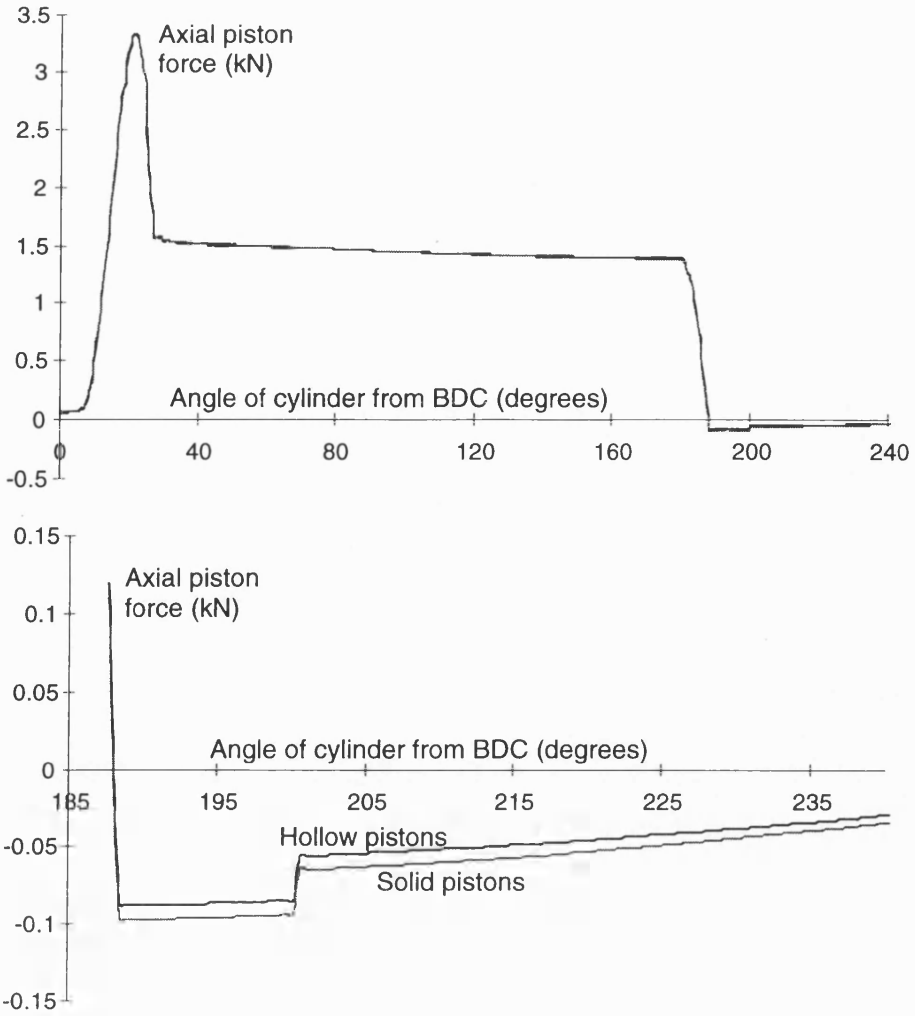

Figure 6.15
The simulatdee axial piston force from hollow and solid pistons

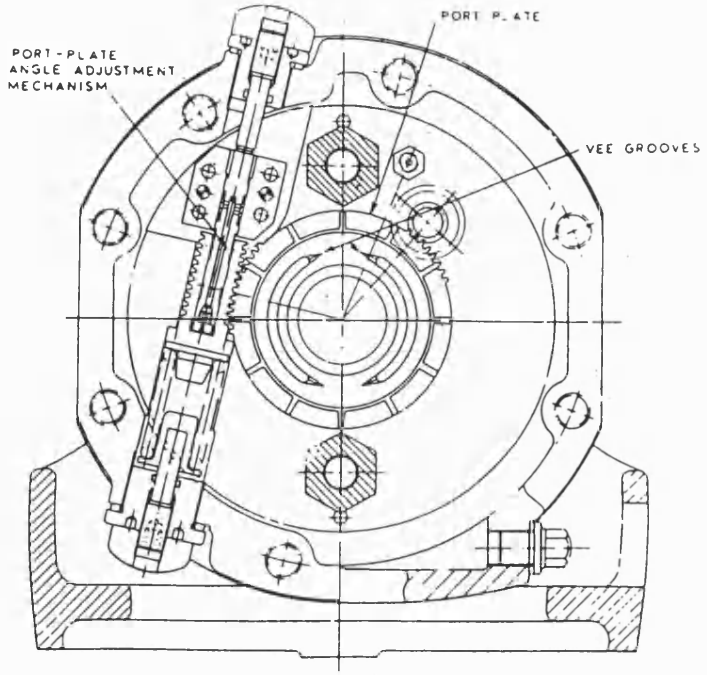

Figure 6.16
A portplate angular adjustment mechanism (from [62])

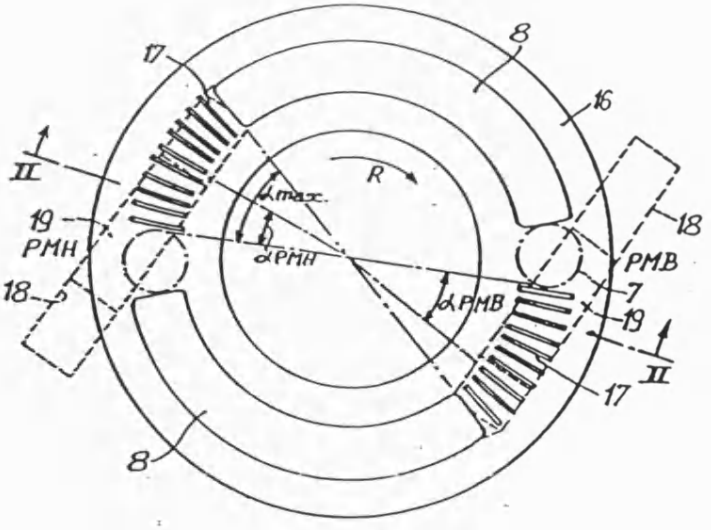

Figure 6.17
Boyer's variable timing portplate scheme (from [64])

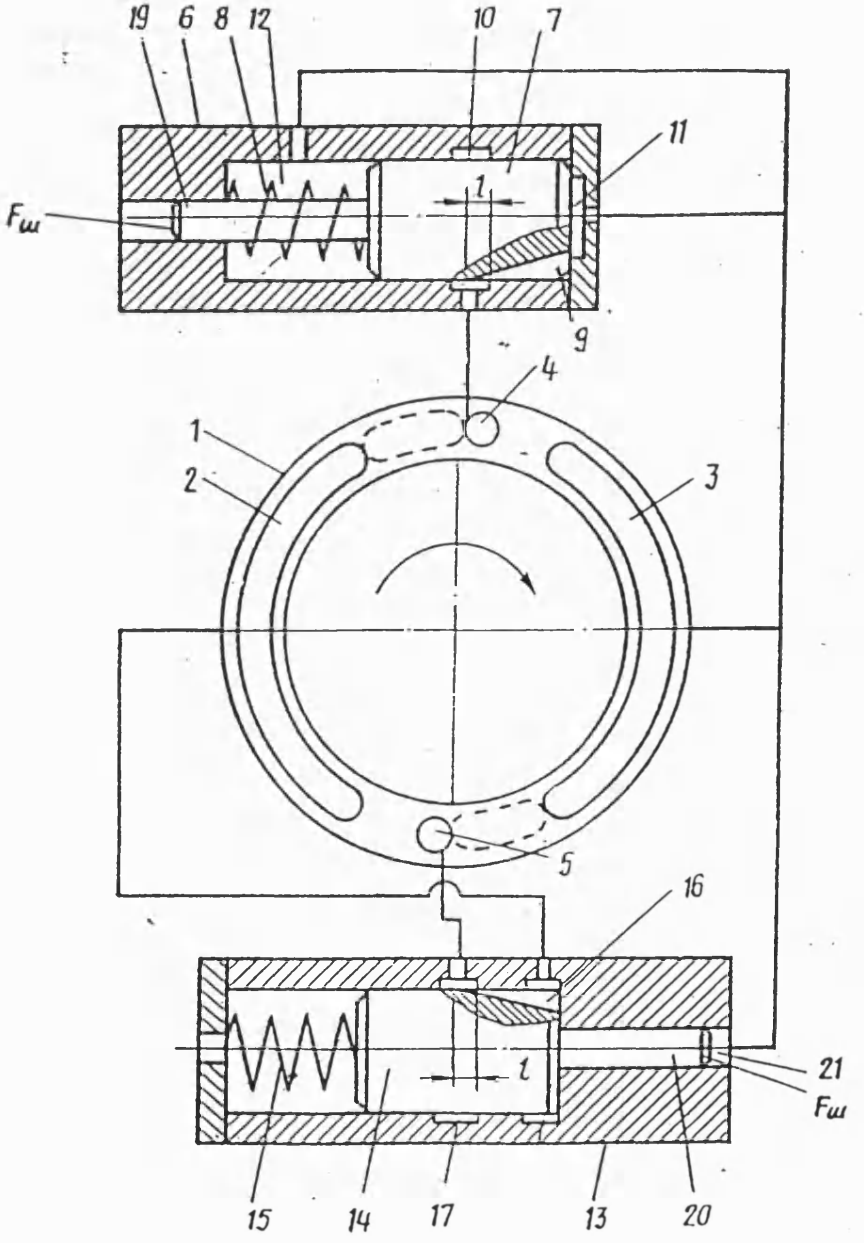

Figure 6.18
Boltyananskii and Levontin's variable timing portplate scheme (from [65])

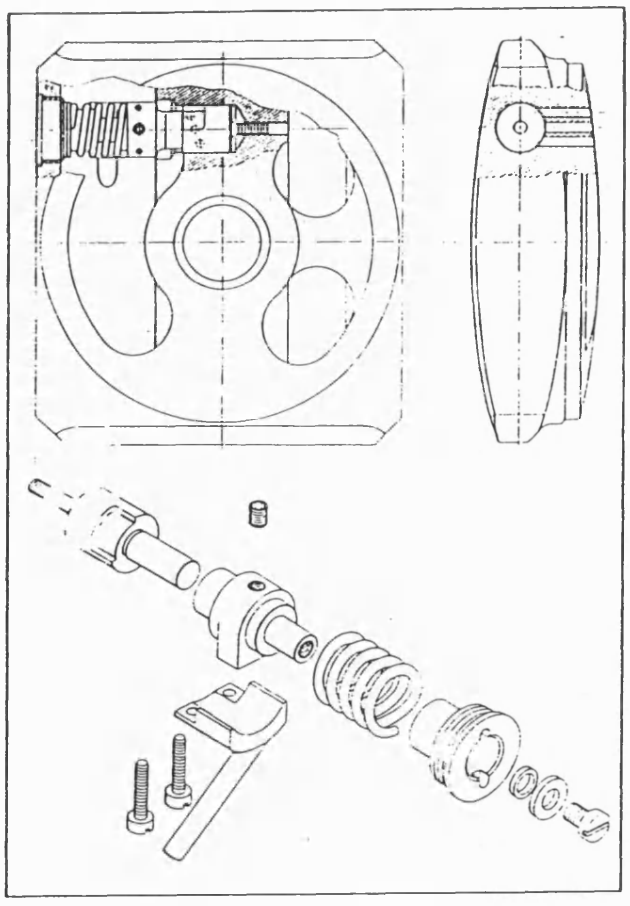

Figure 6.19
Grahl's variable timing portplate scheme (from [63])

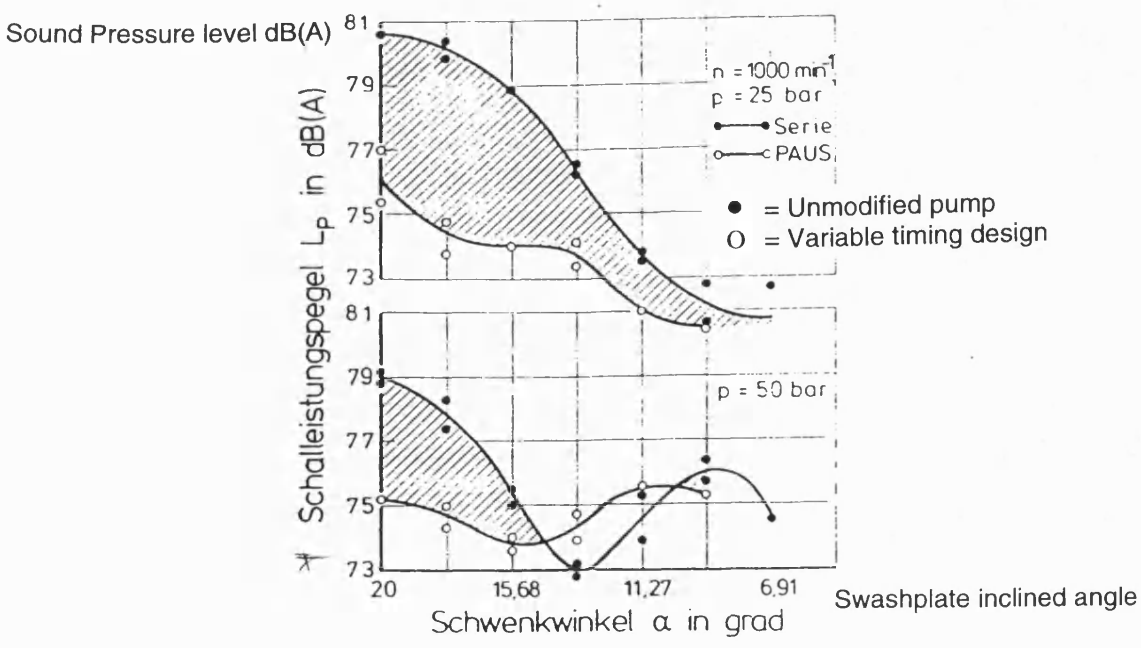

Figure 6.20
Reductions in pump casing ABN achieved by Grahl's mechanism (from [63])

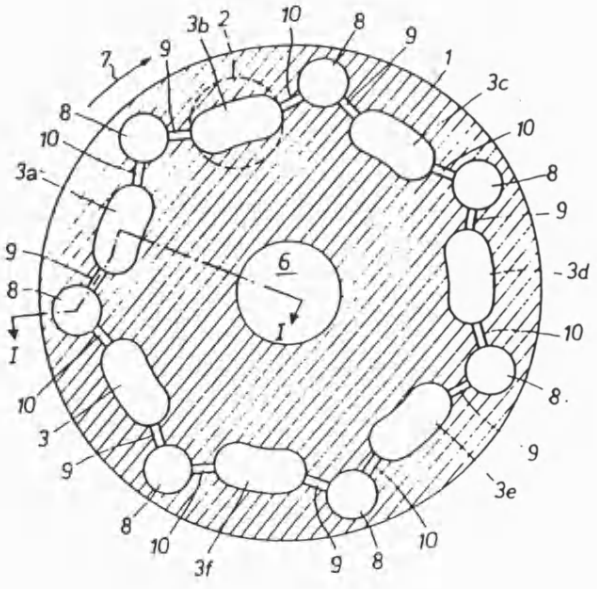

Figure 6.21
Radial section through the cylinder block of Heyl's cylinder inter-pressurisation scheme (from [66])

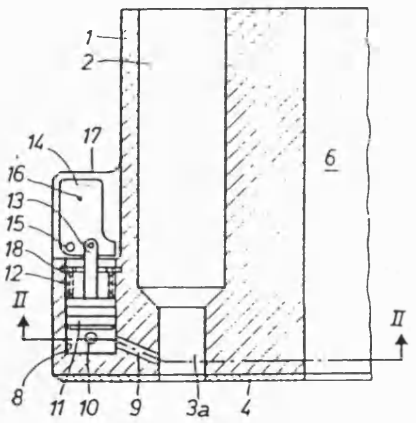

Figure 6.22
Axial section through the cylinder block of Heyl's cylinder inter-pressurisation scheme (from [66])

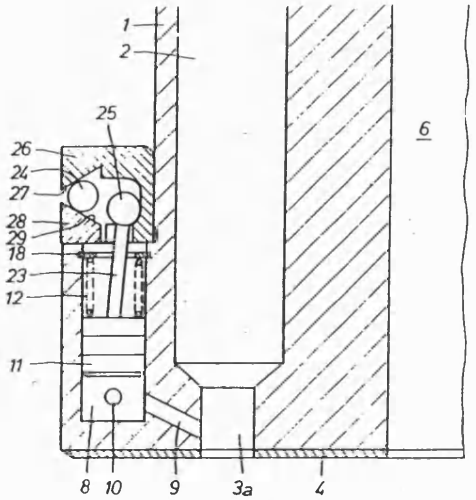

Figure 6.23
Axial section through the cylinder block of Heyl's speed-sensing cylinder inter-pressurisation scheme (from [66])

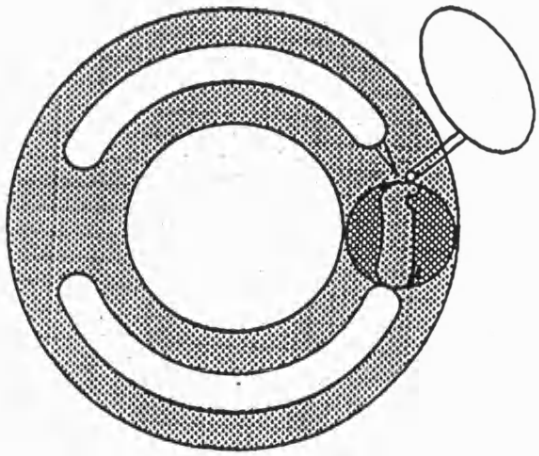

Figure 6.24
Sketch showing the position of the Pre-Compression Filter Volume (from [67])

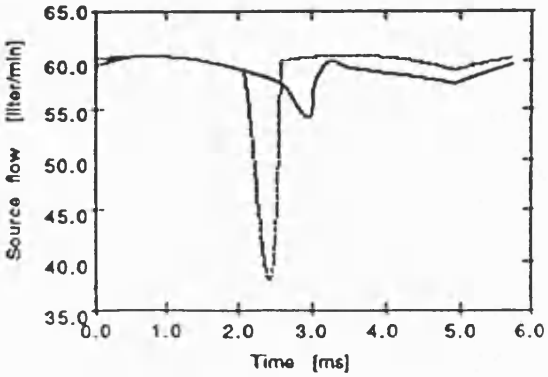

Figure 6.25
Reduction in delivery flow ripple achieved using a PCFV (from [67])

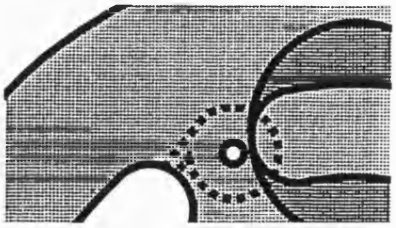

Figure 6.26
Sketch showing the position of the Vortex Diode (from [70])

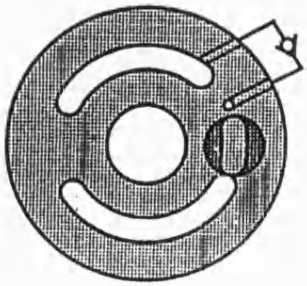

Figure 6.27
Sketch showing the position of a check valve fitted ahead of a delayed delivery port (from [67])

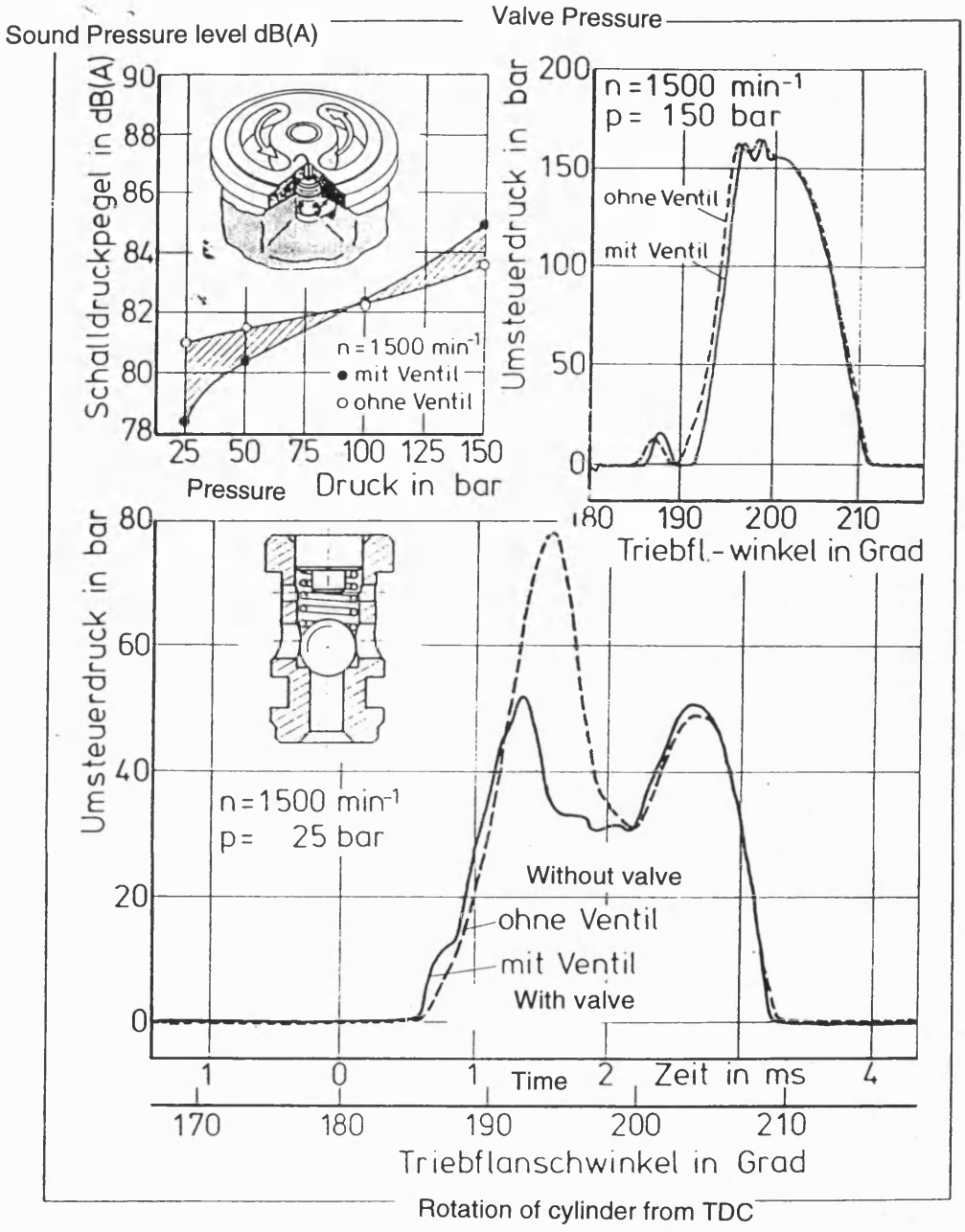

Figure 6.28
Grahl's portplate featuring a check valve ahead of a delayed delivery port (from [63])

7.0 Development of Rotary Valve Pulse Generator

7.1 Introduction

This chapter reports the progress of work carried out to produce a working prototype of the rotary valve pulse generator concept (See 6.2.2.5).

Before the whole rotary valve subsystem could be designed, more information was needed on the pressure and flow characteristics of the rotary valve. In particular, information was required on the pressure difference needed to produce the required flow pulses. If this was too high then the losses incurred by the rotary valve would have too adverse an effect upon the overall pumping efficiency. However, no rotary valve had ever been designed for this purpose and so the required characteristics were unknown. Instead, a design exercise was carried out to modify a rotary valve used frequently at Bath to provide sharp flow pulses for use within the Secondary source FBN test procedure (See 5.2.1).

The rotary valve was optimised to produce flow pulses of a similar size to the flow ripple of the test pump. To produce this size of flow pulse at the pumping frequency required a pressure difference across the valve of 40 bar, which was regarded as sufficiently low for the rotary valve to be viable. The work to modify the rotary valve is outlined in 7.2.

The re-designed rotary valve was used to cancel the delivery flow from the test pump. During this test programme , the valve was driven by an electric motor, synchronised to the pump input shaft using a phase lock loop. Initially, pressure from the laboratory ring main was used to drive the flow pulses through the rotary valve. Later, this pressure difference was produced using an ancillary pump (a small gear pump) fed from the delivery line. This work is outlined in 7.3.

Finally, in 7.4, the main results from this work are discussed, and recommendations are made for further work on this concept.

7.2 Optimisation of the rotary valve

This section presents the work carried out to optimise a rotary valve for the purpose of producing flow pulses large enough to cancel the flow ripple from the test pump.

7.2.1 Specifications for the Pulse Generator

Before the optimisation process could begin, the rotary valve flowrate and the maximum pressure difference allowed to produce this flowrate had to be specified.

The rotary valve was optimised to cancel the delivery flow ripple from the Vickers test pump running at 1500 rev/min. This pump had previously been tested, and the largest delivery flow ripple had been measured at the 250 bar delivery pressure, 20% pump displacement condition. From the pump delivery flow ripple at this condition (See figure 5.25), the peak interference flow was specified as 20L/min, over a pulse duration of 1.5ms, with the period between successive pulses being 4.44ms. The results from 5.3.3 show that the pump flow

ripple varied in size with changes in operating condition. Accordingly, the specified peak flow of 20L/min is the maximum anticipated to be provided by the rotary valve.

The power needed to produce these flow pulses can be estimated as the product of the mean rotary valve flowrate with the mean rotary valve pressure drop. Axial piston pump flow ripple is dominated by fluid compressibility effects (See 3.2.2) and so the mean interference flowrate through the rotary valve can be approximated by the mean loss in pump flowrate due to fluid compressibility.

The pump flowrate lost to compressibility is given by equation 3.14 (See 3.2.5). This expression can be combined with an expression for the ideal pump flowrate (Eq. 3.15) to give the drop in pump efficiency caused by the pressure drop through the rotary valve:

$$\Delta\eta = \frac{q_{comp}\Delta P_r}{q_{ideal}(P_{del} - P_{suc})} = 100\left[\frac{\Delta P_r}{2B_{eff}}\frac{(L_{mean} + RX\tan\beta)}{RX\tan\beta}\right]\% \qquad (7.1)$$

Equation 7.1 shows that the drop in efficiency is independent of the pump delivery and suction pressures. This is because the mean rotary valve flowrate (q_{comp}) is proportional to the pressure rise through the pump ($P_{del} - P_{suc}$).

Equation 7.1 also shows that the drop in efficiency increases at lower pump displacements ($X \rightarrow 0$). This is demonstrated in table 7.1 which shows the drop in test pump efficiency caused by a valve pressure drop of 40 bar:

Table 7.1

Pump Displacement (%)	Drop in Pump Efficiency with ΔP = 40 bar (%)
100	0.77
80	0.92
60	1.16
40	1.65
20	3.12

Clearly, at 20% displacement the power loss due to the 40 bar pressure drop through the rotary valve is a significant proportion of the power delivered by the test pump. However, the drop in pump efficiency between 100% to 60% displacement is close to 1%, which is regarded as an acceptable level of pump loss, and as a result 40 bar was taken to be the maximum allowable pressure drop across the rotary valve.

7.2.2 The Original Rotary Valve

Sketches showing the sleeve and rotor of the standard rotary valve are shown in figures 7.1 and 7.2. The radial width of the rectangular channels on the rotor is equal to the distance between adjacent ports on the sleeve. During a 360° revolution of the rotor, these channels allow four very short duration flow pulses between the high and low pressure ports machined in the sleeve. For two of the four pulses, the volume of the fluid within the channels is initially at high pressure and for the other two pulses this fluid is initially at low pressure. In figure 7.2 the high pressure case is shown with the rotor at 45° and the low pressure case is shown at with the rotor at 135°

The source impedance and internal flow ripple for this valve have been measured using the "Secondary source" technique (See 5.2.1). Initially the valve was tested with flow from a high pressure line being fed through the valve to return. A sketch of this test arrangement is shown in figure 7.3.

Further testing was carried out with high pressure applied to both valve ports so that flow pulses were fed into the measurement section as would be the situation when the rotary valve is used as a source of interference flow. A sketch of this second test arrangement is shown in figure 7.4.

For both test arrangements, the piezoelectric pressure transducers were fitted at distances of 2cm, 31cm, and 72.5cm from the rotary valve casing. The internal diameter of steel pipe chosen for this measurement section was 10mm. The testing was carried out to the procedure previously used for the Vickers test pump (See 5.2.4). The software settings for PROCESS and ACQUIRE [40] are listed in Appendix D

Source impedance spectra for the rotary valve with various mean pressure differences across the valve are shown in figure 7.5. These results are presented as least squares curve fits of the measured impedance spectra to reduce the effects of experimental scatter. These results show that the rotary valve source impedance is largely independent of both the mean flow direction and the pressure difference across the valve.

The spectra of figure 7.5 show the main features of a Helmholtz source impedance model, although around the anti-resonance and below 150Hz, the impedance results deviate from this model. Below 150Hz, this deviation is probably caused by the distance between the three piezoelectric pressure transducers being too short to accurately represent the pressure standing waves at the outlet of the rotary valve.

The internal flow ripple from the rotary valve is shown in figures 7.6 and 7.7. These results were produced using the fitted Helmholtz impedance model shown in figure 7.5. The figures are labelled to show the pressure at both ports of the rotary valve. The positions of these ports, P1 and P2, within the test circuit are shown in figures 7.3 and 7.4.

As could be expected, the size of the rotary valve flow ripple is highly dependent upon the pressure difference across the valve. However, the valve flow ripple is very small compared to that of the test pump. This is shown in figure 7.7 where the two flow ripple traces from figure 7.6 are superimposed onto the flow ripple from the test pump operating at 90 bar delivery pressure and full displacement.

The flow ripple results from figure 7.6 clearly show that two different alternate flow pulses are being generated by the rotary valve. This is due to compressibility of the fluid within the rotor channels. This behaviour can be explained using figure 7.2 and with reference to the solid trace in figure 7.6, where port 1 is at return pressure and port 2 is at 100 bar.

Between 35 and 60ms the flow to return is almost zero. This corresponds to the region between 45° and 135° for the rotor shown in figure 7.2., where the high pressure ports are closed by the bearing face of the rotor. During this period, the fluid within the rotor channels is at low pressure.

At 135°, the rotor channels align to allow a flow pulse between the high and low pressure ports and this time part of the flow from the high pressure port compresses the volume of fluid within the channels. This pressurisation process is exponential and can be seen in the region between 61 and 70ms.

At 85ms, the fluid within the rotor channels is exhausted to the low pressure port and causes a larger flow pulse from the high pressure port.

The rotor and sleeve are both axially symmetrical and so this sequence is repeated over the next 50ms to represent the flow ripple from a single revolution of the rotor driven at 10Hz.

From the flow ripple results of the original rotary valve, it was apparent that two modifications were needed before it could be used to cancel the test pump flow ripple:

1 The rotor channels needed to be widened. This would increase the flow area through the rotary valve and so increase the size of flow pulses at a given pressure drop through the valve.

2 The rotors needed to feature 4 symmetrical rotor channels. This would remove the effect of alternate different sized flow pulses.

The effects of these changes are investigated in 7.2.3.

7.2.3 Development of the Rotary Valve

A series of modifications were made to the original rotary valve to increase the size of the generated flow pulses. Figures 7.1 and 7.2 show the standard rotary valve. A diagram of the rotary valve test circuit is shown in figure 7.4. The last modification of the rotary valve is shown in figure 7.8. For this design, the sleeve ports were widened considerably from the 10mm of the original valve up to 11.5mm. This rotary valve produced pulses which were of the same magnitude as the test pump flow ripple. This is shown in figure 7.9 where flow pulses produced at 225Hz by a 40 bar pressure drop through the rotary valve are compared with the delivery flow ripple from the test pump operating at 250 bar delivery pressure and full displacement.

Figure 7.9 shows that flow pulses from the rotary valve at the pumping frequency and the maximum allowable pressure drop have a peak value of 14.5 L/min, and a duration of 0.4ms; and so are smaller than the specified parameters of 7.2.1. Despite this, it was decided to use this version of the rotary valve to attempt reduction of the test pump flow ripple. This work is reported in 7.3.

7.3 Interference tests using the optimised rotary valve

This section outlines testing that was carried out using the last modification of the rotary valve to cancel the test pump delivery flow ripple. Initially, pressure from the laboratory ring main was used to drive flow pulses through the rotary valve (See figure 7.10). Later, this pressure was produced with an ancillary pump (a small gear pump) fed from the delivery line (See figure 7.11). This testing is outlined in sections 7.3.2 and 7.3.3.

7.3.1 Description of the interference test rig

For all of the interference testing, the interference rotary valve was driven by a DC Servomotor which was synchronised to the rotation of the test pump using a phase lock loop. The main elements of the interference test rig showing the role of the phase lock loop are sketched in figure 7.10. The main components shown in figure 7.10, including the DC servomotor and the phase lock loop circuitry, are specified in Appendix B.

In figure 7.10, the arrangement of the test pump, measurement section and "secondary source" rotary valve are the same as that used to investigate the test pump flow ripple (See figure 5.2 and 5.2.2). In this case the "secondary source" method (See 5.2.1) was used to measure the flow ripple at the branch between the rotary valve outlet line and the main pump delivery line. This was easier than the previous measurements of the pump and rotary valve internal flow ripple because the impedance at the branch could be measured, and the flow at the branch could be calculated in the process software as the circuit entry flow ripple.

All of the transducer distances were measured from the branch rather than from the pump delivery flange. These new spacings were then used in ACQUIRE and PROCESS [40] and are listed along with the other software settings for this testing in Appendix D.

The phase lock loop consists of circuitry that drives the interference rotary valve such that its pulse rate is maintained equal to the pumping frequency of the test pump. The rotary valve produces 4 flow pulses per revolution and the test pump contains 9 cylinders, and so the phase lock loop maintains the speed of the rotary valve at 2.25 times that of the test pump. The speed and position of the rotary valve drive shaft is provided by an encoder fitted to the DC servomotor. The speed and phase demand into the loop comes from an optical sensor which monitors the rotation of an 18-toothed disk fitted to the pump driveshaft.

During testing, the pressure ripple at the branch was monitored by displaying the signal from the piezoelectric transducer nearest the branch on an oscilloscope. The phase lock loop controller features a dial to vary the phase offset between the rotation of the rotary valve and test pump. So, by monitoring the oscilloscope trace, the position of the rotary valve flow pulse could be adjusted until the maximum destructive interference was achieved; where the flow pulse from the rotary valve coincided with the cylinder reverse flows within the test pump.

7.3.2 Interference using flow from the ring main

Figure 7.10 shows the arrangement of the Interference test rig when the flow for the rotary valve is provided by the laboratory ring main.

During each test, the pressure ripple at the branch was monitored on an oscilloscope. The phase offset was adjusted to achieve the greatest destructive interference, and then the pressure drop across the rotary valve was varied until the pressure pulse from the rotary valve was a similar size to the pump cylinder reverse flows.

Interference tests were carried out on the unboosted test pump operating at full displacement and 50, 100, and 150 bar delivery pressure. At 50 bar, the greatest destructive interference was achieved when the rotary valve was pressurised to 60 bar, with a 10 bar pressure drop driving the flow pulses. At 100, and 150 bar, the pump cylinder reverse flows

were larger and the best interference was achieved with a 15 bar pressure drop across the rotary valve. The branch flow ripple for these three cases is shown in figures 7.12a, b, and c.

Figures 7.12a, b, and c show that the rotary valve flow pulse has a significant effect on the pump delivery flow ripple. However, little destructive interference is achieved: in all three cases the rotary valve flow pulse is too sharp, and reduces the pump flow ripple at the first 2 or 3 pumping harmonics only to cause increases between the 4th and 7th harmonics.

For the rotary valve to produce a more rounded flow pulse, then it would require modification to further widen the sleeve ports (See 7.2.3). This would also cause a lower restriction to flow through the valve, and so the pressure drop needed to produce the flow pulse would also be smaller. Instead, the existing rotary valve design would be better suited to interfere with the flow ripple from a less-well timed pump which features much sharper cylinder reverse flows.

During all of the tests, the rotary valve was very noisy, and there was a large amount of mechanical vibration throughout the test rig. The level of vibration and airborne noise remained high even at the conditions shown in figure 7.12, and as a result tests were only carried out up to a pump delivery pressure of 150 bar.

7.3.3 Interference using flow from the ancillary pump

Figure 7.11 shows the arrangement of the interference test rig when the flow for the rotary valve is provided by a small gear pump (3.2cm^3/rev). The gear pump is driven by a variable speed 1.5kW A.C. motor, and is fed with fluid from the delivery line. The inlet line to the gear pump breaks into the main pump delivery line opposite the drilling that carries the interference flow pulses from the rotary valve (See figure 7.11). Using this arrangement, the pressure drop across the rotary valve is controlled by the closure of the restrictor in parallel to the gear pump, and also by the speed of the A.C. motor driving the gear pump.

Interference tests were carried out to the method previously used for the tests powered by the ring main (See 7.3.2). For these tests, the test pump was set to full displacement with 100 bar delivery pressure.

During these tests, it was difficult to identify the rotary valve flow pulse from the oscilloscope monitoring the delivery line pressure close to the branch. To increase the size of the rotary valve flow pulse, the A.C. motor driving the gear pump was set to its maximum speed of 25Hz. The flow pulse was still indistinct and so the restrictor in parallel to the gear pump was closed as far as the motor would allow before stalling. At this point the flow pulse still could not be identified, but flow ripple measurements were taken to investigate the interference effect in more detail. At this condition, the pressure difference across the gear pump appeared to be fluctuating about a mean value of 20 bar. However, the pressures either side of the gear pump were fluctuating very rapidly, and the fact that the motor was almost stalling suggests that the peak pressure difference was much higher than 20 bar.

At this test condition there was a high level of airborne and structureborne noise from the test rig. Changes in the phase offset had no effect upon this noise.

Flow ripple at the branch was measured with a number of different phase offsets between the rotary valve and test pump. Figure 7.13 compares the flow ripple measured at the

branch for two different phase offsets with that of the underlying pump flow ripple. These results show that the gear pump causes a different interference effect to that from the rotary valve pressurised from the ring main (See figure 7.12). The difference is likely to be caused by interaction of flow within the gear pump inlet line with flow at the branch within the delivery line. From figure 7.13 it is difficult to identify any specific effects, although one of the large flow pulses may be caused by the restrictor in parallel to the gear pump: each time the rotary valve closes the pressure at the outlet of the gear pump will rise sharply which will then cause a rapid increase of flow through the parallel restrictor.

Figure 7.13 clearly shows that flow pulses into the delivery line from the inlet to the ancillary pump cause an increase in the delivery line flow ripple. It is likely that any system used to pressurise the rotary valve from the delivery line will also cause this effect. Therefore to reduce the delivery flow ripple, the rotary valve can only be fed with fluid from the suction line, as shown in figure 6.9a. However, this is also problematic, as it will simply increase the pressure ripple in the suction line.

7.4 Review of the rotary valve pulse generator concept

A test rig has been built that has been used to investigate the interference effect of flow pulses through a rotary valve upon the delivery flow ripple of an axial-piston pump.

The main conclusion of the work is that the rotary valve cannot be supplied with fluid from the delivery line (See 7.3.3). Therefore, if the rotary valve is to be used as a "bolt on" unit to existing pumps, the flow for the valve must come from the suction line.

During all of the tests, the rotary valve caused high levels of airborne and structureborne noise; much higher than the pump it was attempting to quieten. This is a major problem, although the valve is a small component and so may be easy to isolate and enclose.

The work during this project has mainly investigated the rotary valve performance. However, to make a working prototype equivalent to the concept scheme of figure 6.9a it would also be necessary to design a device which could store and release the energy from the ancillary pump at the pumping frequency of the main pump. This may not be feasible, and in any case is unlikely to be commercially viable.

The rotary valve concept may have more merit if it was used to periodically bleed flow from delivery pressure to the lower pressure of a chamber connected to the pump. In this case, the need for the accumulator and ancillary pump would be removed and so the whole system could be greatly simplified. To minimise the losses of such a system, the chamber pressure could be discharged through a small motor connected to the main pump input shaft.

Bleeding flow from delivery could be investigated using the existing test rig. From this testing, a new rotor could be optimised to maximise interference of the delivery flow ripple. If the SBN and ABN problems were also solved then this scheme would be promising.

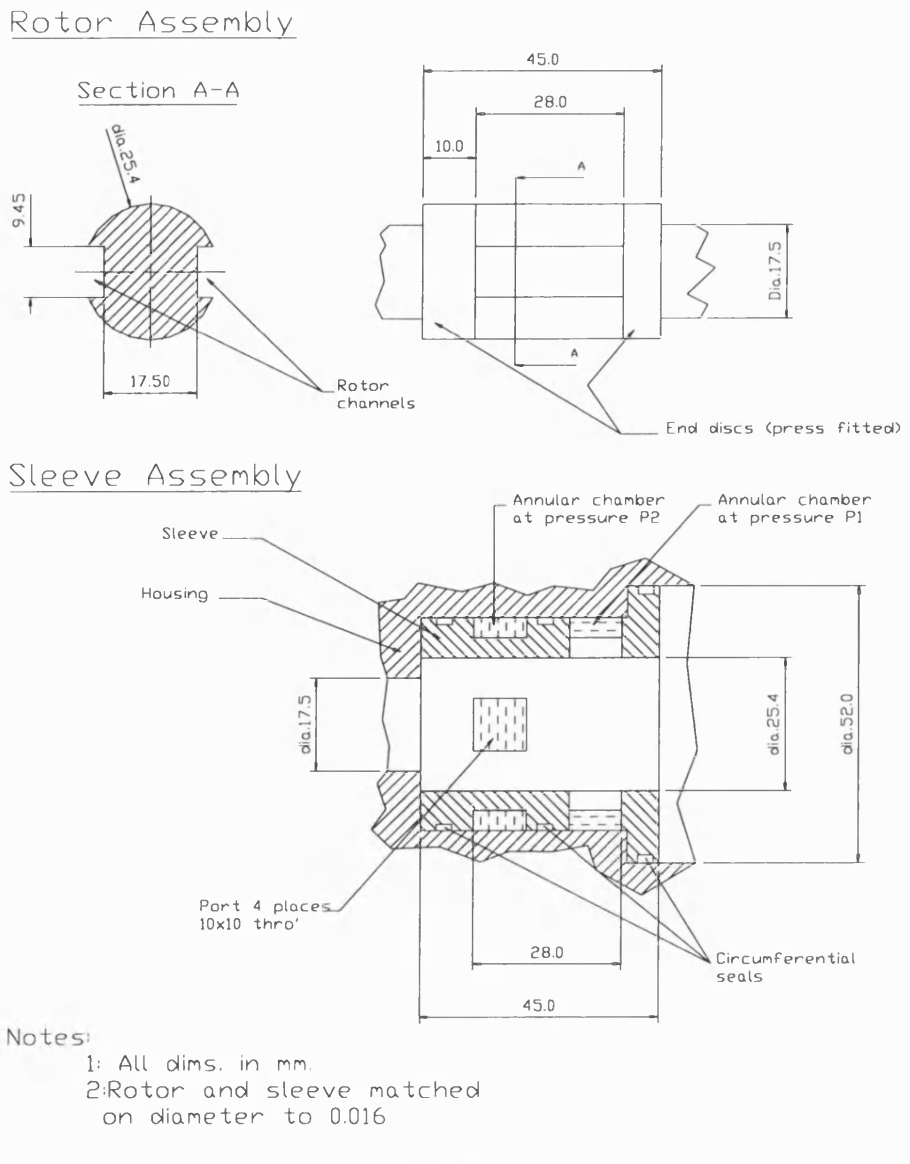

Figure 7.1
Sketch of the rotary valve

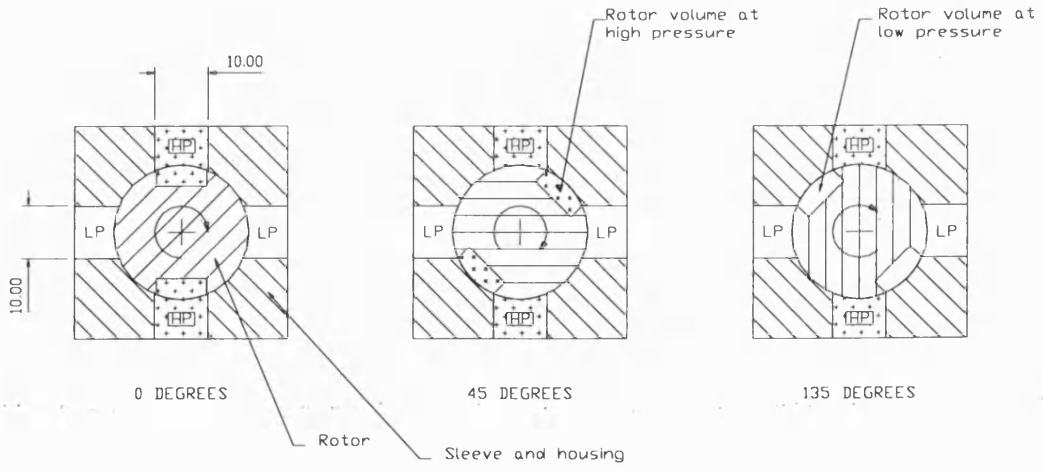

Figure 7.2
Flow paths through the original rotary valve

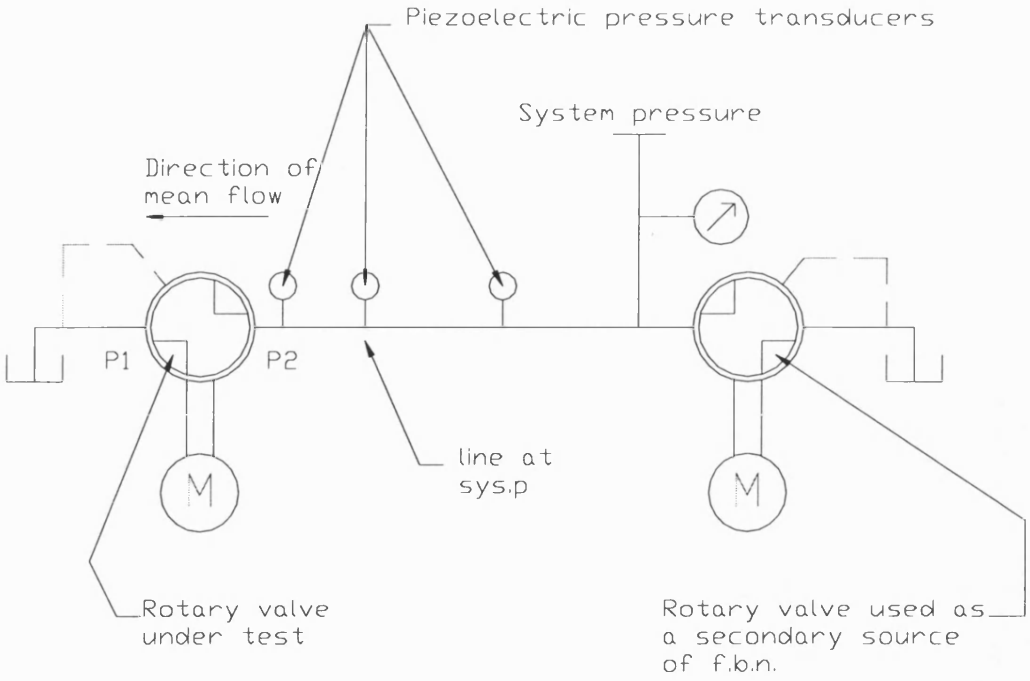

Figure 7.3
Sketch of the first test circuit used to examine the source characteristics of the rotary valve

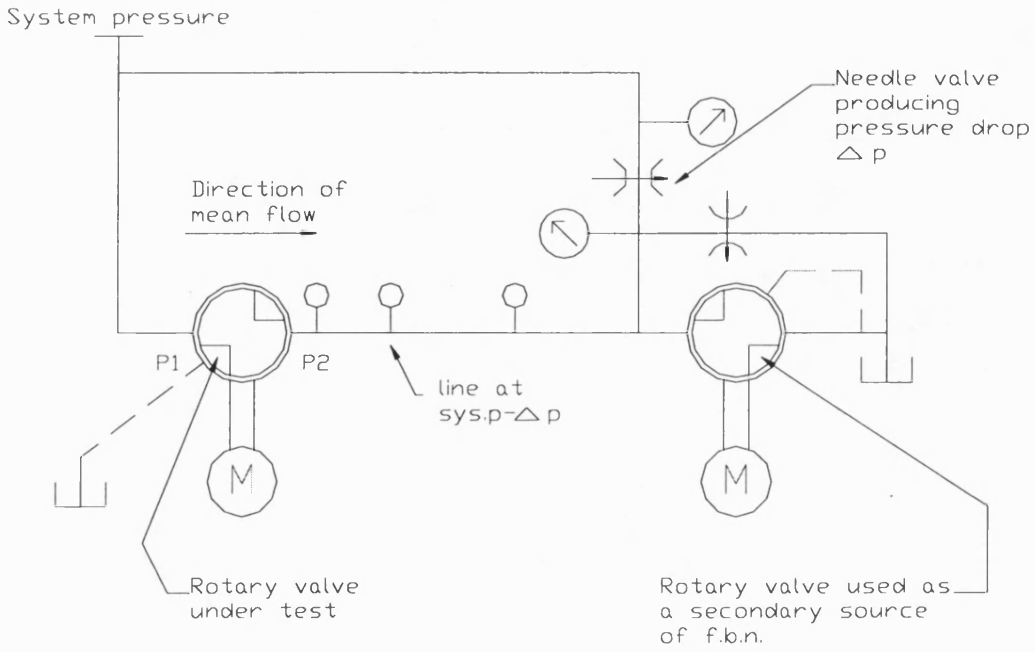

Figure 7.4
Sketch of the later test circuit used to examine the source characteristics of the rotary valve

Figure 7.5
Measured source Impedance spectra from the original rotary valve

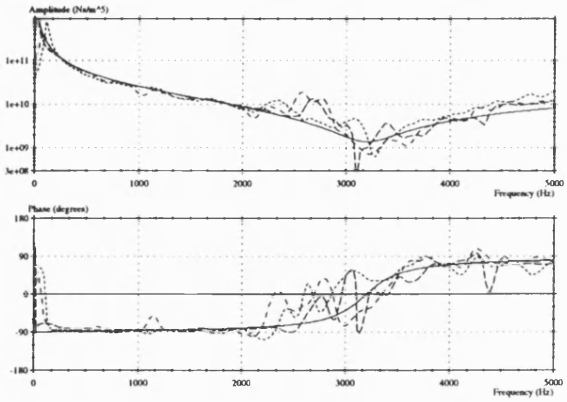

P1 0 bar P2 100 bar 10Hz Clockwise
P1 200 barP2 150 bar 10Hz Anti-Clockwise
P1 200 barP2 200 bar 10Hz Anti-Clockwise
Fitted Helmholtz model

Figure 7.6
Measured Internal flow ripple from the original rotary valve

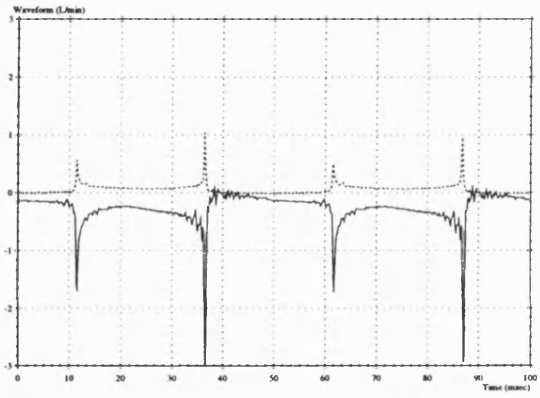

P1 0 bar P2 100 bar 10Hz Clockwise
P1 120 barP2 100 bar 10Hz Clockwise

Figure 7.7
Measured Internal flow ripple from the original rotary valve superimposed onto fthe flow ripple from the test pump.

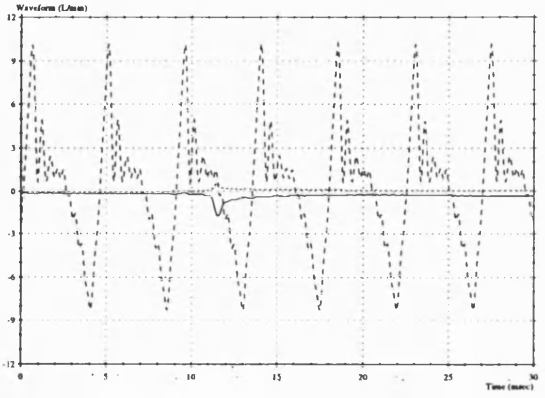

P1 0 bar P2 100 bar 10Hz Clockwise
P1 120 barP2 100 bar 10Hz Clockwise
Test pump @ 100 bar delivery, full displacement

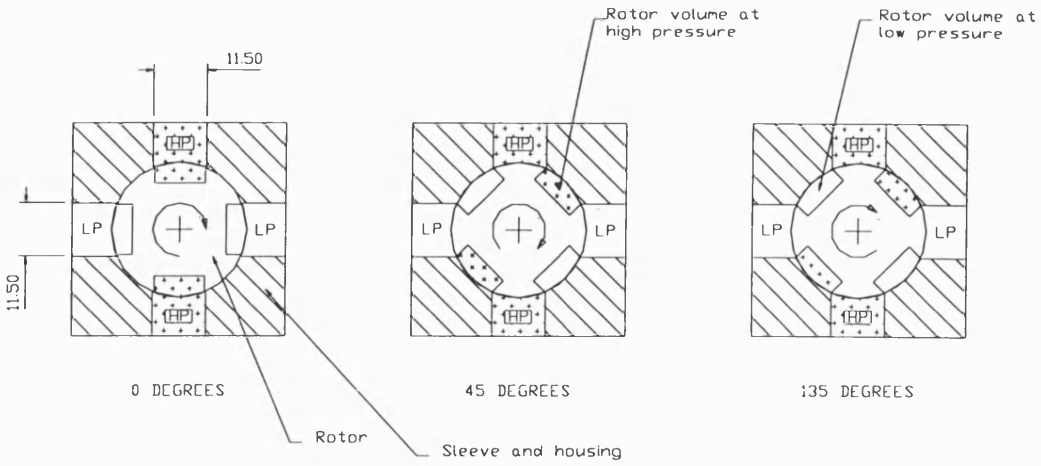

Figure 7.8
Flow paths through the optimised rotary valve

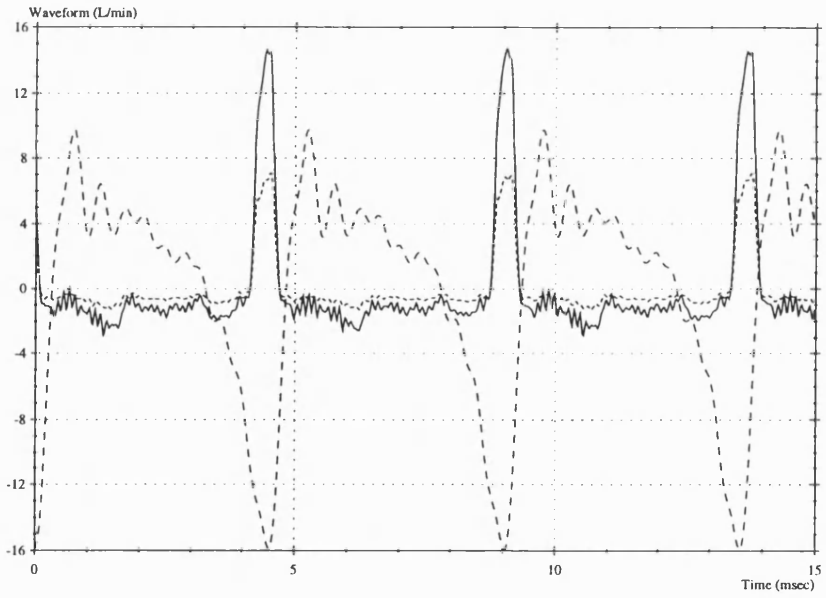

Mod 4 P1 140 bar P2 100 bar @ 225Hz
Mod 4 P1 120 bar P2 100 bar @ 225Hz
Test pump @ 250 bar delivery, full displacement

Figure 7.9
Measured Internal flow ripple from the optimised rotary valve superimposed onto fthe flow ripple from the test pump.

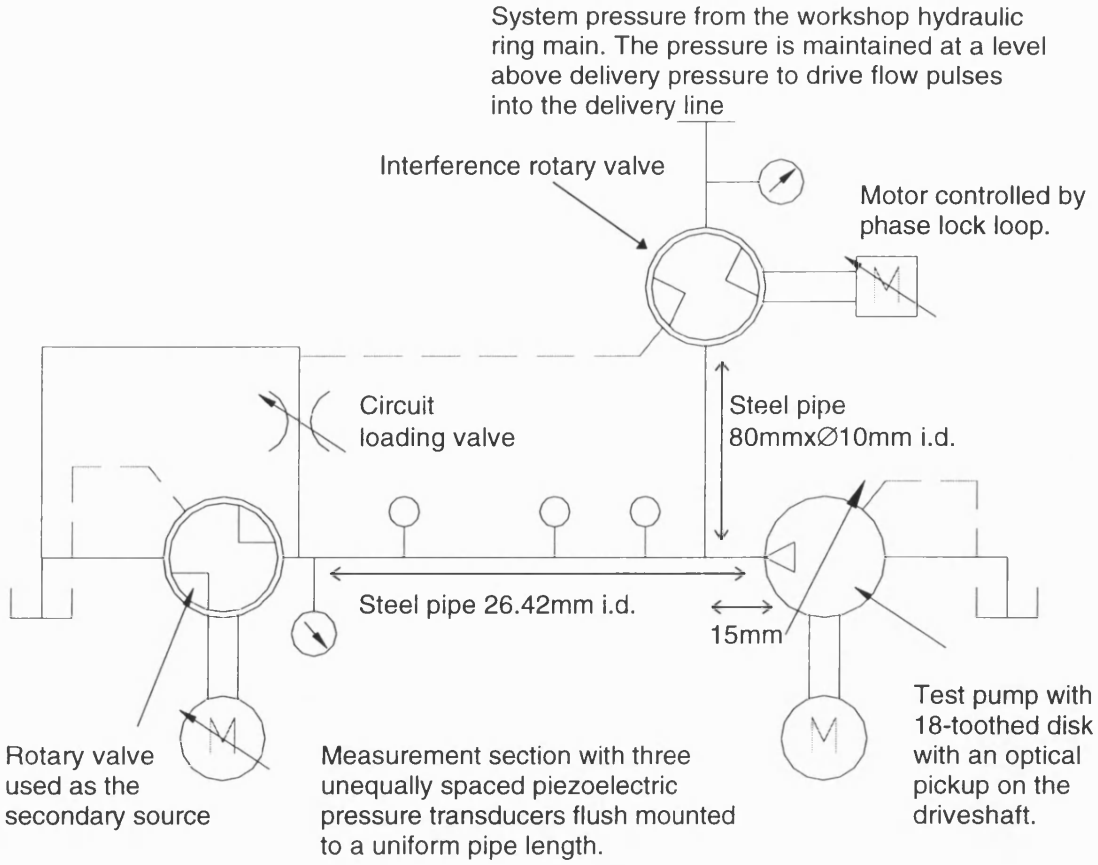

Figure 7.10
Sketch of the test circuit used to produce interference of the test pump flow ripple with the rotary valve supplied from the ring main

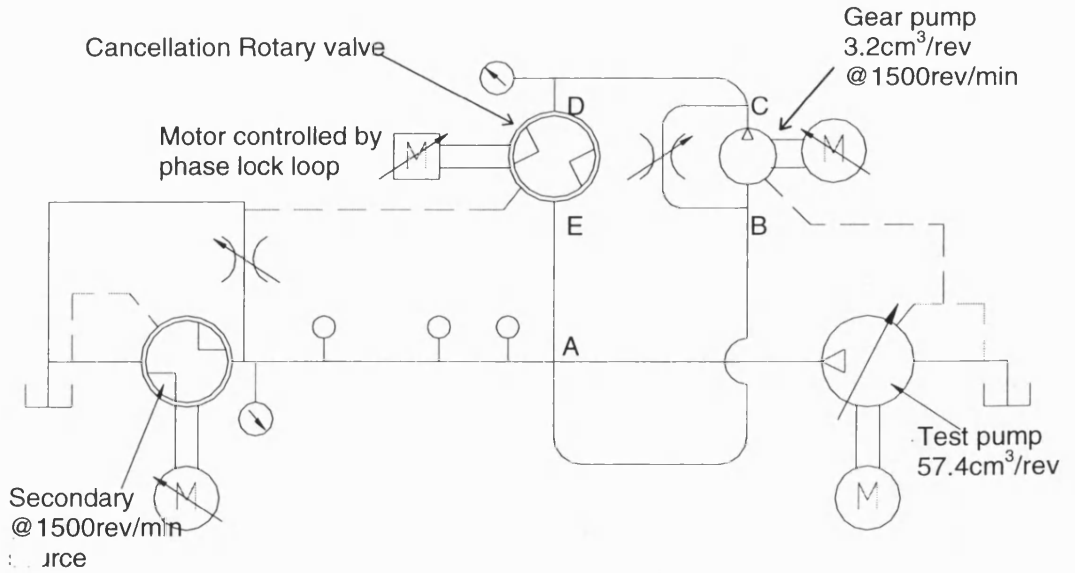

A - B: Flexible hose ∅½"x120mm
B - C: Flexible hose ∅½"x70mm (via restrictor)
C - D: Flexible hose: ∅½"x140mm
E - A: Steel pipe : ∅10mmx80mm

Figure 7.11
Sketch of the test circuit used to produce interference of the test pump flow ripple with the rotary valve supplied from an ancilliary pump

Flow ripple waveform

Flow ripple harmonic amplitudes

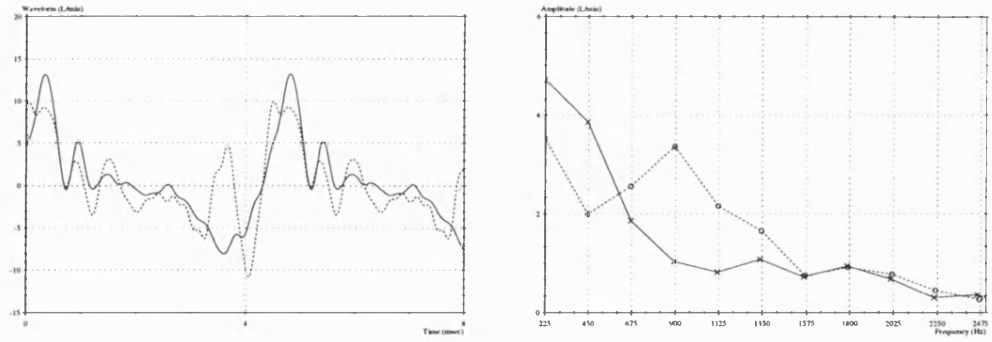

a) Delivery pressure 50 bar
Ring main pressure 60 bar

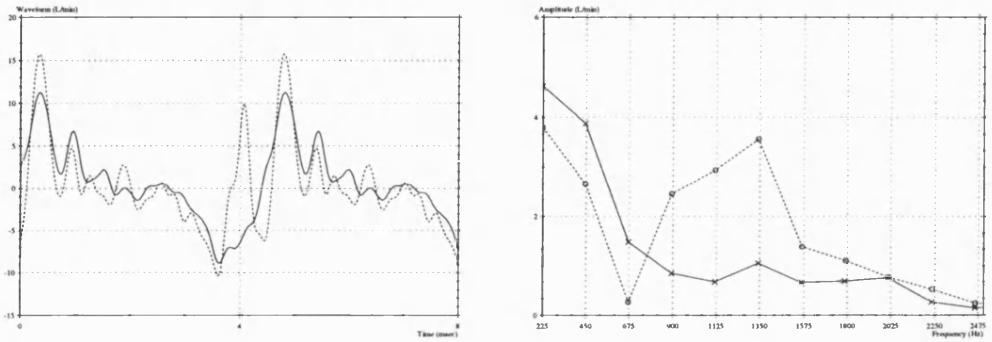

b) Delivery pressure 100 bar
Ring main pressure 115 bar

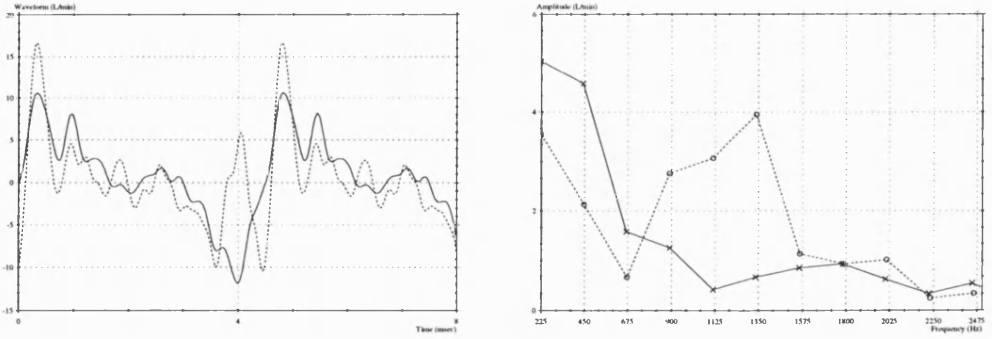

c) Delivery pressure 150 bar
Ring main pressure 165 bar

——————— Branch flow ripple from the test pump with no interference
- Branch flow ripple from the test pump with interference

Figure 7.12a - c
Comparison of the flow ripple measured at the circuit branch with and without interference from the rotary valve supplied by the ring main

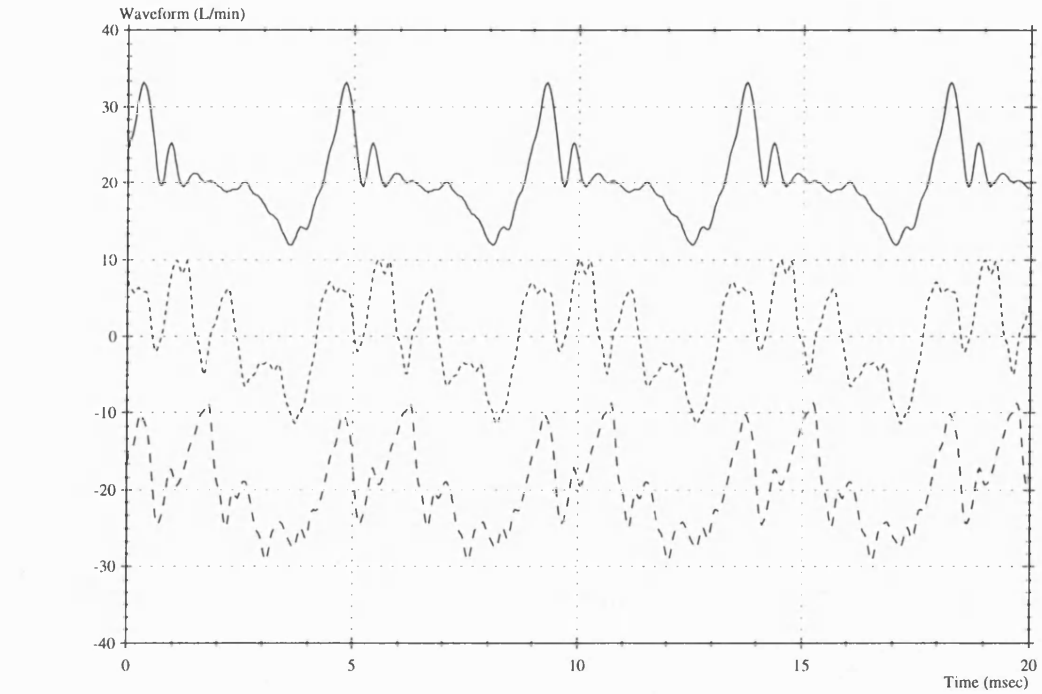

Test pump @ 100 bar delivery, full displacement
Mod 4 P1 120 bar P2 100 bar @ 225Hz **(phase 1)**
Mod 4 P1 120 bar P2 100 bar @ 225Hz **(phase 2)**

Figure 7.13
Comparison of the flow ripple measured at the circuit branch with and without interference from the rotary valve supplied by the ancilliary pump

8.0 Simulation and Design of the HDCV concept

8.1 Introduction

This chapter discusses the work carried out to design a prototype and an accurate simulation model of the Heavily Damped Check Valve (HDCV) concept (See 6.3.4.5).

The design process is described that led to the original prototype scheme. From this initial design, the Bathfp "Dual Cylinder" model (See 4.3.4) was adapted to predict the behaviour of the prototype over a range of pump operating conditions. From initial simulations using the new model, suitable physical parameters for the first prototype were chosen.

The prototype design was manufactured as a modification to the Vickers test pump (See Appendix C). Once fabricated, then a development process was undertaken to minimise the delivery flow ripple from the modified pump over a wide range of operating conditions. This work is reported in chapter 9.

8.2 Design of the HDCV Prototype

This section shows how the HDCV concept was adapted into a prototype design, based upon the Vickers test pump.

8.2.1 Requirements of the HDCV Prototype

1 Reduce the flow ripple from the test pump over a wide range of operating conditions. The operating range is defined as;

Delivery Pressure	50 to 250 bar (gauge)
Suction Pressure	0 bar (gauge)
Pump Displacement	20 to 100%
Pump Speed	1000 to 2000rev/min.

2 Reduce the airborne noise from the pump casing over the same operating range.

3 Design for ease of manufacture. Specifically the prototype should contain a minimum number of machined parts, and should avoid close tolerances that would significantly increase production costs.

8.2.2 The Need for a Heavily Damped Check Valve

The HDCV concept uses the principle of a check valve placed ahead of a late delivery port to equalise cylinders with the delivery pressure (See figures 8.1a and 8.2a). When cylinders then meet the delivery port, rapid cylinder flows are avoided and the pump delivery flow ripple is relatively small.

The particular need for a heavily damped check valve can be explained by first assuming that the check valve behaviour is ideal: it opens instantly when the cylinder pressure exceeds the delivery pressure.

The piston motion at the start of the delivery stroke causes the cylinder pressure to rise towards the delivery pressure. Because the delivery port opens relatively late then the cylinder pressure rises above the delivery pressure. At this point the cylinder pressure causes the check valve to crack open and the ensuing flow through the valve keeps the pressure within the cylinder close to that of the delivery port until the two meet. When the cylinder has passed over the check valve then leakage between the portplate and cylinder block causes the pressure within the portplate check valve drilling to drop and the valve closes in time for the next cylinder to arrive.

The principle of using the action of a check valve ahead of a delayed delivery port is promising; the valve responds directly to the relative pressures of the cylinder and delivery port, and so inherently responds to changes in the pump operating condition.

A check valve could also be placed ahead of a delayed suction port to reduce flow ripple within the suction line. In this case the check valve would act to equalise cylinders to the suction pressure before they meet the suction port. In this case, the check valve would open when the cylinder pressure drops below the suction pressure, and so would be the opposite sense to the check valve used ahead of the delivery port. However, if the pump is unboosted then the maximum pressure difference available to open the valve would be 1 bar: in this case it is unlikely that the check valve could open quickly enough to allow a flow from the suction port to prevent cavitation within the cylinder. For this reason, it is unlikely that a check valve ahead of a delayed suction port would be viable.

Real check valves exhibit inertia effects that present a number of problems. The flow through the check valve between the cylinder and the delivery port will typically occur over a period of a few milliseconds, and so may be severely limited by fluid inertia. In this case the flow through the valve may be insufficient to prevent the cylinder pressure from rising significantly above the delivery pressure.

Real check valves also present noise and wear problems: The rapid switching action of the moving valve element between its end stops is likely to cause the valve to fatigue, and may also cause significant additional structureborne noise from the pump casing (See 6.3.4.4).

To overcome the shortcomings of real check valves, but still retain a self-tuning characteristic, the check valve could be heavily damped (See fig. 8.2b). In this case, the check valve would not respond quickly enough to open and close with each cylinder cycle. Instead, the check valve could be designed to respond to changes in the pump operating condition over a longer duration. If, for a nine cylinder pump operating at 1500rev/min, the check valve was damped to react over one second then this would imply a transient duration of 225 cylinder cycles. In this way the noise, wear and limited fatigue life problems of the undamped check valve would be alleviated.

8.2.3 Operation of the HDCV Concept

At a given pump operating condition, increased damping should cause the moving valve element to settle about a mean opening position and effectively act as a variable

restrictor. Delivery pressure and the compression spring will act to close the valve, and cylinder pressure will act to open the valve (See fig. 8.2b). Flow forces are less predictable, but at small valve openings they will act to close the valve and at larger openings, they will act to open the valve (See 8.3.1.5) . For the valve to be responsive to changes in pump operating condition, it should be designed so that the pressure forces are dominant.

To investigate the valve pressure forces, the effect of fitting a single HDCV to the test pump was considered. Figure 8.1b illustrates the portplate for this scheme.

Each cylinder port overlaps the valve port between 15 and 50° past BDC. The valve would be designed to equalise the pressure at the cylinder port to that of the delivery port for the point where the two ports meet; at 45° past BDC. The optimum valve performance would successfully mimic the action of a delivery port which was optimally delayed for each operating condition. Assuming this optimum performance, then the rise in cylinder pressure for three pump operating conditions would be as illustrated in figure 8.3a. The equivalent HDCV port pressures caused by successive cylinders for these conditions are shown in figure 8.3b.

As can be seen from figure 8.2b, delivery pressure is constantly acting to close the valve. For the 50 bar delivery pressure and 100% displacement condition, the port pressure is always greater or equal to the delivery pressure , and so there is likely to be a net opening force acting on the valve element. However, at the lower displacement and higher delivery pressure conditions, the port pressure drops significantly below the delivery pressure and so the valve is likely to experience a much greater net closing force.

The port pressures illustrated in figure 8.3b neglect the action of the compression spring. For the valve element to be in equilibrium at some opening, then the closing force from the compression spring will be balanced by a mean port pressure that is higher than the delivery pressure. Therefore, as each cylinder passes over the open valve port, it will be over-compressed until it reaches the delivery port, where the cylinder pressure will equalise to the delivery pressure. This over-compression is unavoidable, and is dictated by the spring force at a given valve opening. This effect will reduce the pump mechanical efficiency as it increases the necessary pump input torque. For this reason the stiffness of the valve spring should be minimised.

From this study, it can be concluded that the mean valve opening force increases with pump displacement and decreases with delivery pressure. The combined valve opening action at higher pump flows, and valve closing action at higher delivery pressure constitutes the self-tuning action of the HDCV. Through the self-tuning action, the HDCV opens at conditions requiring early delivery timing, and closes at conditions requiring late delivery timing.

At the most delayed delivery timing specified (250 bar delivery pressure, 20% displacement) then the HDCV will be fully closed. Conversely, at the least delayed delivery timing specified (50 bar, 100% displacement) then the HDCV will be fully open. However, the difference in optimal delivery port delay between these two points may be as high as 20° or 30°. Accordingly, it may not be possible to approach optimal cylinder compression throughout

the specified operating range using a single HDCV. Instead it is more likely that a set of HDCVs would be needed, placed on the cylinder port p.c.d., ahead of the delayed delivery port (See fig. 8.4 which illustrates a double valve arrangement).

The potential benefit to be gained from using a set of HDCVs can be illustrated by using the example of a pump featuring two HDCVs. At high delivery pressure and low pump displacement the required delivery timing is most delayed, and both HDCVs will be closed. As the delivery pressure drops, then the HDCVs will progressively open: The later HDCV will open first, and then as the delivery pressure drops further, the earlier HDCV will open.

For the pump using two HDCVs, the progressive opening action effectively gives the delivery port three different starting points. At pump operating conditions with optimal delivery port delays (See 3.2.2) which correspond to these three delivery starting points, then optimal pre-compression will be achieved. Ideally, a large number of HDCVs would be desirable as this would allow optimal pre-compression for a large number of operating points. However, the available space ahead of the delayed delivery port is limited so a large number of HDCVs will reduce the size of each individual HDCV. This use of smaller HDCVs would then increase fluid inertia effects and may reduce the overall HDCV flow to cause cylinders passing over the HDCVs to over-compress.

The major difficulty with the HDCV concept is in applying the correct level of damping to the moving valve elements. If too much damping is applied then the valve response will be slow and transiently the pump will become noisy during and following changes in operating condition. If too little damping is applied then the valve element will switch rapidly like the undamped check valve. One way to reduce the responsiveness of the moving valve elements is to increase their mass. However, to vary the responsiveness of such a valve would mean re-designing the whole valve to accommodate a different sized valve element.

A more practical method for damping the valve element is to restrict the flow between the valve spring chamber and the delivery chamber using a long, narrow damping orifice (See figure 8.5). In this case, if the valve experiences a rapid closing force then the valve element will move to increase the spring chamber volume. However, the restriction of the damping orifice would cause the spring chamber pressure to drop to create a pressure difference across the valve element which would act to oppose its movement.

Damping orifices were chosen to provide the damping for the HDCV concept. The damping for each HDCV was then varied by changing the length and diameter of the damping orifice used to connect the HDCV spring chambers with the delivery port.

8.2.4 Test Pump Design Constraints

The HDCV prototype was designed as a modification to the Vickers test pump, based on the concept scheme shown in figure 8.5. For this modification, it was envisaged that two components would be re-designed; the portplate, and the valve block (See Appendix C). However, the existing design of the test pump imposed a number of constraints on the design

of the HDCV prototype. Before the HDCV modifications could be carried out then these specific design constraints had to be taken into account.

8.2.4.1 Design Constraints of the Portplate

A new portplate had to be manufactured featuring a number of drillings for the HDCVs ahead of a delayed delivery port. The suction port would be unchanged to allow a fair comparison with the unmodified test pump.

The suction port of the test pump ends at only 6.5° before BDC. The cylinder port subtends an angle of 31.75° (See Appendix C) and so the leading boundary for HDCV portplate drillings is at 25.25° past BDC. Any HDCV portplate drilling before this point would allow flow from a cylinder at high pressure into the suction port.

8.2.4.2 Design Constraints of the Cylinder Block

A further constraint to the design of the HDCV prototype is evident from the distance between adjacent cylinder ports within the cylinder block. If a HDCV drilling within the portplate is large enough to allow a flow path between two adjacent cylinder ports, then a cylinder at delivery pressure could pressurise a following cylinder passing over BDC. This would cause the second cylinder to over-compress (See figure 8.6). For the test pump, the spacing between adjacent cylinder ports is 5mm, and this sets the maximum diameter of the HDCV drillings within the portplate.

To minimise the effects of fluid inertia, the maximum diameter of 5mm was chosen for the HDCV portplate drillings. The angle subtended by a 5mm HDCV port on the cylinder port p.c.d. is 8°.

8.2.4.3 Design Constraints of the Valve Block

The valve block is a casting which houses the portplate, and which contains the delivery and suction chambers (See Appendix C). It was decided that an existing valve block would be machined to contain the HDCV assemblies in the region between BDC and the delivery chamber

The form of the valve block casting in the region between BDC and the delivery chamber placed a number of constraints upon the size and position of each HDCV assembly:

1 The delivery chamber starts at approximately 50° from BDC.

2 The depth of the valve block casting in this region is only 25mm.

The first constraint implies that the trailing boundary for HDCV portplate drillings is at 50° from BDC. Previously, the leading HDCV boundary has been set to 25.25°, and the subtended angle of each HDCV drilling has been set as 8° (See 8.2.4.1 and 8.2.4.2). Consequently, the HDCV portplate drillings can only fall within a 24.75° sector and there is only enough space for three HDCV portplate drillings. However, the HDCV mechanism under the portplate is likely to overlap the drilling diameter, and so realistically there is only space for two HDCV portplate drillings.

The casting depth limits the size of each HDCV assembly. It also restricts the routing of the drillings needed to contain the damping orifices (See figure 8.5).

One problem is that of the alignment between the HDCV drillings in the portplate and the HDCV assemblies housed within the valve block. The necessary alignment was achieved by housing the HDCV assemblies within blank holes in the valve block that were drilled on the same centreline as the HDCV drillings through the portplate.

8.2.4.4 Design Constraints of the Pump Delivery Timing

The goal of the HDCV prototype was to achieve optimal cylinder pre-compression for the test pump for delivery pressures of 50 to 250 bar, and for mean pump flows between 20 and 100% of the pump displacement (See 8.2.1). If cylinder leakage is ignored then the optimal delivery port delay for different pump operating points can be calculated using equation 3.9:

$$\varphi = \frac{\sigma}{2} + \cos^{-1}\left[1 - \left(\frac{P_{del} - P_{suc}}{B_{eff}}\right)\left(\frac{L_{mean}}{RX\tan\beta} + 1\right)\right] \qquad (3.9)$$

However, for the particular case of the unboosted test pump, this equation must be modified. Specifically, the cylinder ports do not leave the suction port until 9.375° past BDC (See 8.2.4.1). This gives a new expression for the optimal delivery port delay:

$$\varphi = \frac{\sigma}{2} + \cos^{-1}\left[\cos(9.375) - \left(\frac{P_{del}}{B_{eff}}\right)\left(\frac{L_{mean}}{RX\tan\beta} + \cos(9.375)\right)\right] \qquad (8.1)$$

Where $\sigma = 31.75°$, $L_{mean} = 35.45mm$, $R = 34.775mm$.

The values of optimal delivery port delay from equation 8.1 were checked using the "Dual Cylinder" simulation model. Throughout the pump operating range the simulation suggested that the cylinders would over-compress using the delivery port delays calculated with equation 8.1. This is because the initial overlapping area between the cylinder and delivery ports is small and so offers a restriction that is not accounted for in equation 8.1. By trial and error, the simulation model was used to find more suitable optimal delivery port delays. In general the values optimised by simulation were about 2° earlier than those predicted by equation 8.1. Table 8.1 shows the optimal delivery port delays found from simulation with B_{eff}=11000 bar:

Table 8.1

	Delivery Pressure (bar)				
	50	100	150	200	250
Pump Displacement (%)	φ (degrees)				
100	28.0	32.3	35.2	37.9	40.0
80	29.0	33.8	37.0	39.7	42.8
60	30.7	35.8	39.7	43.1	46.5
40	33.2	39.5	44.4	48.9	52.9
20	39.0	48.1	55.4	61.8	67.2

To achieve optimal cylinder compression at the 250 bar, 20% displacement condition then both of the HDCVs (See 8.2.4.3) would be closed. This sets the delay of the prototype portplate delivery port to 67.2°.

To achieve optimal cylinder compression at the maximum power condition of 250 bar and 100% displacement then the second HDCV would be open, and the first HDCV would be closed. This sets the delay of the late HDCV portplate drilling to 40°. To achieve optimal pre-compression at the 50 bar, 100% displacement condition, then the delay of the earlier HDCV drilling should be 28°.

8.2.5 Detail Design of the HDCV Prototype

By accounting for the constraints imposed by the design of the test pump (See 8.2.4), a first attempt was made to design an easily-fabricated and robust HDCV prototype. The main elements of the design are illustrated in figure 8.7.

The prototype scheme features 2 HDCVs which are fitted in-between modified versions of the test pump portplate and valve block. Each HDCV assembly consists of a sleeve and matched poppet, a compression spring, and a damping orifice insert and fitting. The details of the design are presented in Appendix E.

8.3 Simulation of the HDCV Prototype

This section describes the digital computer model used to simulate the behaviour of the HDCV prototype (See 8.2 and Appendix E).

The HDCV model was developed from the "Dual Cylinder" model used to simulate the behaviour of conventionally-designed axial-piston pumps (See 4.3.4). Figure 4.9b shows the main elements of the "Dual Cylinder" model, and figure 8.8 shows the equivalent elements of the HDCV model. In figure 8.8, only one HDCV is shown, although the effect of up to four HDCVs can be simulated. Sketches of the prototype design superimposed with the simulation variables of figure 8.8 are presented in figures 8.9a and b.

Each HDCV is simulated as three elements; the port volume between the cylinder and sleeve port; the spring chamber volume, and the spring-loaded poppet. For each HDCV, these elements interact with the pressures and flows from the original "Dual Cylinder" model. The resulting simulation is much more complex. The original model uses 4 differential equations to calculate the pressures and flows within the pump cylinders. For the HDCV model to additionally simulate the behaviour of four HDCVs, then it must manipulate a further 24 differential equations.

The next sections describe the arrangement of the system equations within the HDCV model. Typical results from the model are then analysed using these system equations. Finally, measures that were taken to speed up the simulation process are outlined.

8.3.1 The Equations of the HDCV model

8.3.1.1 The Pump delivery flow

The pump delivery flow from the "Dual Cylinder" model for a pump with no HDCVs is described by equation 4.15 (See 4.3.4.4). For a pump with p HDCVs, then equation 4.15 is expanded is to include flow terms from the sleeve port and the damping orifice of each HDCV:

$$\begin{aligned} totalq = &\sum_{i=1}^{i=n} q_{kin}\left(\omega t + \frac{2\pi i}{n}\right) - \left(q_{del}(\alpha) + q_{kin}(\alpha)\right) - \left(q_{del}(\beta_l) + q_{kin}(\beta_l)\right) \\ &- \sum_{i=1}^{i=n} \frac{2}{n}\left(K_{LC} P_{cyl}(i)^n\right) + \sum_{k=1}^{k=p}\left(q_x(k) + q_d(k)\right) \end{aligned} \qquad (8.2)$$

The contribution of q_d and q_x is illustrated in figures 8.9a and b and defined in 8.3.1.3.

8.3.1.2 The Cylinder Volumes

The differential equations for the cylinder pressure and flow to the delivery port are unchanged from the "Dual Cylinder" model (See 4.3.3.4)

$$P_{cyl} = \int \frac{B_{eff}}{V_{cyl}} q_{net} dt \qquad (4.1)$$

$$q_{del} = \int \frac{P_{del} - P_{cyl} - P_{orif}}{\rho \Gamma_{del}} dt \qquad \text{where;} \qquad (4.5)$$

$$P_{orif} = \left(\frac{q_{del}}{C_q A_{del}}\right)^2 \frac{\rho}{2} \qquad (4.6)$$

$$\Gamma_{del} = \Gamma_{cyl} + \Gamma_{gr} \quad \text{where} \qquad (4.7)$$

$$\Gamma_{cyl} = V_{cyl}/A_P^2 \quad \text{and} \quad \Gamma_{gr} = \int_{x2}^{x1} \frac{1}{a} dx \qquad (4.8 \text{ and } 4.9)$$

For the "Dual Cylinder" model the cylinder flow summation is given by;

$$q_{net} = q_{suc} + q_{del} + q_{pist} - q_{leak} \qquad (4.14)$$

However, the cylinder flow summation is different for the HDCV model;

$$q_{net} = q_{suc} + q_{del} + q_{pist} - q_{leak} - \sum_{j=1}^{j=m} q_p(j) \qquad (8.3)$$

Where Σq_p is the cylinder outflow to the port volume of m HDCVs that overlap the cylinder port (See fig. 8.9b). B_{eff} is assumed to be 11000 bar and C_q assumed to be 0.7 (See 4.3.4)

8.3.1.3 The HDCV Port Volumes

Similar equations to those used for the cylinder volume are used to calculate the pressures and flows within each HDCV port volume:

$$P_{port} = \int \frac{B_{eff}}{V_{port}} q_{pnet} dt \qquad \text{where} \qquad (8.4)$$

$$V_{port} = A_{pop}\left(L_{port} + x\right) \qquad \text{and from figure 8.9b;} \qquad (8.5)$$

$$q_{pnet} = q_p - q_x - q_l - vA_{pop} \qquad (8.6)$$

q_p is the HDCV port volume inflow from the overlapping cylinder port. q_x is the port volume outflow to the delivery port. q_l represents the leakage through the poppet-sleeve clearance from the port volume to the spring chamber volume. vA_{pop} is the flow term due to the motion of the spring-loaded poppet. For the flow between the cylinder port and the HDCV port volume;

$$q_p = \int \frac{P_{cyl} - P_{port} - P_{orifp}}{\rho I_P} dt \tag{8.7}$$

$$P_{orifp} = \left(\frac{q_p}{C_{qp} A_{orifp}} \right)^2 \frac{\rho}{2} \tag{8.8}$$

Where A_{orifp} is the flow area between the cylinder port and the HDCV drilling in the portplate. For the flow through the sleeve ports, between the HDCV port volume and the delivery port;

$$q_x = \int \frac{P_{port} - P_{del} - P_{orifx}}{\rho I_X} dt \qquad \text{and} \tag{8.9}$$

$$P_{orifx} = \left(\frac{q_x}{C_{qx} A_{orifx}} \right)^2 \frac{\rho}{2} \tag{8.10}$$

Where A_{orifx} is equivalent to the area of the circular sleeve port left uncovered by the poppet and so is a function of the poppet displacement (or sleeve port opening), x:

$$A_{orifx} = 2\left[\frac{\pi r^2}{2} + (x-r)\sqrt{r^2 - (x-r)^2} + r^2 \sin^{-1}\left(\frac{x-r}{r} \right) \right] \tag{8.11}$$

The fluid inertia terms, I_x and I_p are modelled by analogy with the single cylinder model with each based upon half the inertia of the fluid within the HDCV port volume. Both are multiplied by a factor, K_i, so that effects of fluid entrainment can be taken into account:

$$I_p = I_x = K_i V_{port} / 2A_{Pop}^2 \tag{8.12}$$

The flow coefficients C_{qp} and C_{qx} are assumed to take the value of 0.7, and K_i is set to 3 (from the results of initial simulations).

8.3.1.4 The Spring Chamber Volumes

Similar equations to those used for the cylinder and HDCV port are used for the pressure in the spring chamber:

$$P_{ch} = \int \frac{B_{eff}}{V_{ch}} q_{chnet} dt \qquad \text{where} \tag{8.13}$$

$$V_{ch} = A_{pop}(K_{ch} L_{ch} - x) \tag{8.14}$$

$$q_{chnet} = vA_{pop} + q_l - q_d \tag{8.15}$$

L_{ch} is the length of the spring chamber when x=0. K_{ch} is a factor used to simulate the effect of different spring chamber volumes. Laminar flow is assumed through the damping orifice. Hagen Pouseuille's equation gives,

$$q_d = \left(\frac{\pi D_{damp}^4}{128 \mu L_{damp}} \right) [P_{ch} - P_{del}] \tag{8.16}$$

The clearance between the matched poppet and sleeve (h) is 0.006mm and so the leakage flow through this clearance is assumed to be laminar. Reynolds equation was used;

$$q_l = \pi D_{pop}\left[\frac{h^3}{12\mu}\frac{dP}{dx} - \frac{vh}{2}\right] \tag{8.17}$$

However, ($\pi D_{pop} vh/2$) has already been taken into account with the vA_{pop} term of equation 8.15 and dP/dx is assumed to take the value of $(P_{port} - P_{ch})/L_{pop}$ and so;

$$q_l = \pi D_{pop}\left[\frac{h^3}{12\mu}\frac{(P_{port} - P_{ch})}{L_{pop}}\right] \tag{8.18}$$

8.3.1.5 The Spring-Loaded Poppets

The acceleration of the spring-loaded poppet is found by summing the different forces acting on the poppet. The poppet acceleration is then integrated to calculate the poppet velocity, and integrated again to give the poppet displacement:

$$v = \int \frac{F_x}{M_{pop}} dt \tag{8.19}$$

$$x = \int v\, dt \tag{8.20}$$

The poppet displacement x, is taken to be the axial distance between the top face of the poppet and the cracking point on the sleeve port (See figure 8.9a). x is positive when the poppet moves to uncover the sleeve port, and is negative when the poppet closes the sleeve port and moves into the overlap region. The net axial force acting on the poppet to open the sleeve ports F_X, has the following components:

$$F_x = F_p + F_s + F_f - F_r(\text{sign}(v)) \tag{8.21}$$

F_P The differential pressure force acting on the axial faces of the poppet

F_s The compression spring force (acting to close the sleeve ports)

F_f The sum of flow forces

F_r The sum of friction forces opposing the motion of the poppet.

The differential pressure force (F_P) is given by

$$F_p = (P_{port} - P_{ch})A_{pop} \tag{8.22}$$

The spring force (F_S) is given by

$$F_s = -(K_p + K_s x) \tag{8.23}$$

Where K_P is the force exerted by the spring when x = 0

The sum of flow forces (F_f) is found from the reaction on the poppet due to the net force acting on the fluid passing through the sleeve port. Figure 8.10 illustrates the case of fluid passing through the sleeve port from the HDCV port volume to the delivery port:

Initial Fluid Momentum = $\rho Q v_1$

Final Fluid Momentum = $\rho Q v_2 \cos\zeta$ (ζ was assumed constant as 69°)

Where $v_1 A_{pop} = v_2 A_{orifx}$ therefore,

$$\text{Net force on fluid} = -F_f = \rho Q v_2\left(\cos\zeta - \frac{A_{orifx}}{A_{pop}}\right) \tag{8.24}$$

Q and v_2 come from the orifice equation. Also, when A_{orifx} is small then the flow force acts on the poppet to close the sleeve port irrespective of the direction of flow. Therefore, the sum of flow forces is given by;

$$F_f = C_{qx} A_{orifx} \left(\frac{A_{orifx}}{A_{pop}} - \cos\zeta \right) \left| (P_{port} - P_{del}) \right| \tag{8.25}$$

The friction force (F_R) is made up from three components; stiction, coulomb friction, and speed-dependent friction.

When $v = 0$ $\quad F_r = F_{stict}$ (8.26)

When $v \neq 0$ $\quad F_r = F_{coul} + F_{sdfc} v$ (8.27)

The friction terms were difficult to quantify: 0.2N was estimated for the stiction force (from a simple test using a spring balance), and this value was also used for the coulomb friction term. The speed-dependent friction term was set to zero since this effect is dominated by the action of the damping orifice.

8.3.2 Simulation Results for the HDCV Prototype

In this section, simulation results from the HDCV model are analysed. Steady state and dynamic characteristics for the HDCV poppets are derived from the model equations. These characteristics are then compared with simulation results. This comparison is carried out for a range of displacements and delivery pressures for the unboosted pump at 1500rev/min.

The simulated transient performance of the HDCVs is compared for two operating conditions. The cylinder pressure and delivery flow at these conditions are then compared with that simulated for the unmodified test pump.

8.3.2.1 Simulation Parameters

All of the simulations in this section are based upon the HDCV prototype design shown in figure 8.11. For this design both of the HDCV assemblies are identical. Parameters not shown in figure 8.11 are listed in table 8.2:

Table 8.2

Parameter		Variable Name	Value
Effective Fluid Bulk Modulus	bar	B_{eff}	11000
Fluid dynamic viscosity	Ns/m^2	μ	0.04
All flow coefficients	-	C_q, C_{qp}, C_{qx}	0.7
Stiction/Coulomb Friction	N	F_{stict}, F_{coul}	0.2
Spring Rate	N/m	K_s	3.33
Spring Preload (@ x=0mm)	N	K_p	7.992
Sleeve Port Inertia Factor	-	K_i	3
Spring Chamber Volume Factor	-	K_{ch}	4
Poppet length	mm	L_{pop}	10.7
Poppet Mass	Kg	M_{pop}	0.003
Poppet Diameter	mm	D_{pop}	5.5
Sleeve Port Diameter	mm	D_{port}	3.6
Damping Orifice Diameter	mm	D_{damp}	0.4
Damping Orifice Length	mm	L_{damp}	8
Cylinder Port Pitch Circle Radius	mm	R	34.78
Mean Effective Cylinder length	mm	L_{mean}	35.45
Swashplate included angle at full flow	mm	β	17.5°
Poppet-Sleeve radial clearance	mm	h	0.006

8.3.2.2 Steady State Poppet Characteristics

The net opening force acting on a HDCV poppet is given by equation 8.21. Under steady state conditions then v = 0 and $F_x = 0$ and so,

$$F_p = -(F_s + F_f) \tag{8.28}$$

Substituting equations 8.22, 8.23 and 8.25 then,

$$(P_{port} - P_{ch})A_{pop} = K_p + K_s x - K_f(x)\left|(P_{port} - P_{del})\right| \qquad \text{where} \tag{8.29a}$$

$$K_f(x) = C_{qx} A_{orifx}\left(\frac{A_{orifx}}{A_{pop}} - \cos\zeta\right) \qquad (\zeta = 69°)$$

However, if $P_{port} < P_{del}$ at steady state then $K_f(x)$ will be zero as the port will be shut. When the port is open:

$$(P_{port} - P_{ch})A_{pop} = K_p + K_s x - K_f(x)(P_{port} - P_{del}) \tag{8.29b}$$

The net inflow to the spring chamber is given by the following expression (See 8.3.1.4):

$$q_{chnet} = vA_{pop} + q_l - q_d \tag{8.15}$$

Under steady state conditions then v = 0 and qchnet = 0 and so,

$$q_d = q_l \tag{8.30}$$

Therefore, from equations 8.17, 8.18 and 8.30,

$$P_{ch} = \frac{K_l P_{port} + K_d P_{del}}{(K_d + K_l)} \tag{8.31}$$

Where $K_d = \dfrac{D_{damp}{}^4}{128\, L_{damp}}$ and $K_l = \dfrac{D_{pop} h^3}{12 L_{pop}}$

From equations 8.29b and 8.31,

$$P_{port} - P_{del} = \frac{(K_p + K_s x)(K_d + K_l)}{K_d A_{pop} + K_f(x)(K_d + K_l)} \tag{8.32}$$

Therefore, under steady state conditions, a given port opening corresponds to a particular pressure drop through the HDCV. This characteristic is shown in figure 8.12a. Using this characteristic then the flow force can be expressed in terms of the port opening from equations 8.29b and 8.32:

$$F_f = \frac{K_f(x)(K_p + K_s x)(K_d + K_l)}{K_d A_{pop} + K_f(x)(K_d + K_l)} \tag{8.33}$$

The flow force calculated from this expression is displayed with the corresponding spring force as a function of sleeve port opening in figure 8.12b. From figures 8.12a and b, it can be seen that the cracking pressure of the HDCV is approximately 3.4bar. Furthermore, the closing force from the compression spring is much larger than that caused by flow forces. The flow forces only become significant at larger sleeve port openings where they cause a significant opening force on the poppet.

The leakage path between the poppet and sleeve is much more restrictive than that through the damping orifice. From the parameters of 8.3.2.1 then,

$$\frac{K_d}{K_l} \approx 2700$$

So, under steady state conditions, if K_l is ignored then from equations 8.31 and 8.32,

$$P_{ch} = P_{del} \tag{8.34}$$

$$P_{port} - P_{del} = \frac{(K_p + K_s x)}{A_{pop} + K_f(x)} \tag{8.35}$$

Under transient conditions the spring chamber pressure will vary from the delivery pressure. If the HDCV port pressure increases then the poppet will move to reduce the spring chamber volume. In this case the restriction of the damping orifice will cause the spring chamber pressure to rise above the delivery pressure. If the port pressure reduces then the opposite will occur and the spring chamber pressure will drop below the delivery pressure.

8.3.2.3 Dynamic Poppet Characteristics

An understanding of the poppet dynamic response is needed to apply the correct level of damping within each HDCV. Each poppet responds to a variation in the HDCV port pressure which is periodic at the pumping frequency. To examine the valve damping then a transfer function is needed that shows the poppet response to changes in the HDCV port pressure.

From equation 8.21, the poppet motion depends on the spring force, the flow forces, the friction forces and the force caused by the pressure difference between the HDCV port and the spring chamber. However, figure 8.12a shows that the flow forces are small compared to the spring force. So, if the flow forces are ignored along with the friction forces then the dynamic force balance on the poppet can be re-expressed using equations 8.21, 8.22, and 8.23,

$$M_{pop} s^2 x = (P_{port} - P_{ch}) A_{pop} - K_s x \tag{8.36}$$

The pressure in the spring chamber is given by equation 8.13 and can be re-expressed as,

$$sP_{ch} = \frac{B_{eff}}{V_{ch}} q_{chnet} \tag{8.37}$$

and the net flow into the spring chamber can be expressed with equations 8.15, 8.17 and 8.18,

$$q_{chnet} = A_{pop} sx - K_D P_{ch} - K_L (P_{ch} - P_{port}) \quad \text{where} \tag{8.38}$$

$$K_D = \frac{\pi D_{damp}^{\ 4}}{128 \mu L_{damp}} \qquad \text{and} \qquad K_L = \frac{h^3}{12\mu} \frac{\pi D_{pop}}{L_{pop}}$$

From equations 8.36, 37 and 38, then the transfer function for the poppet displacement in terms of the HDCV port pressure can be derived:

$$\frac{x}{P_{port}} = \frac{\frac{A_{pop}}{M_{pop}} \left(s + K_D \frac{B_{eff}}{V_{ch}} \right)}{s^3 + \left((K_D + K_L) \frac{B_{eff}}{V_{ch}} \right) s^2 + \left(\frac{B_{eff}}{V_{ch} M_{pop}} A_{pop}^{\ 2} + \frac{K_s}{M_{pop}} \right) s + \left((K_D + K_L) \frac{B_{eff}}{V_{ch}} \frac{K_s}{M_{pop}} \right)} \tag{8.39}$$

Using the figures from 8.3.2.1 and figure 8.11, then values of this equation can be substituted:

$$\frac{x}{P_{port}} = \frac{7.92 * 10^5 (s + 7390)}{s^3 + 7393 s^2 + 7.094 * 10^8 s + 8.206 * 10^9} \text{mm/bar} \tag{8.40}$$

Where, in steady state, s=0 and,

$$\frac{x}{P_{port}} = \frac{A_{pop}K_D}{K_s(K_D + K_L)} = 0.713\text{mm/bar} \qquad (8.40a)$$

This value for the steady state gain agrees with the gradient of the spring dominated portion of the steady state pressure characteristic plotted in figure 8.12a.

Equation 8.39 can be used to show the effect of changing various design parameters. The Bode diagram for equation 8.40 is shown in figure 8.13a together with the equivalent trace when the poppet mass is increased from 3g to 30g. The effect of the valve damping can be clearly seen where the poppet response at low frequency is over 40dB greater than at the pumping frequency of 225Hz. Between 4 and 5 kHz, the resonance of the poppet can be seen: the increased poppet mass reduces the size of this resonance but has very little effect on the response below 1500Hz.

Figure 8.13b shows the effect on the poppet dynamic response of reducing the spring stiffness from 3330N/m to 333N/m. In this case the poppet response above 10Hz is unaffected. Below 10Hz the poppet response is up to 10 times greater. This may be a problem when the pump is starting up or slowing down; the larger response at these lower frequencies may cause the poppets to hit their endstops very violently and so greatly increase the SBN from the pump casing.

Figure 8.13c shows the effect on the poppet dynamic response of increasing the spring chamber volume by 10 times. The compressibility of the chamber is increased and above 50Hz the valve response is significantly increased. The magnitude of the poppet motion at resonance is also increased and the resonant frequency lowered towards the pumping frequency. In practice then, this would suggest that the spring chamber volume should be kept to a minimum.

Figure 8.13d shows the effect of halving the damping orifice diameter from 0.4 to 0.2mm. As expected (See 8.2.3), this change causes a significant increase in the valve damping. The increase in damping is much greater than that achieved by a tenfold increase in the poppet mass, and the damping effect is broadband, affecting all frequencies up to 2000Hz.

Figure 8.13e shows the effect of increasing the sleeve - poppet radial clearance from 0.006mm to 0.06mm. The main effect of this is to attenuate the poppet response at frequencies below 5Hz. Above this frequency there is very little effect. The fact that the valve behaviour is relatively insensitive to this clearance suggests that the poppet and sleeve can be cheaply manufactured to a low dimensional tolerance.

8.3.2.4 Poppet displacement simulation results

For these simulations, the initial displacement of both HDCV poppets was set to give a sleeve port opening of 1mm. During each simulation run, the force balance on the poppets causes them to move from this initial position to new positions that vary according to the pump delivery pressure and displacement.

The movement of the poppets with time from their initial displacements is shown for the 50 bar delivery pressure, 100% pump displacement condition in figure 8.14a. Figures 8.14b

and c show the variation in port and spring chamber pressure for the two HDCVs (See figure 8.11). Figures 8.15a, b, and c show the equivalent simulation results for the 250 bar delivery pressure, 100% pump displacement condition.

At both conditions there is a periodic variation at the pumping frequency in the port and spring chamber pressures which is caused by the changing pressure of successive cylinders passing over the HDCVs. This pressure variation is greatest for the first HDCV port (at 30° past BDC) at the 250 bar condition. In this case the poppet has moved to close the sleeve port and so the port volume of the HDCV is isolated from the delivery chamber. When a cylinder first overlaps this port, the cylinder pressure is low and so the isolated port de-pressurises sharply from the delivery pressure.

The periodic variation in the port pressure gives rise to a variation in the poppet displacement at the same frequency. At the 250 bar condition, the port pressure of the HDCV at 44° can be approximated to a square wave of 10 bar amplitude at the pumping frequency (See figure 8.16a). This square wave can be described at harmonics of the pumping frequency using Fourier series:

$$P_{port}(\omega) = \frac{2}{\pi}\sum_{n=1}^{n=\infty}\left(\frac{1}{n}\sin\frac{n\pi}{2}\cos(n\omega)\right) \qquad (8.41)$$

The individual harmonics from this expression can then be multiplied by the poppet response from equation 8.40 to arrive at the harmonics of the poppet response resulting from the port pressure square wave input. These harmonics have been summed into a time domain waveform in figure 8.16b and show that the poppet response expected from theory is close to that produced by the simulation.

The Bode diagram of figure 8.13a indicates that first-order behaviour dominates the system response at the lower frequencies. The breakpoint of this response is at 2Hz, which implies a system settling time of 0.33 seconds. However, this disagrees with the simulation model which predicts that the poppets would reach their final positions after approximately 50ms (See figure 8.14a). The likely cause of this discrepancy is the set of assumptions used to linearise the system. In particular the operating point chosen for linearisation assumes zero poppet velocity, and so neglects the action of friction forces: the inclusion of friction forces would likely reduce the settling time of the linearised system and so bring it closer to that predicted by the simulation model.

For both pump operating conditions, the movement of the HDCV poppets from their initial position corresponds to a change in the HDCV port pressure. This process can be seen more clearly by examining values of the HDCV port pressure and poppet displacement that have been averaged over single cylinder cycles. Figures 8.17a and b show the mean values of HDCV port pressure and poppet displacement plotted against the steady state pressure characteristic of figure 8.12a (See 8.3.2.2).

For the 50 bar condition, figure 8.17a shows that initially the pressure force acting to push both poppets down (and open the sleeve ports) is greater than the spring force and the flow forces acting to push the poppets up. This causes the poppets to open the sleeve ports

further until they reach the steady state characteristic. At this point both poppets are oscillating about a mean opening where the mean force from the spring and flow forces is balanced by the mean force from the pressure difference across the poppet. From equation 8.28 this can be described by,

$$\overline{F_p} = -\left(\overline{F_s} + \overline{F_f}\right) \tag{8.42}$$

At the 250 bar condition, figure 8.17b again shows that initially the pressure forces are greater than the spring and flow forces. However in this case the poppet of the first HDCV does not settle on the steady-state characteristic: instead it is forced onto the fully closed endstop at x=-2mm and so the force balance between the pressure, spring and flow forces does not apply.

8.3.2.5 Poppet Force and Pressure simulation results

Figures 8.18a to f show simulation results for the 50 bar condition once the poppets have reached their steady positions. Figures 8.18a, c and e show results for the first HDCV port, and figures 8.18b, d and f show results for the second HDCV port. Each trace is plotted over 80° of cylinder motion, which corresponds to two periods of the pumping frequency (9ms for the 9-cylinder test pump running at 1500rev/min).

Figures a and b show the predicted force acting on each poppet due to the pressure difference between the port and spring chamber. The force from the port pressure is subtracted from the spring chamber pressure to give the net closing force due to the differential pressure across the poppet. This force is compared with the spring and flow forces in figures c and d. Figures e and f show the variation in poppet displacement with cylinder motion. From figures c, d, e, and f it is clear that the variation in differential pressure force is the dominant effect causing the periodic poppet motion.

From figure 8.11 it can be seen that each cylinder port meets the HDCV ports at angles of 10.125° and 24.125° past BDC. Figures a and b show that these points correspond to the lowest port pressure during each cylinder cycle.

Figures 8.19a to f show the equivalent results for the 250 bar condition. Figures 8.19a, c and e show the effect of the endstop on the poppet motion within the first HDCV at the 250 bar condition. The sleeve port is closed and so when a low pressure cylinder arrives then the HDCV port pressure drops well below the delivery pressure (A). The spring chamber pressure does not drop so far due to the restriction of the damping orifice and so the poppet is forced upwards onto its endstop. Once the poppet has stopped then the spring chamber pressure begins to recover due to flow through the damping orifice from the delivery chamber (B). During this time the cylinder pressure rises towards the delivery pressure due to the piston delivery stroke (C). At (D) the cylinder pressure rises above the spring chamber pressure and causes a differential pressure force which is large enough to overcome the preload of the valve compression spring. The poppet moves rapidly from the endstop which then causes the spring chamber pressure to rise higher than the port pressure and so forces the poppet back towards the endstop (E). The subsequent oscillation of the port and spring chamber pressure causes an oscillatory differential pressure force on the poppet which can be seen in figure 8.19c. At (F), the port

pressure drops close to the delivery pressure. This is caused by the cylinder passing over the second HDCV port which is open to the delivery port. This second port is at a mean port pressure that is approximately 4 bar above the delivery pressure. This pressure also acts on the first HDCV port and causes the poppet within this HDCV to move gradually away from the endstop (F - G). At (G), the cylinder has passed over the first HDCV port just before the next cylinder begins its motion over the port (A).

Figure 8.19a shows that the poppet is pushed onto its end stop during each cylinder cycle with a force approaching 400N. This repeated impact force may lead to the generation of significant levels of SBN from the pump casing. Furthermore, the sleeve is a relatively weak component and so eventually will be damaged whilst operating at this condition. To reduce this effect the valve response at the pumping frequency should be attenuated.

8.3.2.6 The Relationship between Port Pressure and Port Opening

The simulation results shown in figures 8.14 to 8.19 were carried out at 25 pump operating points between 50 and 250 bar delivery pressure and between 20 and 100% pump displacement for the unboosted pump running at 1500rev/min. Figures 8.20a and 8.20b show the simulated mean displacement of the two HDCV poppets once they have reached their final positions for these 25 operating conditions.

Figure 8.20a predicts that the first HDCV (at 30°) will only open at low delivery pressure and high pump displacement conditions. Figure 8.20b predicts that the second HDCV port will only close at high delivery pressure and low pump displacement conditions. These predictions agree with the findings of the discussion in 8.2.3.

One feature of both figures is that the poppets are always forced onto their fully-closed endstop when the sleeve ports are closed. The reason for this is that when a sleeve port is closed the minimum HDCV port pressure can drop significantly below the delivery pressure. As long as the sleeve port is open then flow from the delivery port will pressurise the low pressure cylinder and so keep the minimum HDCV port pressure close to the delivery pressure.

In figures 8.20a and b the points on the wire frame are those values of mean poppet displacement predicted by simulation alone. The adjacent shaded points were calculated from the simulated value of the mean HDCV port pressure: if the mean port pressure was below the lowest point on the steady-state characteristic (See fig 8.12a) then the poppet was assumed to be held on the fully-closed endstop at $x = -2mm$. Otherwise, the mean poppet displacement was read from the steady state pressure characteristic (fig 8.12a) for the corresponding value of the simulated mean port pressure. Figures 8.20a and b demonstrate the validity of using the steady state pressure characteristic to predict poppet displacements from mean HDCV port pressures over a range of operating conditions.

The overall form of figures 8.20a and b is caused by the variation in mean HDCV port pressure with delivery pressure and pump displacement. The poppet displacements displayed in these figures are for the poppets once they have reached their equilibrium positions where the mean spring chamber pressure is close to the delivery pressure (See 8.3.2.2): given this

condition, each HDCV port will only be open when the mean port pressure is higher than the delivery pressure by a margin great enough to overcome the spring and flow forces.

To predict the conditions for the HDCV ports to open, it is necessary to find expressions for the mean HDCV port pressures in terms of the pump operating condition. When a sleeve port is closed then the mean HDCV port pressure is straightforward to predict; each closed HDCV port volume is much smaller than a cylinder volume and so the HDCV port pressure can be approximated by that of the cylinder passing over the HDCV port. However, when a sleeve port is open then the HDCV port pressure is more difficult to predict because it depends on the relative flows between the cylinder, the HDCV port volume, and the delivery port. For this reason, the opening of the individual HDCV ports has been predicted using expressions for the HDCV port pressure with the ports closed.

As expected (See 8.2.3), figures 8.20a and b show that the second HDCV port (at 44°) only closes when the first HDCV port is closed. Therefore, to calculate the pressure within the closed second HDCV port, the first HDCV port is also assumed to be closed. In this case, the cylinder pressure over the closed ports will rise until the cylinder meets the delivery port, where the cylinder pressure will then equalise to the delivery pressure. The expression for the mean pressure of the closed HDCV port at 44° is derived in Appendix F and is given by,

$$\overline{P}_{port}(2)=\frac{1}{\kappa_c+\kappa_v}\left[\begin{array}{l}K\left\{c\left(\alpha_d+\alpha_2-\frac{\kappa_v}{2}\right)+\frac{180}{\pi}\left(\sin\left(\alpha_2-\frac{\kappa_v+\kappa_c}{2}\right)-\sin\left(\alpha_d-\frac{\kappa_c}{2}\right)\right)\right\}\\ +P_{del}\left(\alpha_2+\kappa_c+\frac{\kappa_v}{2}-\alpha_d\right)\end{array}\right]$$

Where $K=\dfrac{B_{eff}}{\left(\dfrac{L_{mean}}{RX\tan\beta}+\cos\gamma\right)}$ and $c=\cos\gamma$ (8.43)

Figures 8.20a and 8.20b show that the second port is open for most of the simulated operating conditions. Therefore the mean port pressure of the closed first HDCV is calculated assuming that the second HDCV port is open. In this case, when the cylinder meets the second HDCV then it is assumed that the cylinder pressure equalises to the pressure of this second port. When the cylinder finally reaches the delivery port then the cylinder pressure equalises to the delivery pressure as before. However, the second HDCV is assumed to be open and so its port pressure is unknown. For this reason the pressure of the second HDCV port is assumed to equal the cracking pressure of the valve (See 8.3.2.2). From these assumptions, the mean port pressure of the closed HDCV port at 30° is derived in Appendix F and is given by,

$$\overline{P}_{port}(1)=\frac{1}{\kappa_c+\kappa_v}\left[\begin{array}{l}K\left\{c(\alpha_2-\alpha_1)+\frac{180}{\pi}\left(\sin\left(\alpha_1-\frac{\kappa_v+\kappa_c}{2}\right)-\sin\left(\alpha_2-\frac{\kappa_v+\kappa_c}{2}\right)\right)\right\}\\ +P_{crack}\left(\alpha_1+\kappa_c+\kappa_v-\alpha_2\right)\end{array}\right] \quad (8.44)$$

P_{crack} corresponds to a poppet displacement of x=0 and can be expressed from equation 8.35,

$$P_{crack}=P_{del}+\frac{K_p}{A_{pop}} \quad (8.44a)$$

In both cases, the net pressure force acting to open the p'th HDCV can then be deduced from.

$$F_{net}=\left(\overline{P}_{port}(p)-P_{del}\right)*A_{pop} \quad (8.44b)$$

This net pressure force can be compared with the force needed to overcome the pre-load of the compression spring at x=0 (K_P). From 8.3.2.1, K_P = 7.992N and when F_{net} exceeds this value then the HDCV ports will open.

The net valve opening forces from the mean port pressures calculated with equations 8.43 and 8.44 are compared with those predicted by the simulation model in figures 8.21a and b. In figure 8.21a both graphs show that, for the first HDCV port, the net pressure force exceeds the spring pre-load at conditions of low delivery pressure and high pump displacement. This agrees with figure 8.20a which predicts that the first HDCV port opens at these conditions.

In figure 8.21b, both graphs show that the net pressure force drops below the spring pre-load at conditions of high delivery pressure and low pump displacement. Again this agrees with figure 8.20b which predicts that the second HDCV port closes at these conditions.

The pressure forces predicted using equations 8.43 and 8.44 deviate from the simulated values when the mean port pressures exceed the delivery pressure. This is because at these conditions the higher port pressure causes the sleeve ports to open and so equations 8.43 and 8.44 do not apply. Instead, when the sleeve ports are open, then the mean port pressure lies on the steady state pressure characteristic (as demonstrated with figures 8.20a and b).

In figure 8.21a, at high delivery pressure and low pump displacement conditions, the valve opening force predicted using equation 8.44 is higher than the simulated value. The reason for this is that at these conditions, equation 8.44 assumes the second port to be open when the simulation predicts it to close (See figure 8.20b).

The net pressure forces predicted with equations 8.43 and 8.44 are generally lower than those predicted from simulation. This may be due to a partial cylinder compression caused by the closed HDCV port which remains at high pressure after the previous cylinder has completely passed over. This effect would contribute to the simulated pressure force but not to that predicted from equations 8.43 and 8.44.

With higher spring pre-loads then the valve opening will be smaller for a given HDCV port pressure and spring chamber pressure. However, both figures 8.21a and b show that the spring pre-load of 7.992N is small compared to the variation in the differential pressure forces. This suggests that the closure of the HDCV ports is insensitive to changes in the spring characteristics.

8.3.2.7 Simulated Cylinder Pressure and Flow

In this section, cylinder pressure and delivery flow simulated for the HDCV prototype shown in figure 8.11 are compared with those simulated for the standard pump (See Appendix C). For the comparison, the same two pump operating conditions are used that were analysed in section 8.3.2.4.

The results presented in this section are for the physical situation where the HDCV poppets have reached their final positions (See 8.3.2.2).

Figure 8.22 shows the effect of the two HDCVs upon the pressure and delivery flow of a single cylinder at 50 bar delivery pressure and 100% displacement. The cylinder port meets the first open HDCV having travelled 10.125° from BDC. At this point, the cylinder pressure is lower than the delivery pressure and so there is a reverse flow from the delivery chamber into the cylinder (A). The cylinder pressurises rapidly and overshoots the delivery pressure due to fluid inertia within the HDCV port (B). As the cylinder moves further from BDC, the increasing piston velocity causes an increasing cylinder flow through the HDCV to the delivery port (C - D). As the cylinder flowrate increases, the pressure difference across the HDCV rises which, in turn, causes the cylinder pressure to rise. At 24.125° the pressurised cylinder meets the second open HDCV (D). Most of the cylinder flow then passes through the second HDCV (E). This is because the second HDCV sleeve port is further open than that of the first HDCV (See figures 8.14e and f). The total HDCV flow area has now increased and so the cylinder pressure drops. From (E) to (F) the flow through the two HDCV ports continues to increase which again causes a steady rise in the cylinder pressure. At 49.875°, the cylinder port leaves the first HDCV and so the larger cylinder flow can only pass through the second HDCV port (G). This causes a greater restriction to the cylinder flow and so the pressure difference across the second HDCV rises which causes the cylinder to significantly over-pressurise (H). At 51.375°, the cylinder port meets the delayed delivery port (I). This quickly reduces resistance to the cylinder flow, and allows the cylinder pressure to equalise to delivery pressure (J). During this period, flow through the more restrictive second HDCV port reduces until the cylinder leaves the port at 63.875°.

Figure 8.23 shows the effect of the two HDCVs upon the pressure and delivery flow of a cylinder at the 250 bar delivery pressure and 100% displacement condition. For this condition, only the second port is open (See 8.3.2.4) and so the HDCV flow starts later than for the 50 bar condition: - at 24.125° from BDC. The cylinder pressure is slightly lower than the delivery pressure when the cylinder meets the second HDCV port and so initially there is a small reverse flow (A). However, the overlapping flow area between the cylinder and HDCV ports does not increase quickly enough to prevent the cylinder from over-compressing (B). At (C), the HDCV port fully overlaps the cylinder port and the cylinder pressure drops back close to the delivery pressure. The cylinder flow increases as the cylinder moves from BDC which causes the cylinder pressure to rise gradually, as at the 50 bar condition (C - D). However, the second port is further open than at the 50 bar condition (See figures 8.18f and 8.19f) and so the cylinder does not dramatically over-compress ahead of the delivery port. At 51.375°, the cylinder meets the delivery port which again equalises the cylinder pressure to that of the delivery port (E).

Figures 8.22 and 8.23 show that the contribution to the delivery flow from the damping orifices is small. Furthermore, since the net poppet motion during each cylinder cycle is zero (see 8.3.2.4), then the net damping orifice flow to delivery for each cylinder cycle will be zero.

The pressure and delivery flow of a cylinder within the standard pump for the two operating conditions are shown in figures 8.24 and 8.25. For the standard pump at the 50 bar condition, figure 8.24 shows that the relief groove opens too late to prevent the cylinder from

over-compressing dramatically. Conversely, at the 250 bar condition, figure 8.25 shows that the relief groove opens too early to prevent a relatively large reverse flow from the delivery port into the cylinder.

Figure 8.26 allows a direct comparison between the delivery performance of the HDCVs with that of the relief groove. Figures a,c,and e correspond to simulation results for the 50 bar delivery pressure condition. Figures b,d, and f correspond to simulation results for the 250 bar condition.

Figures 8.26a and b show the total contribution of flow from the HDCVs and the delayed delivery port superimposed on the kinematic flowrate due to the piston motion. Figures 8.26c and d show the flow through the relief groove and the delivery port of the unmodified pump. Figures 8.26e and f compare the rise in cylinder pressure simulated for the HDCVs with that simulated for the relief groove of the standard pump.

At the 250 bar condition, traces b and d show that when the cylinder has pressurised to the delivery pressure the cylinder delivery flow is lower than the kinematic flowrate. This is due to leakage from the cylinder which is simulated using equation 4.14. From this equation at 250 bar the cylinder leakage rate is 0.923L/min, and at 50 bar the rate is 0.064L/min. This is borne out by traces a and c where at 50 bar delivery pressure the difference between the delivery flow and the kinematic flow becomes very small.

From these traces it is clear that the HDCVs provide a more controlled cylinder pressurisation than the relief groove. Also the contribution to the delivery flow from the pump fitted with the HDCVs is much more gradual and so is likely to give rise to a lower level of delivery flow ripple.

8.3.2.8 Simulated Pump Delivery Flow Ripple

In this section, the simulated effect of the cylinder flow variations upon the pump delivery flow is investigated.

Figure 8.27 illustrates how the flow ripple from successive cylinders forms the overall pump flow ripple for the 50 bar delivery pressure, 100% pump displacement condition. Similarly, figure 8.28 illustrates the composition of the flow ripple for the pump at the 250 bar, 100% displacement condition.

At the 50 bar condition, the rapid cylinder outflow from the standard pump ensures that the delivery flow ripple from the standard pump is more pronounced than that of the pump fitted with HDCVs. At the 250 bar condition the large cylinder inflow again leads to a flow ripple for the standard pump which is larger than that for the pump fitted with HDCVs.

The frequency spectra of the 50 bar delivery flow ripples shown in figure 8.27 are plotted in figure 8.29a. The frequency spectra of the flow ripple for the 250 bar condition are shown in figure 8.30a.

At the 50 bar condition, figure 8.29a shows that the pump fitted with HDCVs reduces the first flow ripple harmonic by 50% and the second harmonic by approximately 80%, but then

makes little difference to the higher harmonics. At the 250 bar condition, figure 8.30a shows that the pump fitted with HDCVs reduces the first 4 flow ripple harmonics by up to 60%.

8.3.2.9 Simulated Piston Force and Yoke Moments

In this section, the simulated effect of the cylinder pressure upon the total axial piston force and yoke moment is analysed.

The simulated axial piston force for the two pump designs are compared for the 50 bar condition in figure 8.29b and for the 250 bar condition in figure 8.30b. In both cases the pump with HDCVs produces a smaller axial piston force ripple than the standard pump. At the 50 bar condition, the contribution to the overall axial force variation from the large cylinder over-pressurisation (See figure 8.26e) can be clearly identified. At the 250 bar condition, the improvement in the axial force variation from the HDCVs is not so pronounced. This corresponds to the similar cylinder pressurisation caused by the two designs at this condition (See figure 8.26f).

The simulated yoke moment variation for the two pump designs is shown for the 50 bar condition in figure 8.29c, and for the 250 bar condition in figure 8.30c. As for the axial piston force, the HDCVs produce a smaller yoke moment variation than the standard pump. At the 50 bar condition the HDCVs reduce the first yoke moment harmonic by approximately 60%. However, in this case, the third, fourth, and fifth harmonics are increased and so the overall improvement at this condition is not so clear. As with the axial force variation, the yoke moment of the two designs at the 250 bar condition is very similar, with the HDCVs only giving a small improvement.

8.3.3 Problems encountered during the simulation work

Because of the complexity of the HDCV model, the simulations initially ran slowly and the large number of results files were very laborious to process. This section discusses the measures taken to speed up the simulation process.

Without these improvements simulation progress would have been very difficult. Initially, the simulation of a 2-port HDCV design over a range of operating conditions typically required 50 hours of simulation time and 2 days of manual data processing. Once the improvements had been made then the manual data processing was almost eliminated and the simulation run time was reduced to 6 hours.

8.3.3.1 Batch Simulations

The performance of each HDCV prototype was sensitive to small changes in the delivery pressure and pump displacement. Therefore, to describe the behaviour of each design, a large number of simulated operating points was required; 25 operating points were chosen at increments of 20% displacement and 50 bar between 50 bar delivery pressure, 100% displacement, and 250 bar, 20% displacement.

The use of 25 operating points made the simulation exercise very laborious because, for each operating point, the Bathfp model parameters had to be changed and the simulation

results processed. To overcome this problem, all 25 operating points were simulated using a batch file. To do this, the "Dual Cylinder" models were altered to read their model parameters from a set of data files. Also, a program was written to extract and process data from the Bathfp results files. This program also increments a count variable used to change the simulated operating condition. The batch file was written in UNIX shell script and the processing program was written in FORTRAN. The flowchart for the batch file is shown in figure 8.31.

8.3.3.2 HDCV Poppet settling times

Each simulation run had to be long enough to allow the HDCV poppets to reach their final displacements (See for example figure 8.15a). The settling time for the HDCV poppets over the 25 operating conditions varied between 0.02s and 0.30s and so within each batch file all of the simulations had to be run for 0.30s. This caused prohibitively long run times for the batch file; the simulation of a 2-port HDCV design over 25 operating conditions took 50 hours.

To overcome this problem, a technique was developed to interrogate each Bathfp results file to check whether the HDCV poppets had reached their final displacements. Each Bathfp simulation run is reduced to 8 complete periods of the pumping frequency (0.0267s for a nine-cylinder pump running at 1500rev/min). At the end of each simulation run, the poppet displacement data from the last 2 periods of the pumping frequency are compared. If the difference between the 2 sets of data is within a small tolerance then the poppets are assumed to be close to their final displacements. At this point, the flow and pressure data is extracted from the Bathfp results file and the batch file is incremented to the next condition. A flow diagram of the process is shown in figure 8.32. This measure significantly reduced the batch run times; from 50 hours down to 6 hours.

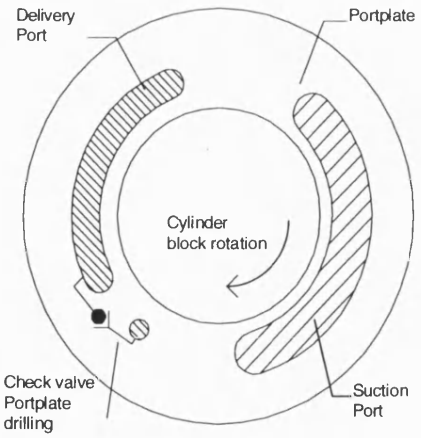

Figure 8.1a
Portplate concept using a check valve

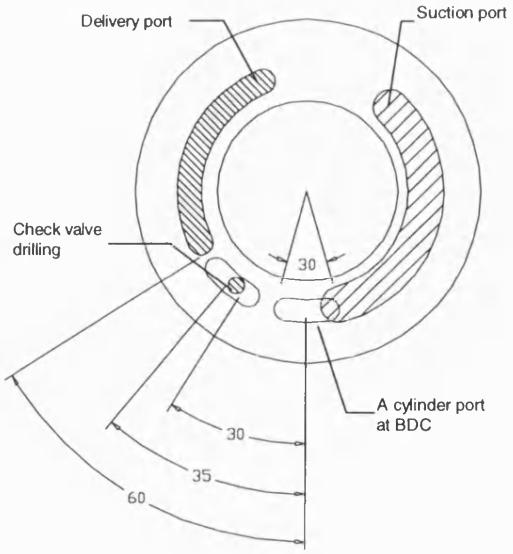

Figure 8.1b
Details for a scheme featuring a single HDCV

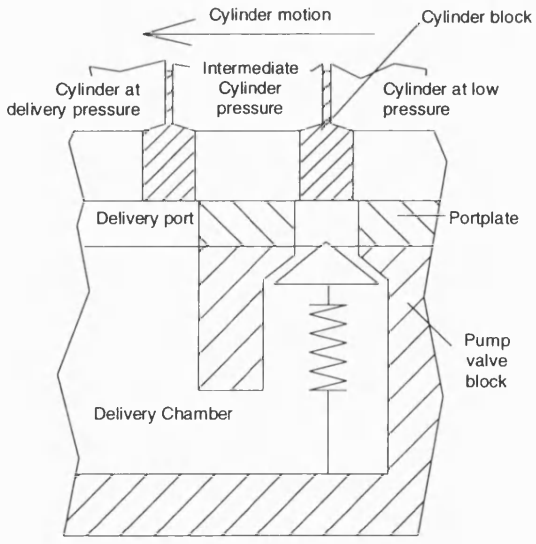

Figure 8.2a
Concept featuring ideal check valve

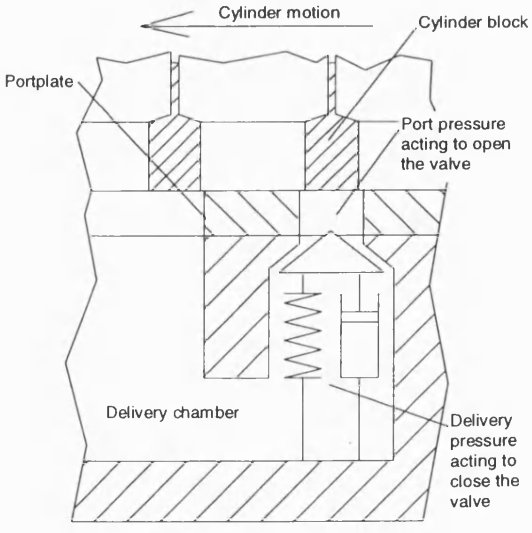

Figure 8.2b
Concept featuring damped check valve

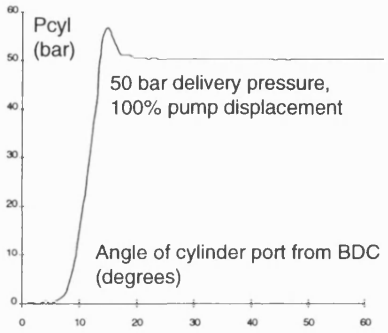

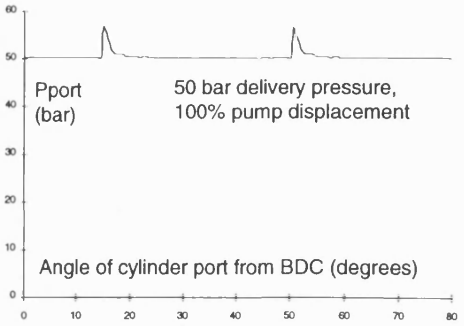

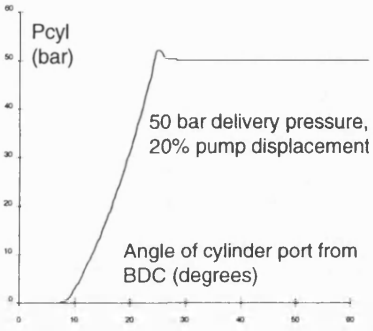

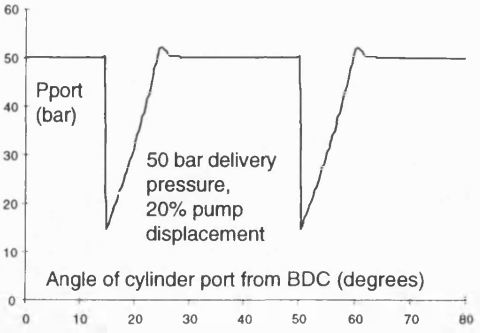

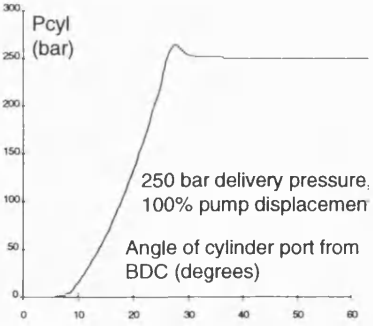

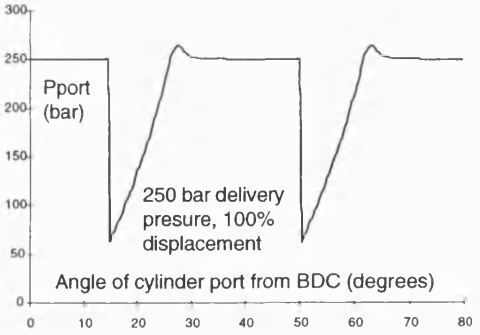

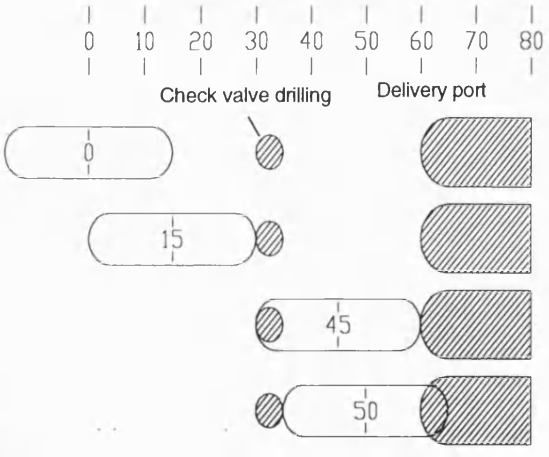

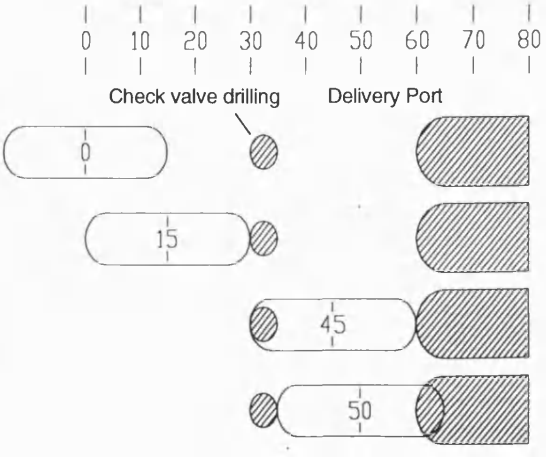

Figure 8.3a
Rise in cylinder pressure
with optimal pre-compression

Figure 8.3b
Variation in port pressure with
optimal cylinder pre-compression

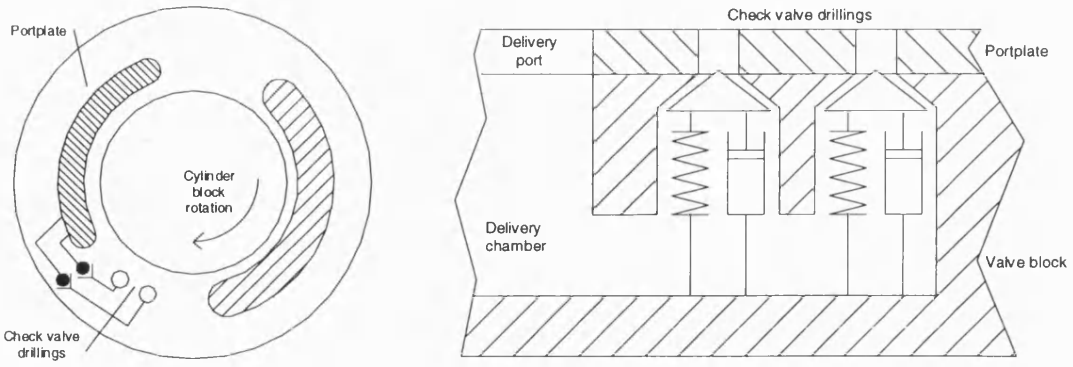

Figure 8.4
Concept sketch featuring a pair of damped check valves

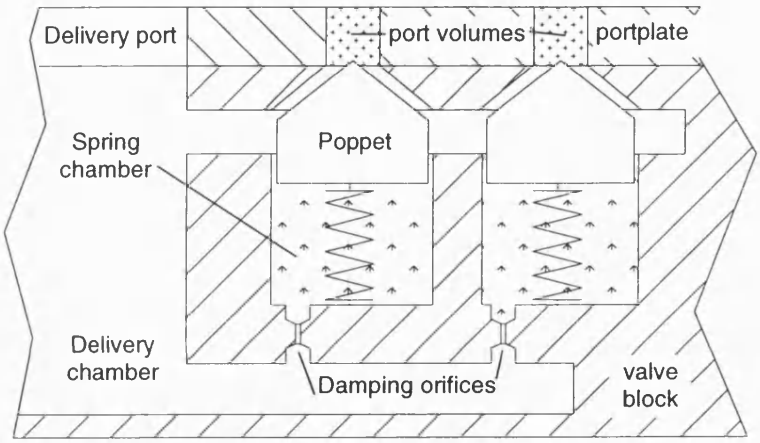

Figure 8.5
Sketch of the HDCV concept featuring two HDCVs

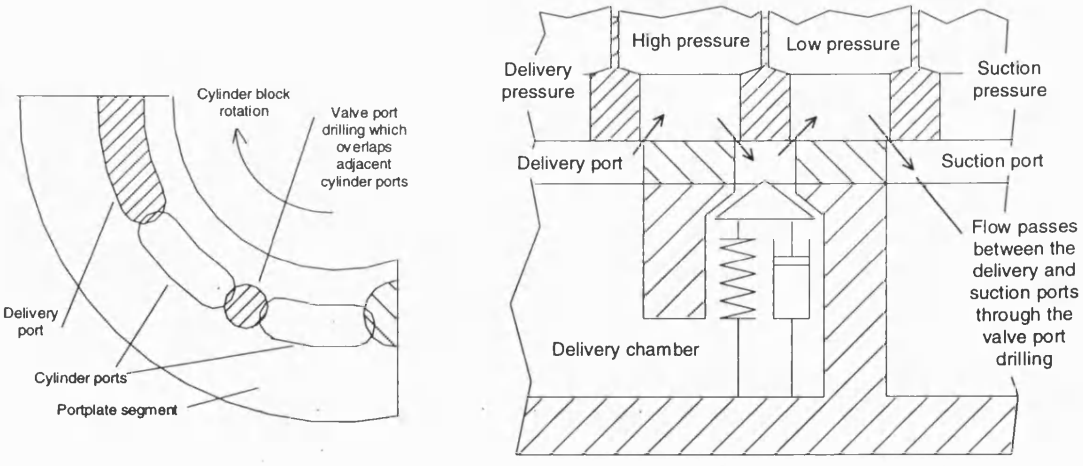

Figure 8.6
A portplate drilling that has too large a diameter

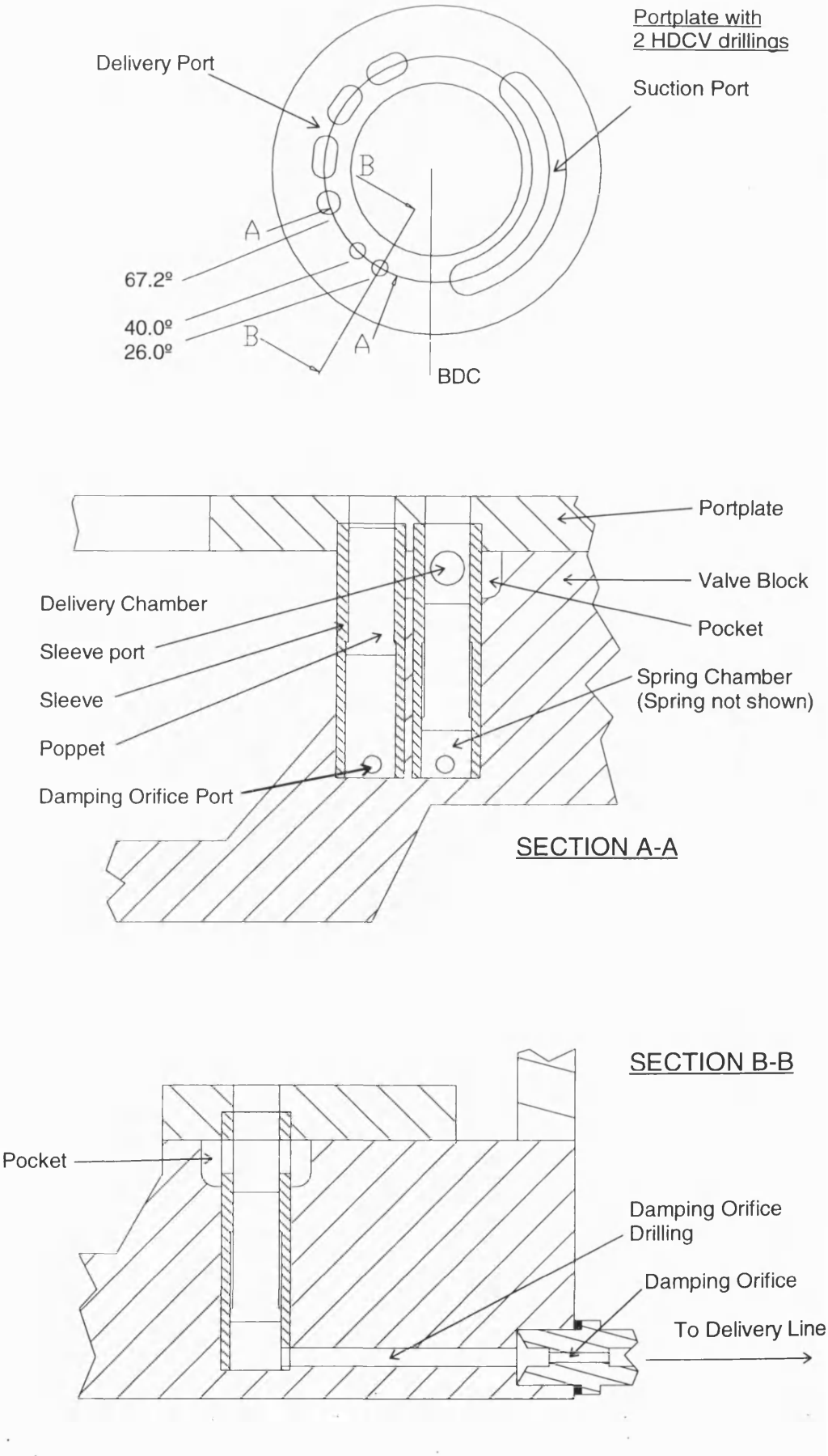

Figure 8.7
HDCV Prototype Scheme

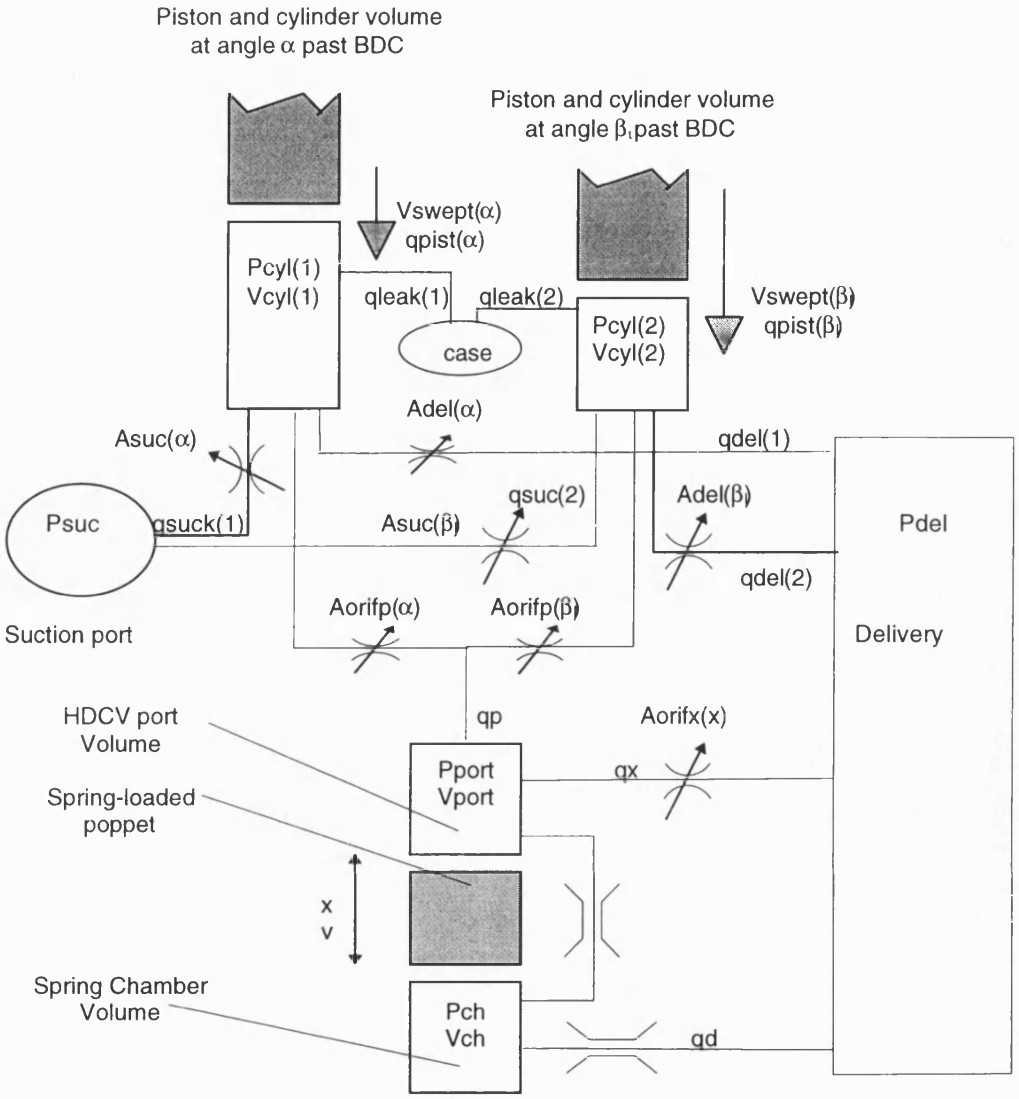

Note:
The effect of upto four HDCV ports can be
although only one is shown for

Figure 8.8
The main elements of the HDCV simulation model

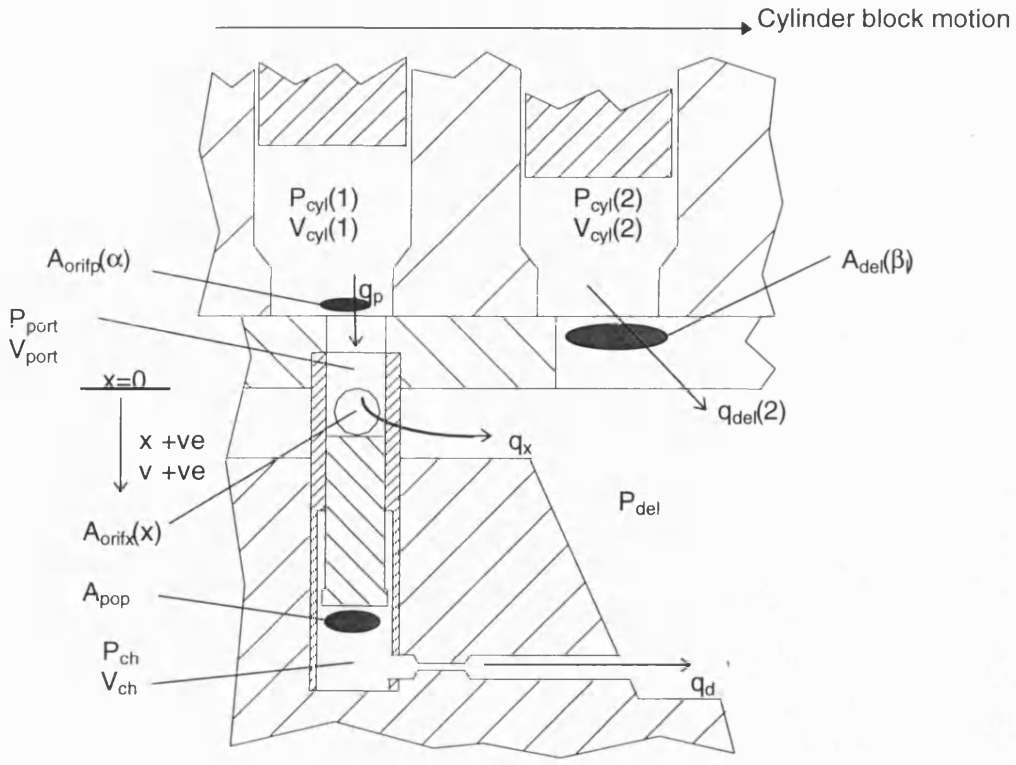

Figure 8.9a
The prototype design superimposed with the simulation variables

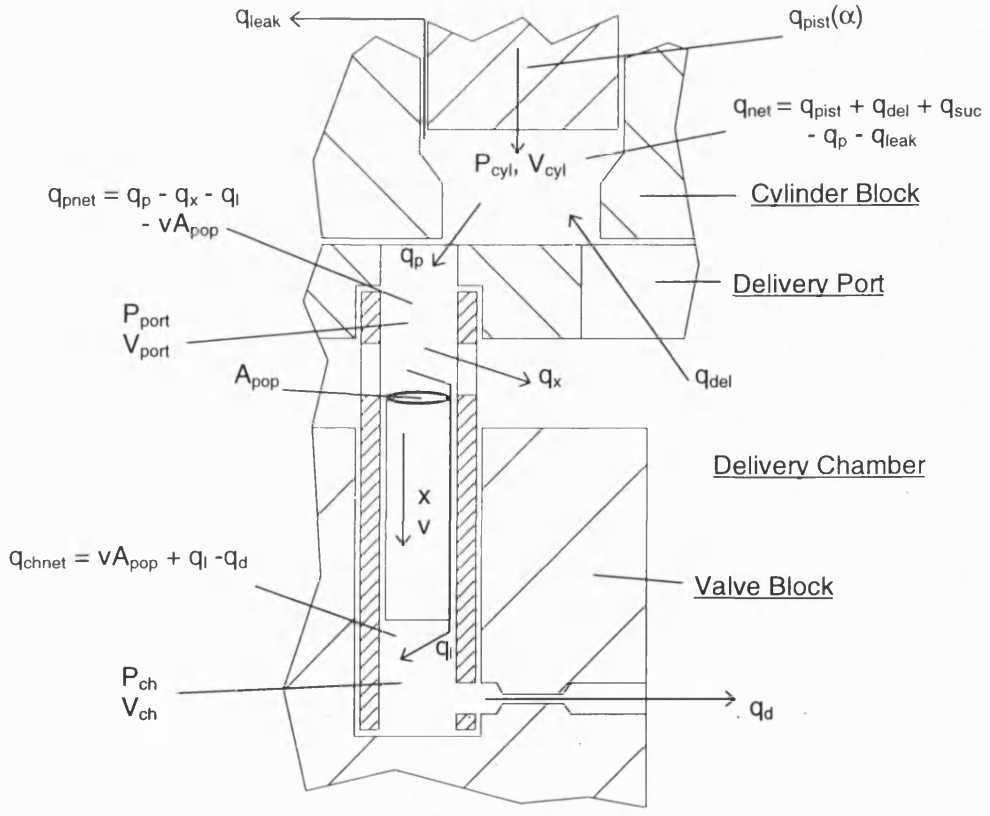

Figure 8.9b
The flow paths and flow summations within the HDCV simulation model

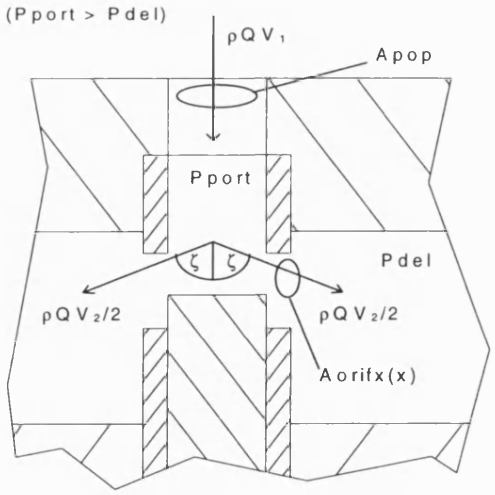

Figure 8.10
The modelling of flow forces within the HDCVs

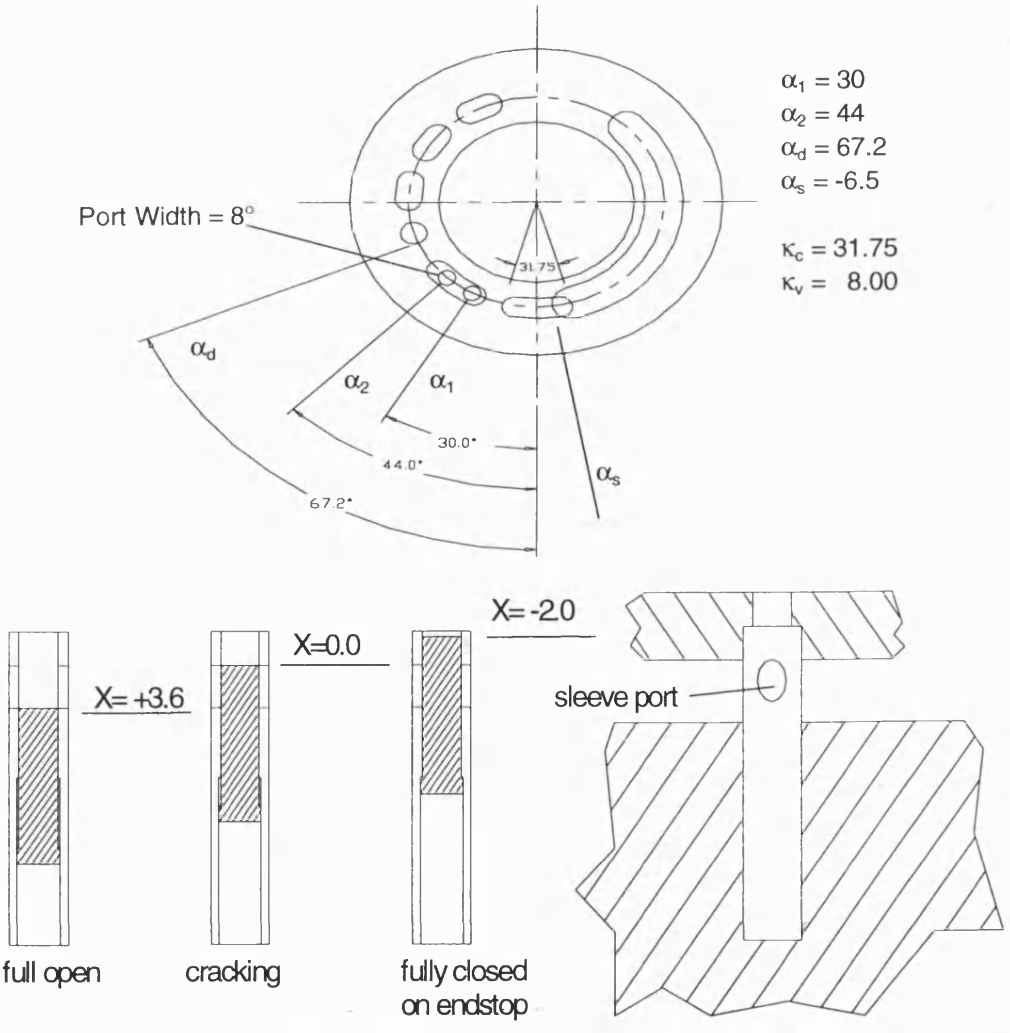

Figure 8.11
Initial simulation parameters for the HDCV prototype

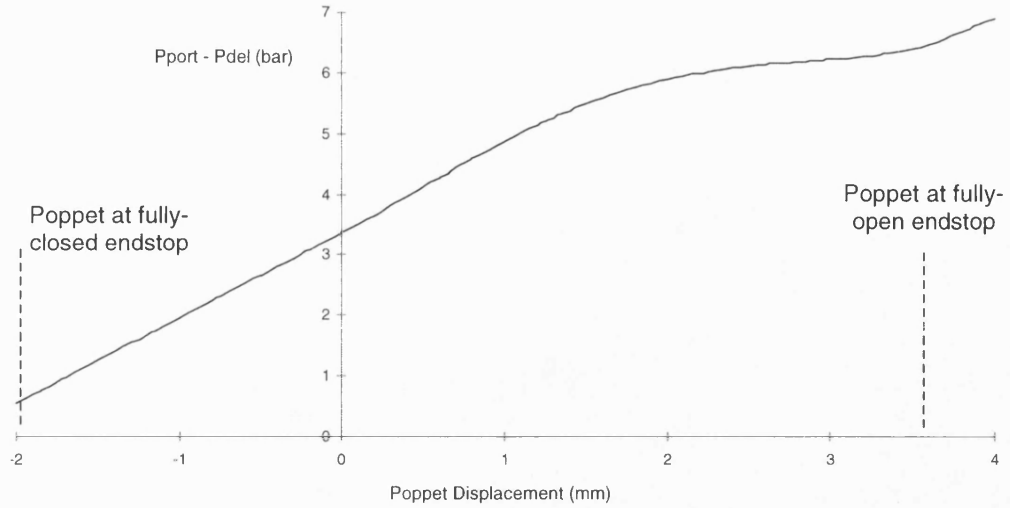

Figure 8.12a
HDCV Poppet steady state pressure characteristic

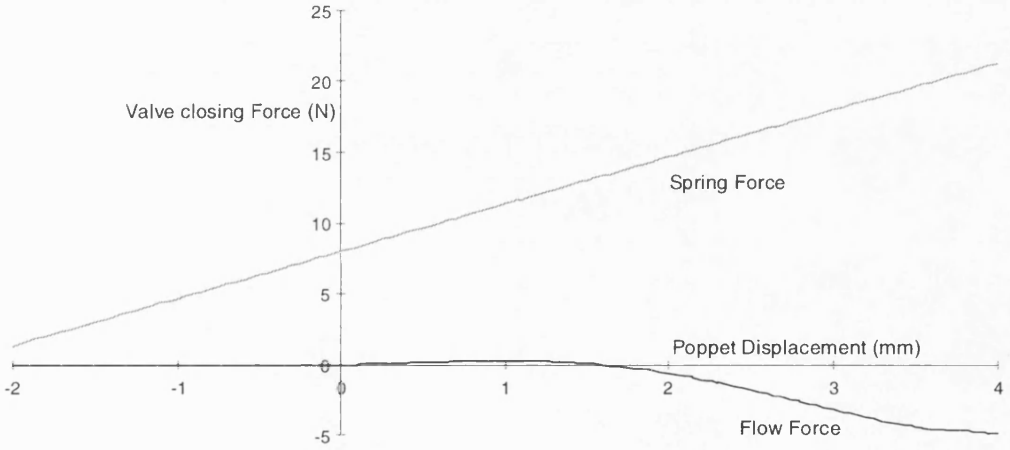

Figure 8.12b
HDCV Poppet steady state force characteristic

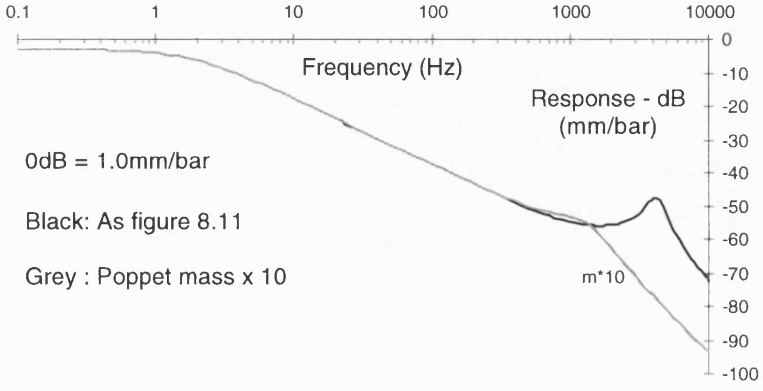

Figure 8.13a
The effect of poppet mass on the linearised poppet dynamic characteristic

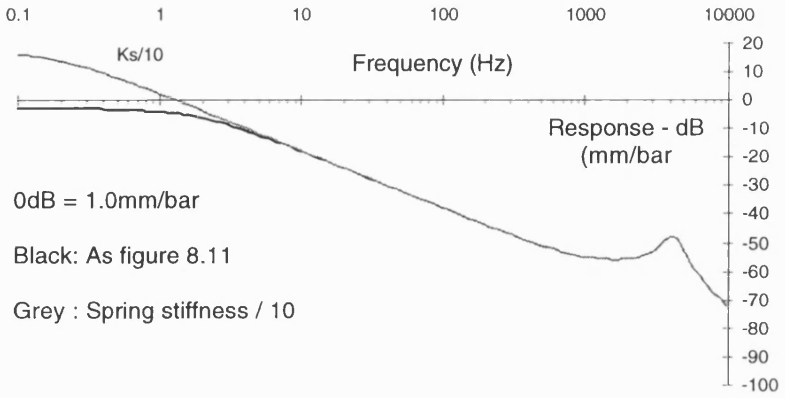

8.13b

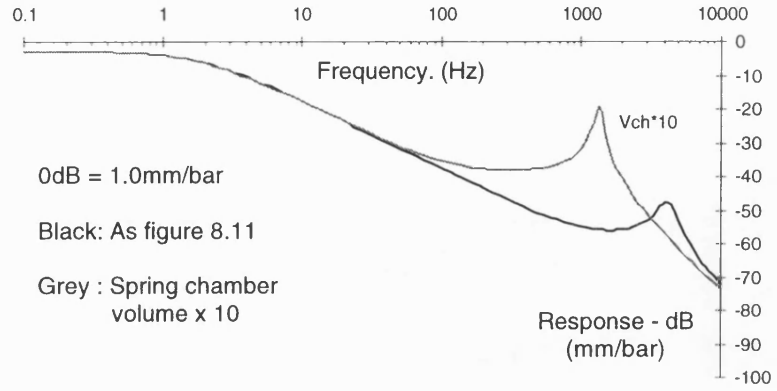

8.13c

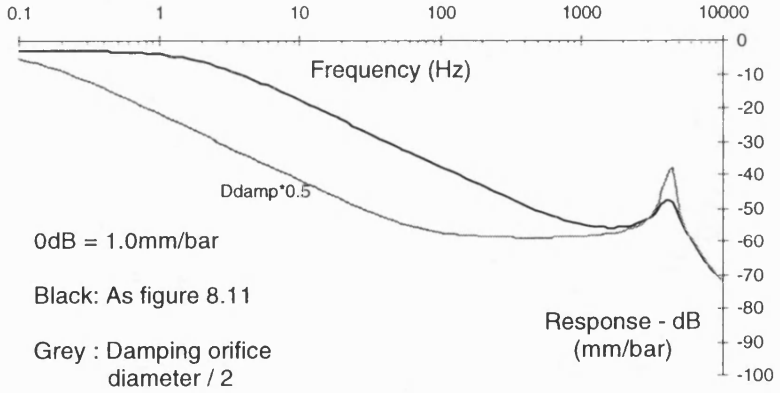

8.13d

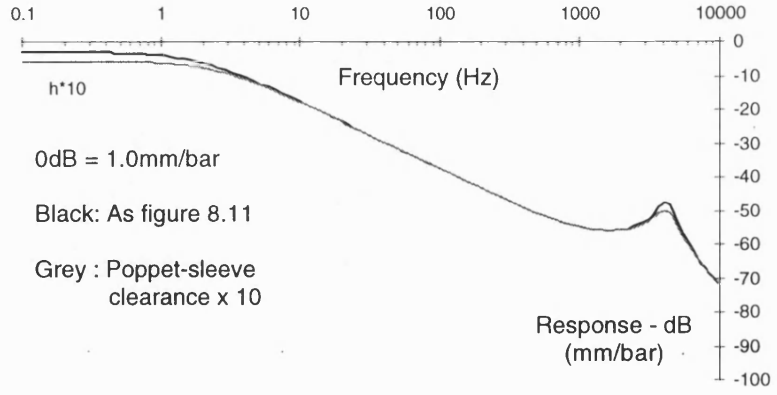

8.13e

Figure 8.13b - e
Parameter sensitivity of the linearised poppet dynamic characteristic

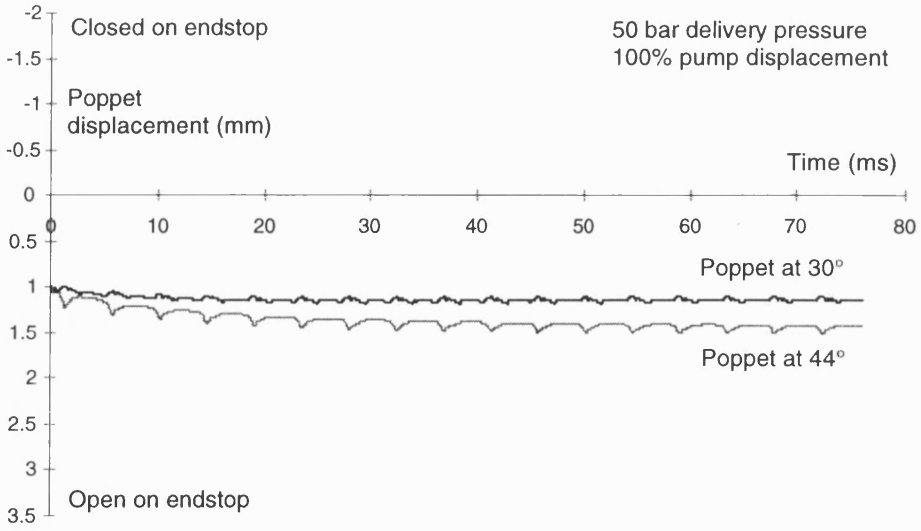

Figure 8.14a
Simulated poppet displacement

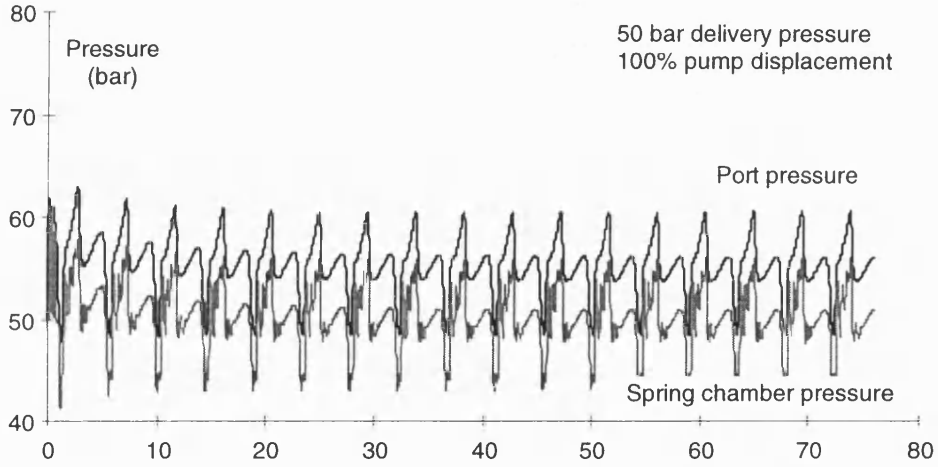

Figure 8.14b
Simulated port and spring chamber pressures for the HDCV at 30° from BDC

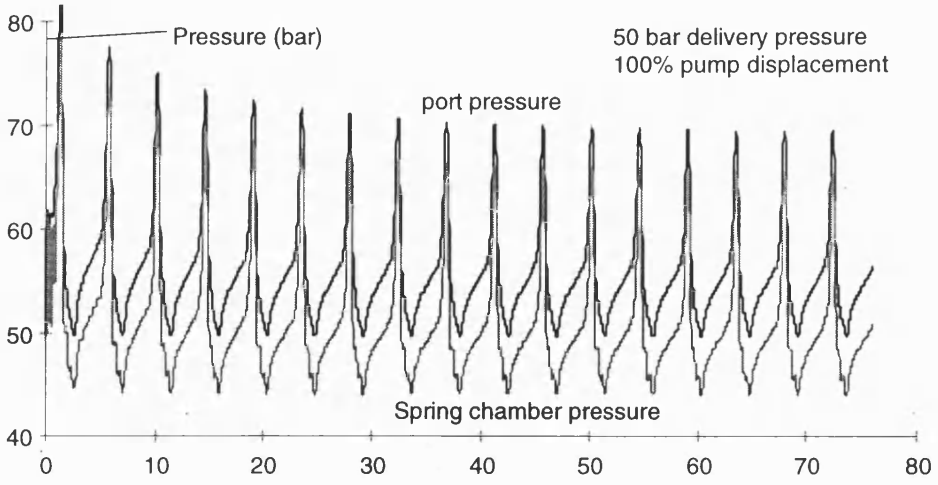

Figure 8.14c
Simulated port and spring chamber pressures for the HDCV at 44° from BDC

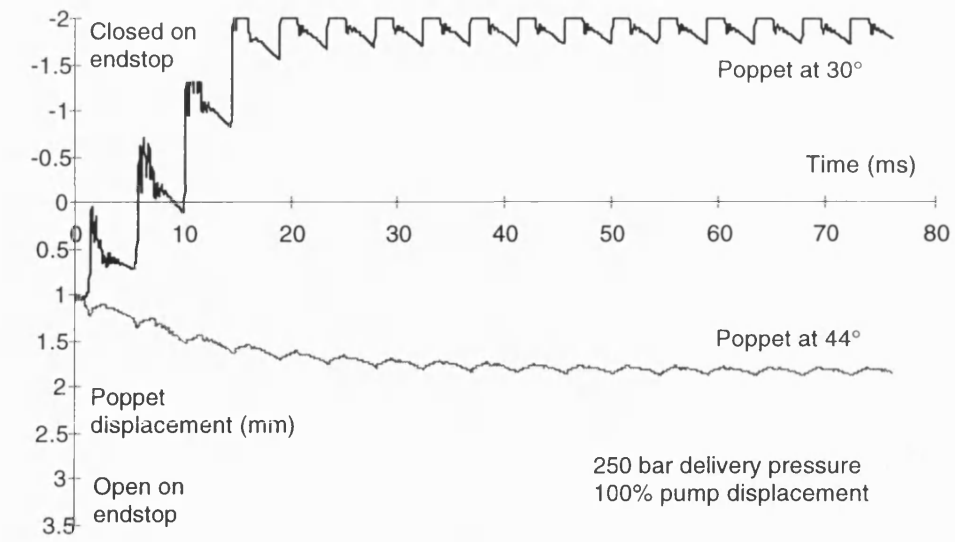

Figure 8.15a
Simulated poppet displacement

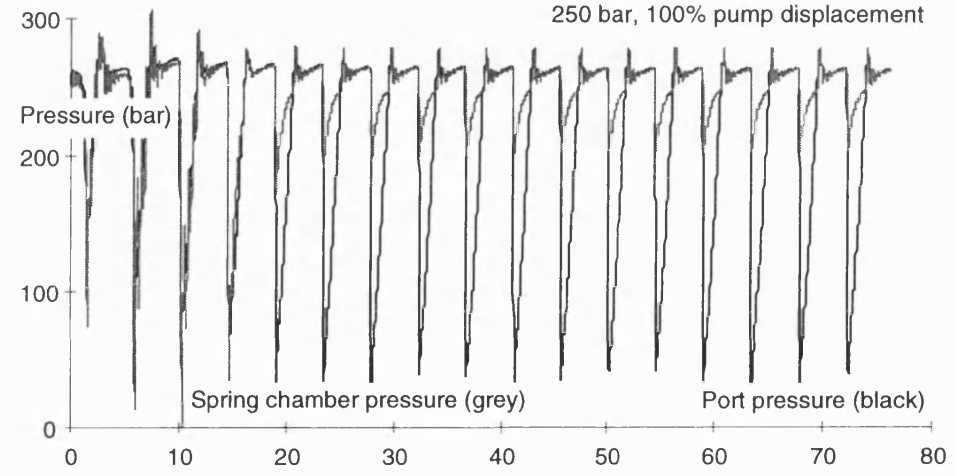

Figure 8.15b
Simulated port and spring chamber pressures for the HDCV at 30° from BDC

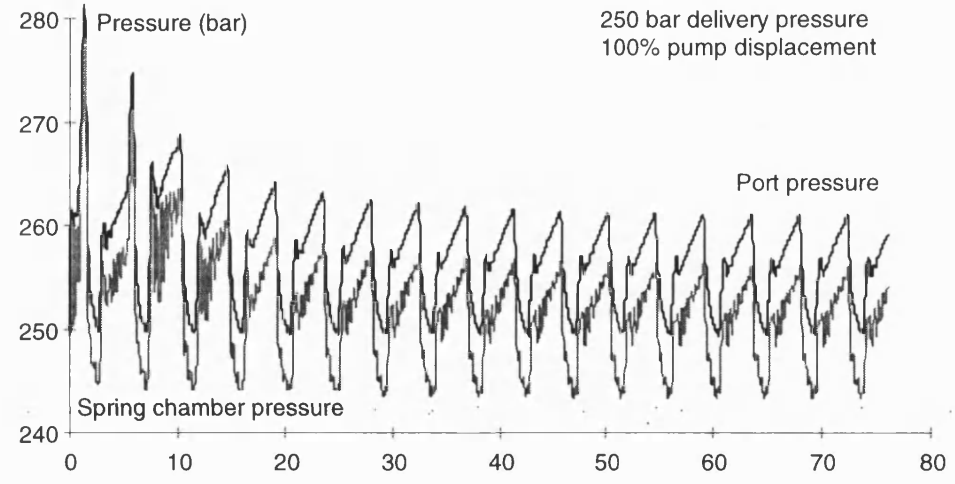

Figure 8.15c
Simulated port and spring chamber pressures for the HDCV at 44° from BDC

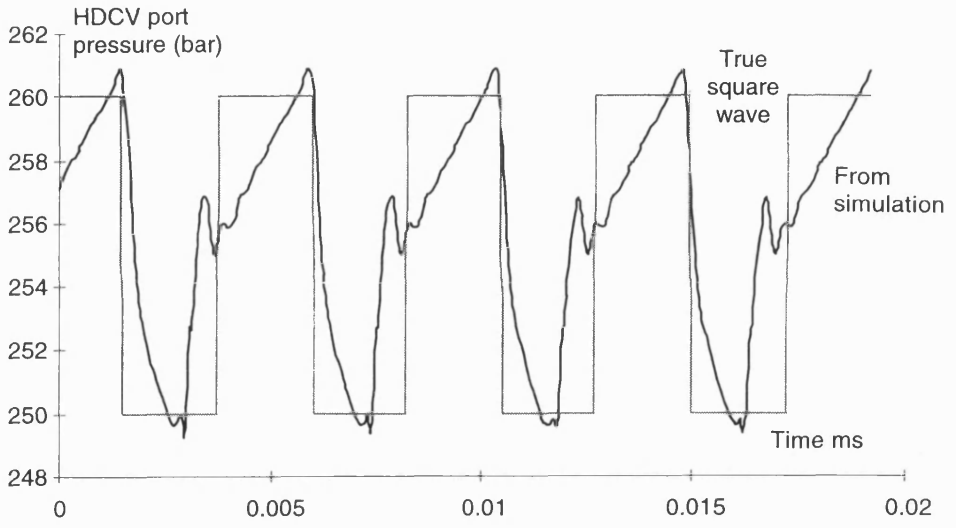

Figure 8.16a
Simulated approximation to a square wave input pressure signal

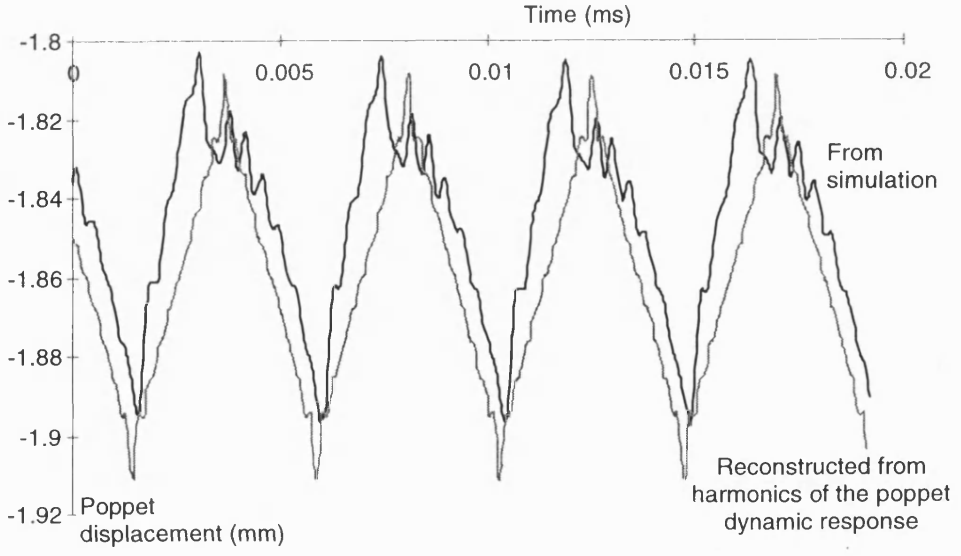

Figure 8.16b
Simulated and linearised poppet response

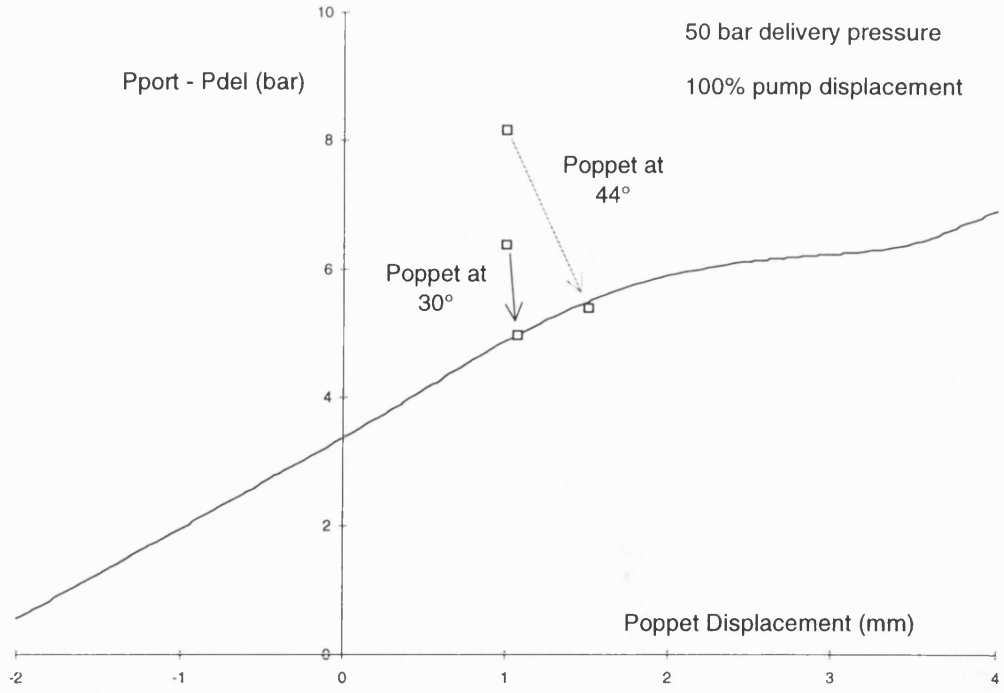

Figure 8.17a
Simulated variation in mean poppet displacement

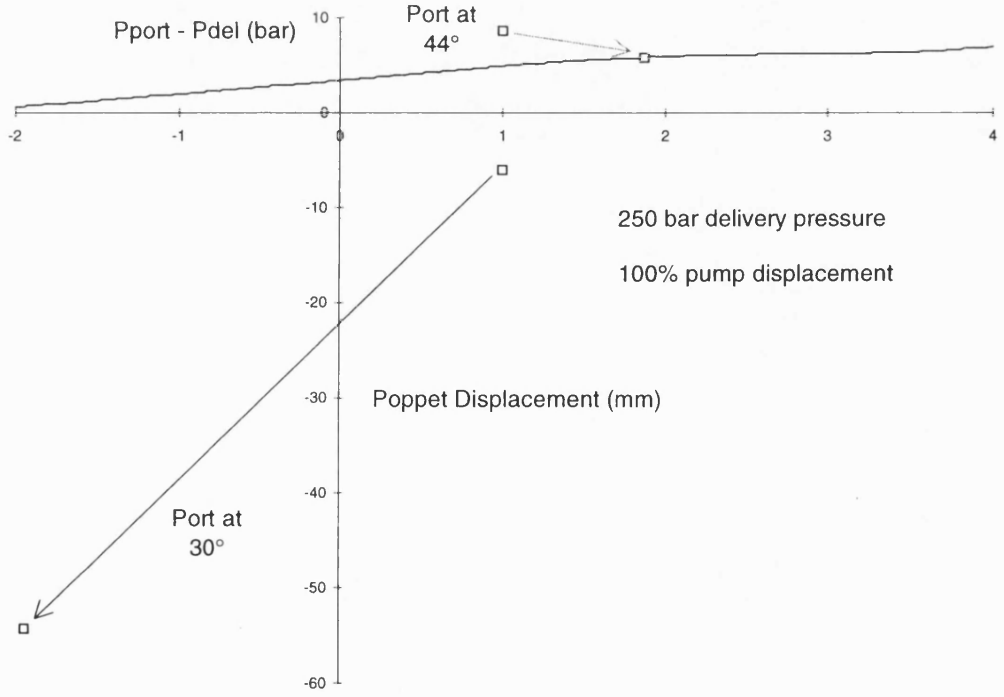

Figure 8.17b
Simulated variation in mean poppet displacement

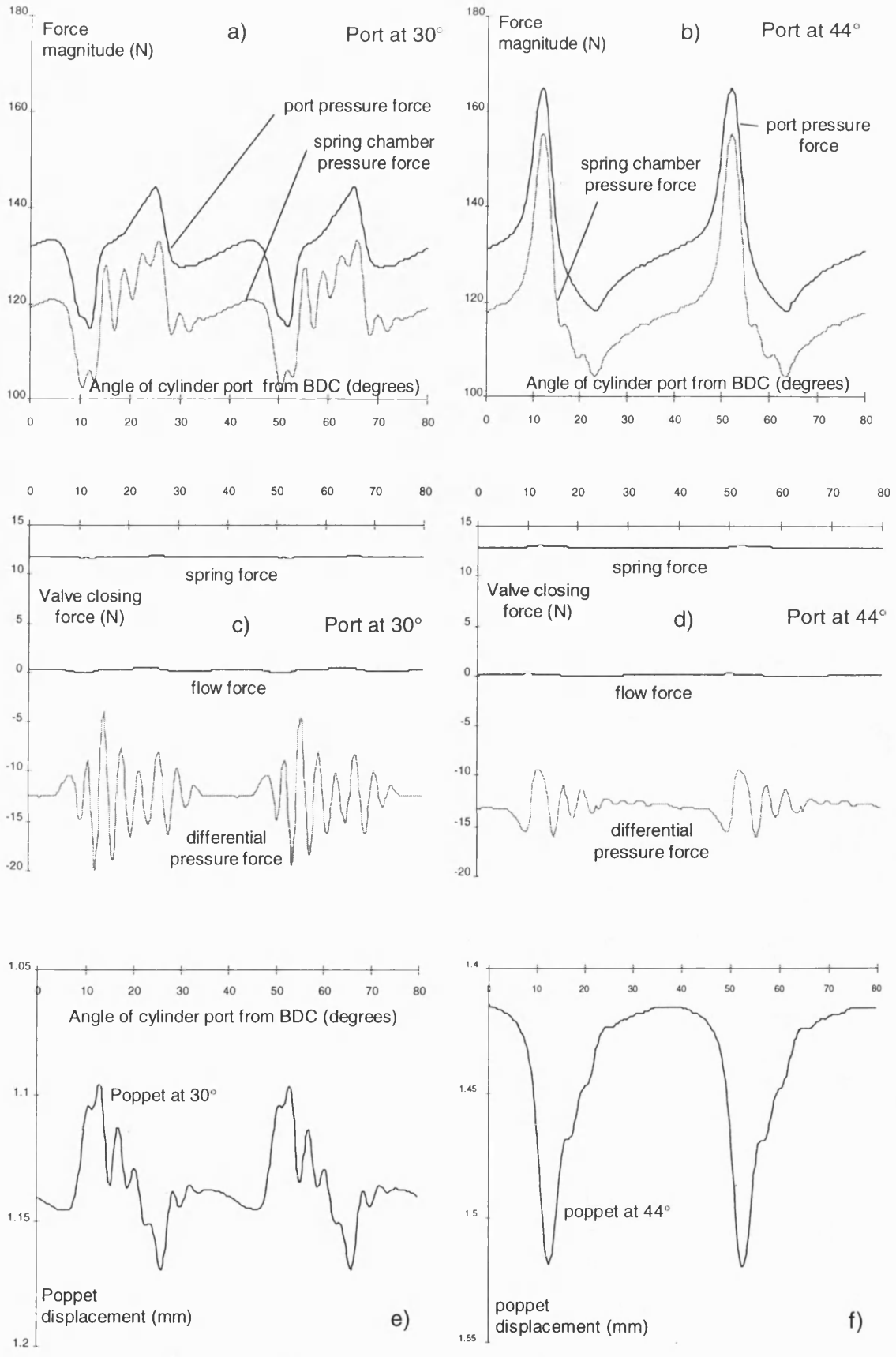

Figure 8.18a - f
Simulated HDCV force, pressure and poppet displacement at 50 bar delivery pressure and 100% pump displacement

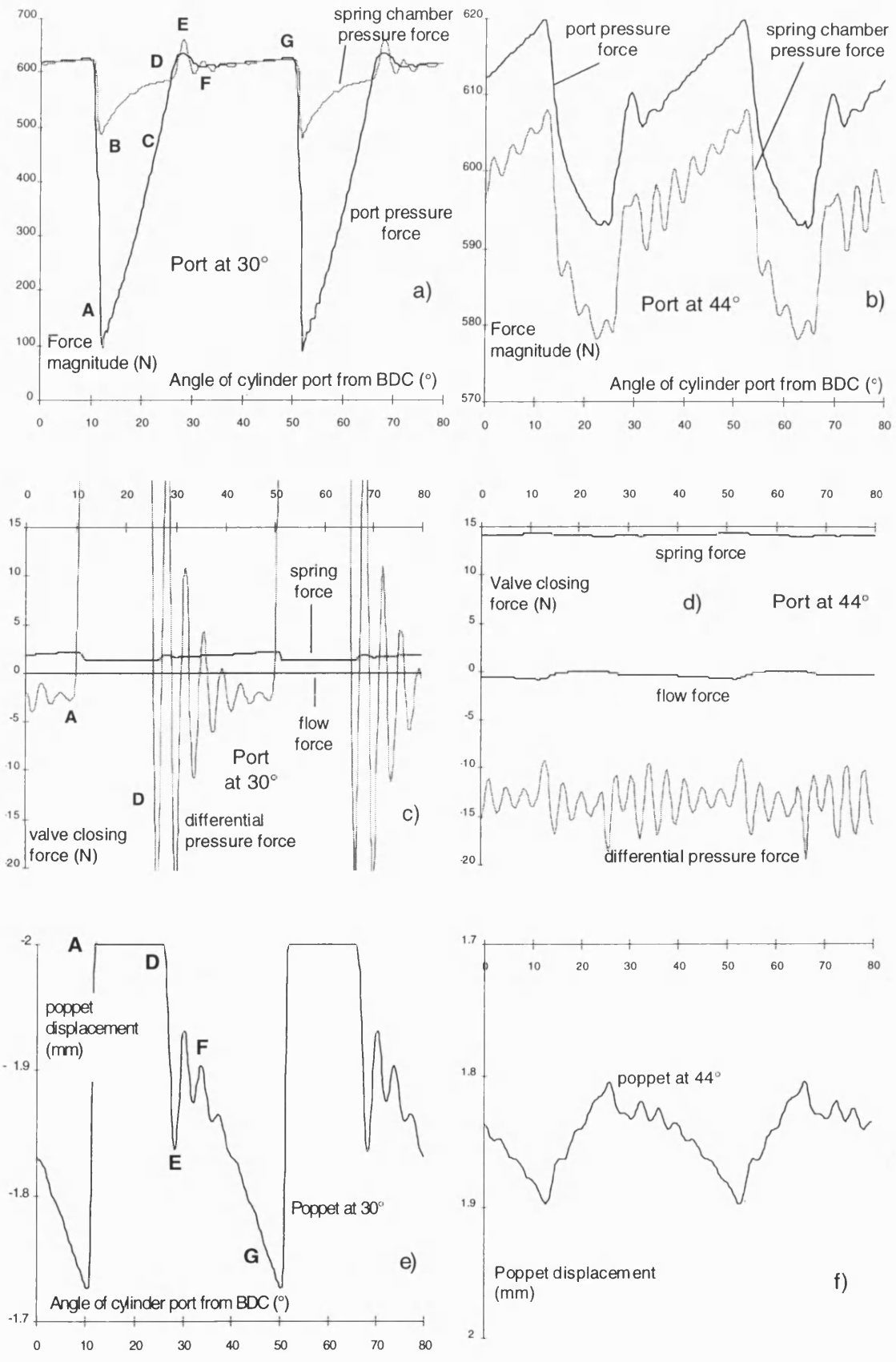

Figure 8.19a - f
Simulated HDCV force, pressure and poppet displacement at 250 bar delivery pressure and 100% pump displacement

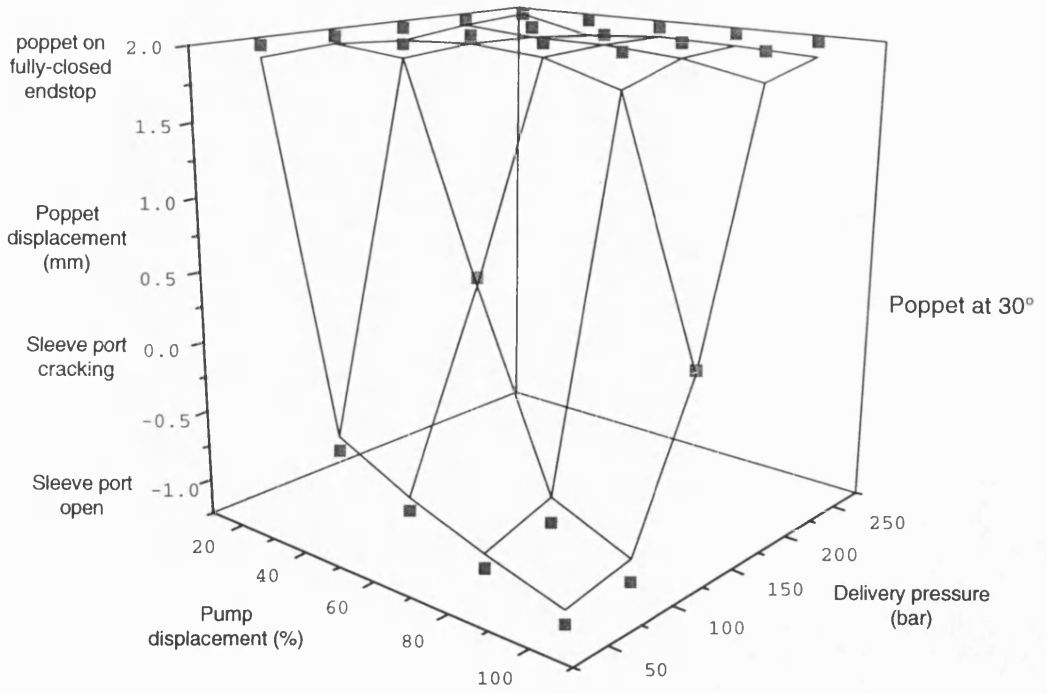

Figure 8.20a
Simulated mean poppet displacement for the HDCV at 30° past BDC

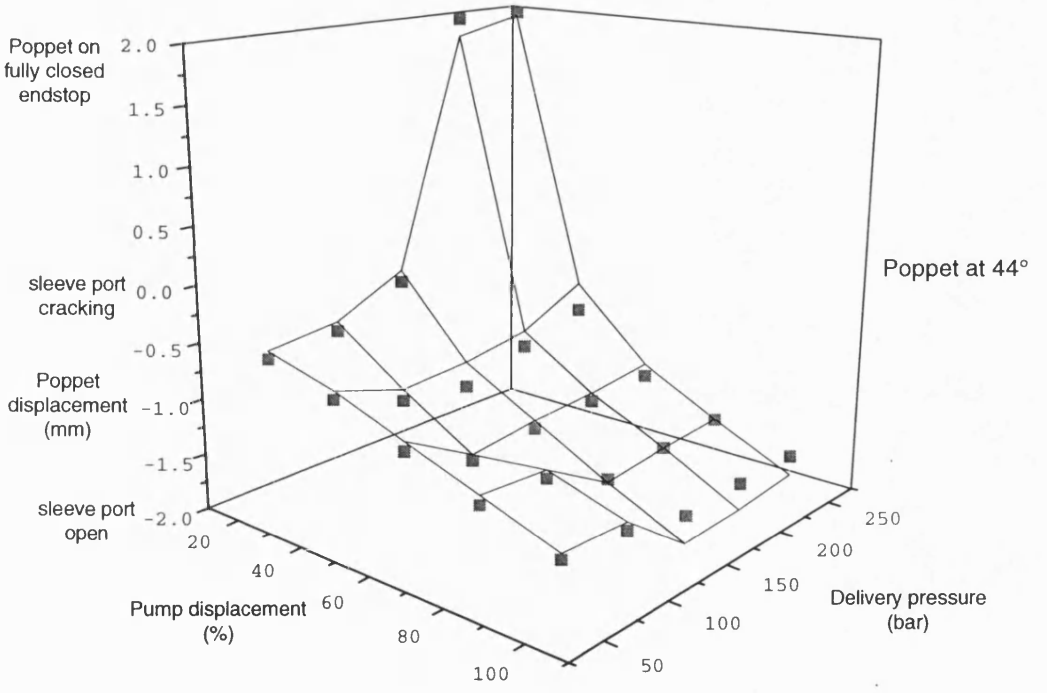

Figure 8.20b
Simulated mean poppet displacement for the HDCV at 44° past BDC

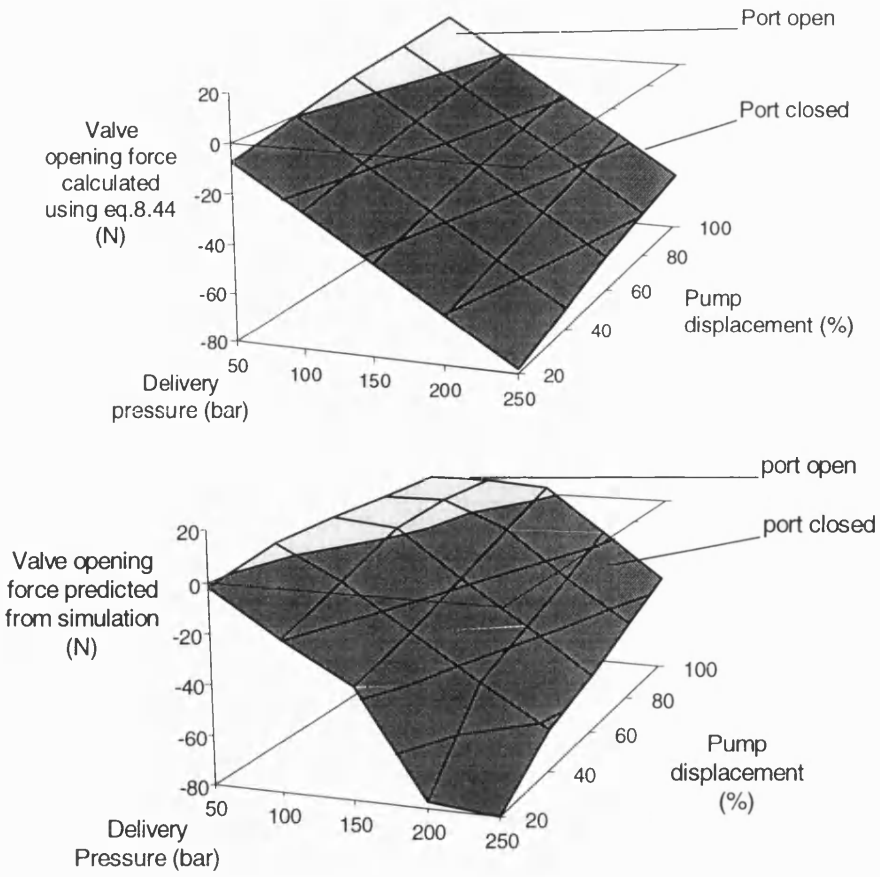

Figure 8.21a
Net opening force for the HDCV at 30° past BDC

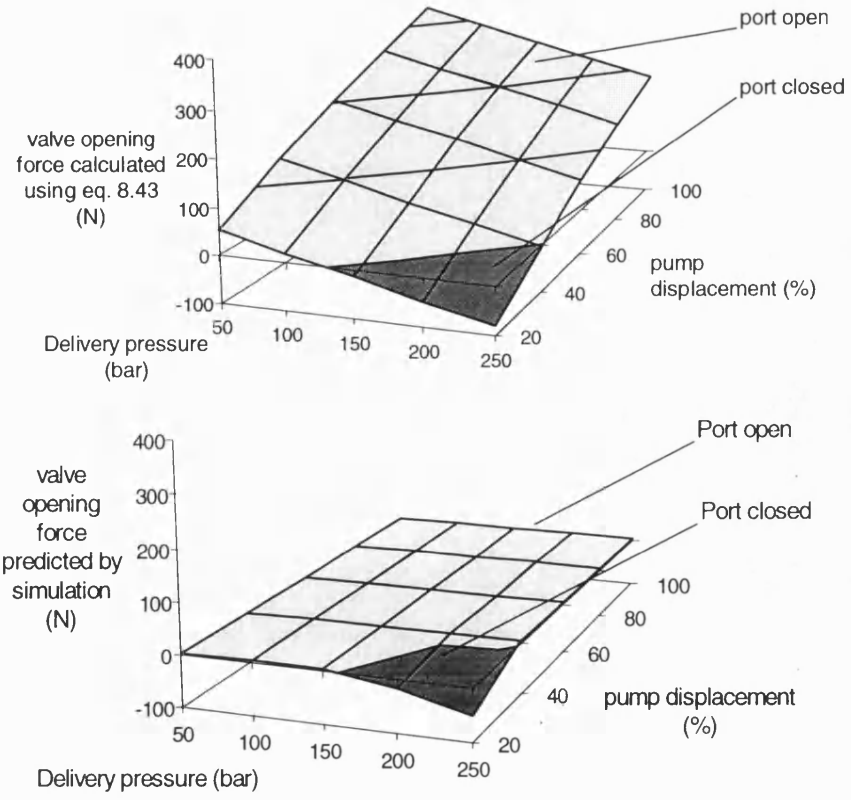

Figure 8.21b
Net opening force for the HDCV at 44° past BDC

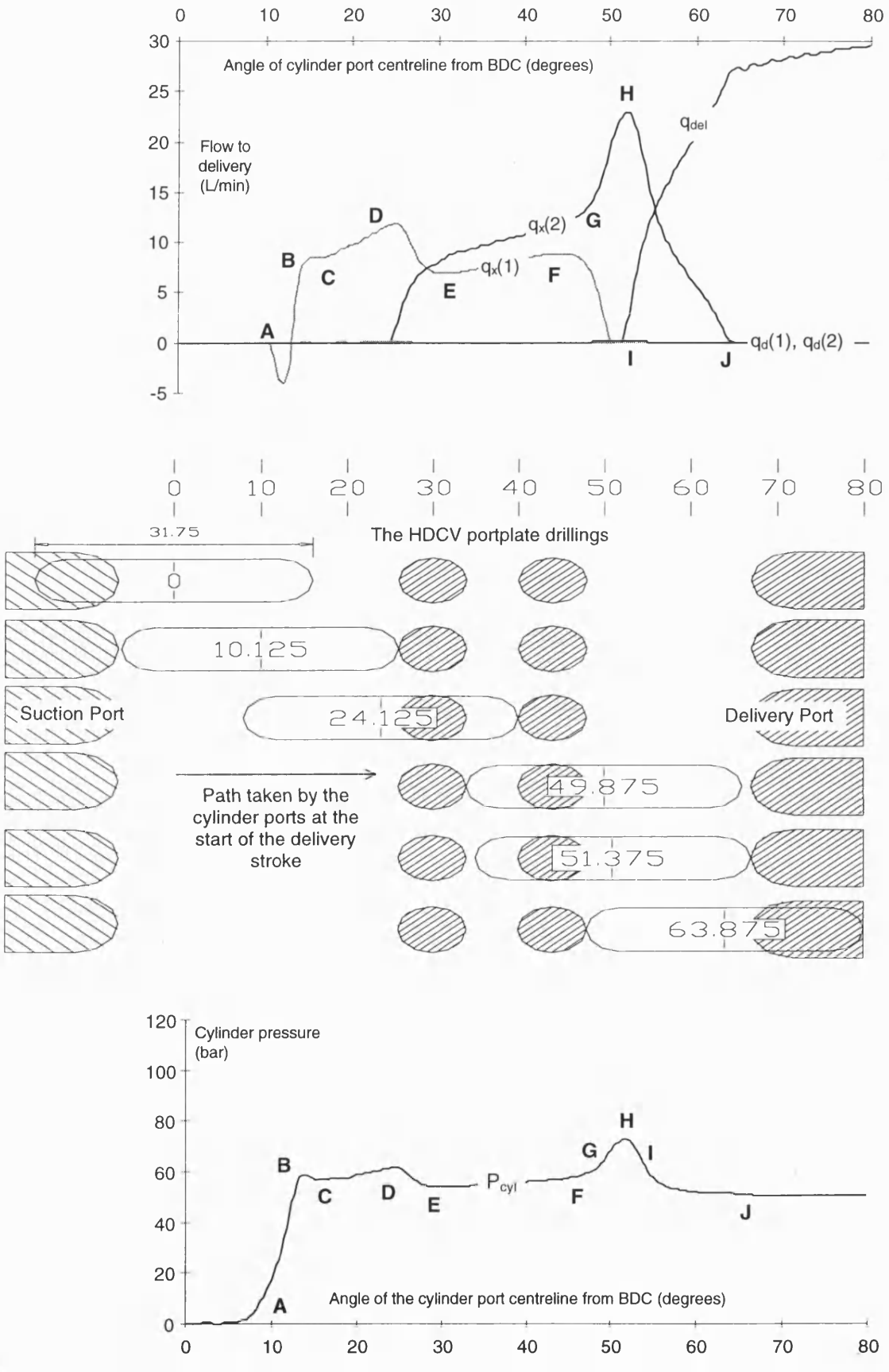

Figure 8.22
Simulated cylinder pressures and flows using the HDCV prototype at 50 bar delivery pressure and 100% pump displacement

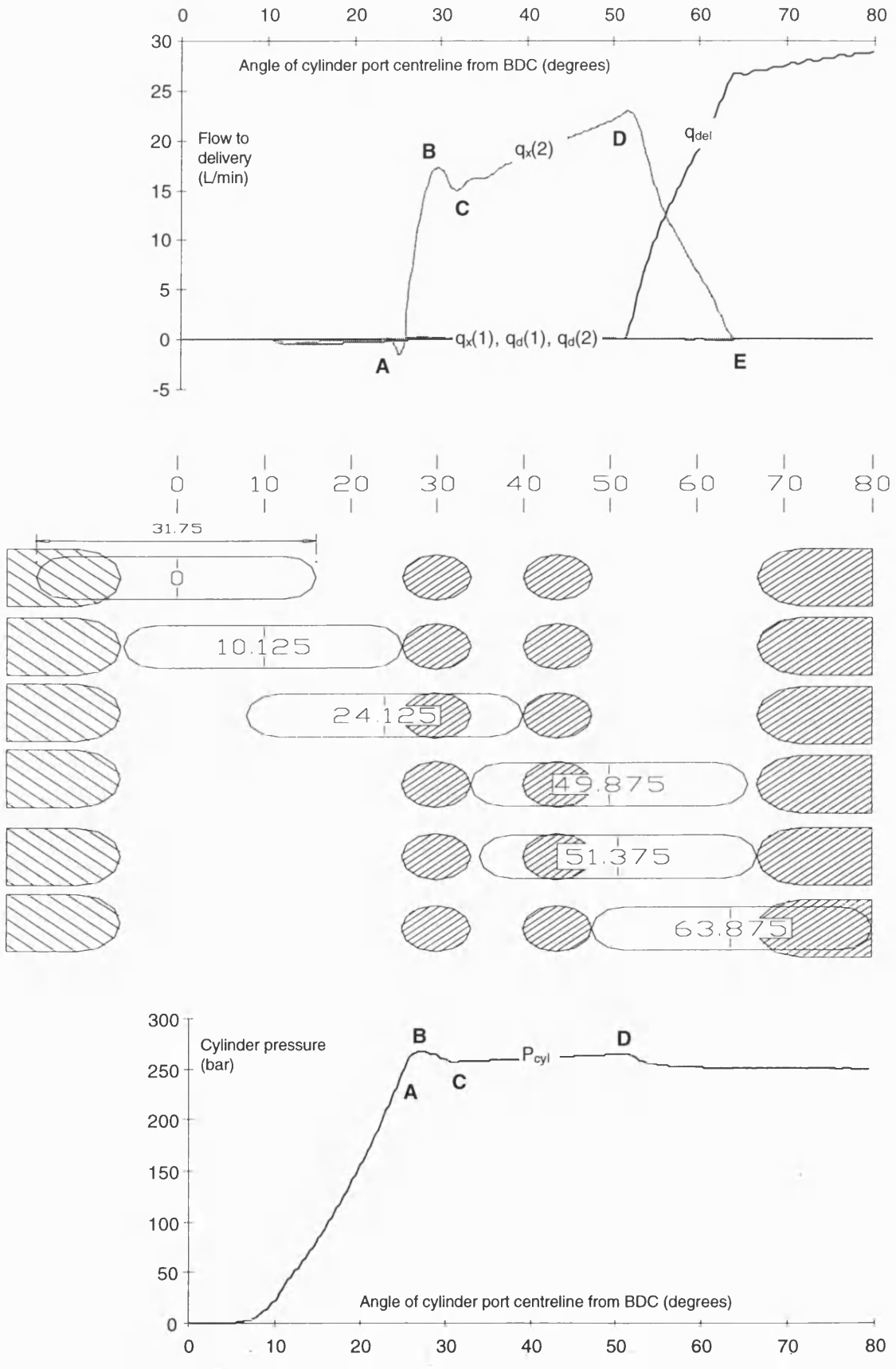

Figure 8.23
Simulated cylinder pressures and flows using the HDCV prototype at 250 bar delivery pressure and 100% pump displacement

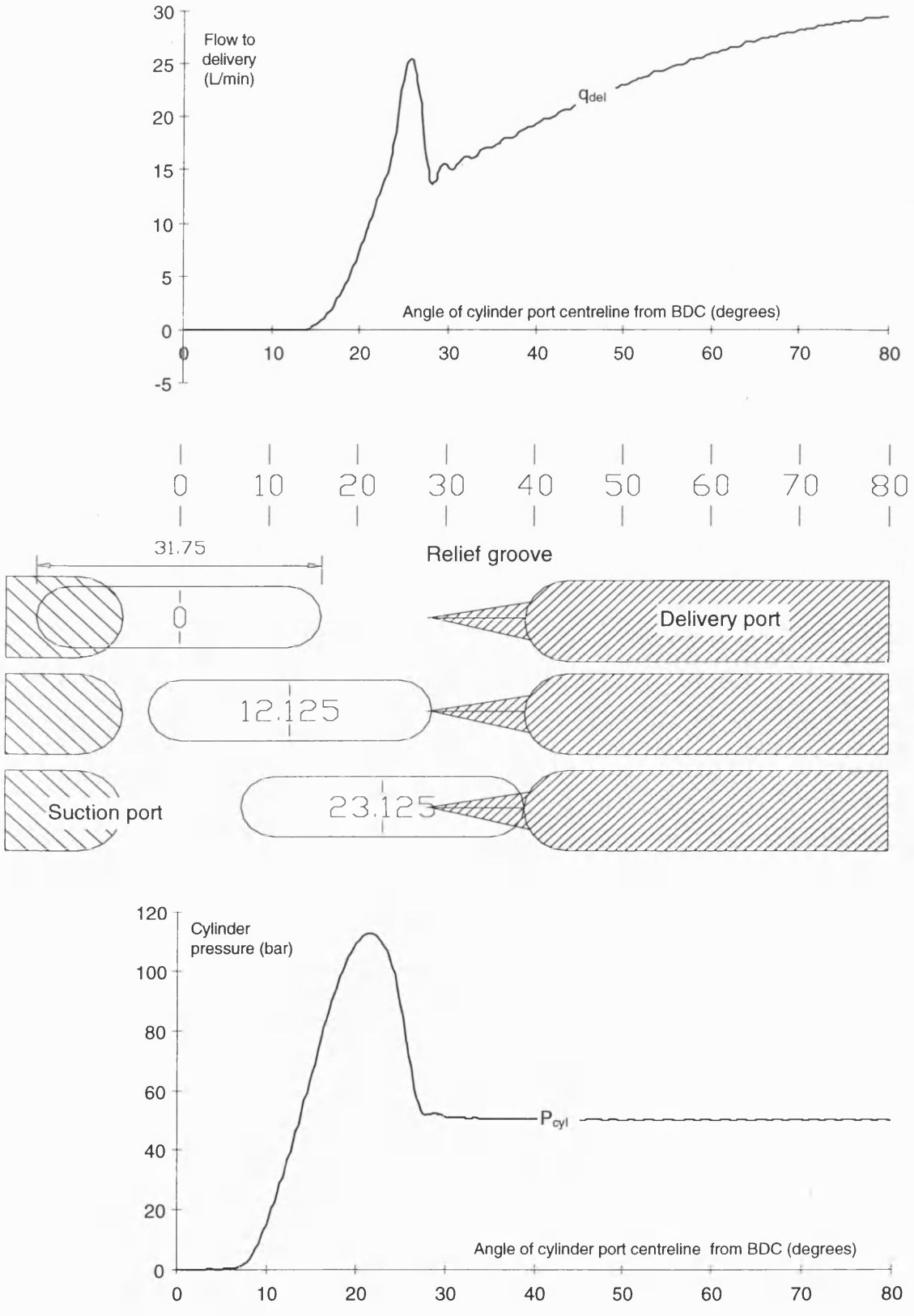

Figure 8.24
Simulated cylinder pressures and flows for the unmodified pump at 50 bar delivery pressure and 100% pump displacement

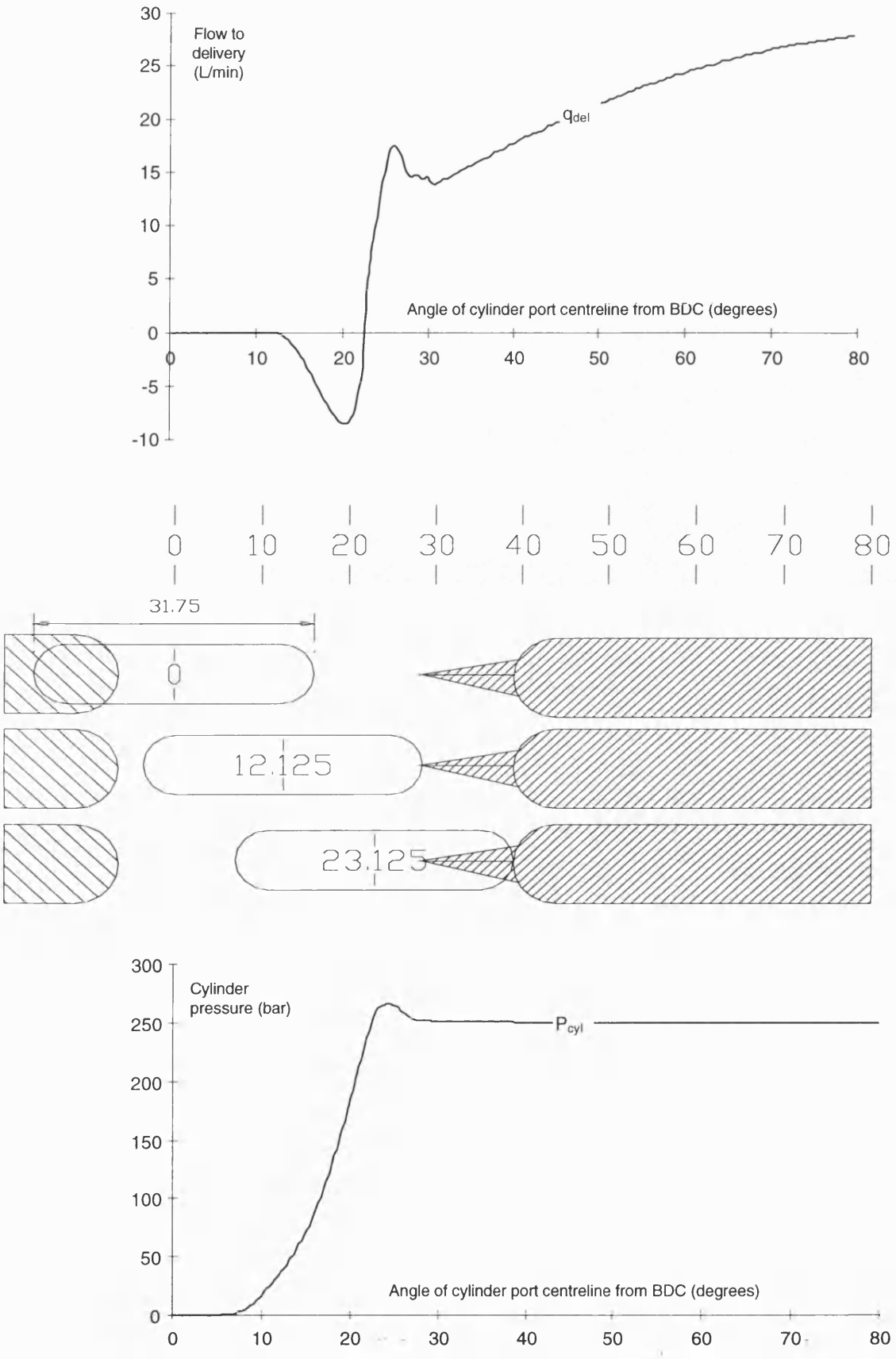

Figure 8.25
Simulated cylinder pressures and flows for the unmodified pump at 250 bar delivery pressure and 100% pump displacement

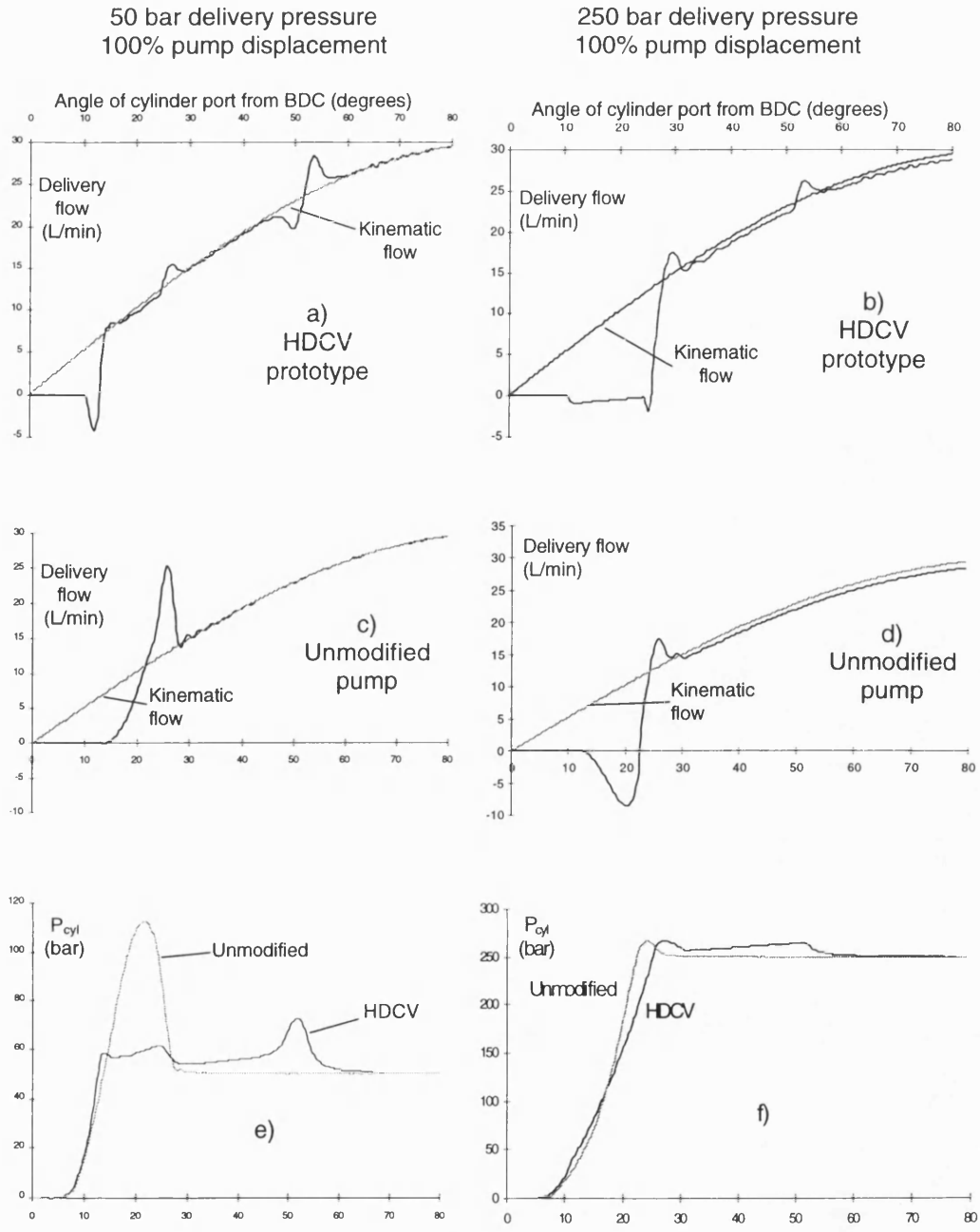

Figure 8.26a - f
Comparison of the simulated cylinder pressures and flows between the HDCV prototype and the unmodified pump

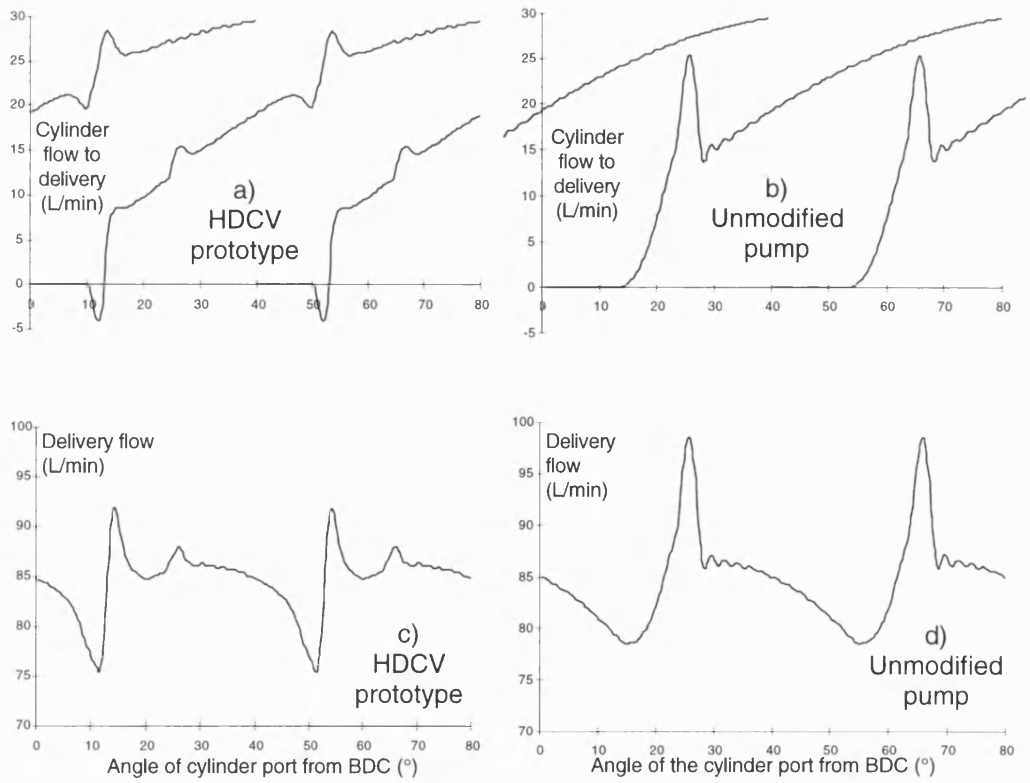

Figure 8.27a - d
Summation of the single cylinder delivery flows to give the simulated pump delivery flow for the HDCV prototype and the unmodified pump at 50 bar and 100% displacement

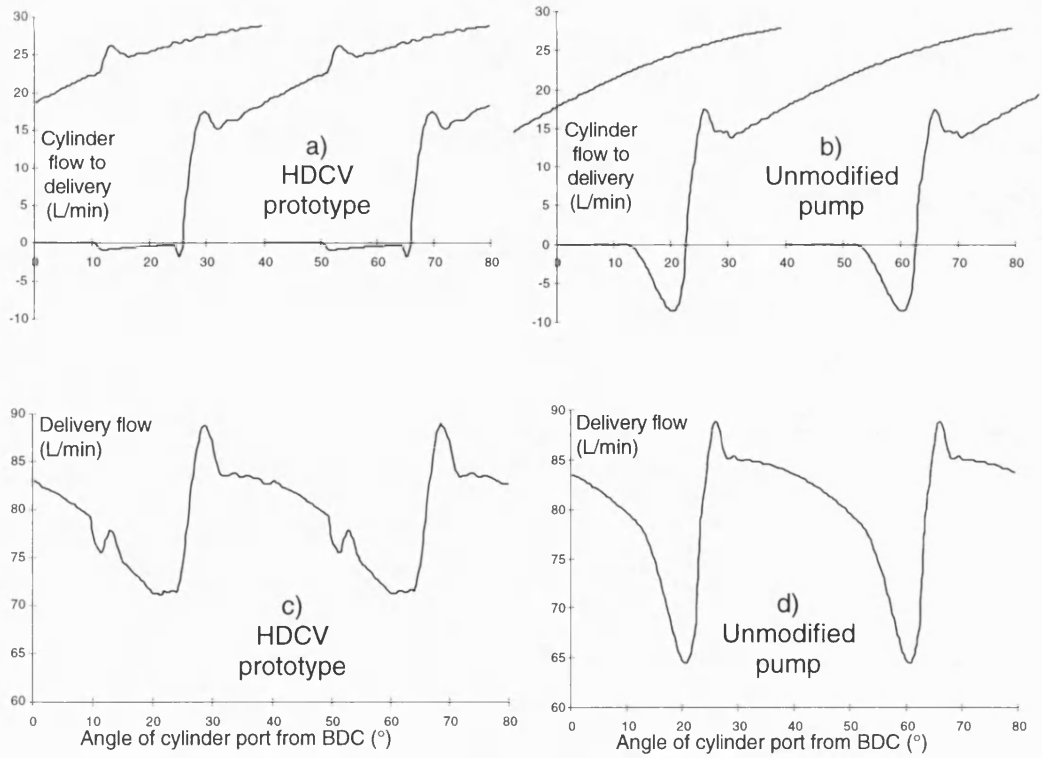

Figure 8.28a - d
Summation of the single cylinder delivery flows to give the simulated pump delivery flow for the HDCV prototype and the unmodified pump at 250 bar and 100% displacement

50 bar delivery pressure,
100% pump displacement

250 bar delivery pressure,
100% pump displacement

a)

Internal flow ripple (L/min)

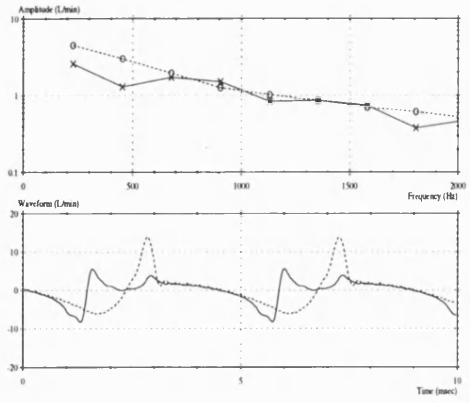

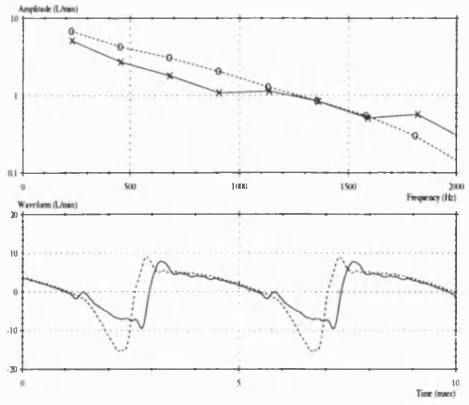

b)

Axial piston force (kN)

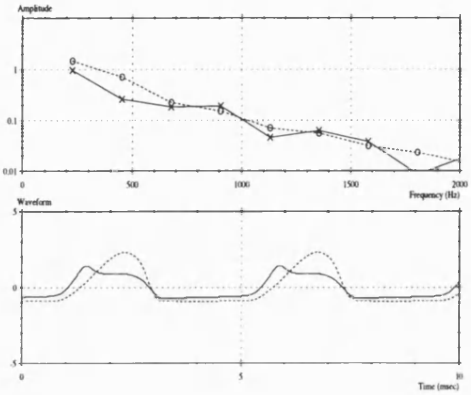

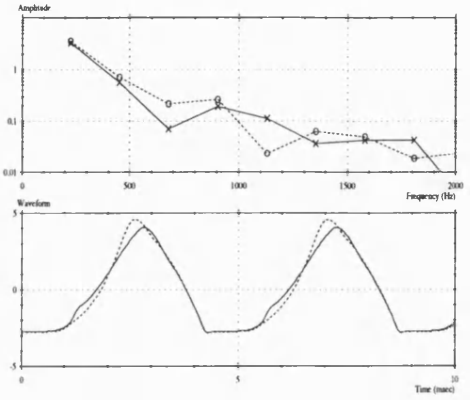

c)

Yoke moment (Nm)

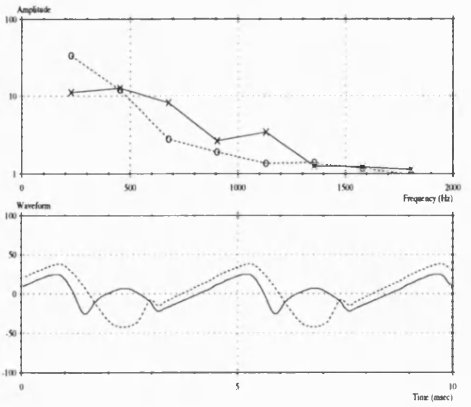

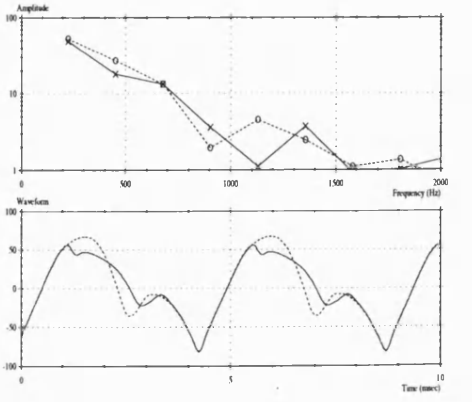

Figure 8.29

Figure 8.30

Performance comparison between the HDCV prototype (solid) and the unmodified pump (dashed)

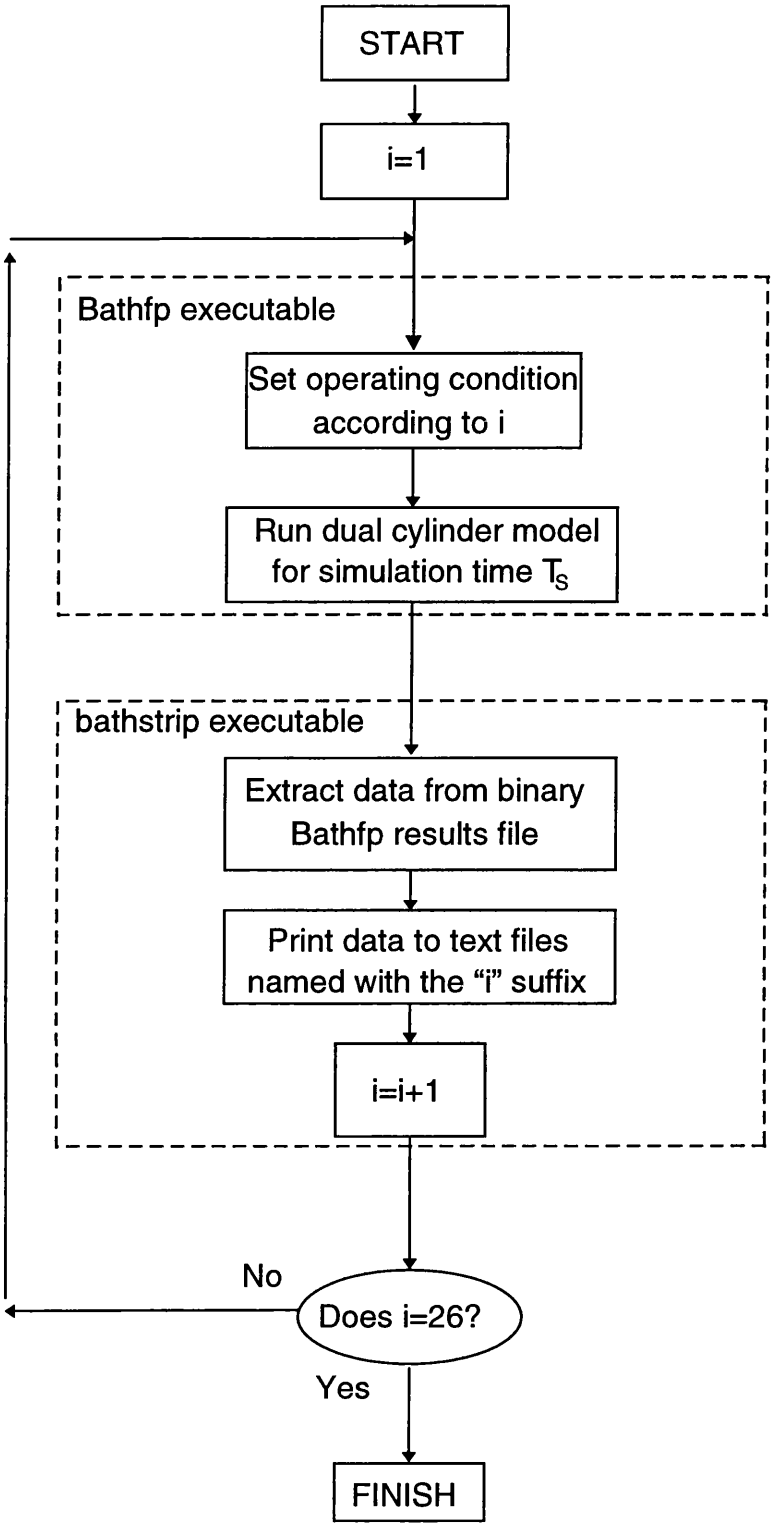

X P_{del}	50 bar	100 bar	150 bar	200 bar	250 bar
100%	i=1	6	11	16	21
80%	2	7	12	17	22
60%	3	8	13	18	23
40%	4	9	14	19	24
20%	5	10	15	20	25

Figure 8.31
Flowchart showing the initial operation of the batch simulations

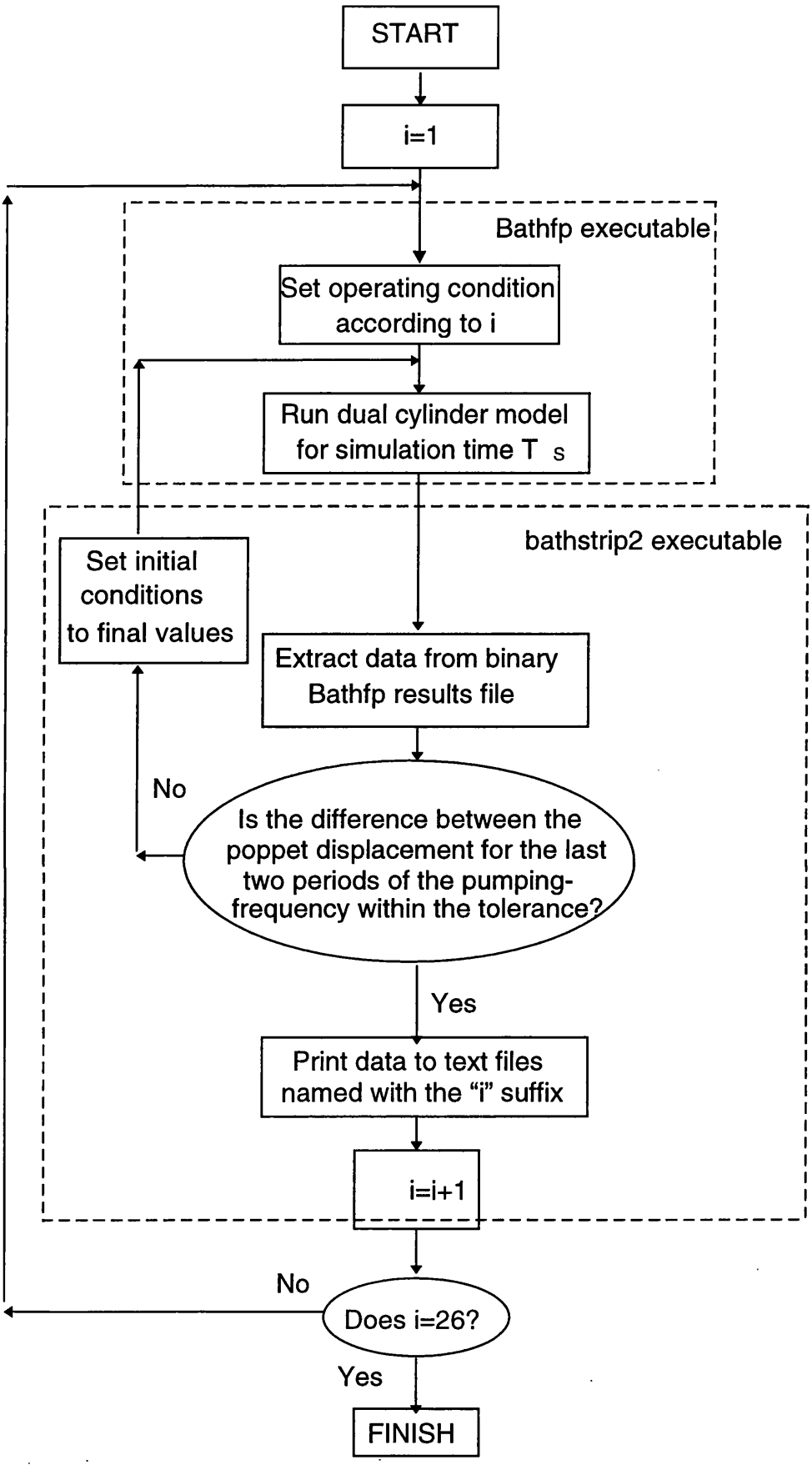

Figure 8.32
Operation of the batch simulations that included interrogation of the Bathfp results files

9.0 Development of the HDCV Prototype

9.1 Introduction

This section describes the development of the HDCV prototype, manufactured as a modification to the Vickers-supplied test pump (See Appendix C). The HDCV development work had two objectives:

1 Produce a HDCV prototype that generates significantly lower levels of delivery flow ripple and airborne noise than the unmodified pump.

2 Validate the simulation model of the test pump incorporating the HDCV prototype design.

During the initial course of development (9.2.1 - 9.2.3), deficiencies were identified in both the 2-port prototype design and the HDCV simulation model. The problems with the simulation model are covered in 9.2.4. The later development towards a successful 3-port design is described in section 9.2.5. The last prototype design was tested more thoroughly and this work is reported in section 9.3.

The final development iteration produced a design which caused a significantly smaller delivery flow ripple than the unmodified pump. This design also affected airborne noise, as demonstrated by the results of a comparative airborne noise test between the modified and unmodified test pumps (9.3.2). The results of this test showed that the prototype HDCV design caused a significant reduction in the airborne noise emitted by the test pump casing.

The development work is reviewed and recommendations are presented for further improvements to the prototype design and the simulation method in section 9.4

9.2 The Development Programme

9.2.1 Introduction

The scheme for a HDCV prototype was conceived with the design process described in section 8.2. Most of the parameters for a first prototype design were quantified by an appreciation of the restrictions imposed by the form of the test pump (See 8.2.5). To quantify the remaining parameters then a simulation model of the HDCV prototype was produced (See 8.3).

One difficulty was that the initial HDCV simulation model had not been validated with test results. Accordingly, the intention of the early development work was to improve both the performance of the HDCV prototype and the accuracy of the simulation model.

The performance of each HDCV prototype was assessed by measurement of the delivery flow ripple from the unboosted test pump. The flow ripple was measured using the secondary source test rig that had previously been used to investigate the delivery flow ripple of the test pump fitted with the standard valve block (See 5.2).

The HDCVs had no effect upon the pump source impedance. However, all of the HDCV prototypes used valve blocks that featured drillings through to the pump pressure compensator (See Appendix C). Therefore the HDCV prototypes had impedance spectra typical of those shown in figure 5.5. These impedance spectra were used with a parallel impedance model to process the pump internal flow ripple (See 5.3.3.1). As seen in 5.3.3.1, this approach leads to a small error in the calculation of the internal flow ripple for the 5th, 6th and 7th harmonics. However, for the purposes of validating the simulation model this error is regarded as insignificant.

The internal flow ripple from the later HDCV prototypes is compared with that from the standard test pump. In this case the internal flow ripple data for the standard test pump is that taken from the valve block that features no drillings to the pressure compensator. For this comparison, the error caused by the side drillings in the valve block used for the HDCV prototype is again regarded as insignificant.

By measuring only the pump delivery flow ripple, the precise behaviour of the HDCV prototype could not be ascertained. In particular it was difficult to establish the exact motion of the HDCV poppets. Instead, it was only possible to make broad observations such as whether the individual sleeve ports were open or closed.

Despite the difficulty in determining the exact behaviour of the HDCV poppets, considerable progress was achieved towards a successful design. The following sections illlustrate the development of the prototype design and the accompanying improvement of the simulation model. The prototype designs featured two and (later) three HDCVs fitted ahead of a delayed delivery port. The performance of the last prototype design is investigated in more detail in section 9.3.

9.2.2 Initial teething problems

The 1st HDCV prototype was based upon the scheme shown in figure 8.7. After the initial design exercise (See 8.2.5), only the poppet length, the characteristics of the compression spring, and the damping orifice lengths and diameters remained unspecified.. Values for the these parameters were estimated by using the simulation model (See Appendix E).

During initial testing, the HDCV prototype did not behave as predicted by the simulation model, and the overall performance of the prototype was poor. To improve the performance a number of teething problems had to be overcome by making changes to the prototype detail design. These measures are summarised below (See Appendix E for details):

1) The pocket containing the HDCV assemblies was enlarged to reduce any losses in the flow between the HDCV sleeve ports and the delivery chamber. The surface area of the new pocket was minimised by milling a cavity at 45° into the valve block. This prevented the delivery pressure in the pocket from lifting the portplate.

2) To prevent the HDCV valve springs from being crushed to their solid length, new end stops were incorporated by adding a "tail" to the HDCV poppets. (See appendix E).

3) Stiffer valve springs were used to reduce the effect of unpredictable flow forces. Specifically the spring rate was increased from 440N/m to 3330N/m with an increase in the spring preload at x=0 from 2.446N to 7.992N.

4) The step on the poppet was identified as a likely cause of the poppet becoming jammed. Accordingly, the poppet and sleeve was redesigned to remove the step.

5) The top face of the poppet was machined to a 45° cone. This helped to strengthen the poppets' top metering edge and so reduce the chance of a burr forming which may cause the poppet to jam. This cone may also help to direct the flow through the sleeve port to allow more accurate prediction of the flow forces acting on the poppet.

6) To vary the damping of the HDCV poppets, a needle valve was placed between the damping orifice of each HDCV and the delivery line. As the needle valves were closed, then the damping applied to the HDCVs was gradually increased.

Once these improvements had been carried out then the HDCV performance was much closer to that predicted by simulation. This is discussed in the next section

9.2.3 Performance of the !st. working prototype

The pump was quietest when the needle valves in series with the damping orifices were fully closed. The pipes connecting the damping orifices to the delivery line were therefore removed and replaced with blank fittings. The orientation of the sleeves was unchanged so that the hole in each sleeve still lined-up with the drilling through to the blanked-off damping orifice.

Figure 9.1 shows the change in the delivery flow ripple caused by blanking off the HDCV damping orifices. The main difference is at the higher flow, and higher delivery pressure conditions where the closure of the damping orifices causes the first HDCV port (@ 30° past BDC) to close. This was probably caused by the HDCV poppets previously being under-damped; each cylinder leaving the first HDCV would pressurise it to above the delivery pressure, causing the under-damped poppet to open wide the sleeve port. When each following cylinder arrives, then the open sleeve port would allow the reverse flow from the delivery port into the cylinder.

At lower displacement conditions then the mean opening force on both poppets is lower (See equations 8.43 and 8.44). Therefore, the poppet of the first HDCV is more likely to be held on its fully-closed endstop despite any lack of damping. This would explain why the closing of the damping orifices makes relatively little difference at the lower displacement conditions.

The finding that the damping orifice was redundant contradicted the results of simulation. As a result, the model was improved (See 9.2.4).

Figure 9.2 compares the measured delivery flow ripple from the unmodified test pump with that produced by the HDCV prototype featuring the blanked-off damping orifices. The results are mixed, with the standard pump producing a marginally lower level of delivery flow ripple for the majority of cases.

The poorer performance of the HDCV prototype falls within three groups, related to the optimal delivery port delay at those operating conditions (from table 8.1 - see 8.2.4.4):

Table 9.1

Group	Operating Condition		Optimal Delivery Delay
1	100 bar	100% flow	32.3°
	100 bar	80% flow	33.8°
	150 bar	100% flow	35.2°
2	150 bar	80% flow	37.0°
	200 bar	100% flow	37.9°
3	150 bar	20% flow	55.4°
	200 bar	20% flow	61.8°

The poor performance within the first group is caused by each cylinder being at a relatively low pressure on meeting the leading edge of the first HDCV. This results in rapid cylinder reverse flows that can clearly be identified in the measured delivery flow ripple (See fig 9.2).

The poor performance within the second group is caused by each cylinder being above delivery pressure on meeting the leading edge of the second HDCV (@ 40° past BDC). This results in a sharp cylinder outflow which is visible in the measured delivery flow ripple. The results from the third group indicate that the second HDCV is also open. However, at these conditions, the cylinders meet the second HDCV whilst significantly below the delivery pressure. As a result, large cylinder inflows can be seen in the measured delivery flow.

The performance of the third group would be improved if a third HDCV was added between the delayed delivery port and the second HDCV; flow through the new port would pre-compress each cylinder later in the delivery stroke and so prevent large cylinder reverse flows. This would also reduce the mean port pressure over the second port to ensure that it stays closed.

A third HDCV may also reduce the flow ripple within the second group of results. The new port would remain open and may act to relieve the cylinder over-compression seen at these conditions.

The problem with the addition of a third HDCV is that the valve block casting runs out into the delivery chamber at the position where a third HDCV would be housed (See 8.2.4). However, on closer inspection of the pump valve block, it was found that a third port could be fitted if the sleeve and poppet were modified. The details of this improvement and the resulting flow ripple from this design are discussed in 9.2.5.

The performance within the first group of conditions could be improved if the first port was further delayed. However, this would simply cause large cylinder reverse flows at conditions with a later optimal delivery timing and so would bring no overall benefit. A more promising solution would be to restrict the flow through this HDCV.

The most straightforward method of introducing a restriction to the first HDCV is to reduce the diameter of the sleeve port drilling. This idea was investigated with the simulation

model. It was found that the poppet compensated for the smaller sleeve port by moving to a greater opening. Smaller sleeve port diameters were investigated but then the effectiveness of the HDCV over a wide range of operating conditions was diminished. It was concluded that the best way to restrict the flow through this HDCV was to reduce the diameter of the HDCV drilling within the portplate. However, all of the available portplates featured drillings that were of the existing 5mm diameter. Therefore it was decided to press on with the third port design without improving the performance of the HDCVs at this group of conditions.

9.2.4 Improvement of the HDCV Simulation Model

Figure 9.3 shows that the delivery flow ripple from the test pump with the closed damping orifices was in broad agreement with that from the simulation model which still assumed that the damping orifices were open. From this, the real and simulated HDCV prototypes now exhibited similar levels of damping despite the closure of the damping orifices in the test pump. This was unexpected because when the simulated damping orifice diameter was set to zero then the poppet response also reduced to zero. This can be seen with equation 8.40a, where if $K_D = 0$ then at steady state,

$$\frac{x}{P_{port}} = \frac{A_{pop}K_D}{K_S(K_D + K_L)} = 0 \text{ mm/bar}$$

This is clearly in error as shown by figure 9.3 where the delivery flow ripple clearly indicates that the first and second HDCVs open and close according to the pump operating point. However, this anomaly could be explained if the flow between each HDCV spring chamber and the delivery port did not exclusively pass through the damping orifice. In this case, when the damping orifice diameter was set to zero then there would still be leakage into the spring chamber from the delivery port. The most likely source of this leakage is through the clearance between the sleeves and sleeve drillings in the valve block (See figure 8.7).

Another feature of figure 9.3 is that at 200 bar delivery pressure and 20% pump displacement, the agreement between simulation and test is poor. The simulation predicts that the second HDCV port remains closed whereas the measured delivery flow ripple shows that the second port stays open. This suggests that the simulation is underestimating the mean port pressure acting to open the second HDCV port. The reason for this may be that the simulation assumes no leakage from the delivery port to the cylinders when the sleeve ports are closed. Such a leakage would help to pre-compress each cylinder to the delivery pressure and so would help to increase the mean port pressure acting to open the HDCVs. Furthermore leakage through a closed HDCV is likely - through the clearance between poppet and sleeve and also between sleeve and the matching counter-bore machined into the portplate (See figure 8.7).

To account for the discrepancies between test and simulation highlighted in figure 9.3, the simulation model was changed in three respects (See figure 9.4):

1 Leakage was included around the outside diameter of each sleeve between the spring chamber and the delivery port - q_{sleak}.

2 Leakage was included around the outside diameter of each sleeve between the delivery port and overlapping cylinder port - q_{cleak}.

3 The sleeve port flow (q_x) was modified so that when each sleeve port was fully covered by the poppet then there was still a small leakage between the poppet and sleeve.

The addition of these flow terms meant that the flow continuity within the simulation volumes was altered (See fig. 9.4):

For the Cylinder volume, equation 8.3 (from 8.3.1.2) became,

$$q_{net} = q_{suc} + q_{del} + q_{pist} - q_{leak} - \sum_{j=1}^{j=m}\left(q_p(j) + q_{cleak}(j)\right) \tag{9.1}$$

and for the spring chamber volume, equation 8.15 (from 8.3.1.4) became,

$$q_{chnet} = vA_{pop} + q_l - q_d - q_{sleak} \tag{9.2}$$

These leakages also contributed to the total delivery flow. Accordingly the flow summation of equation 8.2 (from 8.3.1.1) became,

$$\begin{aligned} totalq = \sum_{i=1}^{i=n} q_{kin}\left(\omega t + \frac{2\pi i}{n}\right) - \left(q_{del}(\alpha) + q_{kin}(\alpha)\right) - \left(q_{del}(\beta_l) + q_{kin}(\beta_l)\right) \\ - \sum_{i=1}^{i=n}\frac{2}{n}\left(K_{LC}P_{cyl}(i)^n\right) + \sum_{k=1}^{k=p}\left(q_x(k) + q_d(k) + q_{cleak}(k) + q_{sleak}(k)\right) \end{aligned} \tag{9.3}$$

The leakage into the spring chamber was assumed to be laminar and was relatively straightforward to estimate. Figure 9.3 confirmed that this leakage provides the same damping that would be expected from the damping orifice alone. Therefore, the q_{sleak} term was scaled such that,

$$q_{sleak} = K_{sl}(P_{ch} - P_{del}) \qquad \text{where} \tag{9.4}$$

$K_{sl} = K_D$ for $D_{damp} = 0.4mm$ and $L_{damp} = 8mm$ (See Eq. 8.38 in 8.3.2.3)

The other two leakages were also assumed to be laminar but were more difficult to estimate. However, the delivery flow ripple from the test pump was known and so the relative magnitude of these leakages was varied until the simulation gave better agreement with the measured results. The final expression for the leakage around the sleeve between the cylinders and the delivery port is given by,

$$q_{cleak} = K_{cl}(P_{cyl} - P_{del}) \qquad \text{where } K_{cl} = 1.5 * K_{sl} \tag{9.5}$$

A relationship of this kind could be expected as the clearance around the sleeve is the same for both flow paths (See figure 9.5). The only difference is that the flow path for q_{cleak} is shorter which gives rise to a multiplication factor (in this case set to 1.5).

The leakage between each poppet and sleeve was accounted for by adding a term to the sleeve port flow area A_{orifx} based upon the clearance between poppet and sleeve. When the sleeve port was closed and $x \le 0$ then,

$$A_{orifx} = hD_{pop}\left(\frac{2x_{lap} + x}{2x_{lap}}\right) \tag{9.6}$$

When the sleeve port was open then (See 8.3.1.3 and equation 8.11),

$$A_{orifx} = 2\left[\frac{\pi r^2}{2} + (x-r)\sqrt{r^2 - (x-r)^2} + r^2\sin^{-1}\left(\frac{x-r}{r}\right)\right] + hD_{pop}\left(\frac{2r-x}{2r}\right)^2 \tag{9.7}$$

Using these assumptions then the maximum leakage is at x=0 where the leakage area is equivalent to the full clearance between the poppet and sleeve. The leakage reduces to a minimum when the port is fully open at x=2r (See Eq 9.7) and also when the poppet is on the fully closed endstop at x=-xlap (See Eq. 9.6).

The delivery flow ripple predicted by the new model is compared with test measurements in figure 9.5. This is the comparison that was carried out in figure 9.3, except that in this case the model assumes the damping orifices to be blanked off, as is the situation with the pump under test.

Over the majority of the operating range, the new features of the simulation model do not affect the predicted flow ripple. However, at 150 bar and 80% displacement then the new model incorrectly predicts that the first HDCV port remains open. This may be due to over-estimation of the new leakage terms between the delivery port and the cylinder ports (q_{cleak} and the change to the sleeve port area). These terms may be predicting significant leakage from the high pressure delivery port into the cylinders. This would cause the individual cylinder ports to pressurise more rapidly which would then increase the opening force acting on the individual HDCV poppets.

At 200 bar and 20% displacement the new leakage terms remove the simulated cylinder over-compression that was present in the original model (See figure 9.3). However the predicted delivery flow ripple at this condition and also at the 150 bar, 80% displacement condition are significantly different to those measured during testing. It is clear that the simulation model needs further improvement, although this is difficult with only the pump delivery flow ripple for validation. To further improve the model test data of the poppet motion would be needed. Empirical data for the various leakage terms would also be needed.

9.2.5 Design and Performance of the improved HDCV Prototype

The main conclusion from testing the previous HDCV prototype was that another HDCV was needed (See 9.2.3). However, a problem was that the valve block casting runs out into the delivery chamber at the point where the new HDCV sleeve assembly would be fitted (See figure 8.7). This problem was overcome by lengthening the sleeve and poppet of the new HDCV (See figure 9.6). The longer sleeve of the third HDCV could then be fitted into a deeper portion of the valve block casting.

The scheme for this prototype is shown in figure 9.6 and the new poppet and sleeve are detailed in Appendix E. The centreline for the third HDCV port is at 58° past BDC. The portplate drilling for this port is the same size as the other HDCV ports (5mm diameter subtending an angle of 8°) and so the leading edge of this port is at 54° past BDC.

The new HDCV featured no damping orifice, and the original HDCVs had their damping orifices replaced with blank fittings, in line with the findings of 9.2.3. The other details of this design corresponded to those of the previous prototype.

This prototype was tested as before. Unexpectedly, the third HDCV port made no difference to the pump flow ripple. What these results implied was that the third port was remaining closed over the whole operating range. This may have been caused by the proximity of the new HDCV with the delivery port; cylinders passing over this HDCV equalised rapidly to the delivery pressure and so the mean port pressure for this valve would always be near to the delivery pressure. The spring chamber pressure would also be close to the delivery pressure and so the differential pressure across the poppet would not become great enough to overcome the cracking pressure set by the preload of the valve spring.

To overcome this problem, the poppet of the new HDCV was redesigned with an unequal face area. This meant that if the pressure difference across the poppet was small then the poppet would still experience a net valve opening force. The new design of poppet and its matching sleeve are detailed in Appendix E.

The new sleeve and poppet were fitted to the test pump and the delivery flow ripple measured. This change made the pump significantly less noisy. For the first time this then enabled testing up to a delivery pressure of 250 bar. At 250 bar and lower displacements the HDCVs definitely reduced the pump airborne noise and so at this point the development exercise was stopped and the test results from the pump analysed in more detail. This work is presented in the next section.

9.3 Performance of the final HDCV prototype

This section describes the findings of test and simulation carried out on the final HDCV prototype. This prototype is sketched in figure 9.6 and detailed in Appendix E.

9.3.1 The reduction in delivery flow ripple

9.3.1.1 Comparison between the 2 and 3 port performance

Figure 9.7 compares the internal flow ripple measured from the final 3-port HDCV prototype with that from the 1st working (2-port) prototype.

At the majority of operating conditions the 3-port design produces a similar delivery flow ripple to that produced by the 2-port design. These are generally conditions where the 2-port design had effectively equalised the cylinders to delivery pressure, and so any benefit from the 3rd port is small.

Four of the operating conditions shown in figure 9.7 are examined in more detail in figures 9.8 - 9.12. In these figures, the positions are highlighted where successive cylinder ports meet the HDCV portplate drillings and the delayed delivery port. In the interpretation of these results the HDCVs at 30°, 44°, and 58° are referred to as the 1st, 2nd, and 3rd HDCVs respectively.

9.3.1.1.1 Comparison at 200 bar, 80% displacement

Figure 9.8 compares the measured internal flow ripple from the 2 and 3 port designs for the pump operating at 80% displacement and 200 bar delivery pressure. From figure 9.8 it can be deduced that the 1st HDCV is closed and the 2nd HDCV open at this condition for both designs.

For the 3-port design, before each cylinder reaches the 3rd HDCV, the delivery flow drops significantly below that of the 2-port design. This suggests that, during this period, the 2nd HDCV of the 3-port design partially closes. Once each cylinder reaches the 3rd HDCV then the delivery flow rises again, indicating that this port is open.

For the 3-port design, when each cylinder reaches the delayed delivery port there is a large cylinder outflow. This indicates that each cylinder has over-compressed due to restriction of the cylinder flow through the HDCVs. The 2-port delivery flow ripple doesn't show this effect and so it can be deduced that the flow area of the 2nd HDCV within the 2-port design is greater than the combined flow area of the 2nd and 3rd HDCVs in the 3-port design at this condition.

9.3.1.1.2 Comparison at 100 bar, full displacement

Figure 9.9 compares the measured internal flow ripple from the 2 and 3 port designs at the 100 bar delivery pressure, full displacement condition. From this figure it can be deduced that the 1st and 2nd HDCVs are open at this condition for both designs.

As with the 200 bar, 80% displacement condition, the delivery flow from the 3 port design drops below that of the 2 port design just before each cylinder reaches the 3rd HDCV. In this case the drop in delivery flow is caused by partial closure of the 1st and 2nd HDCVs. As before, the delivery flow rises on reaching the 3rd HDCV, indicating that the 3rd port is open.

For the 3-port design at the 200 bar, 80% displacement condition there is a rapid cylinder flow into the delivery port caused by partial closure of the 2nd and 3rd HDCVs. At 100 bar and 100% displacement, the partial closure of the 1st and 2nd HDCVs does not appear to cause a similar cylinder outflow. However, at the 100 bar condition such a cylinder outflow may be cancelling with a cylinder inflow from the following cylinder through the 1st HDCV (See figure 9.9). This would explain why the reverse flow through the 1st HDCV has a larger effect upon the delivery flow of the 2-port design than it does on that of the 3-port design.

This interaction between the flow through the delivery port and the 1st HDCV is significant: it demonstrates an inter-cylinder effect that helps to reduce the delivery flow ripple.

The interpretation of figures 9.8 and 9.9 has established that the HDCV poppet motion at the pumping frequency is large. This implies that the HDCVs are still under-damped, despite the blanking-off of the damping orifices. The motion of the HDCV poppets at the pumping frequency makes interpretation of HDCV behaviour from measurements of the delivery flow ripple much more difficult: the main flow changes can still be attributed to particular poppets being open or closed, but the more minor flow changes are now much more difficult to explain. To help explain the effects of adding the 3rd HDCV, figures 9.10a - d

compare simulation results for the 2 and 3 port designs for the 100 bar delivery pressure, full displacement condition.

Figure 9.10a shows the simulated delivery flow ripple for the two designs; figure 9.10b shows the simulated poppet motion; figure 9.10c the HDCV port pressures and figure 9.10d the HDCV port flows.

From figure 9.10b, the comparison of simulated poppet displacement clearly shows that the model overestimates the damping applied to the HDCV poppets. As a result, the simulated flow ripple for the two designs differs from the measured flow ripple shown in figure 9.9. In particular, figure 9.10a shows that the model fails to predict the partial closure of the 1st and 2nd HDCVs for the 3-port design. The model gives better agreement with the measured flow ripple of the 2-port design as this appears less sensitive to the incorrect level of damping used in the simulation model.

The partial closure of the 2nd HDCV within the 3-port design can be explained with the port pressure comparison of figure 9.10c. The 3-port trace shows that the port pressure of the 3rd HDCV remains close to the delivery pressure. This is because the 3rd HDCV poppet has an unequal face area and so is forced to open its sleeve port even if the cylinder above the port is at delivery pressure (See Appendix E). The effect of this on the port pressure of the 2nd HDCV can be seen at 38°. In the 2-port design the increasing piston speed causes the cylinder pressure to rise. However, in the 3-port design, the cylinder meets the 3rd port and is partly de-pressurised. This immediately reduces the cylinder pressure acting on the poppet in the 2nd HDCV. In the under-damped HDCVs of the real pump this probably causes the near closure of the 2nd HDCV. In the much more heavily damped HDCVs of the simulation then the 2nd HDCV only closes by 0.1mm.

In the simulation, the 3rd HDCV reduces the mean port pressure of the 2nd HDCV. This results in a mean closure of the poppet within the 2nd HDCV from an opening of 2.2mm in the 2-port design to one of 1.2mm in the 3-port design (see figure 9.10b).

In the simulation, the reduced opening of the 2nd HDCV port within the 3-port design is accompanied by an increased opening of the 1st HDCV port (See figure 9.10b). This can be explained with figure 9.10d. Between 30 and 50° a smaller proportion of the cylinder flow passes through the 2nd HDCV and a correspondingly larger flow passes through the 1st HDCV. This indicates that the pressure drop through the sleeve port of the 1st HDCV has increased; there is a greater pressure difference across the poppet of the 1st HDCV which causes it to open further the sleeve port.

9.3.1.1.3 Comparison at 200 bar, full displacement

Figure 9.11 compares the measured internal flow ripple from the 2 and 3 port HDCV designs with the pump operating at 200 bar delivery pressure and full displacement. From figure 9.11 it can be deduced that the 1st HDCV is closed within the 2-port design and open within the 3-port design.

These results adhere to the trends that were identified in 9.3.1.1.2 in that the addition of the 3rd HDCV causes the 1st HDCV to open.

A new feature of the 3-port flow ripple occurs just before each cylinder reaches the delayed delivery port (@ 2.7 and 7.1ms in figure 9.11); there is a rapid cylinder outflow indicating that the cylinder has become over-pressurised. These outflows occur when the cylinder ports have left the first HDCV. They suggest that the majority of the cylinder flow passes through the 1st HDCV, possibly to the extent that the 2nd HDCV is closed. This implies that the HDCVs do not always open progressively (as discussed in 9.2.3)

9.3.1.1.4 Comparison at 200 bar, 20% displacement

Figure 9.12 compares the measured internal flow ripple from the 2 and 3 port designs with the pump operating at 200 bar delivery pressure and 20% displacement. From figure 9.12 it can be deduced that for the 2-port design, the 1st HDCV is closed and the 2nd is open. For the 3-port design only the 3rd HDCV is open.

Again, these results adhere to the trends that were identified in 9.3.1.1.2 in that the addition of the 3rd HDCV causes the 2nd HDCV to close. At this condition, the addition of the 3rd port causes a significant reduction in the delivery flow ripple. This is because each cylinder pre-compresses close to the delivery pressure before meeting the leading edge of the 3rd HDCV (As predicted in 9.2.3).

9.3.1.2 Comparison between measurements and simulation

Figures 9.13a and b compare the measured and simulated flow ripple for the final 3-port HDCV prototype over a range of delivery pressures and pump displacements.

To produce the simulation results, the model was altered to account for the unequal poppet area of the 3rd HDCV. At 50 bar delivery pressure, simulation results for the pump operating below full displacement are shown without accompanying test measurements. This is because the test pump could not be de-swashed below 90 bar delivery pressure due to the pre-load of the bias spring acting on the swashplate.

Figures 9.13a and b show that the simulation model only gives partial agreement with the measured internal flow ripple from the 3-port design. By comparison with figure 9.5 it can be seen that the agreement between simulation and test for the 3-port design is generally worse than that achieved for the 2-port design. This is because the 3-port design is more dependent upon the level of damping within the HDCVs; in 9.3.1.1.2 the simulated level of HDCV damping was demonstrated to be far higher than that of the real pump and as a result the 3-port simulations are less accurate than those for the 2-port design.

At lower delivery pressures and higher pump displacements, figures 9.13a and b show that the model over-estimates the size of cylinder reverse flows through the 1st HDCV. This behaviour is examined in 9.3.1.1.2; the relatively small cylinder reverse flow through the 1st HDCV that is seen in the delivery flow ripple is probably caused by partial cancellation with a cylinder outflow from the previous cylinder into the delivery port. In this case the differences

between simulation and test are again caused by over-estimation of the modelled HDCV damping.

At 200 bar and full displacement, figure 9.13b shows that the model does not predict the opening of the 1st HDCV. Also, at 40% displacement for 200 and 250 bar delivery pressure, the model does not predict the opening of the 2nd HDCV. This shows that the model is under-estimating the sleeve port opening forces on the HDCV poppets. The reason for this is likely to be that the model is under-estimating the pressure of cylinders passing over the HDCVs. This has a number of possible causes:

1 The effective fluid bulk modulus within the cylinders during pressurisation is higher than the modelled constant value of 11000 bar

2 The model is over-estimating the cylinder leakage to return (q_{leak})

3 The model is under-estimating the leakage from the delivery chamber through the closed HDCVs into cylinders as they approach the delivery port (See 9.2.4)

A more optimistic interpretation of figures 9.13a and b is that the model correctly predicts whether the three HDCVs are open or closed in 18 out of 21 cases. This means that for the 18 correct cases, the rise in cylinder pressure is quite accurately modelled by the simulation. This is significant as it allows the simulation to be used for predicting effects for subsequent investigation such as the yoke moment ripple (See 9.3.2.2).

At higher delivery pressures and higher pump displacements, figures 9.13b and c show that the model does not predict the large poppet movements that occur at the pumping frequency. This is discussed in 9.3.1.1.2 and is the clearest indication that the simulated HDCV damping is much higher than the damping in the real pump.

Another measure of the HDCV damping is their response to changes in the pump operating condition. In the simulation, the HDCV response to any step change in delivery pressure or pump displacement is typically within 0.3 seconds. On the test rig, step changes in operating condition are not possible and so an ideal comparison with simulation is unavailable. Instead the load pressure can be changed reliably within 0.5 seconds and the HDCV response can be estimated by ear as the time for the pump ABN to stabilize. However, when the test rig load pressure was changed over 0.5 seconds, the HDCV response could be heard to take up to 5 - 6 seconds.

This result contradicts the HDCV flow ripple measurements in that it implies that the simulated HDCV damping is much lower than the damping in the real pump. However, this anomaly may be explained by regarding the large poppet motion seen in the delivery flow ripple as a high frequency effect, and the slow HDCV response to changes in operating condition as a low frequency effect.

In 8.3.2.3, figure 8.13c shows that the compressibility of the spring chamber predominately affects the higher frequency poppet response. Similarly, figures 8.13b and 8.13e show the low frequency poppet response to be dependent upon the spring stiffness and the leakage through the poppet-sleeve clearance. Therefore, the anomalies in the modelled HDCV response could be dealt with separately;

a) The modelled HDCV response at high frequency would be increased if the spring chamber compressibility was increased. This would be accounted for if the effective fluid bulk modulus within the spring chambers is far lower than the modelled constant value of 11000 bar. One reason for this may be that the rapid poppet motion is causing cavitation or air release within the closed spring chambers. The increase in response needed at the higher frequencies is difficult to estimate without direct measurement of the poppet motion. One method would be to reduce the modelled value of fluid bulk modulus within the spring chambers until the delivery flow ripple resembled the measured characteristics.

b) The modelled HDCV response at low frequency would be attenuated if the modelled spring stiffness was increased and if the modelled leakage through the poppet-sleeve clearance was increased. With a combination of these measures, the low frequency poppet response would need to be attenuated by a factor of approximately 20.

Both measures a) and b) could be carried out in a future simulation exercise. However the attenuation in the low frequency response would greatly increase the simulation run times. The simulations are run as batches of 25 operating conditions (See 8.3.3.2), and at each condition, the Bathfp model is run repeatedly until the HDCV poppets have reached their final displacements; if the poppet response is slowed by a factor of 20 then the overall batch run time will be increased by the same factor.

A batch of 3-port simulations takes approximately 10 hours to run on a dedicated SPARC10 processor. If the poppet response is slowed by a factor of 20, then the same batch run would last nearly 9 days.

9.3.1.3 Comparison of the HDCV prototype with the standard pump

Figures 9.14a and b compare the measured internal flow ripple of the final HDCV prototype with that produced by the standard pump. The comparison is carried out with both the flow ripple wave form and the flow ripple amplitude at harmonics of the pumping frequency. Twenty operating conditions are compared for the unboosted pump running at 1500rev/min between 100 and 250 bar delivery pressure and for pump displacements between 20 and 100%.

The HDCV prototype achieves the largest reductions in delivery flow ripple at lower pump displacement conditions. A common factor at these conditions is that the HDCVs significantly reduce the first 4 flow ripple harmonics. At higher harmonics for these conditions, the HDCV performance is more mixed.

At higher pump displacement conditions, the HDCVs again reduce the lower flow ripple harmonics, although in this case the improvements are less distinct. A common factor at these conditions is that the HDCVs increase the 5th to the 8th flow ripple harmonics. This is likely to be caused by rapid movements of the under-damped HDCV poppets. The effect is less common at the lower displacement conditions; lower piston speeds cause the pump cylinders to pressurise more slowly and so any rapid poppet movements are less pronounced.

As demonstrated at the lower displacement conditions, the largest reductions in flow ripple from the standard pump occur when the first 4 flow ripple harmonics are attenuated. This result was expected; previously it had been found that the internal flow ripple from the standard pump was dominated by the first 5 harmonics (See 5.3.3.1).

At higher displacement conditions, increased poppet motion contributes to larger flow ripple from the HDCV prototype. This demonstrates that further reductions in flow ripple could be achieved if the HDCV valve response at these higher frequencies could be attenuated.

Testing was only carried out at a single pump speed of 1500rev/min. To investigate the HDCV performance at other drive speeds, simulations were carried out for the pump running at 1000rev/min and 2000rev/min. These simulations showed that in 80% of cases the HDCV prototype produced a significantly smaller flow ripple than the unmodified pump. Furthermore, the 20% of simulations that predicted no improvement occurred at operating conditions corresponding to those of figure 9.13a and b where the simulations over-estimated the level of flow ripple: from this it can be deduced that the HDCV prototype is likely to perform well at drive speeds of 1000 and 2000rev/min.

9.3.2 The reduction in pump ABN

This section describes test work that was carried out to measure the effect of the HDCVs on airborne noise caused by the pump. The test method is described and ABN levels from the casing of the final HDCV prototype are compared with those of the standard pump.

The ABN caused by the pump was measured using the flow ripple test rig (See figure 5.3). As a result, the ABN measurements were carried out within a confined and highly reverberant test cell. Within this test cell it was impractical to isolate the pump noise from that caused by the A.C. motor and the circuit loading valve. To minimise the influence of noise from the A.C. motor and the circuit loading valve, the ABN was measured close to the pump casing; in this situation it was expected that the incident ABN from the pump casing would be the main effect measured by the meter.

The delivery line of the test circuit was relatively stiff and so could not be regarded as a typical loading circuit. Accordingly, no attempt was made to measure the effect of the pump pressure ripple and casing vibration in causing circuit-excited ABN (See 2.2).

9.3.2.1 Description of test method

During this test exercise, sound pressure levels were measured with a Bruel & Kjaer type 2203 sound level meter. To measure the ABN from the pump casing, this meter was mounted on a tripod with its microphone pointing towards the pump casing at a distance of 10cm. The position of the meter within the test cell is illustrated in figure 5.3.

The ABN readings were measured visually from the moving point readout on the meter. To aid accurate measurement, the moving point meter was damped by using the "slow" setting [71]. The octave filter set was disconnected and the meter input was set to "lin" for unweighted readings, and to "A" for A-weighted readings (See 2.3.1).

To ensure valid comparisons between different SPL measurements, all of the measurements were taken with the sound level meter in exactly the same position and orientation. For all of the different tests, the test cell layout remained as shown in figure 5.3.

9.3.2.2 Comparison of the HDCV prototype with the standard pump

The sound pressure level from the casing of the standard pump was measured over a range of delivery pressures and pump displacements. This was then repeated for the final HDCV prototype. In both cases the pump was run unboosted at 1500rev/min.

Table 9.2 compares the SPL measurements of the two pump designs. The A-weighted measurements are also presented in figures 9.15a, b, and c.

Figure 9.15a shows that the measured SPL from the casing of the standard pump generally increases with delivery pressure. The SPL is less dependent upon the pump displacement. Also, the effect of pump displacement upon the SPL changes with delivery pressure. At 100 bar delivery pressure the SPL is highest at full displacement, whereas at 250 bar the highest SPL occurs at 20% displacement.

Figure 9.15b shows that the SPL measured from the HDCV prototype also increases with delivery pressure, although to a lesser extent than the standard pump. Unlike the standard pump, the SPL from the HDCV prototype generally falls with reducing pump displacement.

A drawback with figures 9.15a and b is that the results include noise from the A.C. motor and the circuit loading valve. The SPL from these sources would be expected to increase with the power output of the pump; i.e. at higher delivery pressures and pump displacements. The finding that the measured SPL does not conform to both these trends shows that ABN from the pump casing is the main effect measured by the sound level meter.

Table 9.2

dB ***dB(A)***	**Delivery Pressure (bar)**							
Disp %	100		150		200		250	
100	95.0$_a$	*92.5$_a$*	96.5	*95.0*	97.0	*94.5*	100.5	*97.0*
	99.5$_b$	*94.5$_b$*	100.5	*97.0*	100.5	*97.5*	100.5	*98.0*
	-4.5$_c$	***-2.0$_c$***	**-4.0**	***-2.0***	**-3.5**	***-3.0***	**0.0**	***-1.0***
80	95.0	*92.5*	96.0	*94.0*	98.5	*96.0*	97.0	*94.0*
	97.5	*93.5*	99.0	*96.5*	101.0	*98.5*	101.5	*97.5*
	-2.5	***-1.0***	**-3.0**	***-2.5***	**-2.5**	***-2.5***	**-4.5**	***-3.5***
60	94.5	*91.5*	95.5	*92.5*	96.0	*92.5*	95.5	*92.5*
	96.5	*92.5*	97.5	*95.5*	99.5	*97.0*	102.0	*98.0*
	-2.0	***-1.0***	**-2.0**	***-3.0***	**-3.5**	***-4.5***	**-6.5**	***-5.5***
40	94.5	*91.0*	94.5	*90.5*	96.0	*93.0*	96.5	*95.0*
	96.5	*93.0*	97.5	*94.5*	98.5	*96.5*	102.0	*98.0*
	-2.0	***-2.0***	**-3.0**	***-4.0***	**-2.5**	***-3.5***	**-5.5**	***-3.0***
20	94.0	*90.0*	95.0	*92.0*	95.0	*92.0*	96.5	*95.0*
	96.5	*93.0*	99.5	*96.5*	101.0	*98.0*	102.5	*99.0*
	-2.5	***-3.0***	**-4.5**	***-4.5***	**-6.0**	***-6.0***	**-6.0**	***-4.0***

a HDCV b Std c (HDCV-Std)

At a given delivery pressure and pump displacement, the contribution to the measured SPL from the A.C. motor and the circuit loading valve will be the same for both pump designs. Therefore, the noise from these sources is removed by regarding the difference in measured SPL produced by the two pump designs, as shown in figure 9.15c.

Figure 9.15c shows that the HDCV prototype causes reductions in the casing SPL of between 1 and 6dB(A) at every measured operating condition. In line with the trends identified from figures 9.15a and b, the largest SPL reductions occur at higher delivery pressures and lower pump displacements. The causes of this general trend were investigated by analysing the variations in the pump FBN and SBN over the same operating conditions.

The internal flow ripple results displayed in figures 9.14a and b could be used to represent the variation in FBN over the operating range. However, a drawback with the internal flow ripple is that it depends on the accuracy of the fitted discharge passageway model [19].

Another rating for pump FBN is the blocked pressure ripple, which is a characteristic that assumes the pump source impedance is much smaller than the entry impedance of the connected load circuit (See 2.4.2.3). It is calculated at a particular frequency as the product of the pump source impedance and the circuit entry flow ripple. The blocked pressure ripple is widely used [19], and was chosen to represent the variation in pump FBN

The pump SBN was not measured and so instead the simulated yoke moment ripple was chosen to represent the variation in pump SBN. The yoke moment ripple was chosen because in 3.3.3 it was demonstrated to have significant potential as a source of axial piston pump SBN.

Figures 9.16a, b, c, and d graphically present A-weighted overall RMS values for the first 20 pumping frequency harmonics of the measured blocked pressure ripple and simulated yoke moment for the two pump designs. The reduction in blocked pressure ripple and yoke moment ripple achieved by the HDCV prototype over the standard pump are shown in figures 9.16e and f. These results are measured in dB(A) for comparison with the ABN reductions of figure 9.15c.

As would be expected, the general form of the reduction in blocked pressure ripple is similar to that seen for the internal flow ripple (See figures 9.14a and b): the reduction is over the whole operating range and is greatest at low flow, high delivery pressure conditions.

Figure 9.16d shows that the yoke moment ripple is increased by the HDCV prototype at low delivery pressure and high displacement conditions. This is probably caused by the opening of the 1st HDCV at these conditions (See figure 9.14a). When the 1st HDCV is open then the cylinders pressurise earlier than those within the standard pump, which then causes a larger change in yoke moment when the cylinder passing TDC depressurises. Once the 1st HDCV closes then the cylinders within the HDCV prototype pressurise later than those in the standard pump; the change in yoke moment caused by the pressurisation of the cylinder at TDC is then less than within the standard pump.

Figures 9.16e and f show that the greatest reductions in blocked pressure ripple and yoke moment ripple coincide with the largest reductions in casing SPL; namely at the high delivery pressure, low pump displacement conditions. Furthermore the reductions in blocked pressure ripple and yoke moment ripple are of the same magnitude as the reductions in casing SPL: the casing SPL reduction is between +1 and +6dB(A); the blocked pressure ripple reduction is between +1 and +10dB(A), and the reduction in yoke moment ripple is between -3 and +4dB(A).

From the results of figures 9.15c and 9.16e and f, it is likely that the reduction in flow ripple and yoke moment ripple are contributing to the overall reduction in casing SPL.

9.3.3 Problems encountered during testing

Two problems became apparent during testing of the final HDCV prototype:

9.3.3.1 Swashplate Instability

During transient conditions, when the pump operating condition was changed, the swashplate occasionally became unstable. In this event the pump displacement suddenly dropped and then oscillated about a small mean flow. This process was typically quite violent and so to prevent any damage to the HDCV mechanism, the pump was unloaded and the drive motor switched off. In all cases when the motor was started up again, then the pump behaved normally. This phenomenon happened only rarely - 5 times in 20 hours of testing.

The swashplate instability is likely to be caused by the HDCVs' effect on the overall yoke moment. Figure 9.17 illustrates the major elements acting on the swashplate about the yoke axis within the standard pump. The bias piston is at delivery pressure, and acts to increase the pump displacement. The control piston is at a pressure determined by the delivery pressure and the setting of the pressure compensator, and acts to reduce the pump displacement. When delivery pressure is below the compensator setting then the control piston is at case pressure and the bias piston holds the swashplate at full displacement.

Figure 9.17 shows the typical distribution of high pressure cylinders relative to the yoke axis within the standard pump. It shows that the net yoke moment from cylinders at delivery pressure will act against the bias piston. Figure 9.17 also shows that cylinders starting delivery produce a yoke moment that acts with the bias piston.

Within the HDCV prototype, the yoke moment opposing the bias piston depends on which of the three HDCVs are open. If the 1st HDCV is open then the cylinders will reach delivery pressure very early, and may cause the net cylinder yoke moment to act intermittently with the bias piston. If all three are closed, then the cylinders will reach delivery pressure very late, and the net yoke moment opposing the bias piston will be high. This is significant because one symptom of the swashplate instability is that the pump displacement drops; this implies that cylinders within the HDCV prototype are acting with the control piston and against the bias piston. Another symptom of the swashplate instability is that it occurs rarely. This implies that the behaviour is abnormal, and may be due to a poppet being temporarily siezed.

Consider the situation where the poppet within the 1st HDCV is jammed shut whilst the pump is operating at low delivery pressure and high pump displacement. Cylinders starting their delivery stroke would then severely over-compress before dropping close to the delivery pressure on meeting the 2nd (open) HDCV. Together with the bias piston (and the bias spring), the increased cylinder over-compression would cause a larger yoke moment which may overcome that from the control piston to cause an increase in pump displacement. The delivery pressure would rise, and the pressure compensator would respond by increasing the pressure within the control piston: the yoke moment opposing the increasing pump displacement would then rise, and so act to oppose the increase in delivery pressure. However, the delivery pressure is low and so a situation could arise where the control piston is at its maximum pressure (delivery pressure), and the net moment on the swashplate still causes an increase in the pump displacement. In this case, the delivery pressure would rise until stopped by the increasing delivery pressure acting on the control piston. In this way, a siezed HDCV poppet could effectively bypass the pressure compensator to increase the pump delivery pressure uncontrollably.

This example does not conform to the instability behaviour encountered during testing, as it does not explain the observed drop in pump delivery flow. However, it does demonstrate the effect that a siezed HDCV could have on the operating condition of the HDCV prototype.

9.3.3.2 Airborne noise tests

A number of airborne noise tests were carried out on the final HDCV prototype. The results shown in figure 9.15 were produced during the first test. The reduction in SPL measured in this test from the HDCV prototype against those of the standard pump are presented in figure 9.18a.

For the second test, the HDCV prototype was modified so that the drilling through each of the first two sleeves did not align with the drillings in the valve block through to the blanked-off damping orifices (See figure 9.6). This reduced the volume in each of the first two HDCV spring chambers by 75%.

Unexpectedly, this change significantly increased the SPL measured from the pump casing. The reduction in SPL caused by this design compared to that of the standard pump is shown in figure 9.18b. The flow ripple was also measured, and was identical to that measured from the earlier tests on the final HDCV prototype.

To investigate further, the sleeves of the first two HDCVs were returned to their original orientation, and the original ABN tests were repeated. During this third test, the SPL levels were higher than those measured during the original test. These results are shown in figure 9.18c, and they show a clear increase in SPL from the original test results shown in figure 9.18a. Again, the measured flow ripple was unchanged.

Initially the difference between these results was attributed to higher fluid temperature during the later tests (40°C rather than 20°C). However, this was discounted when the third test was repeated using fluid at 20°C and caused no change in the pump casing SPL. From these tests a number of points became clear:

a) Changes in fluid temperature between 20 and 40°C did not significantly affect the HDCV performance.

b) The delivery flow ripple remained unchanged during all of these tests

c) Between the first and the third tests, the measured SPL produced by the HDCV prototype increased significantly.

d) The reduction in the spring chamber volume of the first two HDCVs by 75% caused the casing SPL to increase significantly.

From point b), it is clear that the increases in casing SPL of c) and d) were not caused by changes in the pump delivery pressure ripple or yoke moment ripple.

In 9.3.1.1, it was reported that HDCV poppet motion at the pumping frequency could be detected in the delivery flow ripple. Therefore, from point b), it appears that the increase in casing SPL is also unconnected to the motion of the HDCV poppets. However, the delivery flow ripple only indicates the motion of poppets that oscillate around the cracking point of the HDCV sleeve ports: poppets in the overlap region of each HDCV will have little effect on the delivery flow ripple. From this, it is possible that the increase in casing SPL is caused by HDCV poppets in the overlap region of each HDCV which are hitting their endstops.

In 8.3.2.5, the simulation model predicted that poppets may hit their endstops with forces in the region of 400N: if this happened in the real pump then it would definitely affect the structureborne and airborne noise from the pump casing. During the later tests, the HDCV damping may have been lower than during the initial ABN testing. This would cause the poppets to hit their endstops with more force and so increase their contribution to the casing structureborne and airborne noise.

The degradation in performance of the HDCV prototype (c) may be a consequence of the amount of testing that had been carried out (approx. 20 hours). The only components that would have been affected by this were the compression springs within each HDCV. The springs were inspected and it was found that the springs from the first two HDCVs had become slightly deformed, and that their free length had reduced from 12.7mm to just under 12mm. It is likely that this increased the response of the 1st and 2nd HDCVs to cause the increase in casing SPL. However, further tests are needed with new springs to confirm this.

An important point is that the springs had become damaged after only 20 hours of testing. This is probably a consequence of the HDCVs being under-damped, as demonstrated in the measured flow ripple results of 9.3.1.1: the poppet motion at the pumping frequency is significant and implies that over the 20 hours, the springs have undergone over 16 million load cycles for the 9-cylinder pump operating at 1500rev/min.

The reduction in spring chamber volume (d) was expected to increase the damping within the first two HDCVs (See figure 8.13c). However, it appeared to have the opposite effect. The reason for this is unknown, although it may be that the poppet motion within the smaller spring chamber volume encourages cavitation and air release effects. This could dramatically increase the fluid compressibility within the spring chamber, and so lead to a reduction in the HDCV damping.

9.4 Review of the HDCV concept

9.4.1 Performance of the final HDCV prototype

All of the HDCV prototypes have been manufactured as a modification to a Vickers PVH57 inline axial-piston pump. A scheme of the final HDCV prototype is shown in figure 9.6 which features HDCVs that are detailed in Appendix E. Results of testing and simulation show that the final HDCV prototype produced reductions in delivery flow ripple over the whole operating range specified in 8.2.1 (See 9.3.1.3). The casing airborne noise was measured for the pump running at 1500rev/min, and was reduced over a wide range of delivery pressures and pump displacements (See 9.3.2.2). Significantly, the reductions in casing airborne noise are of the same magnitude as the measured reductions in the blocked acoustic pressure ripple and the simulated reductions in yoke moment ripple.

During testing of the final prototype, a number of problems were identified:

1 Very occasionally, the swashplate became unstable (See 9.3.4.1). The cause of this effect is not properly understood, although it is likely to be caused by contamination which causes individual HDCV poppets to sieze.

2 From analysis of the measured delivery flow ripple, the HDCV poppets show significant movement at the pumping frequency (225Hz), indicating that they are under-damped at this frequency. This poppet motion causes an increase in the delivery flow ripple: particularly at high pump displacement conditions (See 9.3.1.3). It is likely that this large poppet motion also reduces the life of the HDCV springs, and causes an attendant increase in the airborne noise from the pump casing (See 9.3.4.2).

3 The HDCV prototype regularly needed 5 - 6 seconds to respond to changes in pump displacement and delivery pressure (See 9.3.1.2). During these periods, the pump typically became very noisy. This indicates that the response of the HDCV poppets at low frequencies is too heavily attenuated.

4 A reduction in the spring chamber volume caused a significant increase in the airborne noise from the pump casing (See 9.3.4.2). The measured delivery flow ripple was unchanged and it is likely that this effect was caused by increased poppet impact on their end stops. Unexpectedly, this implies that the HDCV response had increased: the dynamic analysis carried out in 8.3.2.3 predicted a reduction in poppet response at high frequency with a reduction in spring chamber volume. A possible explanation for this effect is that the poppet response has increased due to the increased cavitation or air-release within the HDCV spring chambers.

To attenuate the HDCV response at the higher frequencies (2), the poppet mass could be increased and the compressibility of fluid within the spring chambers reduced. However, a reduction in spring chamber compressibility has already been attempted without success (4).

To increase the HDCV response at the lower frequencies, lower rate HDCV springs could be used, and the poppet-sleeve clearance could be reduced (see 8.3.2.3). However, lower rate springs may get damaged more easily if the higher frequency attenuation is not achieved. Also, if the poppet-clearance is reduced then the mechanism may be more prone to contamination which may increase the incidence of swashplate instability problems (1).

9.4.2 Performance of the HDCV simulation model

A simulation model has been developed within Bathfp to describe the behaviour of the HDCV prototype (See 8.3). Results from the model agreed with results of steady state and dynamic analysis carried out using the system equations (See 8.3.2.2 and 8.3.2.3)

The simulation model achieves fair agreement with the measured flow ripple of a HDCV prototype with 2 HDCVs (See figure 9.6). The agreement with the measured flow ripple from a 3-port design is worse (See figure 9.13). This is because the 3-port simulations are more dependent upon the modelled HDCV dynamic response. The modelled dynamic response is inaccurate in two respects (See 9.3.1.2):

1 the model under-estimates the HDCV poppet response at the pumping frequency. This is significant as there are large effects that can be seen in the delivery flow ripple that are caused by poppet motion at the pumping frequency.
2 the model over-estimates the HDCV poppet response to low-frequency changes in the pump operating condition.

9.4.3 Recommendations for further work

The initial results from the final HDCV prototype showed it to be significantly less noisy than a conventional "low-noise" axial piston pump. However, before the concept can be regarded as viable then a better understanding of its operation is required. In particular, three effects must be investigated:

a) The swashplate instability

b) The response of the HDCV poppets at the pumping frequency.

c) The response of the poppets to low-frequency changes in the pump operating condition

The swashplate instability can be investigated by electronically monitoring the pump delivery pressure, delivery flow and the pressures within the individual HDCV spring chambers. If a HDCV poppet siezes then the pressure in that particular spring chamber should stop cycling at the pumping frequency. During this period the delivery flow and pressure would be recorded and so the behaviour during the instability could probably be deduced.

The dynamic response of the HDCV poppets is more difficult to investigate, as this would require measurement of the poppet motion within each HDCV.

The technique for measuring the motion of the HDCV poppets should be devised carefully. In particular, care should be taken to ensure that it does not affect the attenuation applied to the HDCV poppets. This would imply a non-intrusive method and may significantly increase the prototype cost.

The simulation work can be carried on by experimenting with different spring chamber compressibilities and leakage assumptions to reach better agreement with the measured flow ripple results. However, this exercise may be more wisely delayed until there are measurements of the poppet motion with which to validate the model. Confidence in the simulation model is only going to be achieved when this data is available.

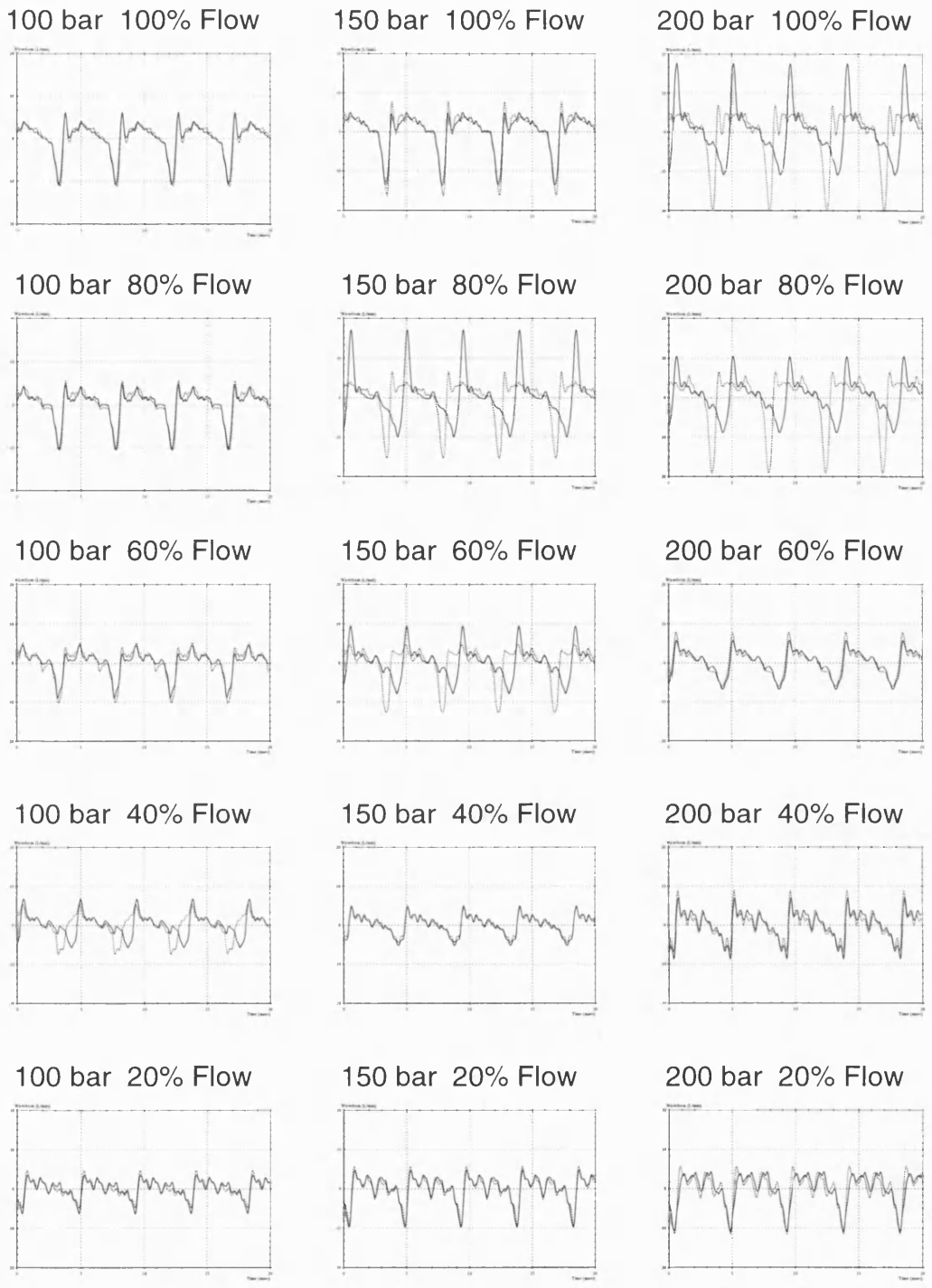

Solid: Damping orifices closed
Dashed: Damping orifices open

Figure 9.1
Internal flow ripple measurements from the HDCV 1st working prototype showing the effect of closing the damping orifices

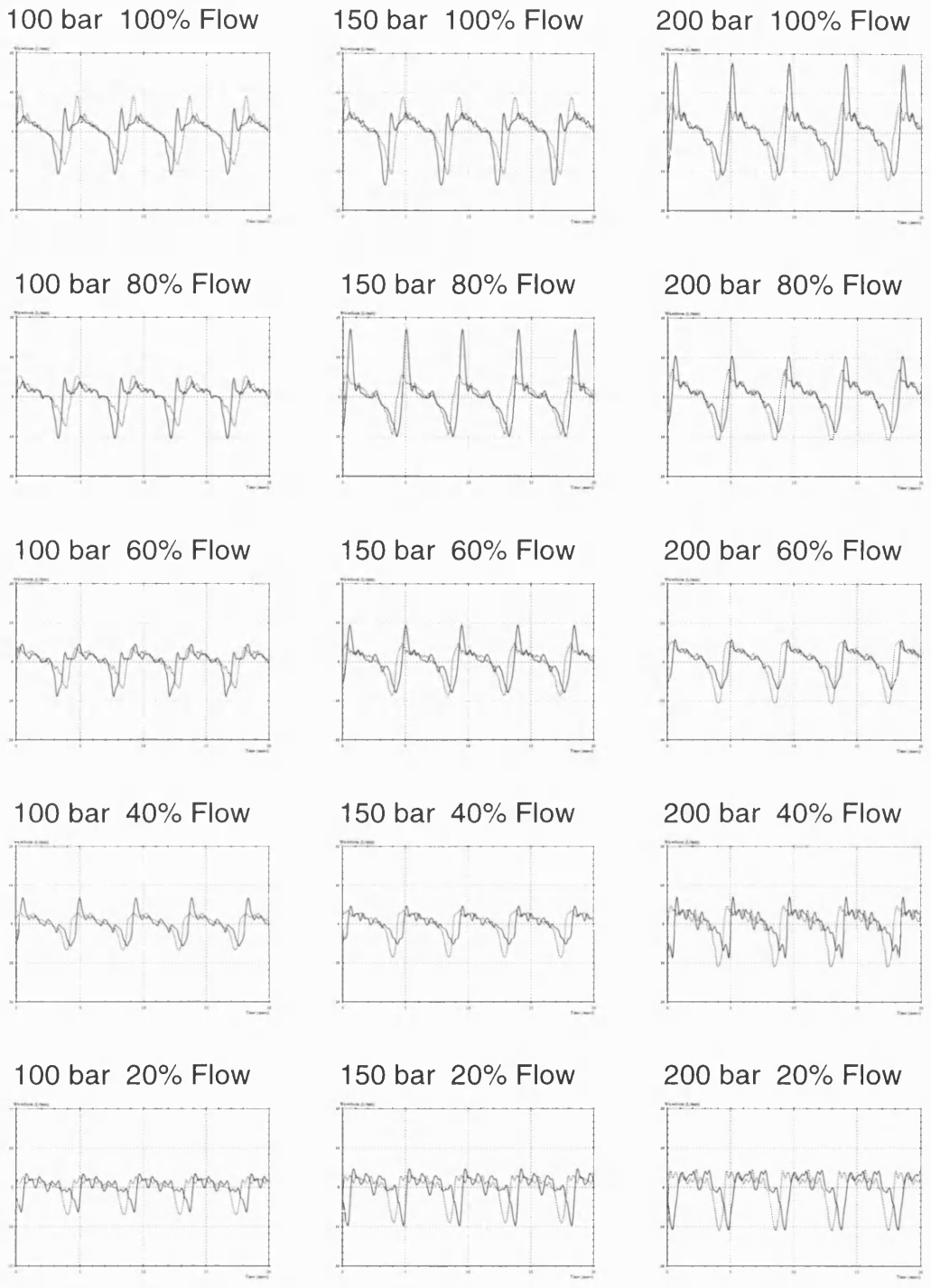

Solid: HDCV 1st working prototype (damping orifices closed)
Dashed: Unmodified pump

Figure 9.2
Comparison between internal flow ripple measurements from
the HDCV 1st working prototype and the unmodified pump

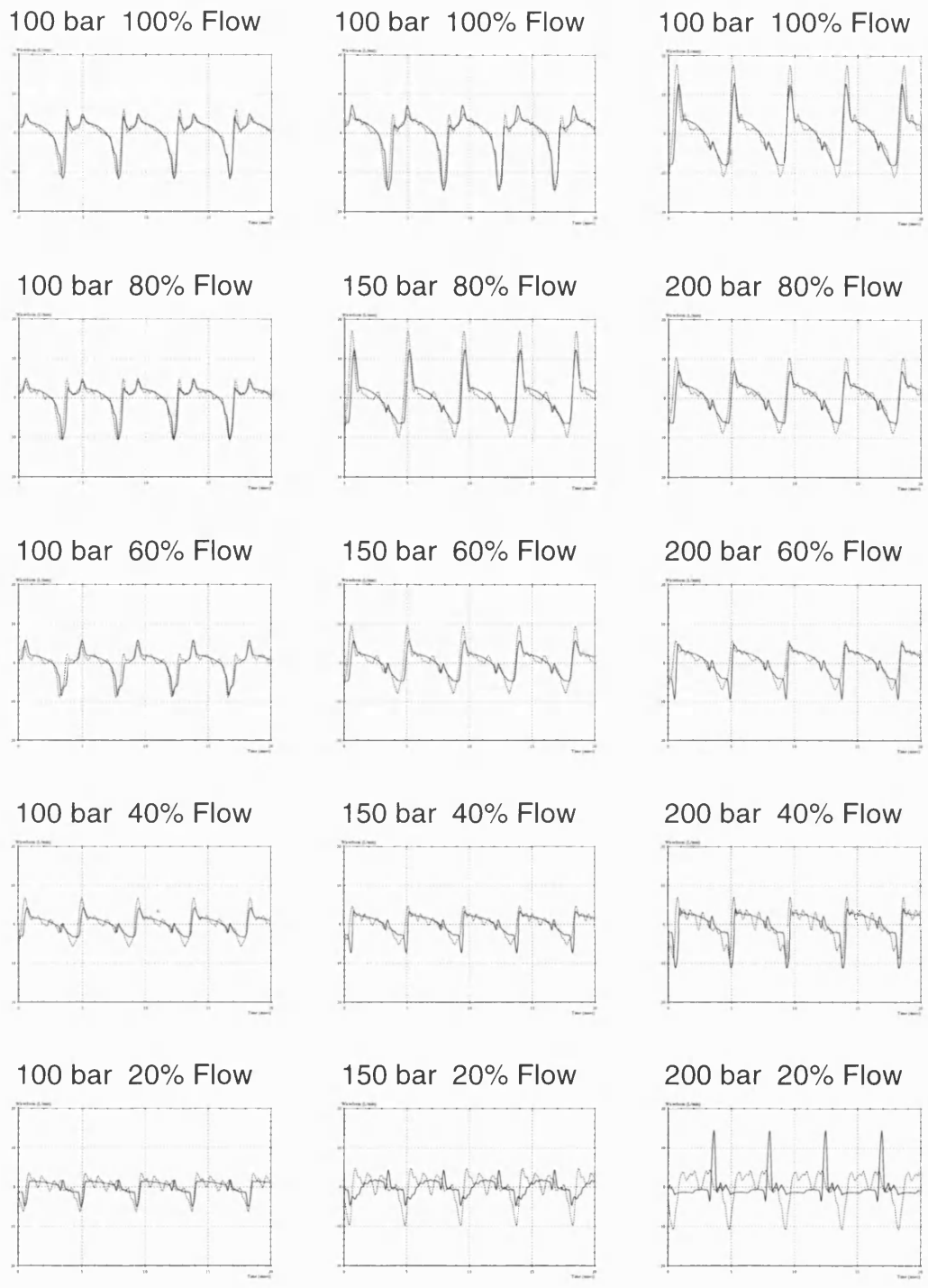

Solid: Simulated
Dashed: Measured

Figure 9.3
Comparison between simulated and measured internal flow ripple
for the HDCV 1st working prototype (damping orifices closed)

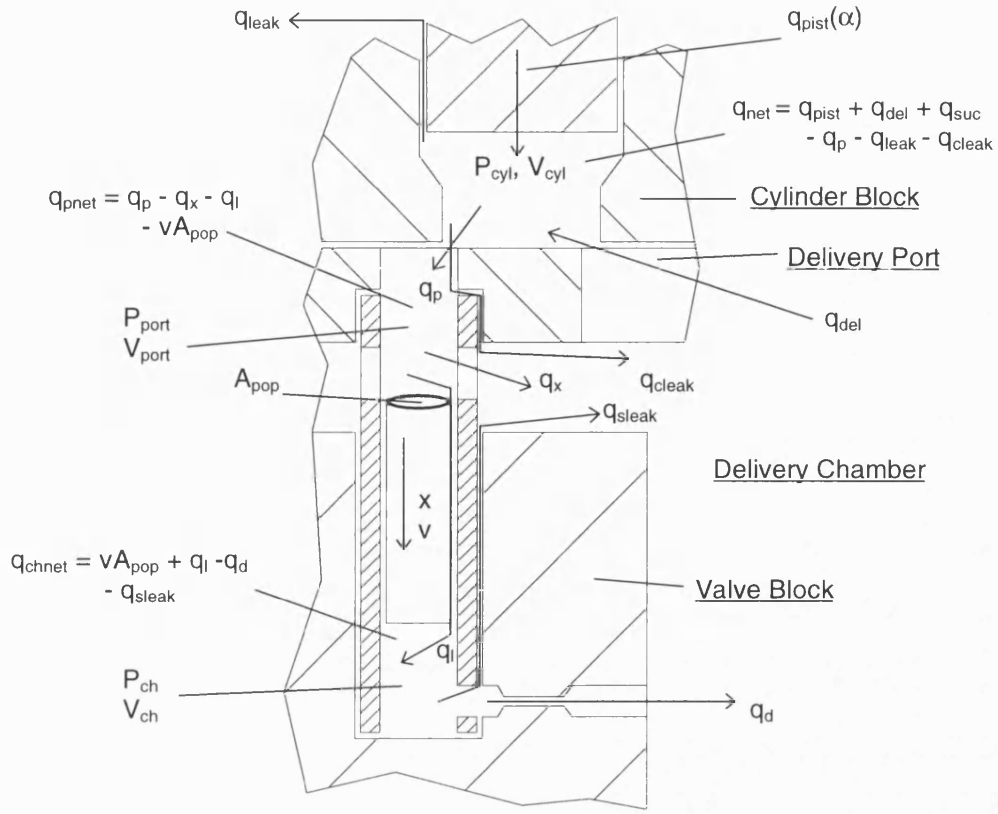

Figure 9.4
The flow paths and flow summations within the improved HDCV simulation model

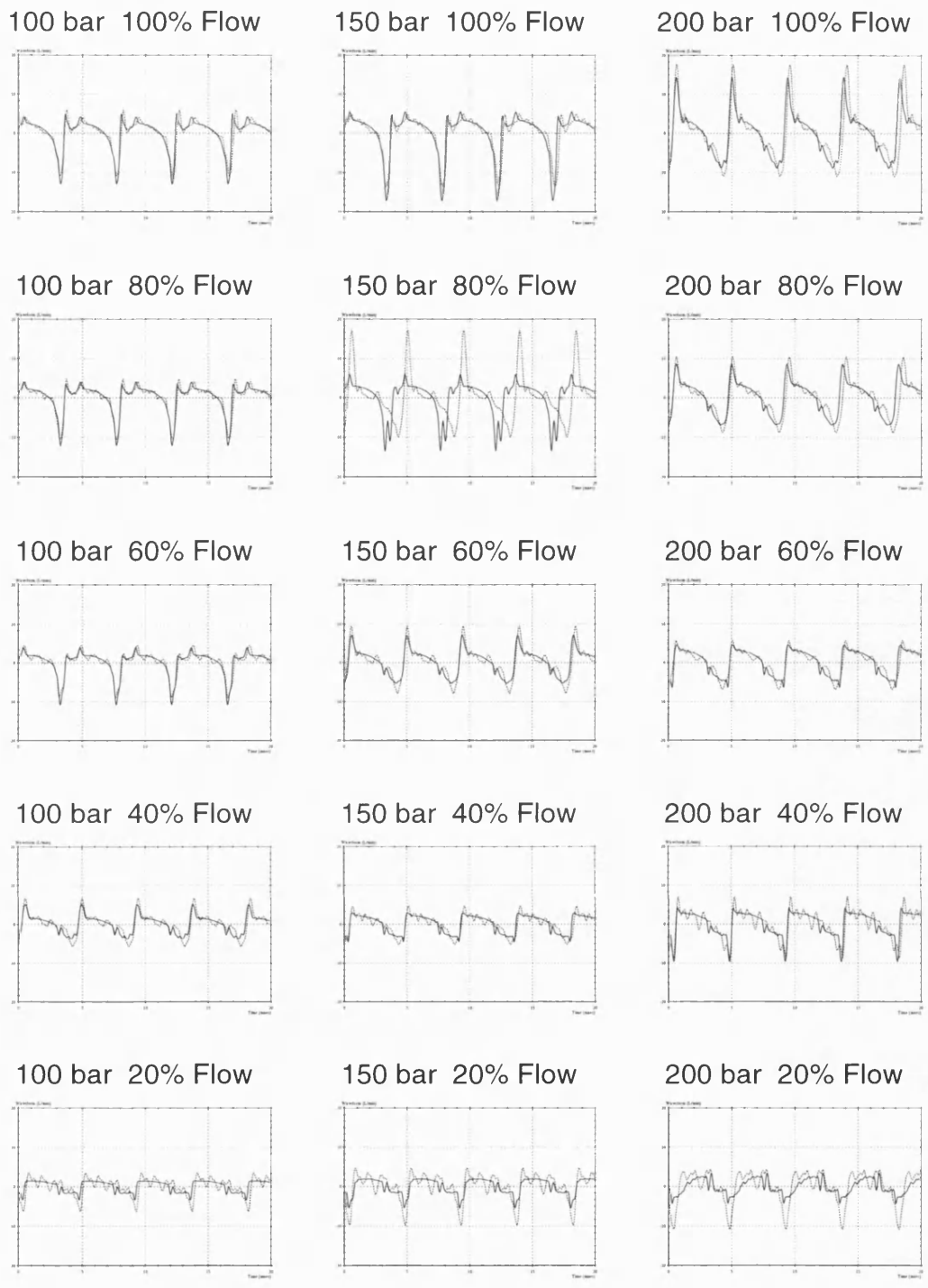

Solid: Simulated
Dashed: Measured

Figure 9.5
Comparison between simulated and measured internal flow ripple
for the HDCV 1st working prototype (damping orifices closed)
using the improved simulation model

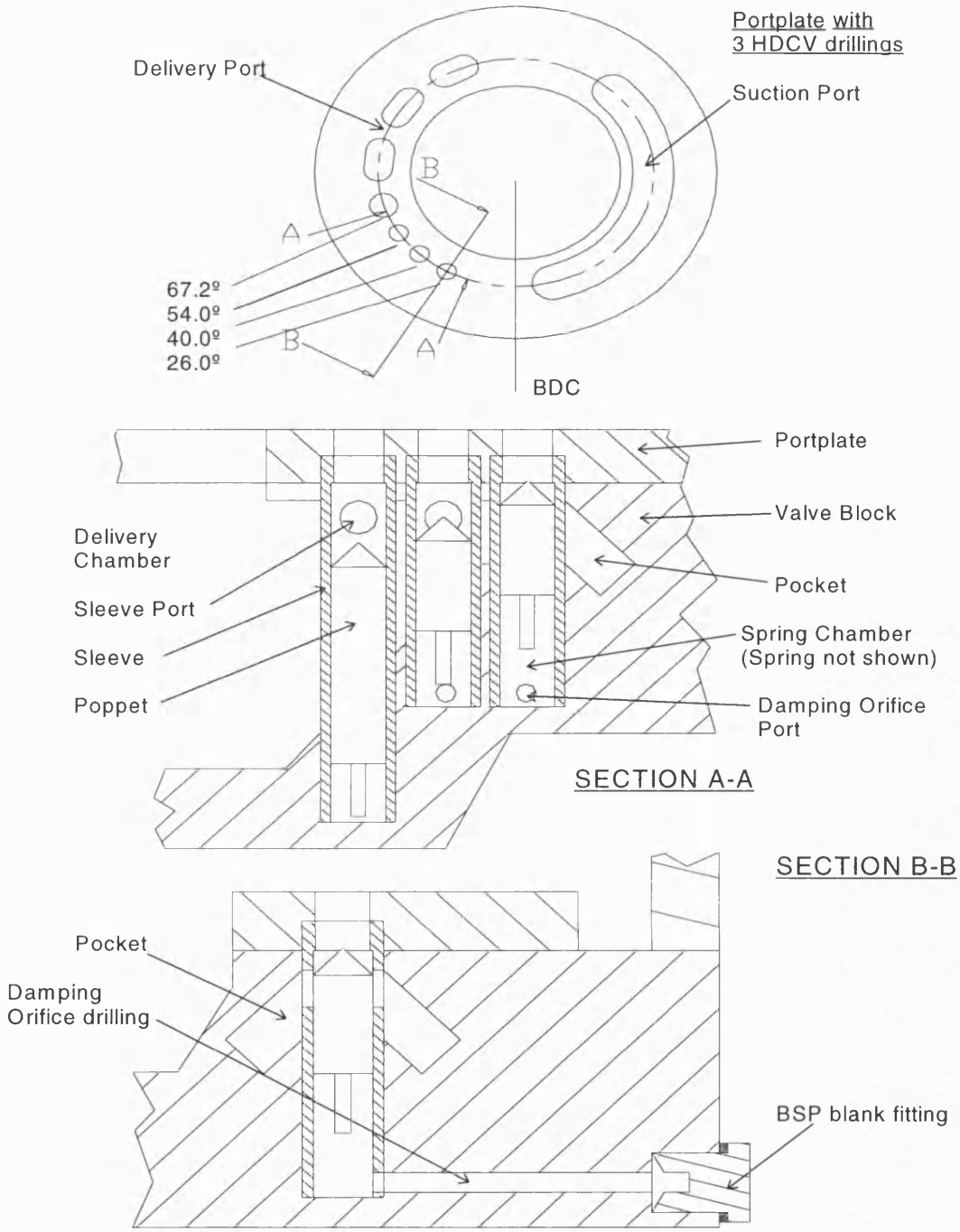

Parameter		Variable Name	Value
Spring Rate	N/m	K_s	3330
Spring Preload (@ x=0mm)	N	K_p	7.992
Poppet length	mm	L_{pop}	10.7, 22.7
Poppet Diameter	mm	D_{pop}	5.5
Poppet Mass	Kg	M	0.003, 0.007
Sleeve Port Diameter	mm	D_{port}	3.6
Slv-Pop diametral clearance	mm	h	0.006
Damping Orifice Diameter	mm	D_{damp}	0
Damping Orifice Length	mm	L_{damp}	0

Figure 9.6
Arrangement and parameters of the HDCV Improved working prototype

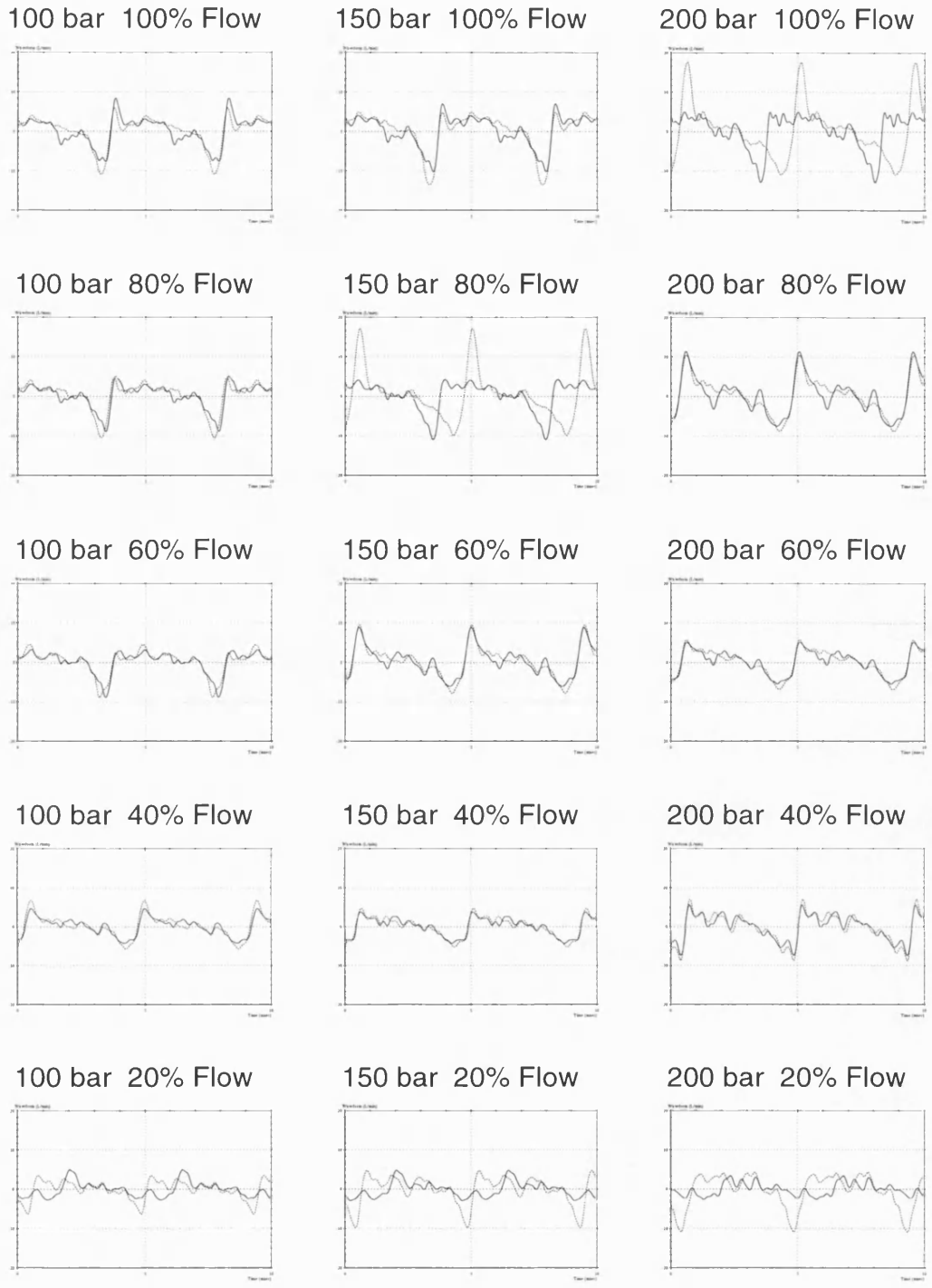

Solid: Measured from the final working prototype
Dashed: Measured from the 1st. working prototype (damping orifices closed)

Figure 9.7
Comparison between the measured internal flow ripple from the
HDCV 1st and final working prototypes

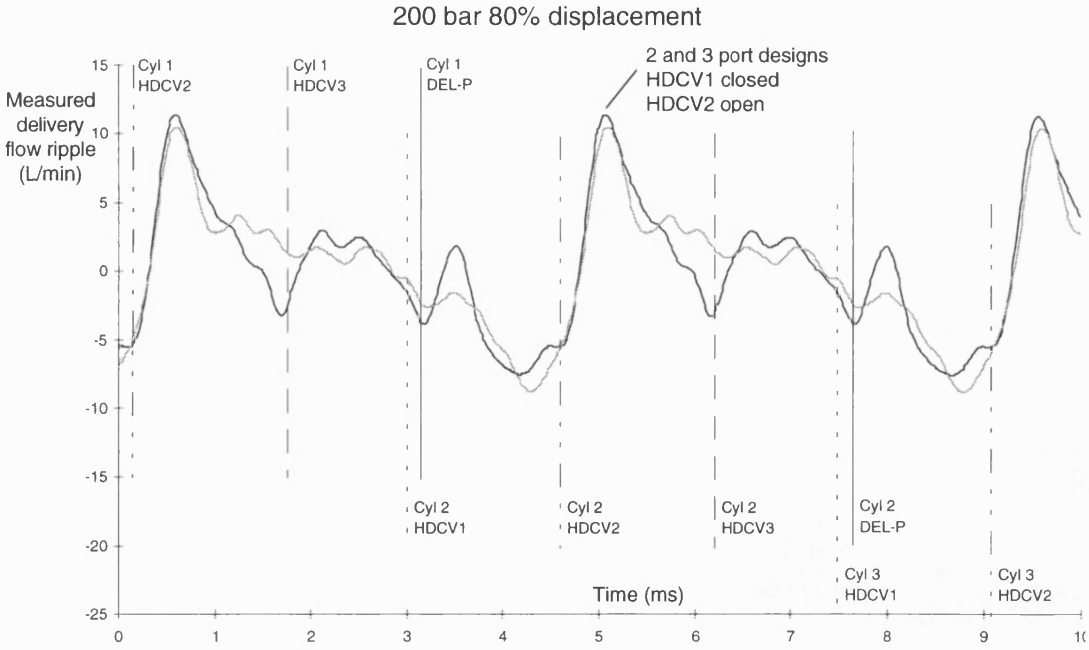

Black: Final HDCV working prototype (3 HDCVs)
Gray: 1st HDCV working prototype (2 HDCVs)

Figure 9.8
Comparison of internal flow ripple measurements from the 1st and final HDCV working prototypes

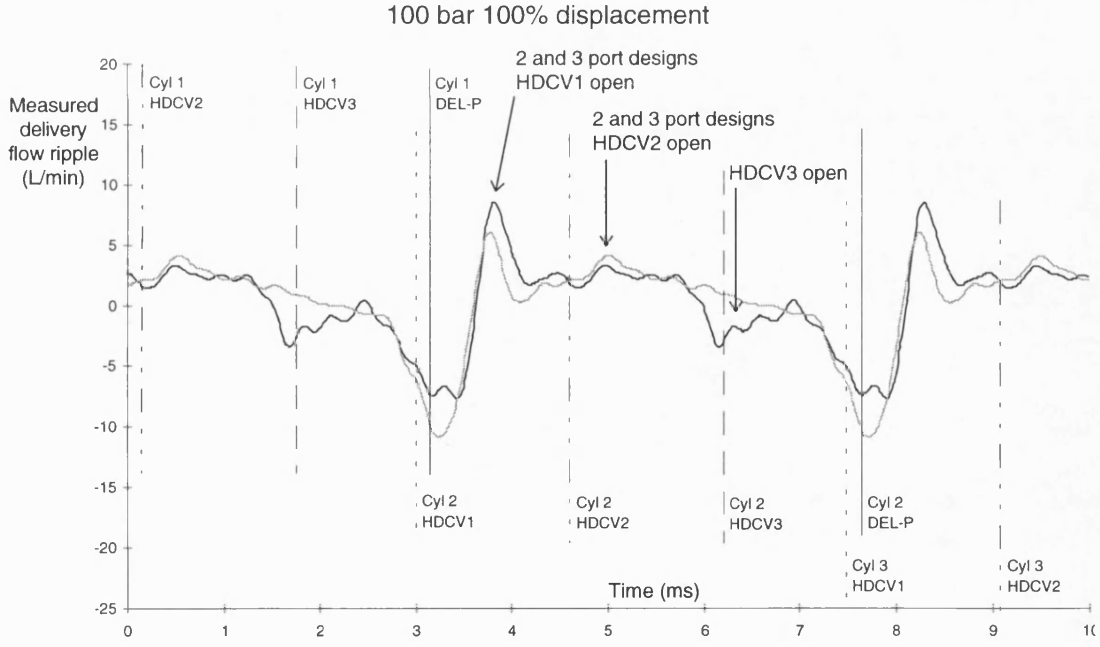

Black: Final HDCV working prototype (3 HDCVs)
Gray: 1st HDCV working prototype (2 HDCVs)

Figure 9.9
Comparison of internal flow ripple measurements from the 1st and final HDCV working prototypes

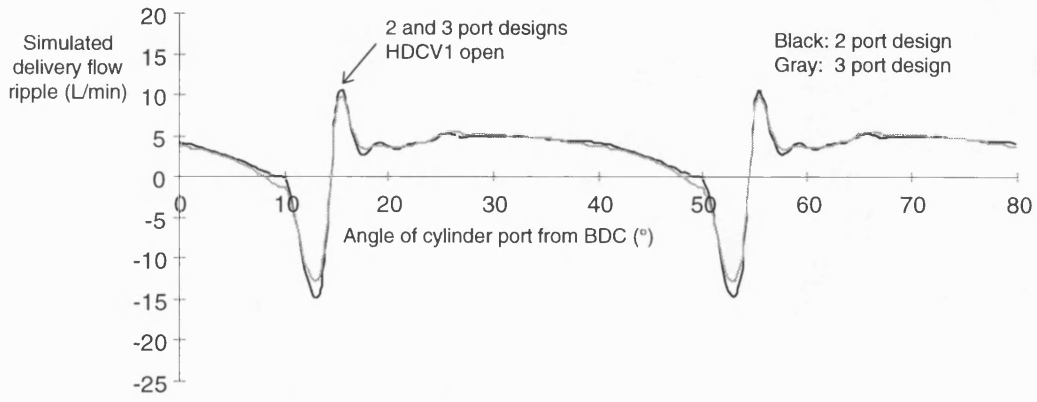

Figure 9.10a
Comparison of simulated delivery flow ripple for the 1st and final HDCV working prototypes at 100 bar and 100% displacement

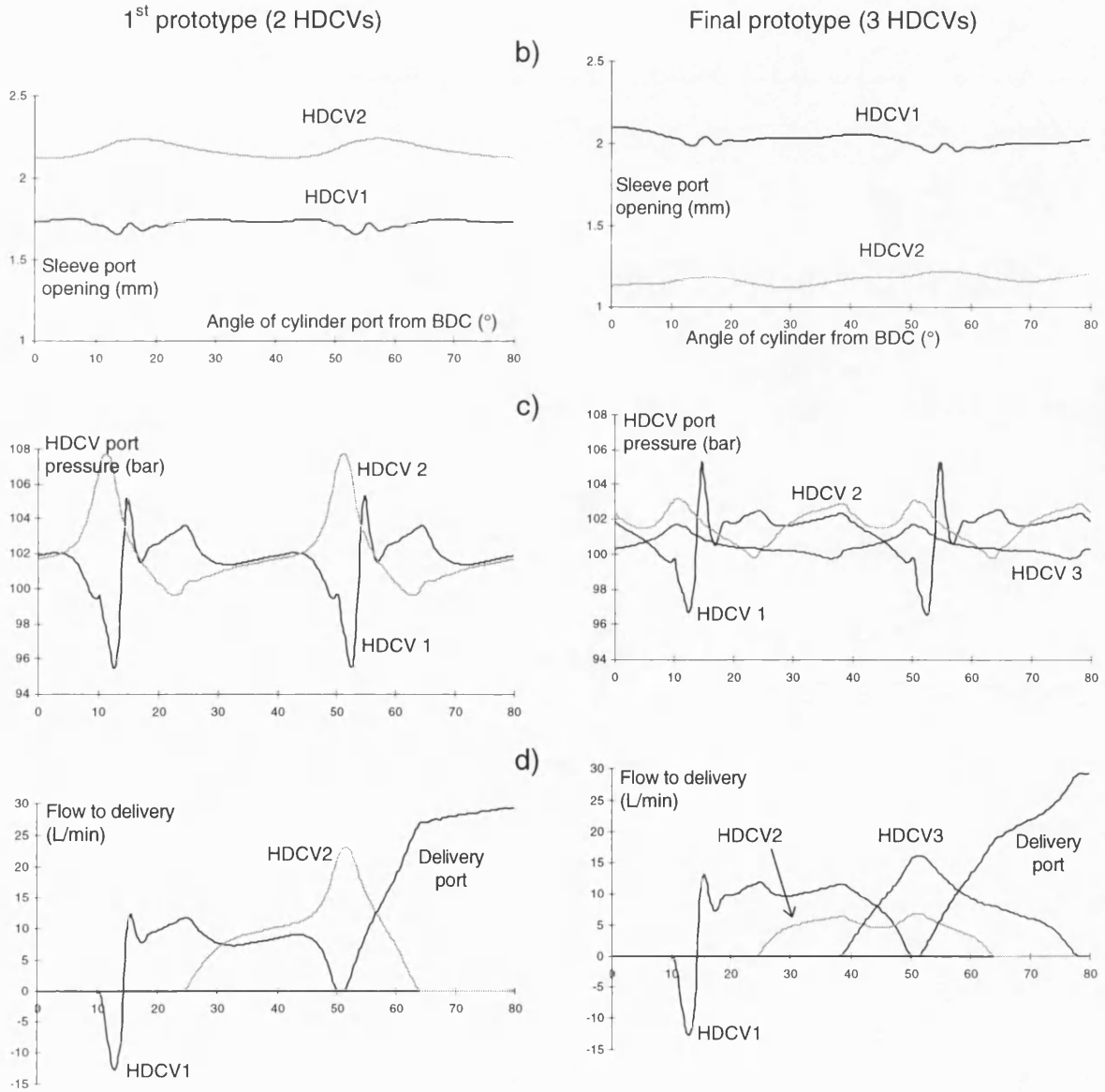

Figure 9.10b - d
Comparison of simulation results for the 1st and final HDCV working prototypes at 100 bar and 100% displacement

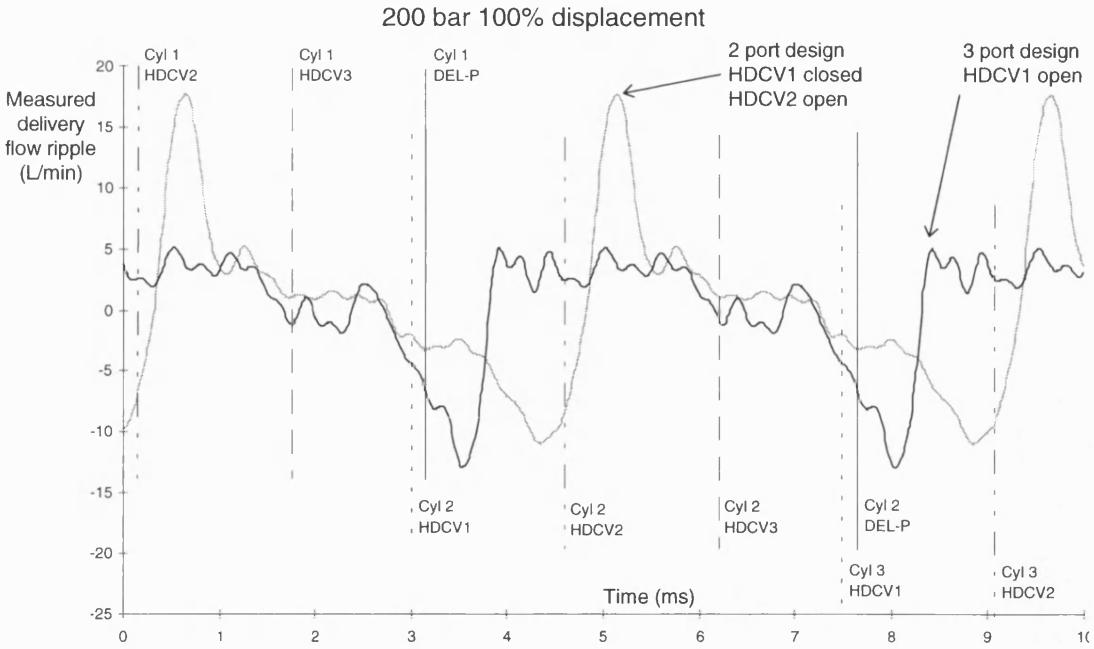

Black: Final HDCV working prototype (3 HDCVs)
Gray: 1st HDCV working prototype (2 HDCVs)

Figure 9.11
Comparison of internal flow ripple measurements from the 1st and final HDCV working prototypes

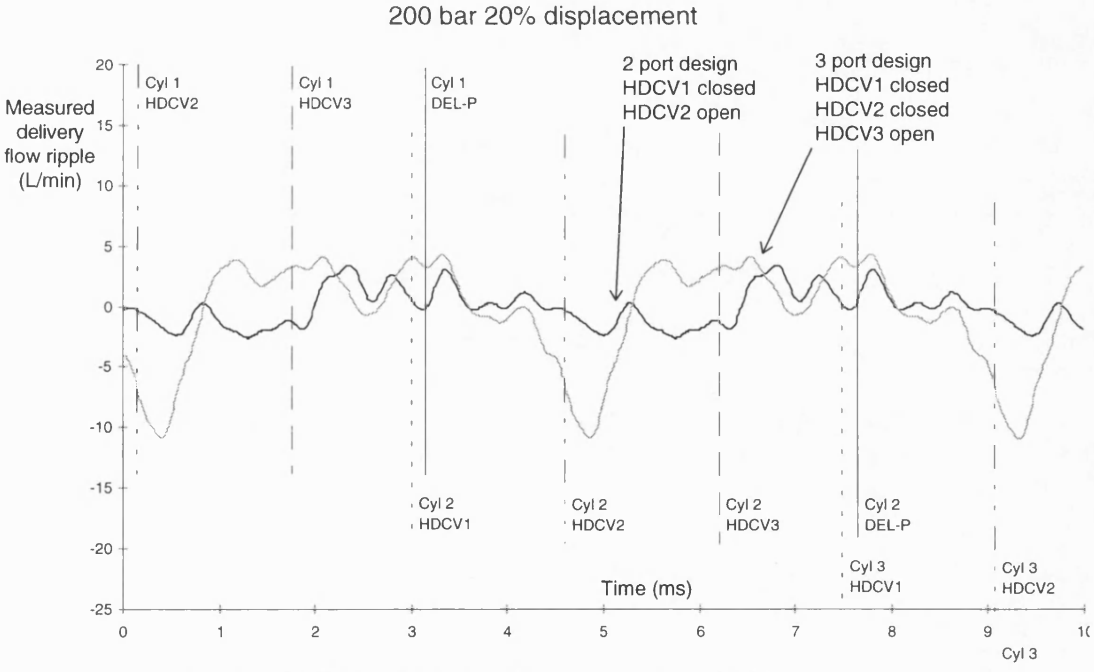

Black: Final HDCV working prototype (3 HDCVs)
Gray: 1st HDCV working prototype (2 HDCVs)

Figure 9.12
Comparison of internal flow ripple measurements from the 1st and final HDCV working prototypes

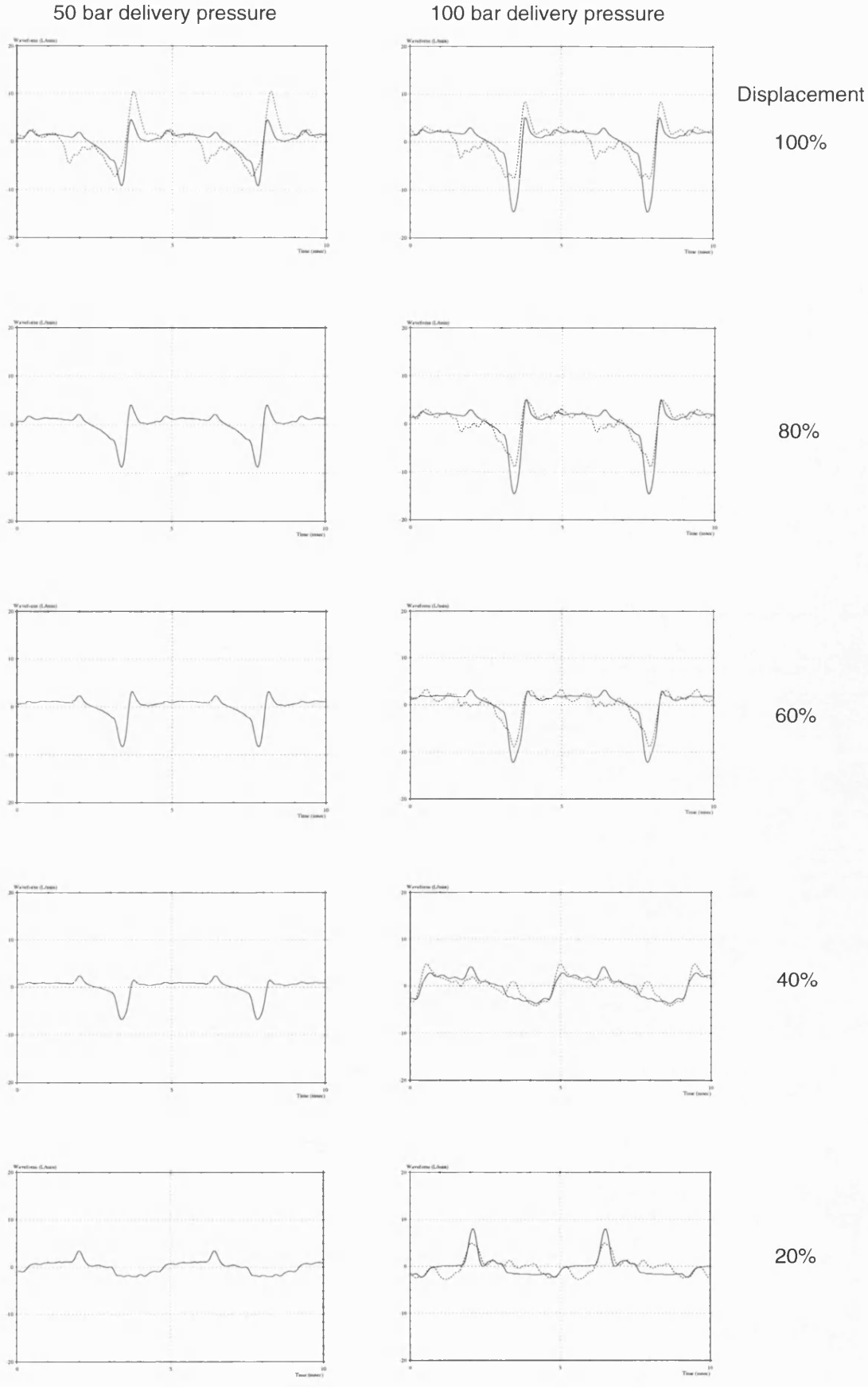

Solid: Simulated
Dashed: Measured

Figure 9.13a
Final HDCV prototype internal flow ripple - Measured and Simulated

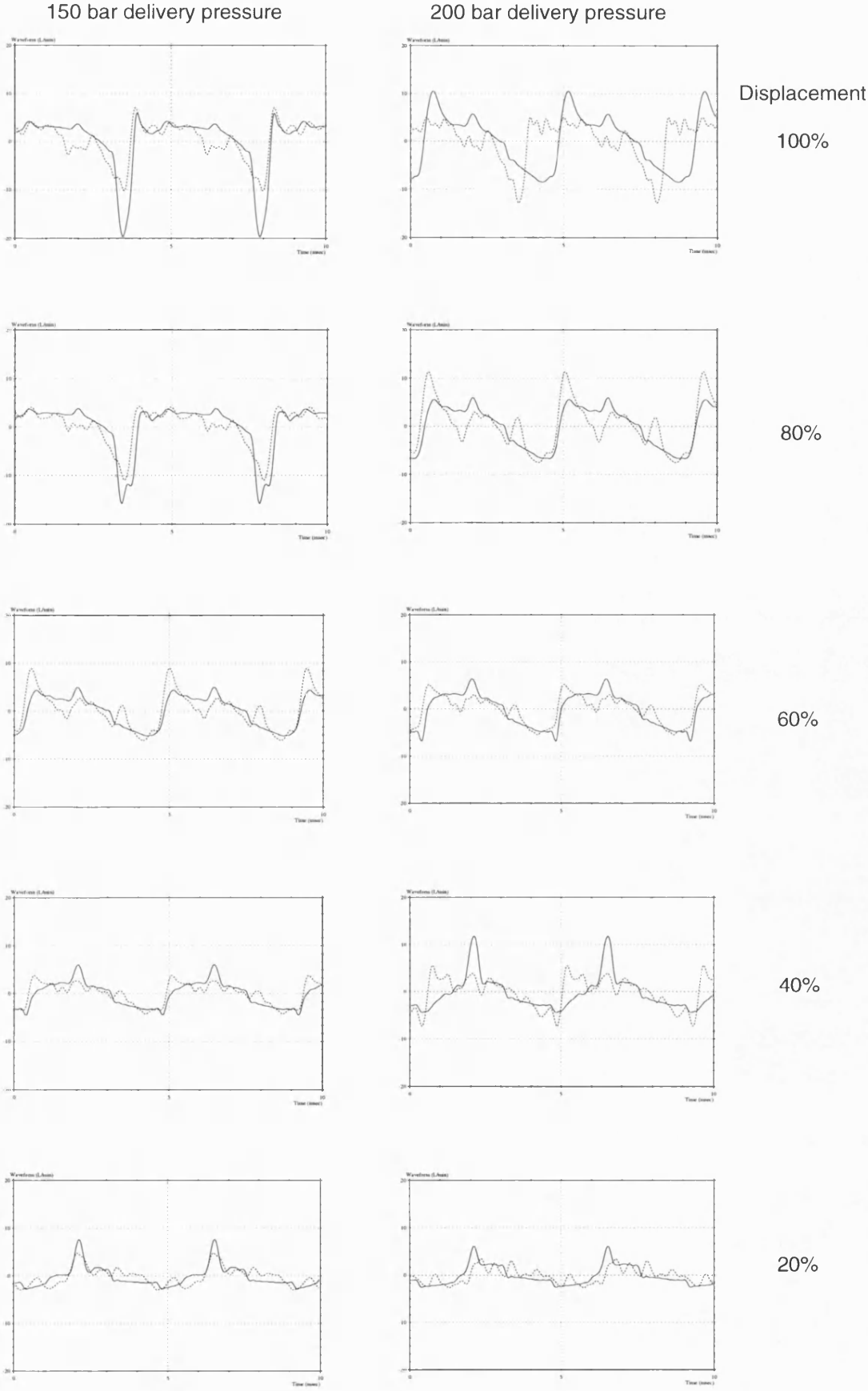

Solid: Simulated
Dashed: Measured

Figure 9.13b
Final HDCV prototype internal flow ripple - Measured and Simulated

250 bar delivery pressure

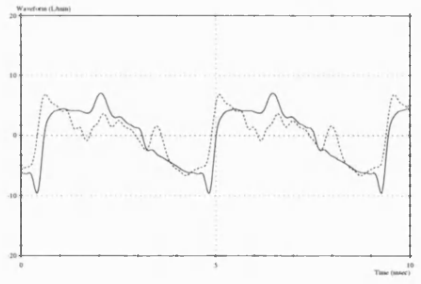

Displacement

100%

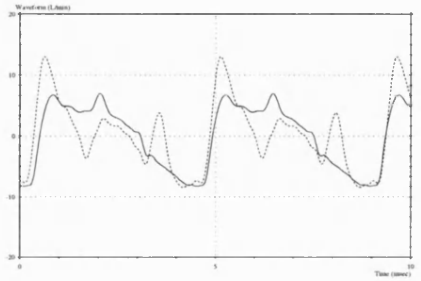

80%

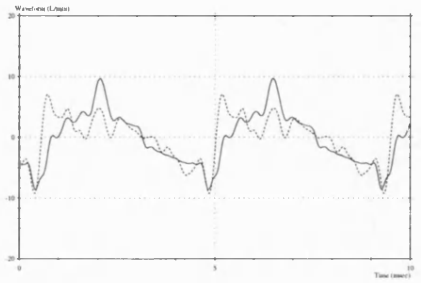

60%

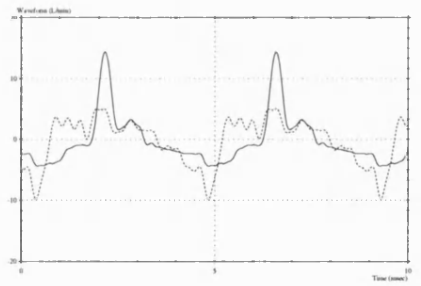

40%

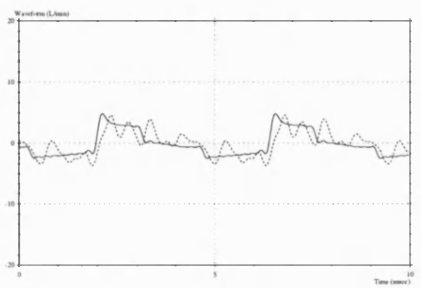

20%

Solid: Simulated
Dashed: Measured

Figure 9.13c
Final HDCV prototype internal flow ripple - Measured and Simulated

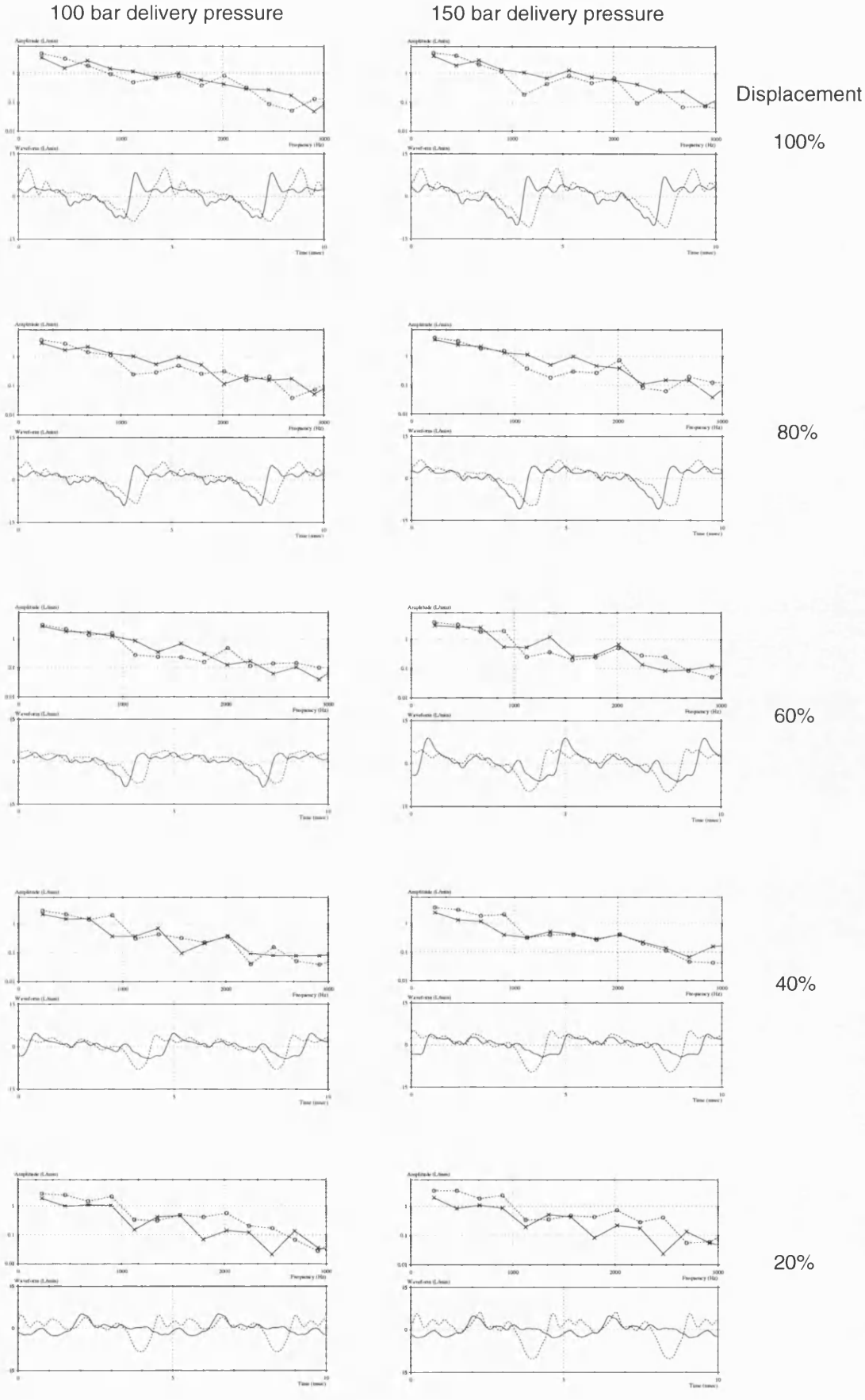

Solid: Final HDCV prototype
Dashed: Unmodified pump

Figure 9.14a
Measured internal flow ripple of final HDCV prototype and unmodified pump

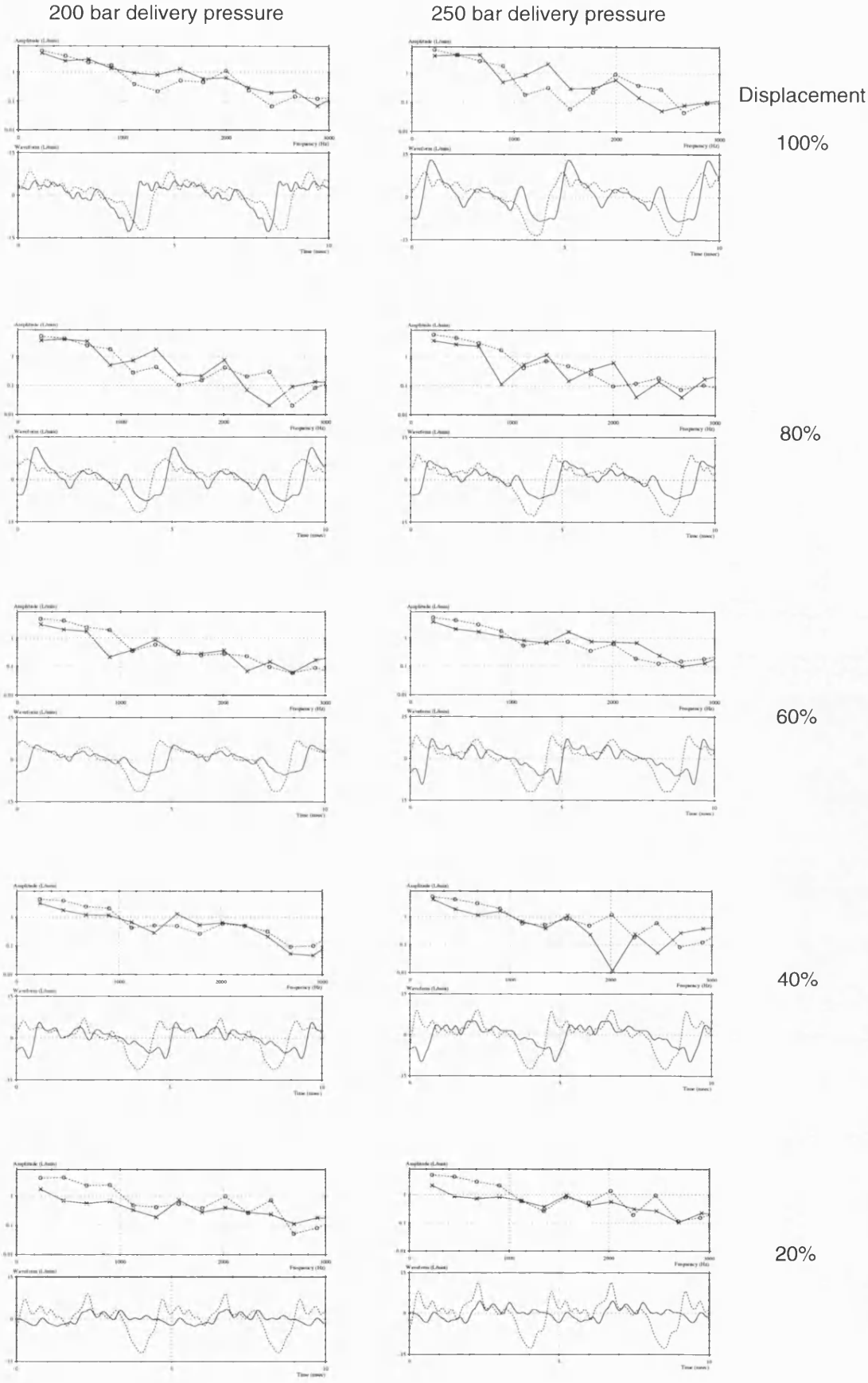

Solid: Final HDCV prototype
Dashed: Unmodified pump

Figure 9.14b
Measured internal flow ripple of final HDCV prototype and unmodified pump

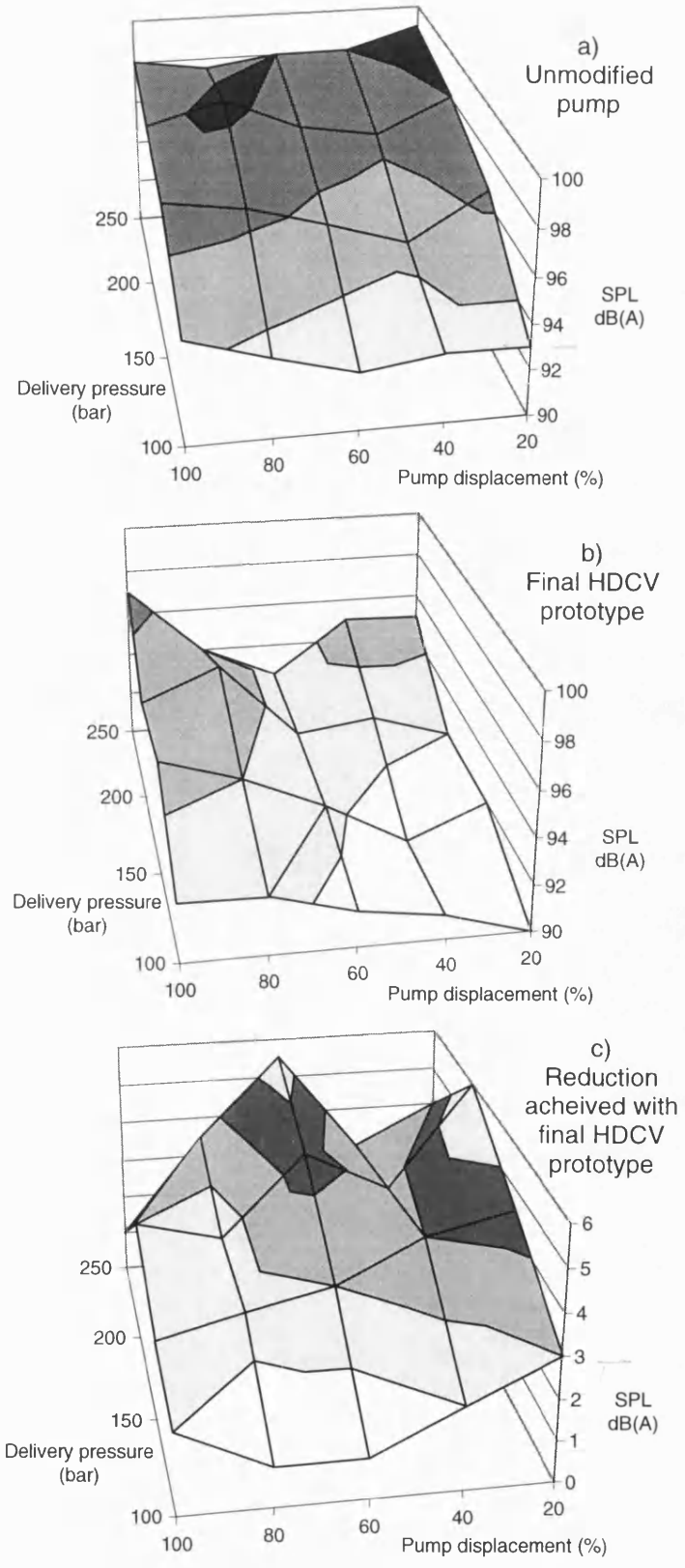

Figure 9.15a - c
"A" - weighted Sound Pressure Level measurements
from the final HDCV prototype and the unmodified pump

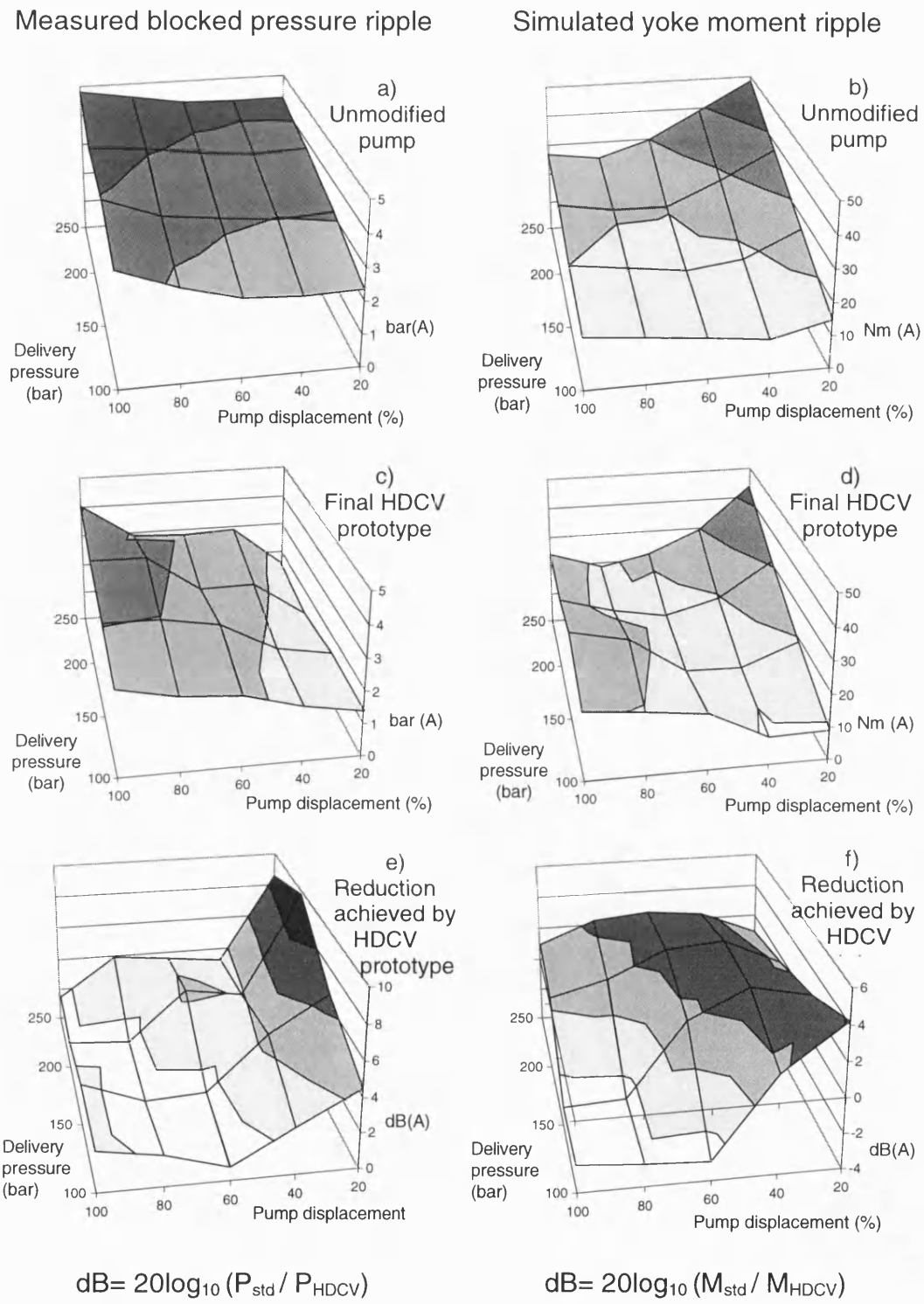

Figure 9.16a - f
"A" - weighted blocked pressure ripple (measured) and yoke moment ripple (simulated) for the the final HDCV prototype and the unmodified pump

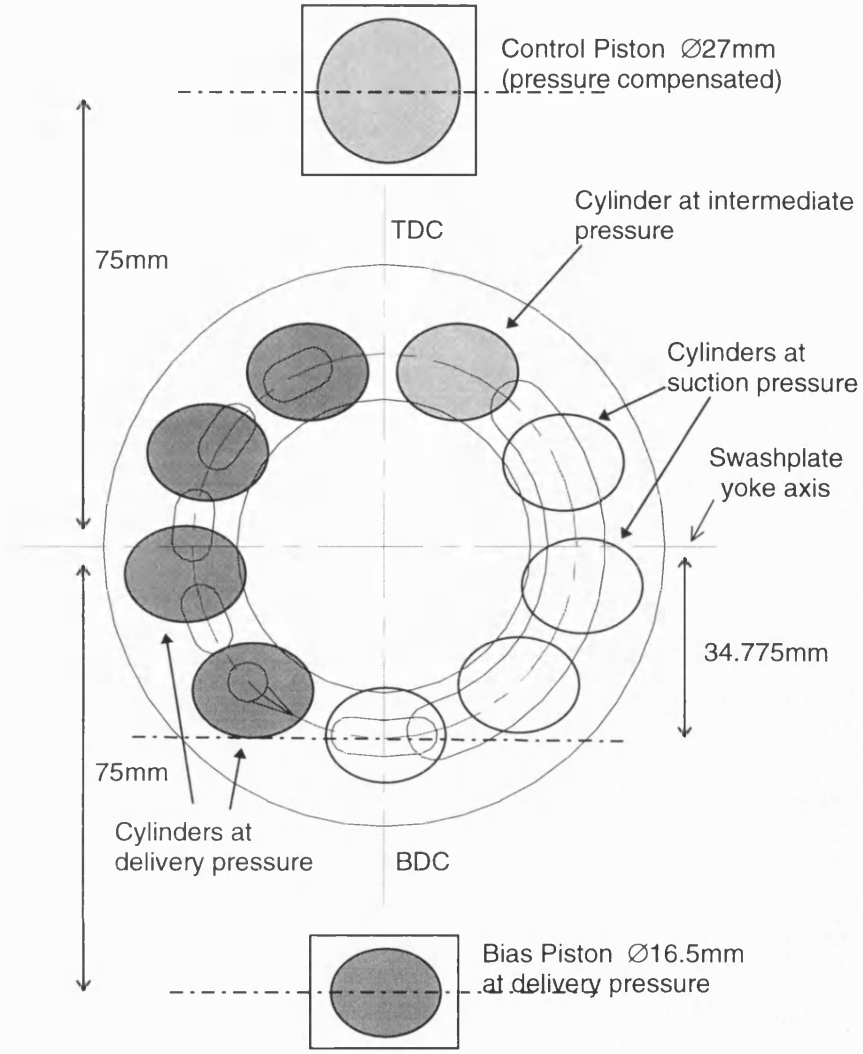

Figure 9.17
Sketch showing the pressure forces acting on the pump swashplate

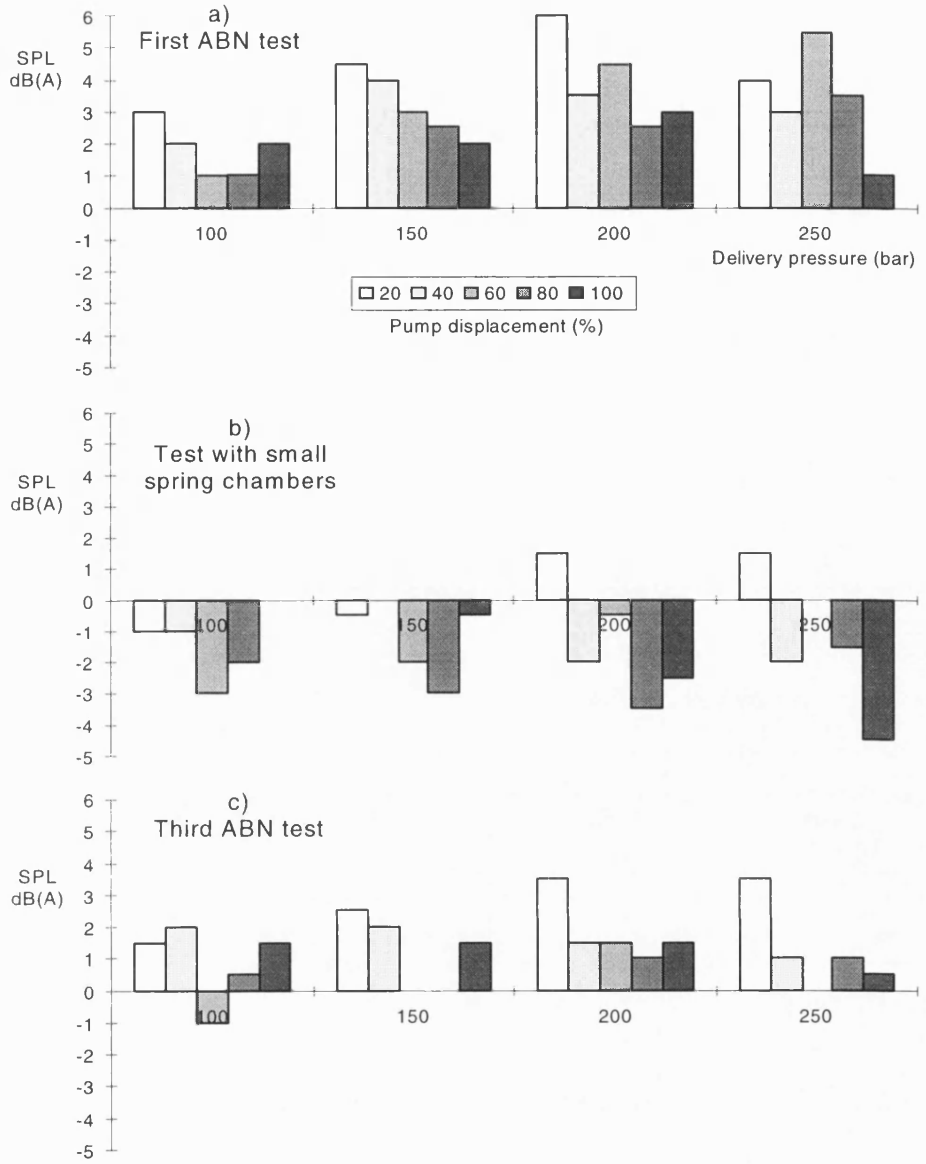

Figure 9.18a - c
Measured reduction in the "A" - weighted Sound Pressure
Level achieved by the final HDCV prototype

10.0 Conclusions

A theoretical and experimental study has been conducted into the reduction of flow ripple from axial piston pumps. One of the concepts considered has been built as a prototype and has met the primary project aim in reducing the flow ripple from an axial piston pump to cause an overall reduction in the pump-generated airborne noise. This prototype design is only applicable to axial piston pumps. However, a number of the other novel concepts considered could employ a principle of operation applicable to other positive displacement pumps and therefore meet the secondary project aim.

10.1 Novel methods to reduce flow ripple

An investigation was carried out into high speed actuation technologies that may be used to directly cancel the lower harmonic components of the pump pressure ripple. Piezoelectric actuators, magnetostrictive actuators and electro rheological fluid devices were all assessed. All three were discounted due to the high cost of their application. In highly critical applications this high cost could be justified, but in a commercial environment they would not be viable.

A literature search was carried out to find different methods that had been attempted to reduce pump pressure ripple. From this search, a number of novel or derivative solutions were considered:

a) a speed sensing silencer which uses a control element to vary the flow area at the neck of a Helmholtz resonator unit.

b) a 3-dimensional multi-lobed cam acting as a delivery pressure sensing version of the mechanism that was originally developed by Lipscombe to cancel gear pump pressure ripple [7].

c) a rotary valve pulse generator used to cancel the pump delivery pressure ripple.

d) a heavily damped check valve placed ahead of a delayed delivery port which would reduce delivery pressure ripple by limiting the effect of rapid cylinder flows at the start of the delivery.

Of these solutions, c) and d) were developed further.

10.2 The Heavily Damped Check Valve Concept

A prototype of the heavily damped check valve (HDCV) concept was manufactured as an inexpensive modification to the test pump. The final version of this prototype reduced the flow ripple from the pump to cause an overall reduction in the pump-generated airborne noise.

The final HDCV prototype caused reductions in delivery flow ripple and casing airborne noise between delivery pressures of 100 and 250 bar, and between pump displacements of 20 and 100% for the unboosted pump running at 1500rev/min. These results demonstrate that the HDCV prototype can respond to changes in both the pump displacement and the pump

delivery pressure. This is a significant advantage over the rival PCFV mechanism [61] which has only demonstrated the ability to respond to changes in delivery pressure.

The final HDCV prototype is still at a very early stage of development, and a number of significant problems persist:

a) very occasionally, the swashplate becomes unstable. The cause of this effect is not properly understood, although it is likely to be caused by contamination which causes the HDCV poppets to seize.

b) the HDCV poppets show significant movement at the pumping frequency, indicating that they are too lightly damped. This causes an increase in the delivery flow ripple and reduces the life of the HDCV springs.

c) the HDCV prototype regularly needed 5 - 6 seconds to respond to changes in pump displacement and delivery pressure. This indicates that the HDCV poppets are over-damped at low frequencies.

10.3 The Rotary Valve Pulse Generator Concept

A test rig was built to measure the flow ripple and impedance characteristics of a rotary valve pulse generator. Measurements from this rig were used to optimise the rotary valve for sending flow pulses into the pump delivery line to cancel the test pump flow ripple.

A separate test rig was built to investigate the interference effect of flow pulses from the optimised rotary valve upon the delivery pressure ripple of the test pump. The optimised rotary valve was driven using a DC servomotor with its rotation controlled within a phase locked loop synchronised to the pumping frequency of the main pump: in this way the flow pulses from the optimised rotary valve could be exactly synchronised with the test pump flow ripple.

The rotary valve was initially fed with flow from the laboratory ring main and was seen to have a significant interference effect on the pump delivery pressure ripple. In a more realistic test, the rotary valve was fed by a small gear pump whose inlet line came from the main pump delivery line. During this test, flow ripple back through the gear pump inlet line reduced the effectiveness of the device. From this, it is concluded that for this scheme, the rotary valve must be fed with flow from the main pump suction line.

For the rotary valve unit to be built as an attachment for existing pumps then a device would be needed to store and release energy from the pump feeding the rotary valve. This action would be needed at the pumping frequency of the main pump, and it is unlikely that such a device would be commercially viable.

The rotary valve concept may have more merit if it was used to periodically bleed flow from the pump delivery pressure to a chamber at a lower pressure. In this case, the pump to feed flow to the rotary valve would be replaced by a motor which would discharge the chamber pressure and contribute to the input power of the main pump.

10.4 Simulation Work

Initial simulations using the Bathfp "Cappa Suite" single cylinder model underestimated the pump internal flow ripple. Simulation accuracy was improved by reducing the fluid bulk modulus from 17000 to 11000 bar. This accounted for the effects of air release within the suction chamber. More sophisticated models of instantaneous and delayed air release were also used, but on occasion they were found to give spurious results.

The "Cappa Suite" single cylinder model was extensively modified to create the "Dual Cylinder" model. This new model significantly speeded up the simulation process, and provided additional information on the swashplate forces and moments, and also on the pumping efficiency.

The "Dual Cylinder" model was used to compare the test pump with units of similar capacity but with 10 cylinders, and solid pistons. These simulations showed that both of the alternative pump configurations produced a lower delivery flow ripple than the test pump at the expense of an increase in the yoke moment ripple. However, the pump with solid pistons caused large reductions in the pump flow ripple with only small increases in the yoke moment ripple. From this, solid-pistoned pumps are likely to be viable, although their mass should be minimised (possibly using low-mass inserts) to help prevent "piston pounding".

The "Dual Cylinder" model was extended to predict the behaviour of the HDCV prototype. The model could only be validated against the measured delivery flow ripple and achieved acceptable agreement. Generally, the model correctly predicted which of the HDCV ports were open and closed. However, the model did not predict the large response of the HDCV poppets at the pumping frequency. As a result, a smoother delivery flow ripple than that found from measurement is predicted.

10.5 Test Work

The measured source impedance of the test pump featured two effects caused by drillings from the delivery chamber through to the swashplate servo mechanism. An inertial effect occurs below 300Hz when there is flow through the pressure compensator to the swashplate control piston. The second effect is a resonance between 700 and 1300Hz which is caused by the drillings behaving as a branch resonator. This second effect causes the pump source impedance to resemble that of a parallel Helmholtz impedance model.

Tests have been conducted on the test pump modified to feature no drillings from the delivery chamber through to the swashplate servo mechanism. The source impedance of this pump resembles that of a conventional Helmholtz discharge passageway model.

The internal flow ripple of the original and modified pumps was established using the "Secondary Source" method. The internal flow ripple from the two discharge passageways differed in the frequency range of the branch resonator impedance feature (1). This difference is probably caused by shortcomings in applying the parallel Helmholtz model to the discharge passageway that features drillings.

The internal flow ripple measured from the test pump features fluid compressibility effects that are the same magnitude as those predicted from simple theoretical considerations.

10.6 Recommendations for further work

1 The HDCV prototype should be developed further to improve its performance and its reliability. To do this, the causes of the swashplate instability and the anomalies in the HDCV damping need to be understood. The swashplate instability could be investigated by fitting pressure transducers to measure the pressure within the individual HDCV spring chambers. The anomalies in the HDCV damping could be investigated by measuring the motion of the individual HDCV poppets. This may be difficult as the measurement technique must be non-intrusive.

2 The HDCV simulation model is at a very advanced stage of development and has already helped to explain some of the effects seen in measurements of the pump delivery flow ripple. The model should be developed further by validating it with new types of measurement from the HDCV prototype (i.e. poppet displacements and velocities, and measurements of the spring chamber pressures).

3 The existing test rig should be used to investigate destructive interference of the test pump flow ripple using an optimised rotary valve bleeding flow pulses from the delivery line

4 Development work should be carried out on axial piston pumps fitted with solid pistons.

5 A prototype version of the speed-sensing Helmholtz resonator should be manufactured and developed.

6 A prototype for the 3-dimensional multi-lobed cam concept should be built and developed. Initially it could be tested using the rotary valve cancellation test rig.

7 Improvements in the modelling of air release and cavitation are required to avoid the need to estimate the fluid bulk modulus.

8 A new parallel impedance model of the pump discharge passageway is needed for flow referral within pumps featuring pilot drillings inside the delivery chamber.

References

1 **Atkinson, R.H.,** "Noise reduction in vane and piston pumps"
Proc. 39th. NCFP, Los Angeles USA, 1983, pp318-324

2 **Heron, R.A., Hansford I.** "Airborne noise due to structure borne vibrations transmitted through pump mountings and along circuits"
I.Mech.E. seminar Quiet Oil Hydraulic systems, London UK., 1977, pp41-50

3 **Hughes, M.L.** "Flexural vibrations in rigid pipework due to liquid borne noise"
I.Mech.E. seminar Quiet Oil Hydraulic systems, London UK., 1977, pp51-58

4 "Quieter Fluid Power Handbook"
British Hydro-Mechanical Research Association publication

5 **Skaistis, S.** "Noise Control of Hydraulic Machinery"
Marcel Dekker, Inc., New York, 1988.

6 **Johnston, D.N.** "Measurement and Prediction of the Fluid Borne Noise Characteristics of Hydraulic Components and Systems"
PhD. Thesis, School of Engineering, University of Bath, U.K. 1987.

7 **Lipscombe, B.R.** "The reduction of gear pump pressure-ripple by source flow modification."
PhD. Thesis, School of Engineering, University of Bath, U.K. 1986.

8 **Edge, K.A., Lui, Y.** "Reduction of Piston Pump Pressure Ripple."
Proc. 2nd. International Conference Fluid Power Transmission and Control, Zejiang University China, 1989, pp779-784

9 **Edge, K.A., Johnston, D.N.** "The 'secondary source' method for the measurement of pump pressure ripple characteristics. Part 1: description of method."
Proc. I.Mech.E., Part A, Vol.204, 1990, pp33-40

10 **Edge, K.A., Johnston, D.N.** "The 'secondary source' method for the measurement of pump pressure ripple characteristics. Part 2: experimental results."
Proc. I.Mech.E., Part A, Vol.204, 1990, pp41-46

11 **Edge, K.A., Darling, J.** "Cylinder pressure transients in oil hydraulic pumps with sliding plate valves"
Proc. I.Mech.E., Part B1, Vol.200, 1986, pp45-54

12 **Harris, R.M., Edge, K.A., Tilley, D.G.** "The suction dynamics of positive displacement axial piston pumps"
ASME WAM, Nov. 8 - 13, 1992, Anaheim, USA.

13 "Pump Flow Ripple - Fluid Power 2 Course Notes"
University of Bath, School of Mechanical Engineering, 1995

14 **Bergemann, M.** "Noise problems of hydraulic piston pumps with odd and even numbers of cylinders."
Proc. 9th. Int. Fluid Power Symposium, Oxford, UK, 1990, pp235-248

15 **McCloy, D., Martin, H.** "Control of Fluid Power - 2nd. Ed."
Ellis Horwood ltd., London, 1980, pp229-260

16 **Watton, J.** "Fluid Power Systems"
Prentice Hall ltd., London, 1989, pp95 - 119

17 **Bowns, D.E., McCandlish, D.** "Pressure Ripple Propagation"
I.Mech.E. seminar Quiet Oil Hydraulic systems, London UK., 1977, pp93-102

18 **Bowns, D.E., Edge K.A., Tilley, D.G.** "The assessment of pump fluid borne noise"
I.Mech.E. seminar Quiet Oil Hydraulic systems, London UK., 1977, pp115-125

19 **Johnston, D.N., Longmore, D.K.** "Rating of Pump Fluid-borne Noise"
A.S.M.E. Congress and Exposition., Chicago, Nov 1994.

20 **Larsson, P., Palmberg, J.O., Weddfelt, K.** "Analysis and measurement of Pressure Ripple of Fluid Power Pumps"
8th. IASTED Int. Symp., MECO '86, Sep 3-5, 1986, Taormina, Italy

21 **Edge, K.A.** "The theoretical prediction of the impedance of positive displacement pumps"
I.Mech.E. seminar Quieter Oil Hydraulics, London UK., 1980, pp95-103

22 **Davidson, L.C.** "The Internal Impedance of Centrifugal and Positive Displacement Pumps"
A.S.M.E. Conference on Noise and Fluids Engineering., Atlanta, Georgia, Nov. - Dec. 1977.

23 **Edge, K.A., Wing, T.J.** "The measurement of the fluid borne pressure ripple characteristics of hydraulic components"
Proc. I.Mech.E., Part B, Vol.197, 1983, pp247-254

24 **Johnston, D.N.** "Pressure Ripple Analysis Software Package PRASP: User Guide and Reference Manual Ver 2.02b"
University of Bath, School of Mechanical Engineering, 1995

25 **Lipscombe, B. R.** "The Reduction of Gear Pump Pressure Ripple by Source Impedance Modification"
MSc. Thesis, School of Engineering, University of Bath, U.K. 1981.

26 **Foster, K., Hannan, D.M.,** "Fundamental Fluid-borne and airborne noise generation of axial piston pumps"
I.Mech.E. seminar Quiet Oil Hydraulic systems, London UK., 1977, pp29-40

27 **Viersma, T.J.** "Analysis, Synthesis, and Design of hydraulic servo systems and pipelines"
Elsevier, 1980. ISBN 0-444-41869-5

28 **Zaichenko, I.Z., Boltyanaskii,A.D.** "Reducing noise levels of axial plunger pumps"
Russian Engineering Journal, Vol XIXX, No.4, 1969.

29 **Helgestad, B.O., Foster, K., Bannister, F.K.** "Pressure Transients in an axial-piston hydraulic pump"
Proc. I.Mech.E., Vol. 188, No.17/74, 1974

30 **Martin, M.J., Taylor, R.** "Optimised port-plate timing for an axial piston pump"
Proc. 5th. International Fluid Power Symposium, Durham UK., 1978, pp51-66

31 **Kelsey, J.S., Taylor, R., Wood, K.** "The practical benefits of optimising the port plate timing for an axial piston pump"
I.Mech.E. seminar Quieter Oil Hydraulics, London UK., 1980, pp15-20

32 **Foster, K., Kelsey, J.S., Taylor, R.**"Fluid Properties: The effect of the fluid being pumped on the noise emitted by an axial piston pump"
I.Mech.E. seminar Quieter Oil Hydraulics, London UK., 1980, pp71-77

33 **Darling, J.** "Piston-Cylinder Dynamics in Oil Hydraulic Piston Pumps"
PhD Thesis, School of Engineering, University of Bath, UK. 1985.

34 **Palmberg, J-O. "**Modelling of Flow Ripple from Fluid Power Piston Pumps"
Proc. 3rd International Fluid power workshop, Bath UK, 1990, pp207-227

35 **Harris, R.M., Edge, K.A., Tilley, D.G.**"Reduction of Piston Pump Cavitation by means of a Pre-expansion Volume"
Proc. 5th International Fluid power workshop, Bath UK, 1992, pp167-183

36 **Richards, C.W.., Tilley, D.G., Tomlinson, S.P., Burrows, C.R.** "A Second Generation Package for Fluid Power Systems"
Proc. 9th. Int. Fluid Power Symposium, Oxford, UK, 1990, pp315-322

37 **Harris, R.M.** "The CAPPA suite: Bathfp Model Reference Guide for Computer Aided Pump Performance Analysis. Parts 1 and 2"
University of Bath, School of Mechanical Engineering, August 1991 and August 1992.

38 **Burrows, C.R., Tomlinson, S.P., Hogan, P.A.** "Some Modelling Aspects of Bathfp"
Proc. 4th International Fluid power workshop, Bath UK, 1991, pp201-215

39 **Richards, C.W., Tilley, D.G., Tomlinson, S.P., Burrows, C.R.** "Type-Insensitive Codes for the Simulation of Fluid Power Systems"
ASME WAM, Nov. 25 - 30, 1990, Dallas, USA.

40 **Johnston, D.N.** "Analysis Package for *Secondary Source* Test Method for Hydraulic Components FBN2 :User Guide and Reference Manual Ver 3.5"
University of Bath, School of Mechanical Engineering, June 1994

41 "PVH Piston Pumps"
Vickers Inc., Troy, Michigan, U.S.A. 1993

42 **Dorey, R.E.** "Modelling of Losses in Pumps and Motors"
Proc. 1st International Fluid power workshop, Bath UK, 1988, pp71-97

43 **Zeiger, G., Akers, A.** "Torque on the Swashplate of an Axial Piston Pump"
Trans. ASME Journal of Dynamic Systems, Measurement and Control, Vol107, September 1985,, pp220-226

44 **BS6335: 1990.**"Methods for determining pressure ripple levels generated in hydraulic fluid power systems and components. Part 1. Secondary source methods for pumps."
British Standards Institution, London, 1990.

45 **Johnston, D.N., Edge, K.A.**"In-situ measurement of the wavespeed and bulk modulus in hydraulic lines"
Proc. I.Mech.E., Part I, Vol.205, 1991, pp191-197

46 **Whitson, R.J.** "The measured transmission loss characteristics of some hydraulic attenuators."
I.Mech.E. seminar Quieter Oil Hydraulics, London UK., 1980, pp105-115

47 **Weddfelt, K.** Measurement of Pump Source Characteristics by the Two-Microphone Method"
2nd. Tampere Int. Conf. on Fluid Power, Mar19-21, 1991, Tampere Univ., Finland

48 **Guy, T.B.** "Attenuation of fluid noise in hydraulic machines by a new energy absorption technique".
Thermofluids Conference, Hobart Aus. Dec 1 - 3 1976.

49 **Chaplin, B.** "Anti-noise - the Essex breakthrough"
Chartered Mechanical Engineer, January 1983.

50 **Rebel, J.** "Active Liquid Noise-Suppressions in Oil Hydraulics."(In German)
VDI-Zeitschrift, Vol.119, 1977, pp937-943

51 **Kojima, E., Shinada, M.** "Development of an active attenuator for pressure pulsation in liquid piping systems."
Proc. 3rd International Fluid power workshop, Bath UK, 1990, pp104-123

52 **Kojima, E., Shinada, M., Yamaoka, T.** "Development of an Active Attenuator for Presure Pulsation in Liquid Piping Systems. (Trial Construction of the System and Fundamental Experiments on Attenuation Characteristics)"
Trans. JSME Series B, Vol. 36, No.2, 1993, pp230-237

53 **Kojima, E., Shinada, M., Yamaoka, T.** "Development of an Active Attenuator for Presure Pulsation in Liquid Piping Systems. (Trial Construction of the System and Fundamental Experiments on Attenuation Characteristics)" (In Japanese)
Trans. JSME, part B, Vol. 61, No 588, August 1995, pp2987-2995

54 **Schoenau, G.T., Burton, R.T., Beasant, R.W., Wilson, J.N.** "Investigation of a novel electrofluidic element."
Proc. BHRA conference on Hydraulics,Pneumatics, and fluidics in control and automation, Toronto, Canada, 1976, pp83-94

55 "The Piezo Book"
Burleigh instruments (UK) ltd., 11, Hatfield rd., St. Albans, Hertfordshire, 1992

56 **Bullough, W.A.** "Innovative Electron-Hydraulic developments for the fluid power industry."
Fluid Power - Proc. 9th. international symposium, Oxford UK, 1990, pp55-66

57 **Stangroom J. E.** "Electro-Rheological Fluids - An Introduction"
ER. Fluid Developments ltd., Vincent works, Brough, Bradwell, Sheffield, Great Britain.

58 **Pinkos, A., Shtarkman, E., Fitzgerald, T.** "Active damping using ERM fluids"
Automotive Engineering, June 1993, pp19-23

59 **Greenough, R.D., Jenner, A.G., Wilkinson, A.J.** "Actuation and control of Giant Magnetostrictive materials"
Proc. I.Mech.E. Seminar on Machines, Actuators and Controls, March 1993, pp67-72.

60 **Haarhaus, M., Haas, H.J.** "Untersuchung neuer Wege zur Gerauschminderung bei Axialkolbeneinheiten" (In German)
Olhydraulik und Pneumatik, vol 29, 1985, no.3, pp218-220

61 **Pettersson, M.** "Design of Fluid Power Piston Pumps, with Special Reference to Noise Reduction"
PhD. Thesis, Division of Fluid Power Technology, Department of Mechanical Engineering, Linköping University, Sweden, 1995

62 **Currie, J.A., Kane, J.** "The Design of Low Noise Hydraulic Equipment"
Proc. 1st. European Fluid Power Conference, paper no. 29, NEL, East Kilbride. 1973

63 **Grahl, T.** "Geräuschminderung an Axialkolbenpumpen durch variable Umsteuersysteme" (In German)
Olhydraulik und Pneumatik, vol 33, 1989, no.5, pp437-443

64 **Boyer J.J.** "Noise reducing device for swash-plate pump - has pressure responsive piston to control trapped volume in delivery ports."
Patent no. FR2408050

65 **Boltyanski, A.D., Levontin A.L.** "Axial piston pump distributor system has spool valve springless chambers connected to delivery port and valves with varying area slots to reduce noise and vibration."
Patent no: SU1186823

66 **Heyl W** "Hydraulic piston pump noise reduction - involves pressure and pump speed controlled throttle valve in duct correcting adjoining cylinders."
Patent no.: DE2850803

67 **Pettersson, M., Weddfelt, K., Palmberg, J.O.** "Methods of reducing flow-ripple from fluid power piston pumps - A Theoretical Approach"
Trans. SAE., no. 911762, 1991

68 **Weddfelt, K., Pettersson, M., Palmberg, J.O.** "Methods of reducing flow-ripple from fluid power piston pumps - An Experimental Approach"
Trans. SAE., no. 911763, 1991

69 **Pettersson, M., Weddfelt, K., Palmberg, J.O.** "Reduction of Flow-ripple from Fluid Power Machines by means of a Pre-compression Filter Volume."
Proc. 10th. Aachen Kolloquium on Fluid Power technology, 1992, pp181-197

70 **Weddfelt, K., Pettersson, M., Palmberg, J.O.** "An Investigation of the possibilities of using Fluidic Components in the Fluid Power Area"
Proc. Flucome '94, Toulouse, France, 29Aug - 1 Sep 1994, pp137-142

71 "Instructions and Applications - Bruel & Kjaer Precision Sound Level Meter Type 2203"
Bruel & Kjaer, Copenhagen, Denmark, December 1968

72 **Johnston, D.N., Drew, J.E.**"Measurement of positive displacement pump flow ripple and impedance"
Proc. I.Mech.E., Part I, Vol.210, 1996, pp65-74

73 "Manual of Pump Controls"
Vickers Systems Ltd., Havant U.K, May 1994

Appendix A: Derivation of Pump Source Characteristics

This appendix shows the derivation of expressions for pump source impedance. From this impedance then the equation for the pump internal flow ripple is also derived. These expressions are derived for three different cases:

1 A distributed parameter model

2 A Helmholtz model which includes the friction, compressibility and inertia effects within a pump discharge passageway.

3 A parallel Helmholtz model

1. The Distributed Parameter Model

Plane wave propagation theory was used by Bowns and McCandlish [11], Viersma [27], and later by Johnston [12], to model the pressure fluctuations produced in a simple pipe. From the assumptions shown in 2.4.2.2, the wave equation can be applied to the 1-dimensional flow within a uniform pipeline:

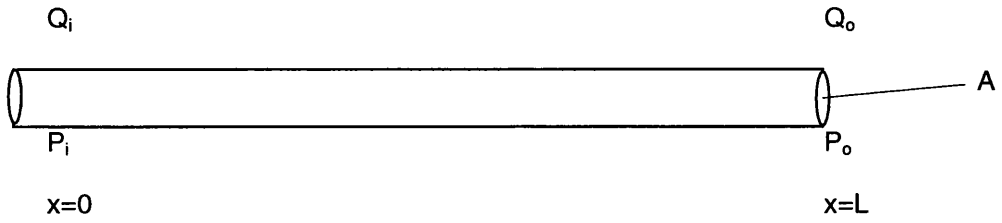

As solutions of the wave equation then the pressure and flow ripple at a particular frequency can be expressed by:

$$P = Fe^{-\gamma x} + Ge^{+\gamma x} \tag{A.1}$$

$$Q = \frac{Fe^{-\gamma x}}{Z_o} - \frac{Ge^{+\gamma x}}{Z_o} \tag{A.2}$$

Where $$Z_O = \frac{\sqrt{(\rho B_{eff})}}{A}\xi \tag{A.3}$$

And $$\gamma = j\omega\sqrt{\left(\frac{\rho}{B_{eff}}\right)}\xi \tag{A.4}$$

The complex coefficient ξ, represents the effects of fluid viscosity [3].

At x=0 equations A.1 and A.2 give

$$P = F + G$$

$$Q = \frac{F}{Z_o} - \frac{G}{Z_o}$$

which can be expressed in matrix form:

$$\begin{bmatrix} P_i \\ Q_i \end{bmatrix} = \begin{bmatrix} 1 & 1 \\ 1/Z_o & -1/Z_o \end{bmatrix} \begin{bmatrix} F \\ G \end{bmatrix} \tag{A.5}$$

At x=L equations A.1 and A.2 give

$$P = Fe^{-\gamma L} + Ge^{+\gamma L}$$

$$Q = \frac{Fe^{-\gamma L}}{Z_o} - \frac{Ge^{+\gamma L}}{Z_o}$$

$$\begin{bmatrix} F \\ G \end{bmatrix} = \begin{bmatrix} \frac{1}{2}e^{\gamma L} & \frac{Z_o}{2}e^{\gamma L} \\ \frac{1}{2}e^{-\gamma L} & -\frac{Z_o}{2}e^{-\gamma L} \end{bmatrix} \begin{bmatrix} P_o \\ Q_o \end{bmatrix} \qquad (A.6)$$

Combining A.5 and A.6 gives the 4 pole equation:

$$\begin{bmatrix} P_i \\ Q_i \end{bmatrix} = \begin{bmatrix} \cosh\gamma L & Z_o \sinh\gamma L \\ \frac{1}{Z_o}\sinh\gamma L & \cosh\gamma L \end{bmatrix} \begin{bmatrix} P_o \\ Q_o \end{bmatrix} \qquad (A.7)$$

For fluidborne noise analysis, a pump is normally represented with a Norton model with the source flow ripple in parallel with a source impedance:

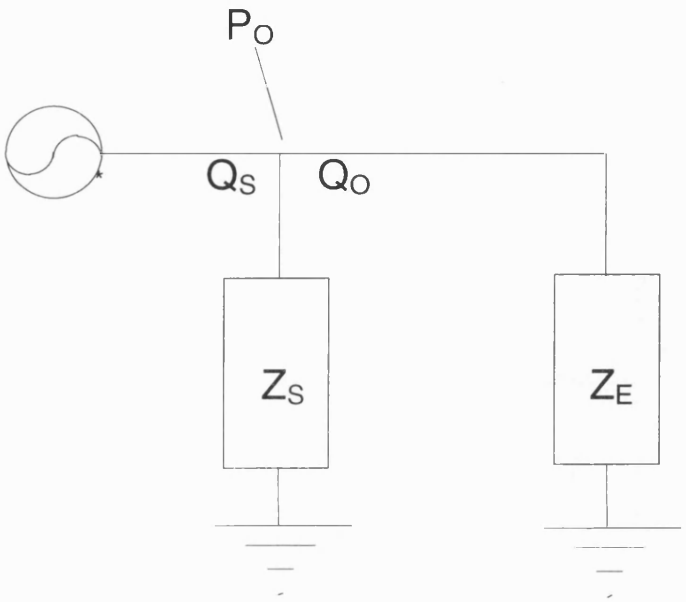

For this system:

$$P_O = Q_O Z_E \qquad (A.8)$$

$$Q_S = P_O\left(\frac{1}{Z_S} + \frac{1}{Z_E}\right) \qquad (A.9)$$

$$Q_O = \frac{Q_S Z_S}{Z_S + Z_E} \qquad (A.10)$$

$$Q_O = Q_S - \frac{P_O}{Z_S} \qquad (A.11)$$

To find Z_S, the pump source flow is set to zero:

$$Q_S = 0 \qquad (A.12)$$

The pump source impedance is measured at the pump exit, and so from A.11 and A.12,

$$Z_S = -\frac{P_O}{Q_O} \qquad (A.13)$$

Edge[16], Edge and Wing[18], and Johnston[12] showed that for most pumps, the source impedance can be represented as a short length of pipe of constant cross-sectional area A_P and length l_P with a closed end. For this case the 4 pole equation becomes,

$$\begin{bmatrix} P_i \\ Q_s^* \end{bmatrix} = \begin{bmatrix} \cosh\gamma L_p & Z_{op}\sinh\gamma L_p \\ \frac{1}{Z_{op}}\sinh\gamma L_p & \cosh\gamma L_p \end{bmatrix} \begin{bmatrix} P_o \\ Q_o \end{bmatrix} \quad \text{(A.14)}$$

γ is given by equation A.4 and Z_{OP} is the characteristic impedance of the pump discharge passageway given by equation A.3:

$$Z_{OP} = \frac{\sqrt{(\rho B_{eff})}}{A_P}\xi$$

Setting Q_S^* to zero gives,

$$0 = \frac{1}{Z_{OP}}(\sinh\gamma L_P)P_O + (\cosh\gamma L_P)Q_O \quad \text{(A.15)}$$

and from A.13 and A.15 the pump source impedance is given by,

$$Z_S = -\frac{P_O}{Q_O} = \frac{Z_{OP}}{\tanh\gamma L_P} \quad \text{(A.16)}$$

If the coefficient ξ, representing the effects of fluid viscosity is ignored then A.16 can be converted into,

$$Z_S = \frac{Z_{op}}{j\tan\left(\omega\frac{L_p}{c_o}\right)} \quad \text{(A.17)}$$

To calculate the internal flow ripple, Q_S^* is re-introduced to equation A.15 such that,

$$Q_S^* = \frac{1}{Z_{OP}}(\sinh\gamma L_P)P_O + (\cosh\gamma L_P)Q_O \quad \text{(A.18)}$$

So, from A.8,

$$Q_S^* = \frac{Q_O Z_E}{Z_{OP}}(\sinh\gamma L_P) + (\cosh\gamma L_P)Q_O \quad \text{(A.19)}$$

and from A.10,

$$Q_S^* = \frac{Q_S Z_S}{Z_S + Z_E}\left[\frac{Z_E}{Z_{OP}}(\sinh\gamma L_P) + (\cosh\gamma L_P)\right] \quad \text{(A.20)}$$

which reduces to the final expression for the pump internal flow ripple by substituting the previously derived expression for the pump source impedance (A.16):

$$Q_S^* = Q_S\cosh\gamma L_P \quad \text{(A.21)}$$

2. The Helmholtz Model

If friction and fluid inertia effects are included then the discharge passageway can taken as a compressible volume, an inertia and a resistance (i.e. equivalent to the electrical analogy of a simple RLC network), and can be analysed using a transmission matrix [72]:

$$\begin{bmatrix} P_i \\ Q_S^* \end{bmatrix} = \begin{bmatrix} t_{11} & t_{12} \\ t_{21} & t_{22} \end{bmatrix} \begin{bmatrix} P_o \\ Q_o \end{bmatrix} \quad \text{(A.22)}$$

If $P_o = 0$ then

$$P_i = Q_o(R + j\omega L) = Q_o(t_{12}) \quad \text{(A.23)}$$

$$\begin{aligned} Q_S^* &= Q_o + P_i(j\omega C) = Q_o(1 + j\omega C(R + j\omega L)) \\ &= Q_o(t_{22}) \end{aligned} \quad \text{(A.24)}$$

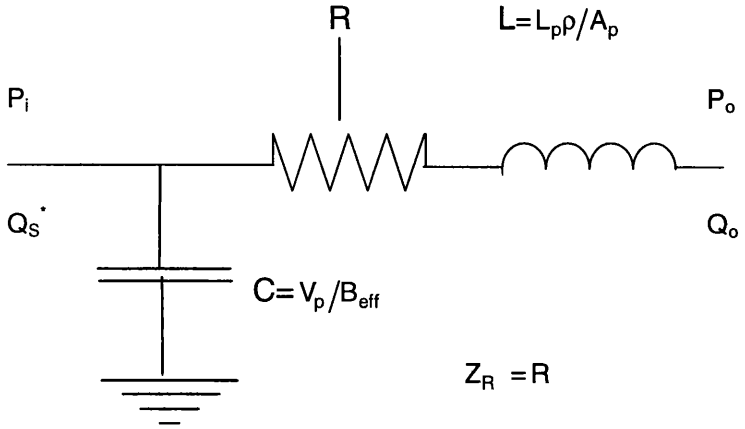

$$Z_R = R$$

$$Z_L = j\omega L$$

$$Z_C = \frac{1}{j\omega C}$$

If $P_o = P_i$ then $Q_o = 0$ and,

$$P_i = P_o = P_o(t_{11}) \tag{A.25}$$

$$Q_S^* = P_i(j\omega C) = P_o(j\omega C) = P_o(t_{21}) \tag{A.26}$$

Equations A.23 - 26 provide the matrix elements of A.22 to give:

$$\begin{bmatrix} P_i \\ Q_S^* \end{bmatrix} = \begin{bmatrix} 1 & R + j\omega L \\ j\omega C & 1 + j\omega C(R + j\omega L) \end{bmatrix} \begin{bmatrix} P_o \\ Q_o \end{bmatrix} \tag{A.27}$$

To find the pump source impedance then $Q_i = 0$ (As with the distributed parameter model - see Eq.A.12), and so from A.27,

$$0 = P_o(j\omega C) + Q_o(1 + jwC(R + j\omega L)) \tag{A.28}$$

And from A.13 and A.28,

$$Z_s = -\frac{P_o}{Q_o} = \frac{1 + j\omega C(R + j\omega L)}{j\omega C} \quad \left(= \frac{t_{22}}{t_{21}} \right)$$

Therefore the pump source impedance is given by,

$$Z_S = \frac{1}{j\omega C} + R + j\omega L \tag{A.29}$$

which then converts to

$$Z_s = R + j\omega \frac{l_p \rho}{A_p} + \frac{B_{eff}}{j\omega V_p} \tag{A.30}$$

As with the distributed parameter model (See Eq A.18), the internal pump flow ripple can found from elements of the discharge passageway transmission matrix [72]:

$$Q_S^* = t_{21} P_O + t_{22} Q_O \tag{A.31}$$

where a similar manipulation arrives at the expression for the pump internal flow ripple in terms of the pump exit flow ripple:

$$Q_S^* = t_{22} Q_S = Q_S(1 + j\omega C(R + j\omega L)) \tag{A.32}$$

3. The Parallel Helmholtz Model

This model is based upon the conventional Helmholtz model and is used to model discharge passageways that feature drillings to connected volumes. This system is analysed using the method used for the Helmholtz model [72]. The impedance network for this system is as below:

$$\begin{bmatrix} P_i \\ Q_S^* \end{bmatrix} = \begin{bmatrix} t_{11} & t_{12} \\ t_{21} & t_{22} \end{bmatrix} \begin{bmatrix} P_o \\ Q_o \end{bmatrix} \tag{A.22}$$

If $P_o = 0$ then

$$P_i = Q_o(R_1 + j\omega L_1) = Q_o(t_{12}) \tag{A.33}$$

$$\begin{aligned} Q_S^* &= Q_o + P_i(j\omega C_1) = Q_o(1 + jwC_1(R_1 + j\omega L_1)) \\ &= Q_o(t_{22}) \end{aligned} \tag{A.34}$$

If $Q_o = 0$ then

$$\frac{P_i}{P_o} = \frac{Z_{R1} + Z_{L1} + Z_{R2} + Z_{L2} + Z_{C2}}{Z_{R2} + Z_{L2} + Z_{C2}} \tag{A.35}$$

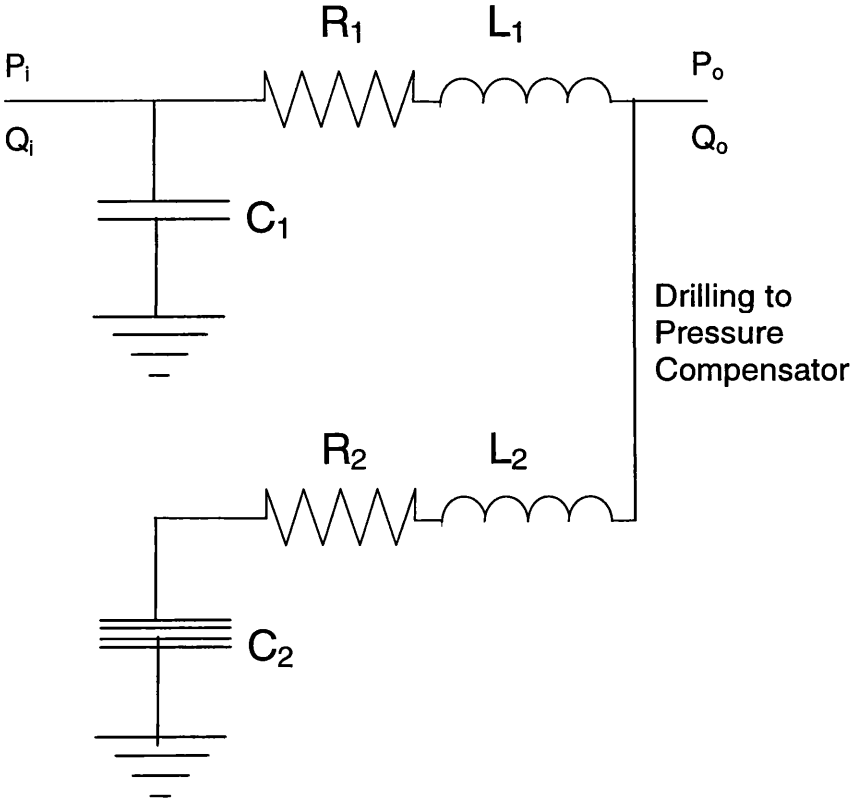

$$P_i = P_o\left[\frac{j\omega C_2(R_1 + R_2 + j\omega(L_1 + L_2)) + 1}{jwC_2(R_2 + j\omega L_2) + 1}\right] = P_o(t_{11}) \tag{A.36}$$

$$Q_S^* = P_i\left(\frac{1}{Z_{C1}} + \frac{1}{Z_{R1} + Z_{L1} + Z_{R2} + Z_{L2} + Z_{C2}}\right) \tag{A.37}$$

and substituting A.35 into A.37 gives,

$$\begin{aligned} Q_S^* &= P_o\left(\frac{Z_{R1} + Z_{L1} + Z_{C1} + Z_{R2} + Z_{L2} + Z_{C2}}{Z_{C1}(Z_{R2} + Z_{L2} + Z_{C2})}\right) \\ &= P_o(t_{21}) \end{aligned} \tag{A.38}$$

Equations A.33, 34, 36 and 38 provide the matrix elements of A.22 and so by analogy with the previous models,

$$Z_s = \frac{t_{22}}{t_{21}} = \frac{(Z_{R1}+Z_{L1}+Z_{C1})(Z_{R2}+Z_{L2}+Z_{C2})}{Z_{R1}+Z_{L1}+Z_{C1}+Z_{R2}+Z_{L2}+Z_{C2}} \qquad \text{(A.39)}$$

As with the previous models, the internal pump flow ripple can be found using element t_{22} of the discharge passageway transmission matrix and in this case the result unchanged from that derived for the conventional Helmholtz model:

$$Q_S^* = t_{22}Q_S = Q_S(1+j\omega C(R+j\omega L)) \qquad \text{(A.40)}$$

Appendix B Details of the Test Rig Equipment

1. FBN test rig equipment

The following specifications refer to equipment shown in the FBN test rig figures 5.1, 5.2, 5.3, 7.3, and 7.4.

1.1 Return Line Flowmeter

Type	Float meter
Manufacturer	UCC
Model	Flowline FM.26-332-212
Serial No.	N/A

1.2 Measurement Section Pressure Transducers

Type	Piezoelectric
Manufacturer	AVL
Model	6QP 500
Serial No.s	754,1327,1333

Serial No.	Gain pC/Kp/cm^2	Gain pC/bar	Gain (est) bar/V
754	7.26	7.401	13.51
1327	6.58	6.707	14.91
1333	7.38	7.523	13.29

2. Interference test rig equipment

The following specifications refer to equipment shown in the interference test rig figures 7.14 and 7.15. A diagram of the phase lock loop circuitry is shown in figure B.1.

2.1 Cancellation rotary valve drive motor

Type	DC Servomotor fitted with 512 ppr encoder and marker pulse
Manufacturer	SEM
Model	HD92L-4 - 44T
Controller	Eurotherm type 560/0107/4/1/0/3

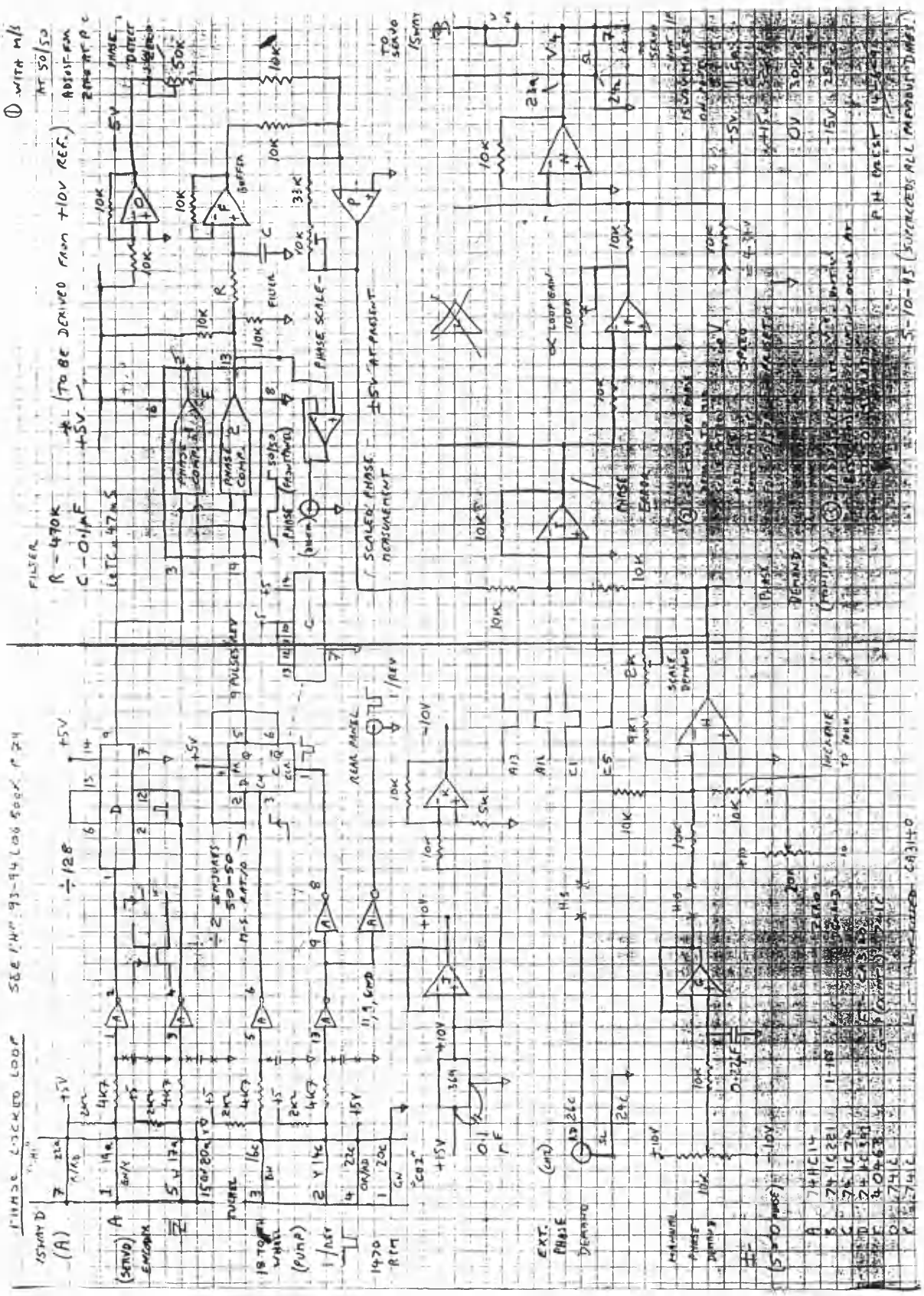

Figure B.1

The Phase-locked loop hardware used during the rotary valve interference testing

Appendix C Details of the test pump

This appendix describes the layout and quantifies the physical parameters of the test pump used during the course of the project. After initial tests, the valve block from the original pump was replaced with one that featured no pilot drillings in the discharge passageway (see Chapter 5). The differences between the original and the modified valve blocks are outlined. The figures of this chapter have been reproduced from a Vickers publication [73].

Towards the end of the project, the original valve block and portplate were modified according to the HDCV prototype design. The details of this design are given in Appendix E.

The port dimensions and timing are shown with the portplate sketch illustrated in figure C.2. The cylinder block and piston assemblies are sketched in figure C.3 in which the swashplate is shown at the full displacement condition.

The pressure compensation mechanism is shown in the hydraulic diagram of figure C.4 and in the sketch of figure C.5. When the delivery pressure is low then the pressure force acting on the pressure compensator spool is insufficient to overcome the pre-load of the compensator spring. At this condition the control piston is pressurised via line A from line D which is at suction pressure. The bias piston is connected to delivery pressure via line A and so the swashplate is held at full displacement. When the delivery pressure rises to the pressure setting of the compensator then the compensator spool moves to connect the control piston to line C which is also at delivery pressure. When this occurs then the yoke moment from the control piston overcomes that from the bias piston and the swashplate tilts tp produce a lower pump displacement.

The pressure compensation within the modified valve block is illustrated with figures C.6 and C.7. The valve block modification was carried out so that the pump source impedance could be measured without pilot drillings B and C breaking into the discharge passageway. For this scheme, the control piston is isolated and so, when the swashplate is stationary, it remains at the case pressure. The bias piston is connected through port B to the delivery line outside the pump casing. This pressure is throttled with a needle valve. For a low displacement the needle valve is closed and the pressure within the bias piston drops due to leakage. The yoke moment due to the pressurised cylinders then forces the swashplate to a smaler displacement. When the required displacement is reached then the needle valve between port B and the delivery line is cracked open to provide a pressure in the bias piston to balance the swashplate against the cylinder forces.

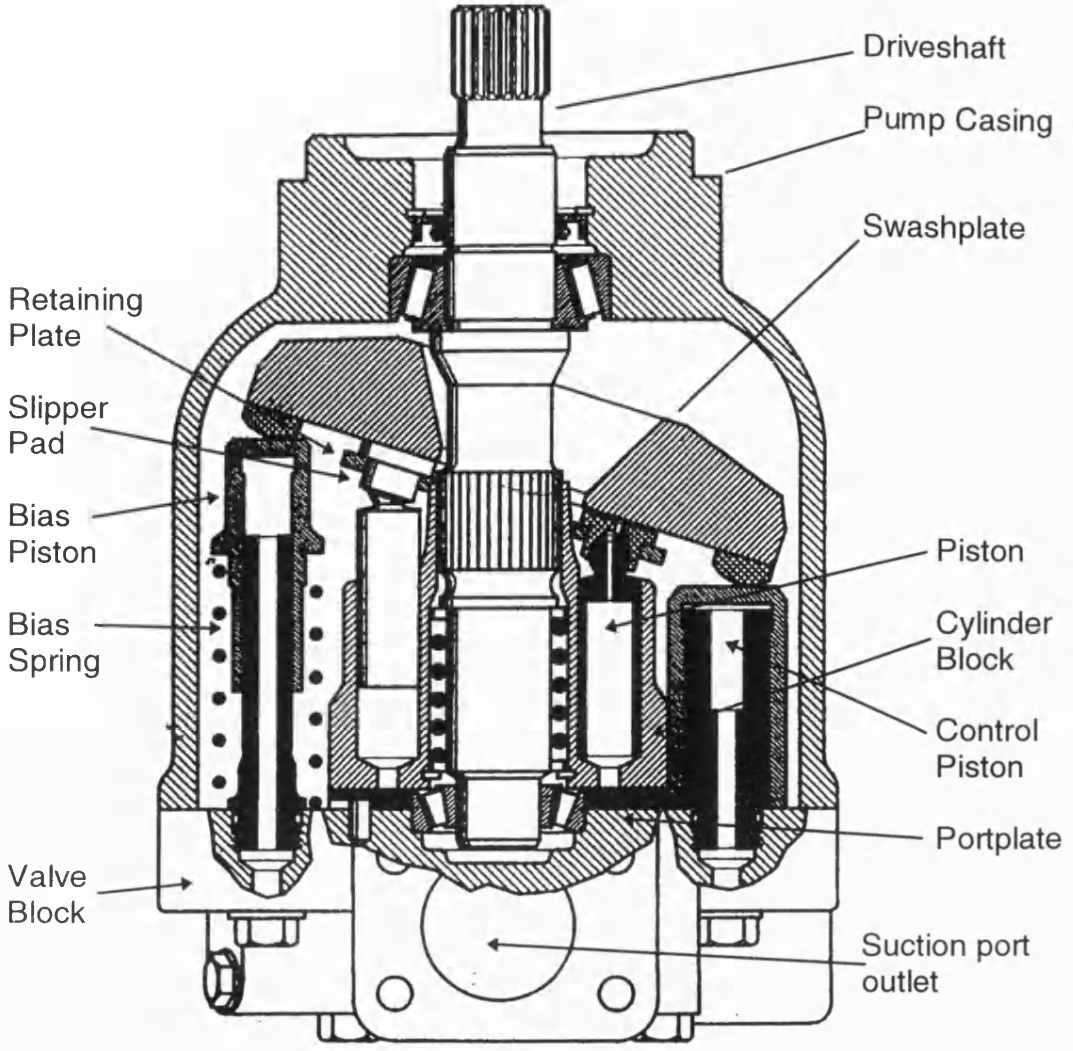

Figure C.1 Section through Vickers PVH series pump [from 73]

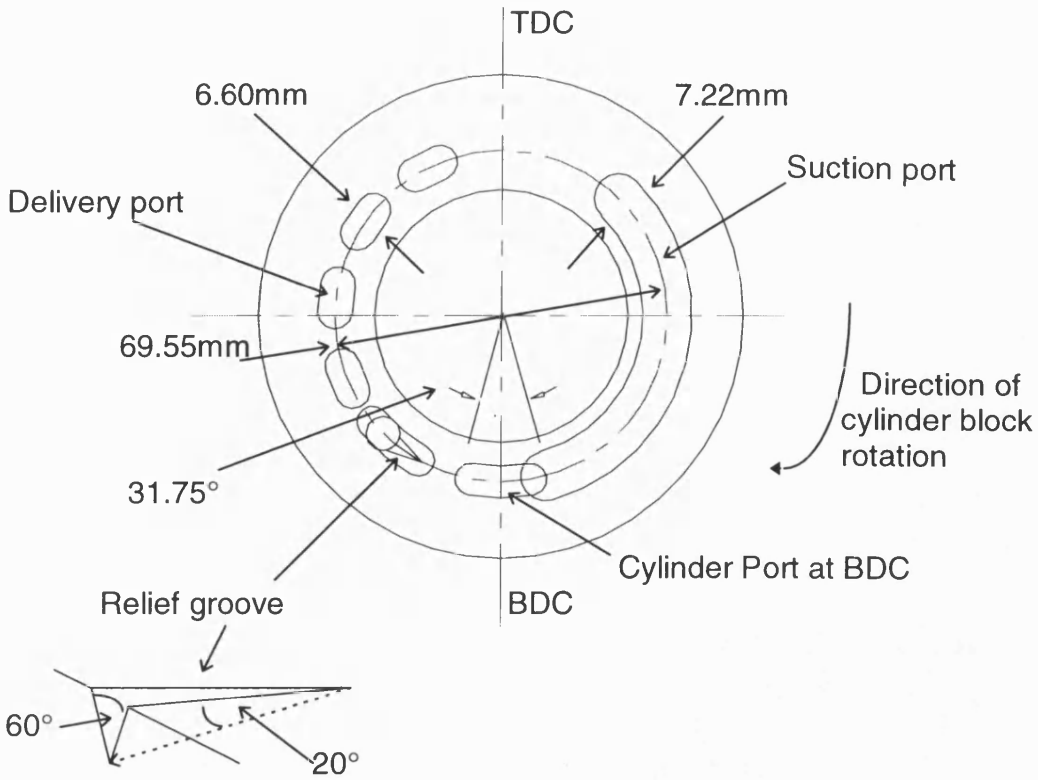

Portplate Feature	Angle from BDC (degrees)
Start of relief groove	28.0
Lead radius of Delivery Port	39.0
Range of 1st. Delivery Port Bridge	50.0 to 57.0
Range of 2nd. Delivery Port Bridge	78.5 to 85.5
Range of 3rd. Delivery Port Bridge	107.0 to 114.0
Range of 4th. Delivery Port Bridge	135.5 to 142.5
End of Delivery Port	164.0
Range of Suction Port	216.25 to 353.0

Figure C.2 Port details for the Vickers PVH57

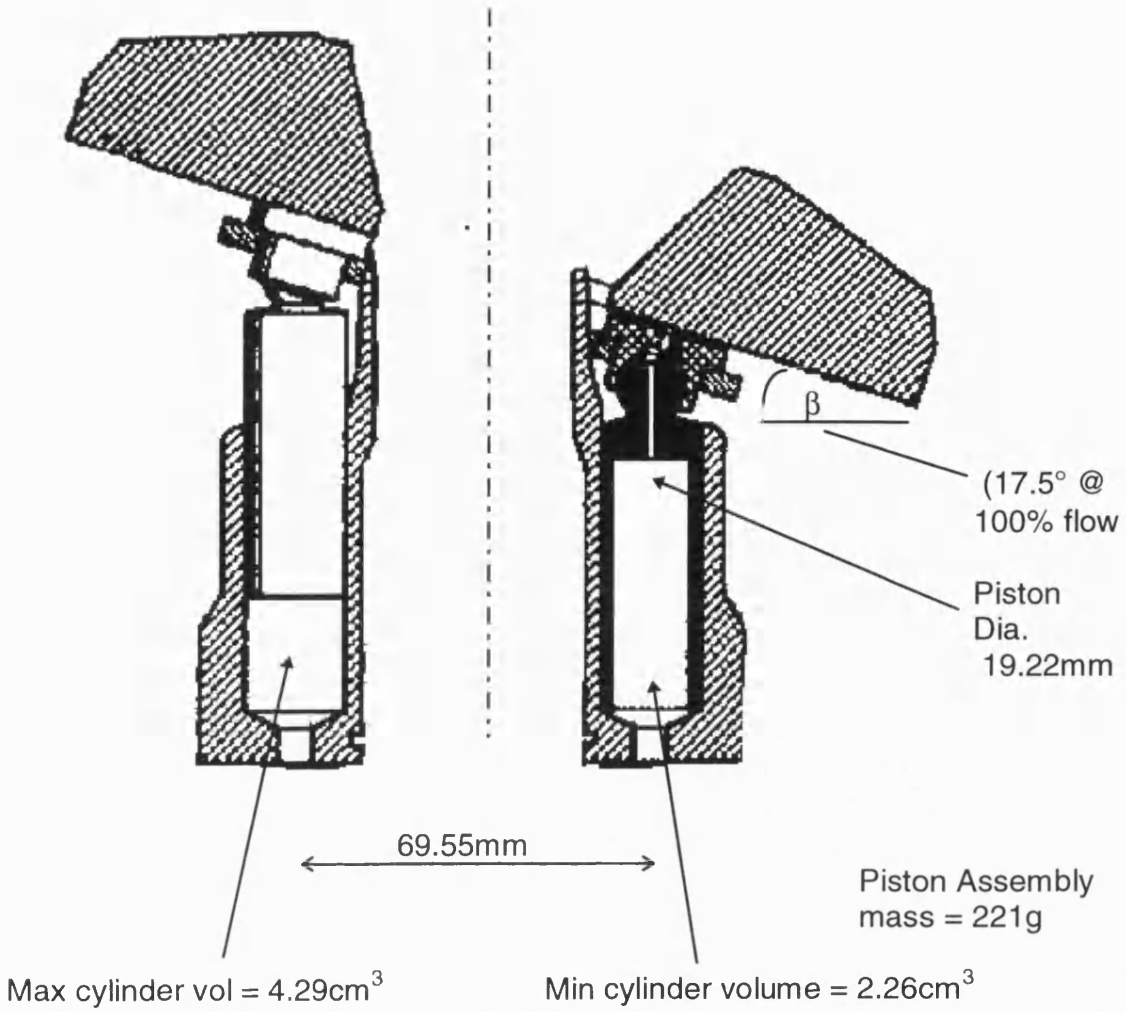

Figure C.3 Rotating Group details for the Vickers PVH57

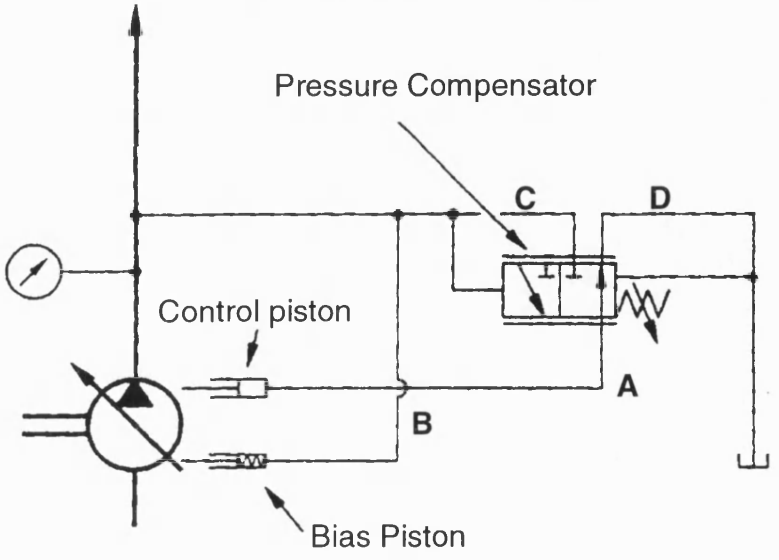

Figure C.4 Hydraulic diagram for the pressure compensated PVH57

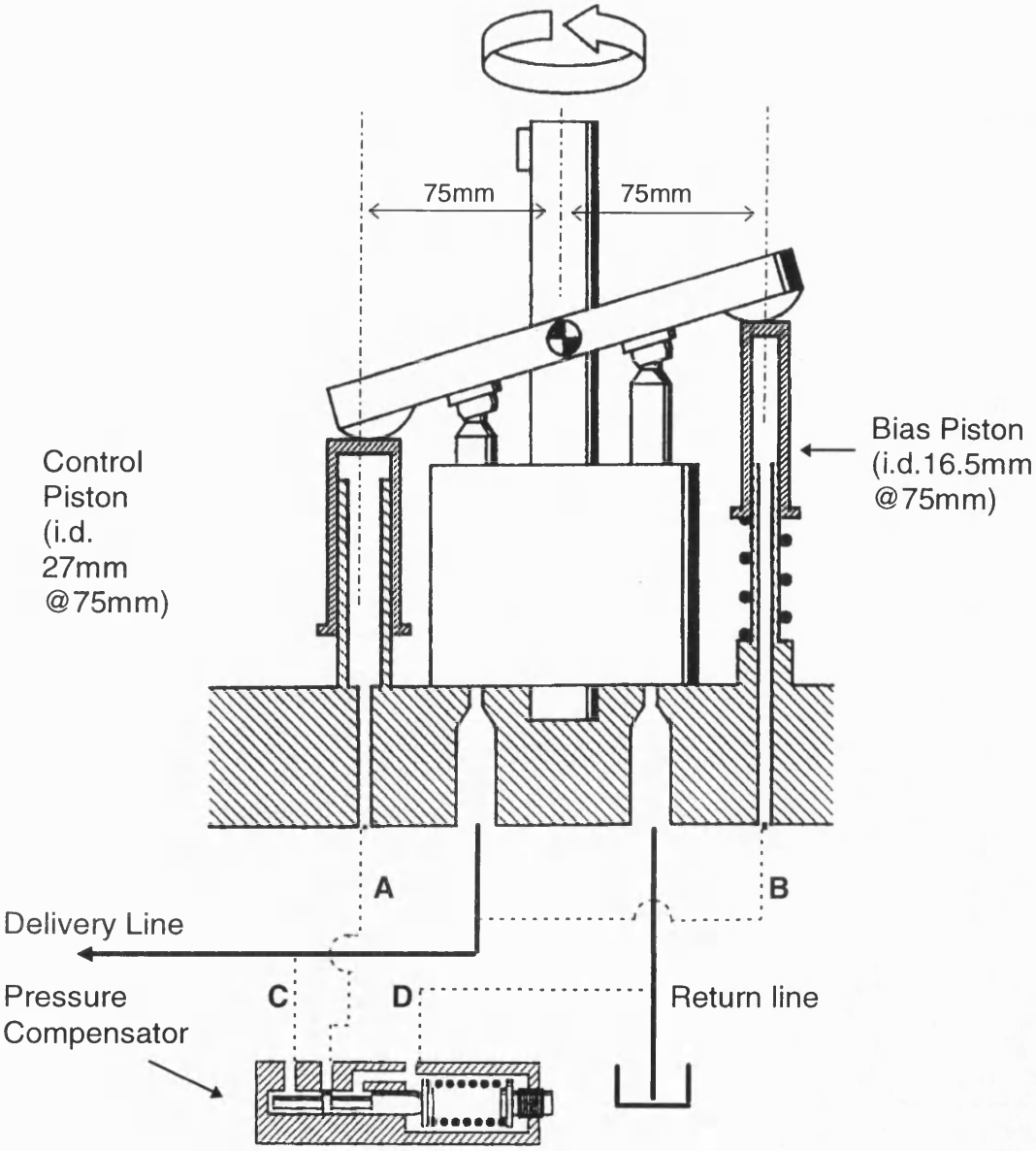

Figure C.5 Scheme showing the Pressure Compensation for the PVH57

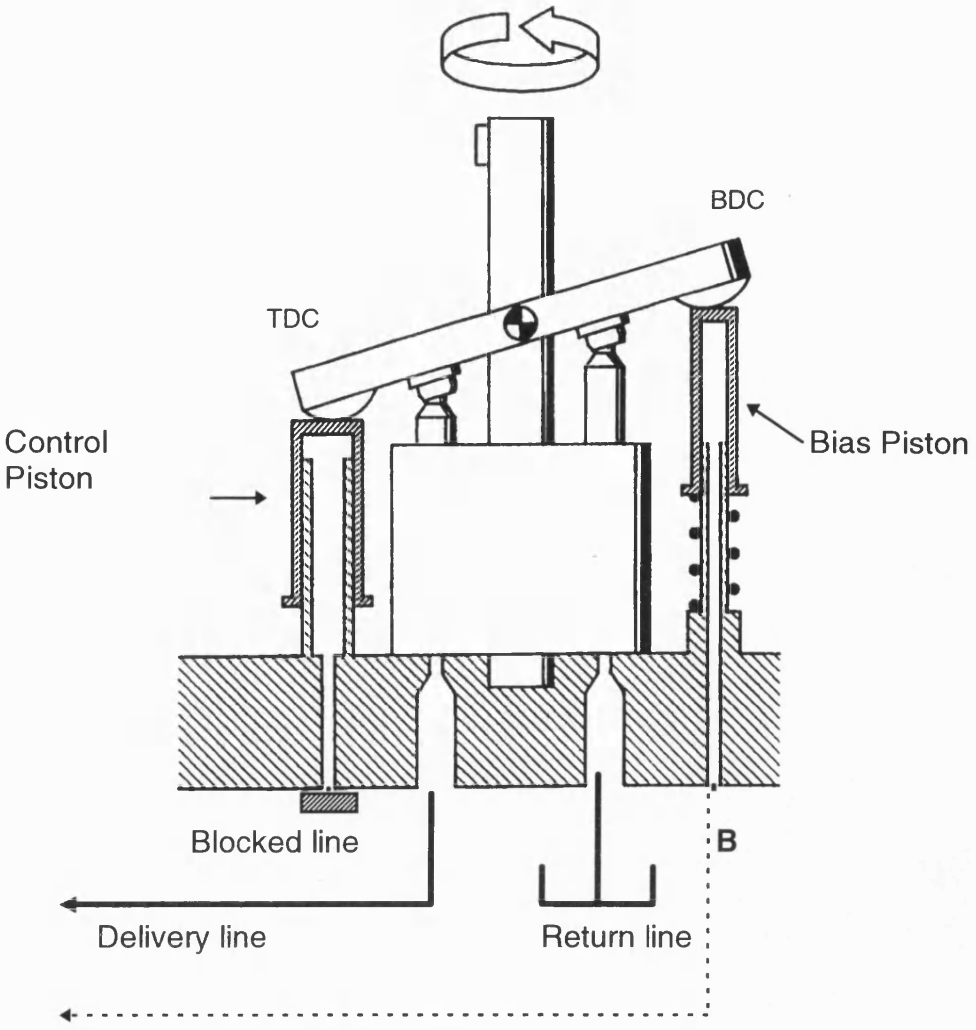

Figure C.6 Pressure Compensation within the modified PVH57

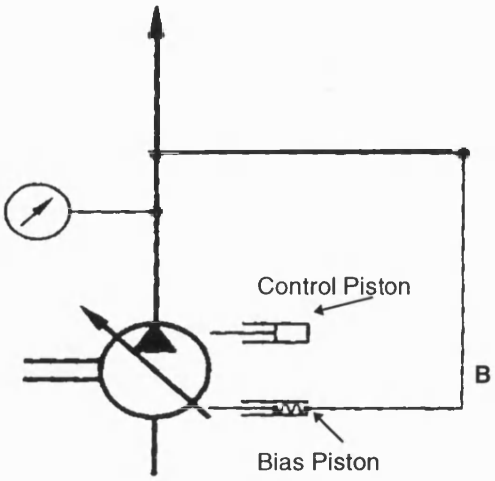

Figure C.7 Hydraulic diagram for the modified PVH57

Appendix D Settings used for the FBN2 Software

1. Parameters used for testing the Vickers test pump.

These parameters were used in ACQUIRE during testing of the Vickers pump:

FBN2 Version 4.000 Harmonic calibration data read from CAL2706.DAT

Pipe diameter	26.4 mm	Adaptor diameter	26.4 mm
Pipe thickness	2.67 mm	Reference diameter	26.4 mm
Adaptor length	79 mm		

Transducer distance	calibration factor
0.080 m	1.3510 bar/V
0.490 m	1.3000 bar/V
0.780 m	1.3000 bar/V

2. Parameters used for testing the rotary valve.

These parameters were used in ACQUIRE during the testing of the rotary valve

FBN2 Version 4.000 Harmonic calibration data read from CAL2706.DAT

Pipe diameter	10.0 mm	Adaptor diameter	0.0 mm
Pipe thickness	2.54 mm	Reference diameter	10.0 mm
Adaptor length	0 mm		

Transducer distance	calibration factor
0.020 m	1.3510 bar/V
0.310 m	1.3000 bar/V
0.725 m	1.3000 bar/V

3. Parameters used for the cancellation testing.

These parameters were used in ACQUIRE during the cancellation testing

FBN2 Version 4.000 Harmonic calibration data read from CAL2706.DAT

Pipe diameter	26.4 mm	Adaptor diameter	26.4 mm
Pipe thickness	2.67 mm	Reference diameter	26.4 mm
Adaptor length	79 mm		

Transducer distance	calibration factor
0.065 m	1.3510 bar/V
0.475 m	1.3000 bar/V
0.765 m	1.3000 bar/V

Appendix E The detail design of the HDCV prototype

This appendix details the HDCV prototypes described in chapters 8 and 9.

1. The Initial Prototype

Figure E.1 illustrates the design of the initial prototype. The parameters of this design were decided in the design process of section 8.2.5 and the simulation work of 8.3.

2. The 1st Working Prototype

Due to teething problems, the initial prototype was extensively modified to produce the 1st working prototype (See section 9.2.2). The portpalte for this design remained unchanged, but the valve block and HDCV assemblies were redesigned. The new valve block design is illustrated in figure E.2. The poppet and sleeve of the redesigned HDCV assemblies are detailed in figure E.3.

3. The Improved Working Prototype

The improved working prototype featured a 3rd. HDCV assembly (See figure 9.7 and section 9.2.5). The poppet and sleeve for this 3rd HDCV are detailed in figure E.4.

4. The Final Working Prototype

The final working prototype featured a modified poppet and sleeve for the 3rd. HDCV which are detailed in figure E.5.

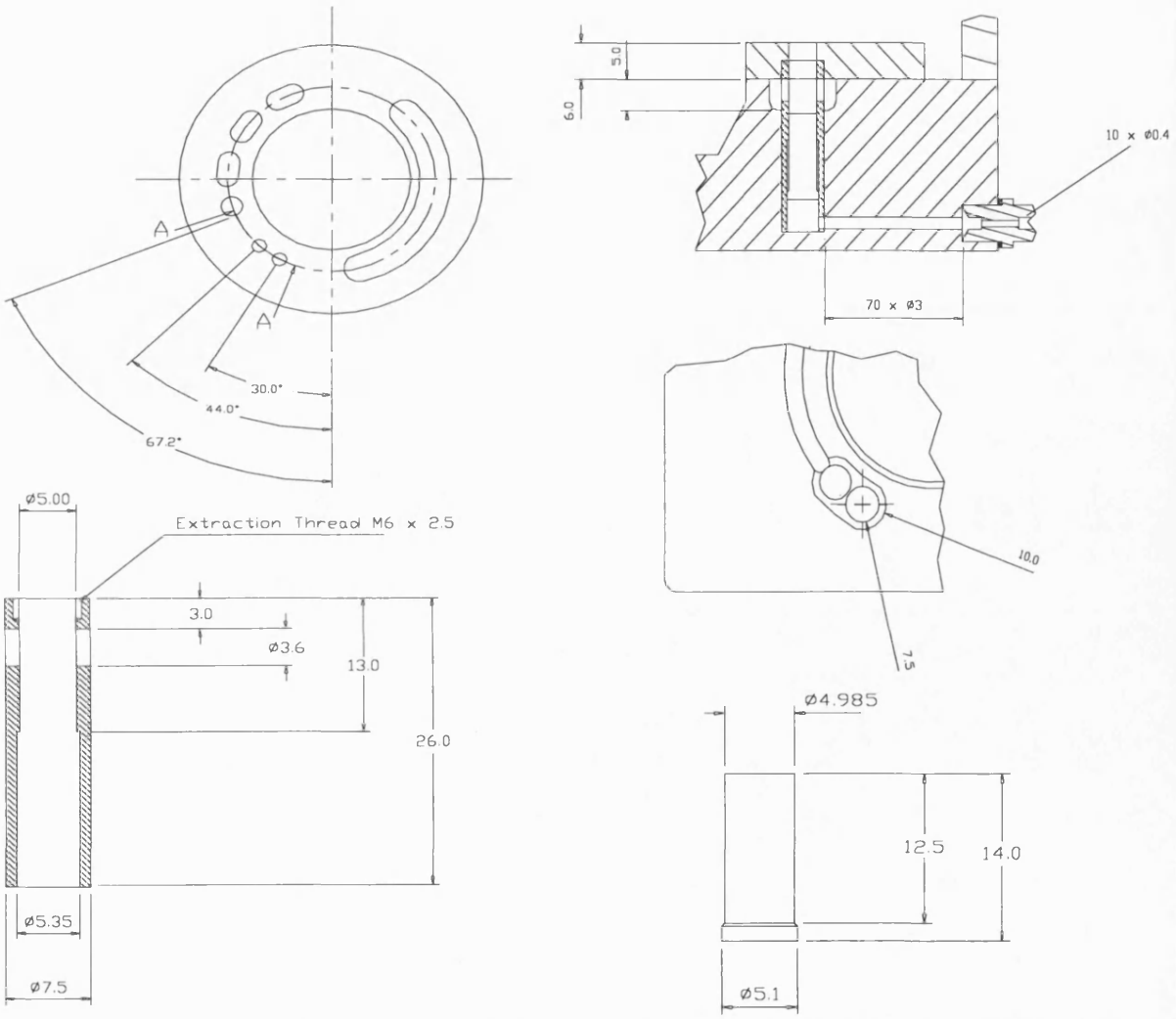

Parameter		Variable Name	Value
Spring Rate	N/m	K_s	440
Spring Preload (@ x=0mm)	N	K_p	2.446
Poppet length	mm	L_{pop}	10.7
Poppet Diameter	mm	D_{pop}	5.0
Poppet Mass	Kg	M	0.003
Sleeve Port Diameter	mm	D_{port}	3.6
Poppet-Sleeve radial clearance	mm	h	0.006
Damping Orifice Diameter	mm	D_{damp}	0.4
Damping Orifice Length	mm	L_{damp}	8

Figure E.1 Dimensions for the initial HDCV prototype

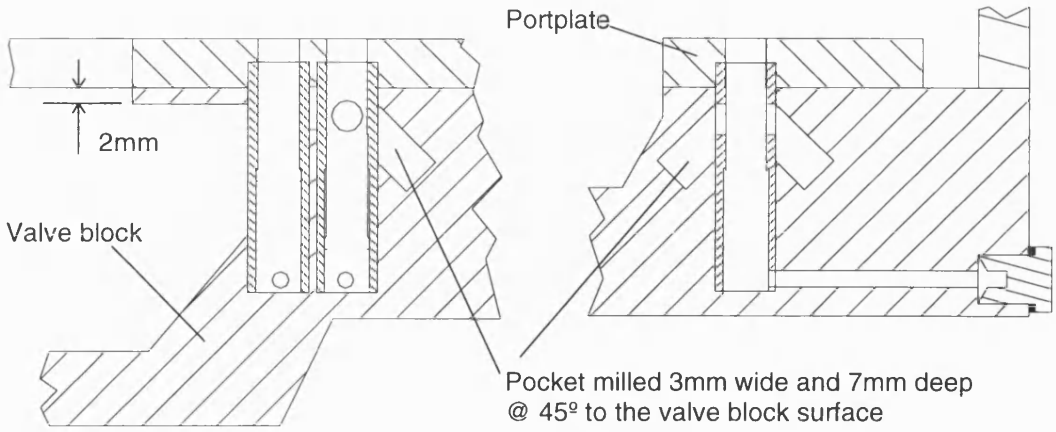

Figure E.2 Scheme of valve block of the 1st HDCV working prototype (showing the position of the HDCV sleeves)

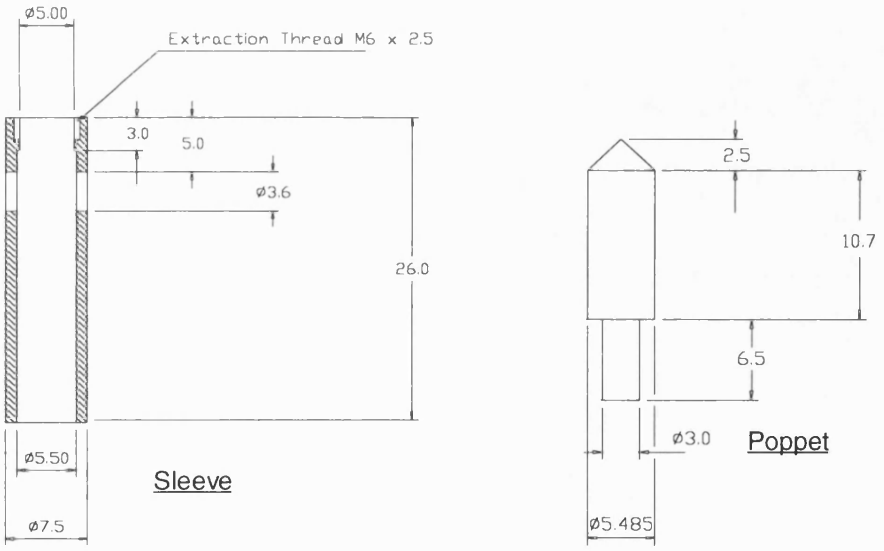

Figure E.3 Details of the poppet and sleeves design used for the 1st HDCV working prototype

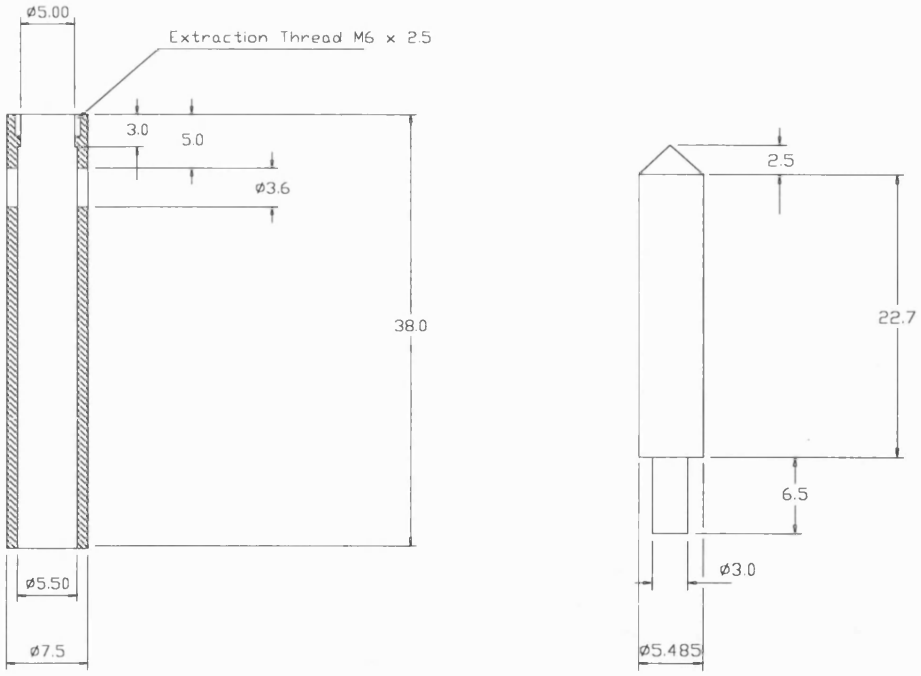

Figure E.4 Details of the poppet and sleeve used for the 3rd HDCV of the improved HDCV working prototype

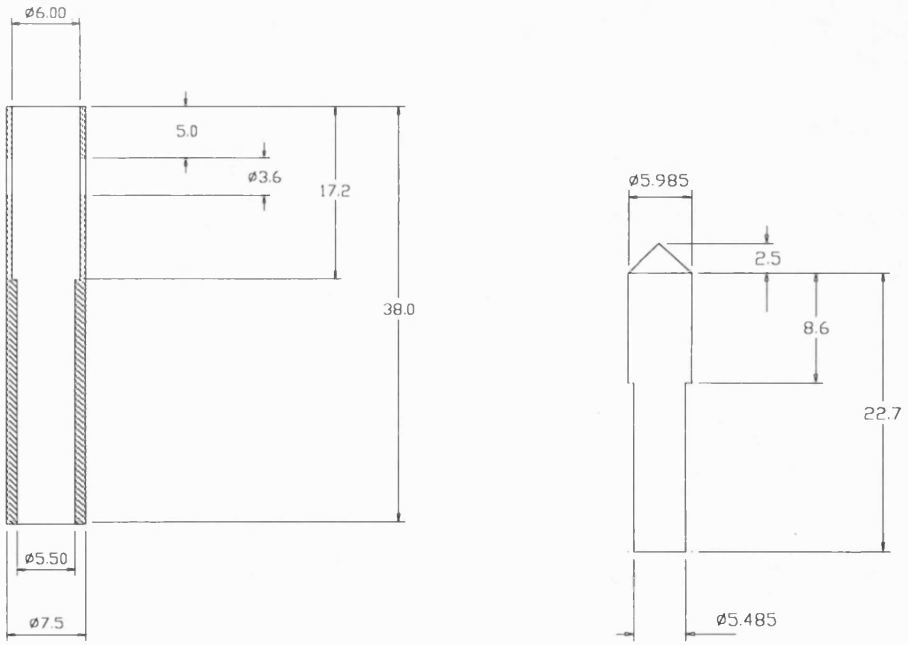

Figure E.5 Details of the poppet and sleeve used for the 3rd HDCV of the final HDCV working prototype

Appendix F Derivation of Mean Port Pressure Expressions

The purpose of this appendix is to show the derivation of expressions for the mean HDCV port pressure. This is then used in section 8.3.2.5 to predict the likely sleeve port openings at different delivery pressures and pump displacements. The equations shown apply to a pump fitted with two HDCVs ahead of a delayed delivery port in the scheme shown in figure 8.11.

Neglecting leakage then the pressure in a cylinder that has left the suction port, but is before the delivery port is given by;

$$\frac{P_{cyl}-P_{suc}}{B_{eff}}=\frac{V_{suc}-V_{cyl}(\theta)}{V_{suc}} \qquad \text{(E.1)}$$

The test pump is unboosted and so P_{suc} = 0 bar (gauge)

V_{suc} is the cylinder volume on leaving the suction port according to figure 8.11 such that,

$V_{suc}=V_{cyl}(\theta)$

When $\theta=\gamma=\left(\frac{\kappa_c}{2}+\alpha_s\right)$ and $V_{cyl}=A_{pist}(L_{mean}+R\tan\beta\cos\gamma)$ (E.2 and 3)

Therefore, from equations E.1, 2 and 3,

$$\frac{P_{cyl}}{B_{eff}}=\frac{R\tan\beta(\cos\gamma-\cos\theta)}{(L_{mean}+R\tan\beta\cos\gamma)} \quad \text{or} \quad P_{cyl}=\frac{B_{eff}(\cos\gamma-\cos\theta)}{\left(\frac{L_{mean}}{R\tan\beta}+\cos\gamma\right)} \qquad \text{(E.4 and 5)}$$

This equation applies until the cylinder reaches the delivery port or an open HDCV. At this point, cylinder pressure equalises to the pressure of delivery or of the open HDCV.

1. The Mean Port Pressure of the HDCV @ 44°

To calculate the mean port pressure of the HDCV at 44°, both HDCV ports are assumed to be closed (See 8.3.2.5). Therefore, equation E.5 describes the cylinder pressure until the cylinder reaches the delivery port. At this point the cylinder pressure equalises to the delivery pressure;

$$P_{cyl}=P_{del} \qquad @ \qquad \theta=\alpha_d-\left(\frac{\kappa_c}{2}\right) \qquad \text{(E.6)}$$

Furthermore, each cylinder passes over the port in the region illustrated in figure 8.11:

$$\alpha_2-\left(\frac{\kappa_c+\kappa_v}{2}\right)\le\theta\le\alpha_2+\left(\frac{\kappa_c+\kappa_v}{2}\right) \qquad \text{(E.7)}$$

Therefore, if both ports are closed and the port pressure can be approximated by the cylinder pressure then from E.5, E.6, and E.7,

$$P_{port}(2)=\frac{B_{eff}(\cos\gamma-\cos\theta)}{\left(\frac{L_{mean}}{R\tan\beta}+\cos\gamma\right)} \qquad \alpha_2-\left(\frac{\kappa_c+\kappa_v}{2}\right)\le\theta\le\alpha_d-\left(\frac{\kappa_c}{2}\right) \qquad \text{(E.8)}$$

$$P_{port}(2)=P_{del} \qquad \alpha_d-\left(\frac{\kappa_c}{2}\right)\le\theta\le\alpha_2+\left(\frac{\kappa_c+\kappa_v}{2}\right) \qquad \text{(E.9)}$$

For the case shown in figure 8.11, the HDCV port drillings subtend very nearly the same angle as the distance between adjacent cylinder ports. Therefore, the mean port pressure can be calculated by integrating equations E.8 and E.9 to give for the closed second HDCV:

$$\overline{P}_{port}(2)=\frac{1}{\kappa_c+\kappa_v}\left[\begin{array}{l}K\left\{c\left(\alpha_d+\alpha_2-\frac{\kappa_v}{2}\right)+\frac{180}{\pi}\left(\sin\left(\alpha_2-\frac{\kappa_v+\kappa_c}{2}\right)-\sin\left(\alpha_d-\frac{\kappa_c}{2}\right)\right)\right\}\\+P_{del}\left(\alpha_2+\kappa_c+\frac{\kappa_v}{2}-\alpha_d\right)\end{array}\right]$$

$$K=\frac{B_{eff}}{\left(\frac{L_{mean}}{R\tan\beta}+\cos\gamma\right)} \qquad \text{and} \qquad c=\cos\gamma \qquad \text{(E.10)}$$

2. The Mean Port Pressure of the HDCV @ 30°

To calculate the mean port pressure of the HDCV at 30°, the HDCV port at 44° is assumed open and the port at 30° assumed closed (See 8.3.2.5). Therefore, equation E.5 describes the cylinder pressure until the cylinder reaches the HDCV port at 44°. At this point the cylinder pressure equalises to the pressure of the HDCV port at 44° (Assumed to be at its cracking pressure: $P_{crack} = P_{del}+3.4bar$). When the cylinder then meets the delivery port then it will finally equalise to the delivery pressure. So,

$$P_{cyl}=P_{port}(2) \qquad @ \qquad \theta=\alpha_2-\left(\frac{\kappa_c+\kappa_v}{2}\right) \qquad \text{and then} \qquad \text{(E.11)}$$

$$P_{cyl}=P_{del} \qquad @ \qquad \theta=\alpha_d-\left(\frac{\kappa_c}{2}\right) \qquad \text{(E.6)}$$

From figure 8.10, each cylinder passes over the port when,

$$\alpha_1-\left(\frac{\kappa_c+\kappa_v}{2}\right)\le\theta\le\alpha_1+\left(\frac{\kappa_c+\kappa_v}{2}\right) \qquad \text{(E.12)}$$

Therefore, if both ports are closed and the port pressure can be approximated by the cylinder pressure then from E.5, E.11, E.6 and E.12,

$$P_{port}(1)=\frac{B_{eff}\,(\cos\gamma-\cos\theta)}{\left(\frac{L_{mean}}{R\tan\beta}+\cos\gamma\right)} \qquad \alpha_1-\left(\frac{\kappa_c+\kappa_v}{2}\right)\le\theta\le\alpha_2-\left(\frac{\kappa_c+\kappa_v}{2}\right) \qquad \text{(E.13)}$$

$$P_{port}(1)=P_{crack} \qquad \alpha_2-\left(\frac{\kappa_c+\kappa_v}{2}\right)\le\theta\le\alpha_d-\left(\frac{\kappa_c}{2}\right) \qquad \text{(E.14)}$$

$$P_{port}(1)=P_{del} \qquad \alpha_d-\left(\frac{\kappa_c}{2}\right)\le\theta\le\alpha_1+\left(\frac{\kappa_c+\kappa_v}{2}\right) \qquad \text{(E.15)}$$

Therefore, for the case shown in figure 8.10, the mean port pressure can be calculated by integrating equations E.13, E.14, and E.15 to give an expression for the mean port pressure of the HDCV at 30° (See E.10):

$$\overline{P}_{port}(1)=\frac{1}{\kappa_c+\kappa_v}\left[\begin{array}{l}K\left\{c(\alpha_2-\alpha_1)+\frac{180}{\pi}\left(\sin\left(\alpha_1-\frac{\kappa_v+\kappa_c}{2}\right)-\sin\left(\alpha_2-\frac{\kappa_v+\kappa_c}{2}\right)\right)\right\}\\+P_{crack}(\alpha_1+\kappa_c+\kappa_v-\alpha_2)\end{array}\right] \qquad \text{(E.16)}$$